MODELING THE EFFECTS OF SHOT-PEENED RESIDUAL STRESSES AND INCLUSIONS ON MICROSTRUCTURE-SENSITIVE FATIGUE OF NI-BASE SUPERALLOY COMPONENTS

A Dissertation
Presented to
The Academic Faculty

by

William D. Musinski

In Partial Fulfillment
of the Requirements for the Degree
Doctor of Philosophy in the
George W. Woodruff School of Mechanical Engineering

Georgia Institute of Technology
August 2014

MODELING THE EFFECTS OF SHOT-PEENED RESIDUAL STRESSES AND INCLUSIONS ON MICROSTRUCTURE-SENSITIVE FATIGUE OF NI-BASE SUPERALLOY COMPONENTS

Approved by:

Dr. David L. McDowell, Advisor
George W. Woodruff School of Mechanical Engineering
Georgia Institute of Technology

Dr. Ken Gall
Materials Science and Engineering
Georgia Institute of Technology

Dr. Richard W. Neu
George W. Woodruff School of Mechanical Engineering
Georgia Institute of Technology

Dr. Julian J. Rimoli
Guggenheim School of Aerospace Engineering
Georgia Institute of Technology

Dr. Olivier N. Pierron
George W. Woodruff School of Mechanical Engineering
Georgia Institute of Technology

Dr. Patrick J. Golden
Materials and Manufacturing Directorate
Air Force Research Laboratory

Date Approved: 28 April 2014

ACKNOWLEDGEMENTS

Completion of this work could not have been possible without the immense support from multiple people throughout my doctoral studies. First and foremost, I would like to thank my advisor, Dr. David L. McDowell for his patience, guidance, and encouragement throughout the completion of this work. I am truly grateful for the ability to pursue independent research under his direction. I have developed tremendously as a research professional and technical writer under his advisement which I will take with me for the rest of my life. I also would like to thank my dissertation reading committee, Drs. Richard Neu, Olivier Pierron, Ken Gall, Julian Rimoli, and Patrick Golden for reviewing this dissertation, attending the proposal and defense, and offering criticisms regarding this work. I also would like to thank Dr. Richard Neu for his teaching insight offered during the period I spent with him for teaching practicuum.

I have deeply enjoyed the great friendships and discussions with all my McDowell lab mates and others outside of the McDowell group. When I first started at Georgia Tech, I appreciate the senior members who got me started in the right direction, including Rob Matthews, Dr. Craig Przybyla, Dr. Rajesh Prasannavenkatesan, Dr. Moses Owolabi, Dr. Jason Mayeur, Dr. Ryan Austin, Dr. Garritt Tucker, and Dr. Nima Salajegheh. To all those who shared MRDC 3338, I enjoyed the deep (and sometimes not so deep) discussions regarding research, sports, and other life happenings. Specifically, I would like to thank Dr. Jeff Lloyd, Dr. Brett Ellis, Dr. Gustavo Castelluccio, Jin Song, Sam Britt, Ben Smith, Shreevant Tiwari, Dr. Anirban Patra, Matthew Priddy, Shuozhi Xu, and Dr. Jagan Padbidri, who have certainly enriched my time at Georgia Tech. I also enjoyed friendships outside the McDowell group including Dr. Mike Kirka, Siddharth Avachat, Chris Lammi, and Barrett Hardin.

I am extremely grateful for funding from multiple sources starting with the Pratt and Whitney/Georgia Tech Center of Excellence under technical lead Bob Grelotti,

fellowships provided by the George W. Woodruff School of Mechanical Engineering, and support from the Carter N. Paden, Jr. Distinguished Chair in Metals Processing held by Dr. David L. McDowell. I am also thankful for the last couple of years of support from the Air Force Research Laboratory in the form of a Southwestern Ohio Council for Higher Education (SOCHE) internship. There are many colleagues at AFRL that have provided technical and non-technical support in my research endeavors including Drs. Patrick Golden, Andy Rosenberger, Sushant Jha, Reji John, Dennis Buchanan, Jon Miller, Garth Wilks, and Christopher Crouse.

I am thankful for the computational resources provided by the Georgia Tech Partnership for an Advanced Computing Environment (PACE) and the U.S. Air Force Research Laboratory (AFRL) DoD Supercomputing Resource Center (DSRC) that supported many of the parametric studies performed in this work.

I would like to thank my mom and dad, Rose and Anthony, my older brothers, Brian and Aaron, and my extended family and friends who have supported me throughout my career. Last and definitely not least, I owe a great deal of gratitude towards my wife, Melissa. Thank you for loving and supporting me throughout this difficult process.

TABLE OF CONTENTS

LIST OF TABLES

LIST OF FIGURES

LIST OF ABBREVIATIONS AND SYMBOLS

1D/2D/3D	One/two/three-dimensional
AFRL	Air Force Research Laboratory
ALA	As large as
BC	Boundary condition
BVP	Boundary value problem
CG	Coarse-grained
CPFEM	Crystal plasticity finite element method
CTD	Crack tip displacement
CTOD	Crack tip opening displacement
CTSD	Crack tip sliding displacement
DIC	Digital image correlation
DS	Directionally-solidified
EBSD	Electron backscatter diffraction
EPFM	Elastic-plastic fracture mechanics
FCC	Face-centered cubic
FEM	Finite element method
FG	Fine-grained
FIB	Focused ion beam
FIP	Fatigue Indicator Parameter
FS	Fatemi-Socie
GB	Grain boundary
HAGB	High angle grain boundary
HCF	High cycle fatigue
HIP	Hot-isostatically-pressed
ICME	Integrated Computational Materials Engineering
ISV	Internal state variable
LAGB	Low angle grain boundary

LCF	Low cycle fatigue
LEFM	Linear elastic fracture mechanics
NMI	Non-metallic inclusion
PM	Powder metallurgy
PSB	Persistent slip band
PSC	Physically small crack
RMS	Root mean square
SEM	Scanning electron microscope
SIF	Stress intensity factor
SX	Single crystal
TEM	Transmission electron microscope
TMF	Thermomechanical fatigue
UMAT	User Material Subroutine
VHCF	Very high cycle fatigue
XRD	X-ray diffraction

α	Slip system or twist angle
α_g	Crack incubation variable
β	Tilt angle
$\boldsymbol{\sigma}$	Cauchy stress
$\boldsymbol{\sigma}^{pk2}$	Second Piola-Kirchhoff stress
$\boldsymbol{E}^e$	Elastic Green strain
$\boldsymbol{F}$	Deformation gradient
$\boldsymbol{F}^e, \boldsymbol{F}^p, \boldsymbol{F}^\theta$	Elastic, plastic, and quasi-thermal portions of deformation gradient
$\boldsymbol{I}$	Identity tensor
$\boldsymbol{L}^p$	Plastic velocity gradient
$\boldsymbol{m}^{(\alpha)}$	Normal direction for slip system α in current configuration
$\boldsymbol{m}_o^{(\alpha)}$	Normal direction for slip system α in reference configuration
$\boldsymbol{s}^{(\alpha)}$	Direction of slip for slip system α in current configuration
$\boldsymbol{s}_o^{(\alpha)}$	Direction of slip for slip system α in reference configuration

$\chi^{(\alpha)}$	Back stress on slip system (α)
$\dot{\gamma}^{(\alpha)}$	Shearing rate of slip system (α)
$\kappa^{(\alpha)}$	Threshold stress on slip system (α)
$\overline{d}_{GB}$	Normalized grain boundary distance
$\rho^{(\alpha)}$	Dislocation density for slip system (α)
$\tau^{(\alpha)}$	Resolved shear stress on slip system (α)
A_{FS}^{env}	MSC growth constant for environment *env*
a_N	Crack length at cycle N
$D^{(\alpha)}$	Drag stress on slip system (α)
d_2, d_3	Size of secondary and tertiary γ' precipitates
d_{grn}	Grain size
f_{p1}, f_{p2}, f_{p3}	Volume fraction of primary, secondary, and tertiary γ' precipitates
K	Stress intensity factor
k	Fatemi-Socie constant
N_{DB}	Number of cycles to debond inclusion from matrix
n_{env}	MSC growth exponent for environment *env*
N_{inc}	Number of cycles to incubate a crack
N_{LEFM}	Portion of fatigue life due to long crack (LEFM) growth
N_{MSC}	Portion of fatigue life due to microstructurally small crack growth
N_{PSC}	Portion of fatigue life due to physically small crack growth
N_T	Total number of cycles to failure
R_{GB}	Grain boundary resistance factor for MSC growth

SUMMARY

The simulation and design of advanced materials for fatigue resistance requires an understanding of the response of their hierarchical microstructure attributes to imposed load, temperature, and environment over time. For Ni-base superalloy components used in aircraft jet turbine engines, different competing mechanisms (ex. surface vs. subsurface, crystallographic vs. inclusion crack formation, transgranular vs. intergranular propagation) are present depending on applied load, temperature, and environment. Typically, the life-limiting features causing failure in Ni-base superalloy components are near surface inclusions. Compressive surface residual stresses are often introduced in Ni-base superalloy components to help retard fatigue crack initiation and early growth at near surface inclusions and shift the fatigue crack initiation sites from surface to sub-surface locations, thereby increasing fatigue life. To model the effects of residual stresses, inclusions, and microstructure heterogeneity on fatigue crack driving force and fatigue scatter, a computational crystal plasticity framework is presented that imposes quasi-thermal eigenstrain to induce near surface residual stresses in polycrystalline Ni-base superalloy IN100 smooth specimens with and without nonmetallic inclusions. In addition, the effect of near surface inclusions in notched Ni-base superalloy components on MSC growth and fatigue life scatter was investigated in this work. A fatigue indicator parameter (FIP)-based microstructurally small crack (MSC) growth model incorporating crack tip/grain boundary effects was introduced and fit to experiments (in both laboratory air and vacuum) for the case of 1D crack growth and then computationally applied to 3D crack growth starting (1) from a focused ion beam (FIB) notch in a smooth specimen, (2) from a debonded inclusion located at different depths within notched components containing different notch root radii, and (3) from inclusions located at different depths relative to the surface

in smooth specimens containing simulated shot-peened induced residual stresses. Computational predictions in MSC growth rate scatter and distribution of fatigue life were in general accordance with experiments.

The general approach presented in this Dissertation can be used to advance integrated computational materials engineering (ICME) by predicting variation of fatigue resistance and minimum life as a function of heat treatment/microstructure and surface treatments for a given alloy system and providing support for design of materials for enhanced fatigue resistance. In addition, this framework can reduce the number of experiments required to support modification of material to enhance fatigue resistance, which can lead to accelerated insertion (from design conception to production parts) of new or improved materials for specific design applications. Elements of the framework being advanced in this research can be applied to any engineering alloy.

CHAPTER 1
INTRODUCTION

1.1 Motivation

Nickel-base superalloys are used in aircraft gas turbine engine components (ex. blades, disks, spacers, and seals) due to their enhanced strength, creep resistance, fatigue resistance, and corrosion resistance at elevated temperatures ($\sim$ 650-1000°C). The fatigue mechanisms of Ni-base superalloys depend strongly on the response of their hierarchical microstructure attributes to imposed load, temperature, and environment over time [1–4]. In the high cycle fatigue (HCF) regime, since fatigue is a weakest-link phenomenon, cyclic plastic strain is often limited to a few fatigue critical "hot spots" where microstructure flaws (inclusions, pores, larger and/or favorably oriented grains, etc.) promote localized plastic slip intensification, fatigue crack formation and early growth. Thus, the ability to predict the microstructure features that promote plastic slip intensification is crucial in materials design for fatigue resistance. Current materials design methods for HCF resistance in Ni-base superalloys suffer from many problems and uncertainties: (1) an extensive amount of time is required (5-10 years) to qualify a new Ni-base superalloy material, (2) expensive material costs and time required to complete HCF experiments leads to limited experimental data sets, (3) variance in microstructure leads to scatter in fatigue response, (4) size effects (specimen- versus component-sized parts), and (5) different competing fatigue mechanisms are present depending on applied load, temperature, and environment. Therefore, limited experimental data are available to fully characterize the fatigue mechanisms responsible for the probabilistic distribution of HCF lives under a given temperature and loading condition. Understanding the life-limiting tail of this distribution is crucial for minimum fatigue life design because often turbine engine components are designed for a certain level of fatigue risk (usually 0.1% probability of failure [5]). Thus, we seek to use computational and probabilistic methods concurrently as a design tool to reduce the number of costly experiments required to predict the microstructure-sensitive HCF

and VHCF response of Ni-base superalloy components.

1.2 Aircraft Gas Turbine Engine Design Considerations

Nickel-base superalloys are processed through various techniques (casting, powder metallurgy), depending on the location-specitic microstructure desired (single crystal, directionally solidified, polycrystal) and the end product application (turbine disks, spacers, seals, blades). As shown in Figure 1.1, very fine-grained microstructures could potentially be used in disk bore regions (stress concentration regions) due to their very high strength and structural homogeneity. In the disk rim region, higher temperatures require the microstructure to be more creep-resistant, and, as a result, coarse-grained polycrystalline Ni-base superalloys could potentially be used in this region. Directionally-solidified and single crystal microstructures are used in the highest temperature locations such as turbine blades because they are more creep resistant through suppression or elimination of grain boundary diffusional creep and intergranular oxidation mechanisms at elevated temperatures. Hence, location-specific design of components (e.g., dual or hybrid microstructures [6]) could be used to optimize microstructure to meet operational requirements at different component regions.

The design of aircraft gas turbine engine components is complex and multifaceted. As shown in Figure 1.2, engineers and designers must consider the effect of the high-temperature operating environment on many input parameters, including:

- **Environmental effects:** At such high temperatures, these alloys are susceptible to environmental degradation, as shown in Figure 1.2 for a DS superalloy with fatigue crack formation at an oxide spike [11].

- **Microstructure effects:** Fatigue failure mechanisms depend on microstructure characteristics and loading conditions. For example, in fine grained Ni-base superalloys, tensile dwell periods can change the microstructurally small crack (MSC) growth mode from transgranular to intergranular resulting in a faster MSC growth rate [12].

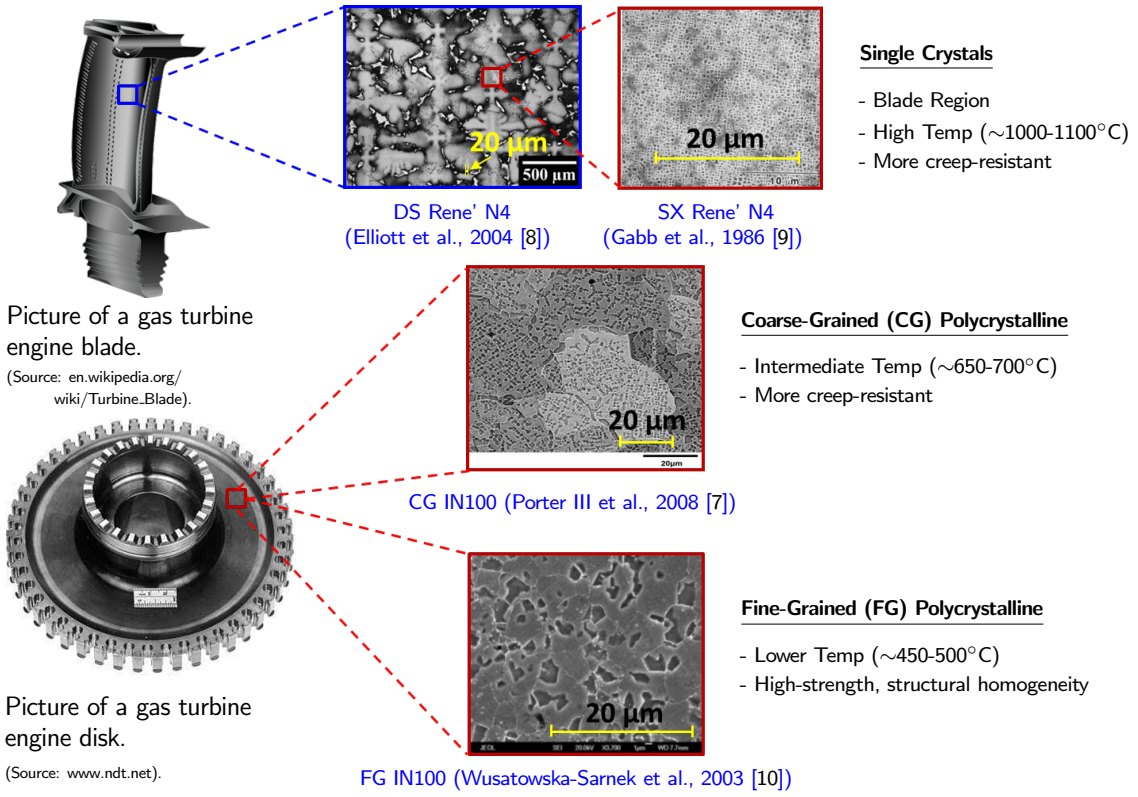

Figure 1.1: Potential use of single versus polycrystalline Ni-base superalloys.

- **Notch effects:** Notches exist in aircraft gas turbine engine components (e.g. cooling holes, disk bore, etc.) due to geometric/functional design requirements and are preferential zones for fatigue crack formation and early growth.

- **Inclusion and pore effects:** Materials processing induced inclusions and pores are often the life-limiting defect in these alloys.

- **Complex loading effects:** These components are subjected to very complex combined low cycle fatigue (LCF), HCF and thermomechanical fatigue (TMF) loading [13].

- **Residual stress relaxation effects:** At such extreme loading and temperature environments, residual stress relaxation can occur through fatigue loading and by means of thermal recovery [14–16].

The determination of these input parameter effects and optimization of aircraft gas turbine engine component design normally require extensive, time-consuming

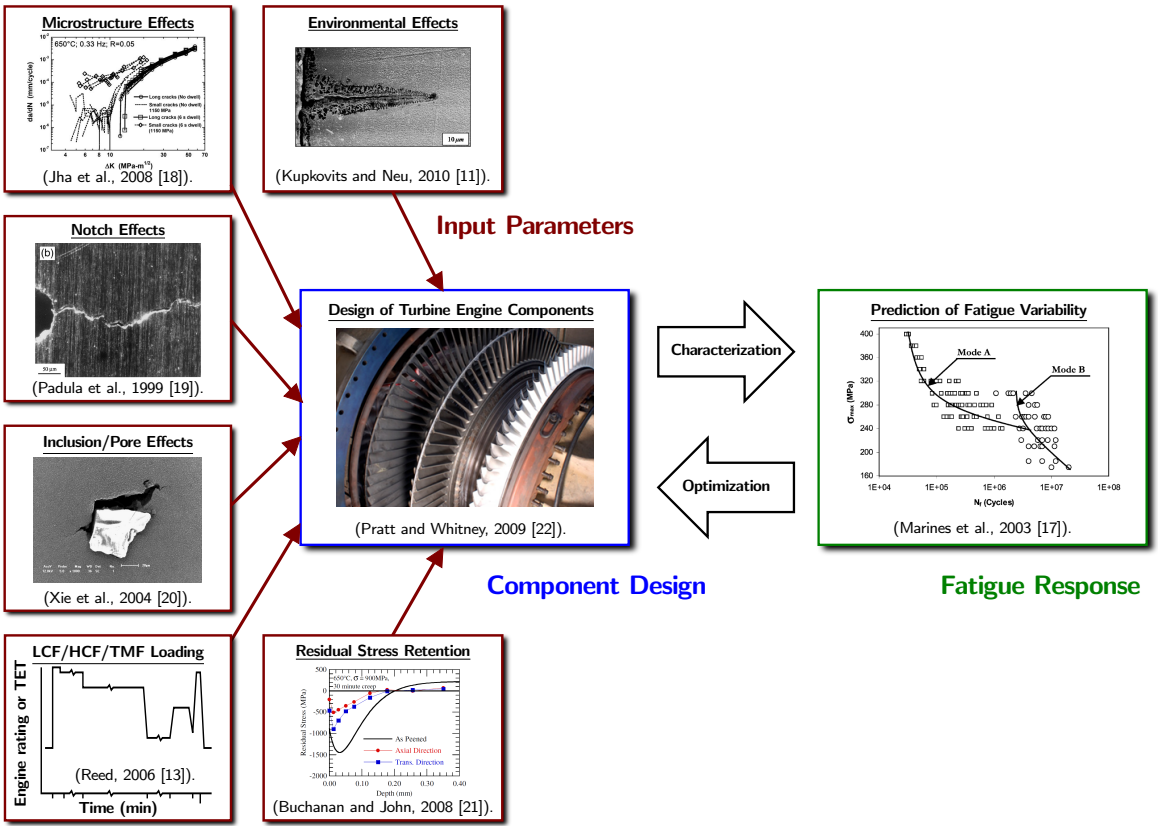

Figure 1.2: Multifaceted design of aircraft gas turbine engine components.

experimental characterization/optimization design loops to systematically establish the relative effect each individual input parameter has on fatigue variabilty. This work seeks to assist in reducing the number of experiments required by developing computational schemes that can help design, analyze and qualify new microstructures that are more fatigue resistant for a given application. Specifically, the purpose of this work is to analyze the effects of notches, inclusions, and process-induced residual stresses on the microstructure-sensitive HCF/VHCF (very high cycle fatigue) failure of smooth and notched polycrystalline Inconel 100 (IN100) Ni-base superalloy components.

1.3 Scope and Layout of Thesis

The main focus of this work is to use computational crystal plasticity to model the deformation and fatigue behavior of polycrystalline Ni-base superalloy IN100 smooth and notched components for applications in high temperature gas turbine

engine disks. An emphasis is placed on the following four areas: (1) simulating the effect of grain boundary character on MSC propagation, (2) determining the effect of inclusion depth on fatigue of notched components, (3) developing a framework to impose residual stresses using an eigenstrain approach within a finite element framework that is universally applicable to any specimen geometry, and (4) simulating the effectiveness of shot peening in suppressing near surface crack initiation from inclusions in polycrystalline IN100 at an elevated temperature of 650°C, which is representative of the operating temperature for coarse grain Ni-base superalloys. As a result, the remaining chapters of this Dissertation are framed as follows:

- Chapter 2 presents the polycrystalline plasticity framework used to model the complex deformation behavior of Ni-base superalloy IN100 at elevated temperatures.
- Chapter 3 describes how MSC propagation is modeled through a polycrystalline microstructure accounting for the grain boundary effects on MSC growth.
- Chapter 4 applies the framework described in Chapter 3 to the problem of inclusions located within the subsurface of notched polycrystalline IN100 components to determine the effect of inclusion depth on fatigue life.
- Chapter 5 presents an eigenstrain-based approach to apply an initial distribution of residual stresses within a crystal plasticity finite element method (CPFEM) model.
- Chapter 6 simulates the effectiveness of shot-peened residual stresses on suppressing fatigue crack formation and early growth for inclusions located near the surface of smooth specimens.
- Finally, Chapter 7 provides a summary and conclusions from this work, and suggests potential avenues for future work.

CHAPTER 2
POLYCRYSTALLINE PLASTICITY FRAMEWORK FOR IN100

2.1 Introduction

Nickel-base superalloys are processed through various techniques, depending on the end product characteristics and microstructure desired. The two means of preparing billets are casting and powder metallurgy (PM) techniques. These billets can be further processed through hot-isostatic pressing, extrusion, forging, machining and final protective coating application. Over the years, casting techniques have drastically improved the creep characteristics of Ni-base superalloys. The advent of directionally solidified and single-crystal superalloys greatly suppress or eliminate the grain boundary diffusional creep mechanism at higher temperatures. These types of casting processes allow for preferential orientation of the crystals to maximize fatigue resistance in that orientation.

For components made of many different chemical constituents, powder metallurgy processes are preferred in order to reduce individual phase segregation. The use of very fine powder and appropriate particle sifting techniques [13] can help decrease the number of nonmetallic inclusions and pores, which have a significant effect on fatigue crack nucleation and crack growth. Powder metallurgy has also been used to process very fine-grained Ni-base superalloy microstructures with very high strength and structural homogeneity. These fine-grain Ni-base superalloy microstructures are typically used for components operating in the intermediate temperature ($\sim 650°C$) regime such as disks, spacers and seals.

Nickel has a face-centered cubic (FCC) crystalline structure that is stable from room temperature to its melting point. Nickel-base superalloys are often strengthened through solid solution strengthening of the γ matrix and precipitation strengthening using $L1_2$ (ordered FCC) $\gamma^{'}$ precipitates in the austenitic γ matrix. Typically there can be three different size distributions of $\gamma^{'}$ precipitates (≈ 1.0 μm, ≈ 0.1 μm, and

$\approx$ 0.01 μm in diameter), often referred to as primary, secondary, and tertiary γ' precipitates, respectively. The larger primary γ' precipitates form during the first step of heat treatment (for subsolvus heat treatment) and typically form high-angle grain boundaries between the primary γ' precipitates and the γ matrix. The secondary and tertiary precipitates form during cooling and subsequent aging. These two precipitates are coherent with the γ matrix. Due to the unique deformation mechanisms in the ordered Ni_3Al γ' precipitates, these alloys display an anomalous yield strength with increasing temperature, up to about 800°C.

One of the limiting factors in fatigue performance in PM nickel-base superalloys is the presence of nonmetallic ceramic inclusions that serve as crack initiation sites [23,24]. These inclusions are often introduced to the molten metal, due to erosion or spalling of the crucible, tundish or nozzle, prior to the gas atomization process used to create the powder [13, 25]. To reduce the size and frequency of these particles, the metal powder is repeatedly sieved with screens of progressively finer mesh size to remove the largest harmful oxide particles [13, 25]. This screening process also removes the largest metal particles which reduces usable metal particle yield and increases overall production cost.

2.2 Key Features for Microstructure of Consideration

In this study, a supersolvus coarse-grained Ni-base superalloy Inconel 100 (IN100) is modeled. IN100 was first developed in cast form in the early 1960s and has been significantly improved due to PM processing. The use of PM processing is appropriate when considering the chemically complex microstructure with over 10 constituent elements (ref. Table 2.1). IN100 is used extensively for intermediate temperature ($\sim$ 650°C) applications such as turbine engine disks due to its enhanced strength, creep, fatigue, and corrosion resistance at these temperatures. The particular microstructure studied here is the coarse grain (CG) "super weak" microstructure outlined by Milligan et al. [26].

Following the forging process, the PM-processed Ni-base superalloy is heat-treated to create the final desired microstructure. The microstructure features differ depending

Table 2.1: Chemical Constituents of IN100 and Its Phases (Weight Percent) [27]

Alloy/Phase	Ni	Al	Cr	Co	Mo	Ti	V	Fe	C	Zr	B
IN100	56.0	4.9	12.3	18.3	3.3	4.3	0.70	0.10	0.06	0.02	0.02
γ matrix	38.7	2.25	24.5	27.8	5.73	0.93	0.05				
γ' ppt	71.8	7.06	2.59	8.94	1.42	6.97	1.23				

on the heat treatment process. A typical heat treatment for IN100 consists of a subsolvus (at 1143°C) or supersolvus (at 1205°C) heat treatment for 2 hours, followed by subsequent stabilization (at 982°C) for 1 hour and aging (at 732°C) for 8 hours [27], as shown in Figure 2.1. The γ' solvus temperature, or the temperature at which the phase transformation of $\gamma \rightarrow (\gamma + \gamma')$ occurs upon cooling, is approximately 1185°C. Often Ni-base superalloys are characterized based on whether the first heat treatment is above or below the solvus temperature (respectively, supersolvus and subsolvus). The heat treatment is selected based on the desired material properties of the end product. The strength of IN100 is highly dependent on a number of interrelated microstructure features including the volume fraction, particle size, particle distribution, and grain sizes of the γ matrix and γ' precipitate phases.

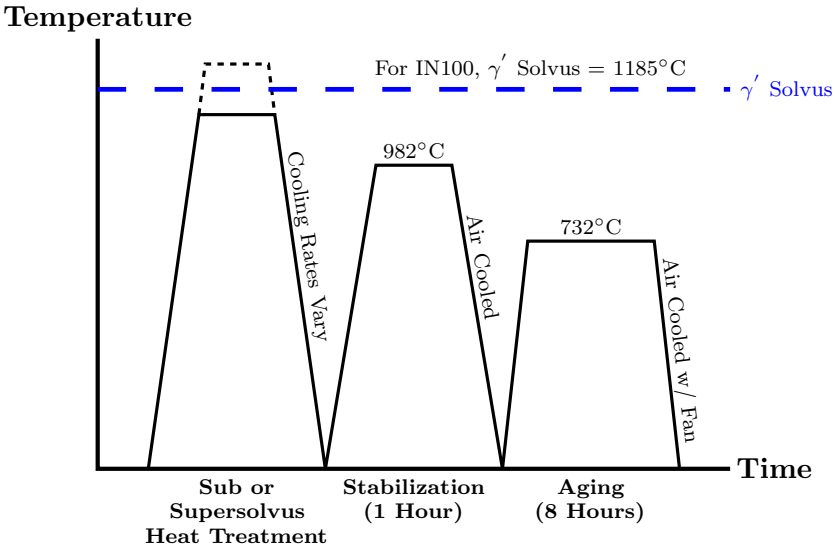

Figure 2.1: Typical heat treatment for subsolvus and supersolvus IN100 microstructures. After ref. [27].

Other minor phases are present in these alloys including carbides and borides. These phases are present in very low quantities (total volume fraction equal to about

1.6 %). Elongated carbides of the $M_{23}C_6$ type tend to form at the grain boundaries while smaller spherical particles of MC type are more predominantly located within the grain structure. Although it is possible to form topologically close-packed (TCP) phases σ, μ, and Laves phases in IN100, the exposure time required to form such phases is longer than the typical processing regime of these microstructures [28]. Therefore, the TCP phases are not present in the IN100 microstructures used in this study.

2.2.1 Fine Grain IN100

Fine-grained IN100 is produced using a subsolvus heat treatment. The primary γ' precipitates created in this step help control the grain size of the γ matrix through grain boundary pinning. As stated previously, the secondary and tertiary γ' precipitates are formed during subsequent cooling and aging processes. An example of a fine grain IN100 microstructure is shown in Figure 2.2 via scanning electron micrope (SEM) and transmission electron microscope (TEM) images. Note that the size of the primary γ' is of the same order of magnitude as the γ matrix grain size. Typical microstructure details of a subsolvus fine grain IN100, including size and volume fractions of each phase, are summarized in Table 2.2.

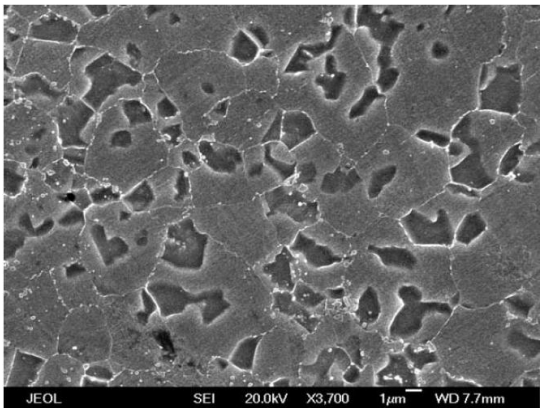

(a) Grain structure showing γ matrix (lighter gray) and primary γ' precipitate (darker gray) distribution [10].

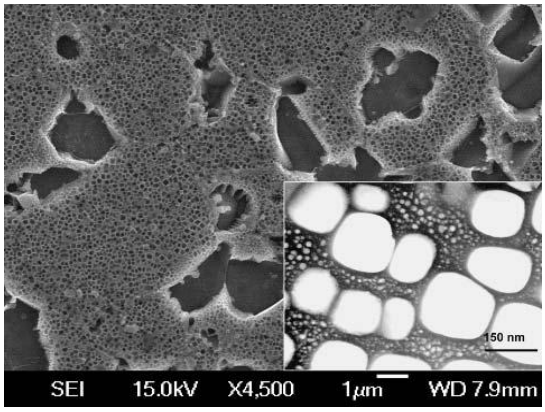

(b) Grain structure showing closer view of γ matrix (lighter gray) and primary γ' precipitate (darker gray) distribution. The inset is a dark-field TEM image which shows morphology of cuboidal secondary (large white) and tertiary (small white dots) γ' distribution [28].

Figure 2.2: SEM and TEM images of a fine grain subsolvus IN100 microstructure.

2.2.2 Coarse Grain IN100

Coarse grain IN100 microstructures are created through supersolvus heat treatment. During this heat treatment the primary $\gamma^{'}$ are dissolved, resulting in a bimodal distribution of precipitates. An example of a coarse grain IN100 is shown in Figure 2.3. As seen in these SEM images, the coarse grain IN100 has a bi-modal distribution of secondary and tertiary $\gamma^{'}$ precipitates. These precipitates are formed in the cooling and aging processing steps after the supersolvus heat treatment. The key microstructure details of the supersolvus coarse grain IN100 used in this study are summarized in Table 2.2.

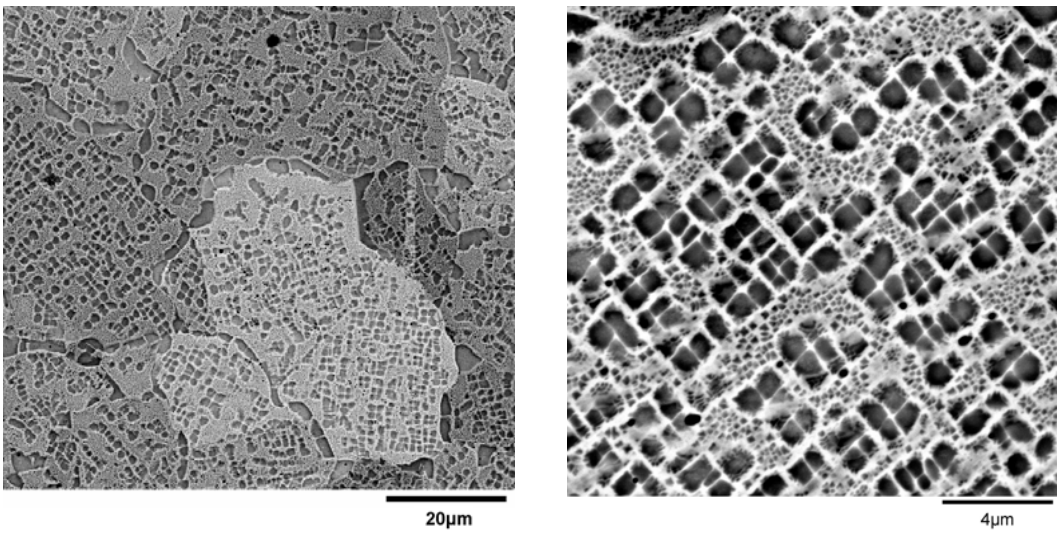

(a) Grain structure showing secondary $\gamma^{'}$ distribution.

(b) Grain structure showing secondary and tertiary $\gamma^{'}$ distribution.

Figure 2.3: SEM images of a coarse grain supersolvus IN100 microstructure [7].

Table 2.2: Microstructural Details for IN100 [26].

Material	Primary $\gamma^{'} f_{p1}$	Secondary $\gamma^{'} d_2$(nm)	Secondary $\gamma^{'} f_{p2}$	Tertiary $\gamma^{'} d_3$(nm)	Tertiary $\gamma^{'} f_{p3}$	Grain d_{gr}(µm)
Coarse Grain (CG)	-	340	0.46	11	0.137	34
Fine Grain (FG)	0.25	109	0.32	21	0.024	4.2

2.3 Crystal Plasticity Finite Element Model for IN100

To model the complex behavior of the coarse grain IN100 microstructure, a fully three-dimensional computational crystal plasticity finite element method (CPFEM) model is used. The crystal plasticity model used here follows that of Przybyla and McDowell [29]. The key points of this model are reviewed here. More details on the development of the IN100 model and the numerical implementation technique in ABAQUS can be found in the work of Shenoy et al. [30, 31] and McGinty [32], respectively. The IN100 constitutive model is a rate-dependent, microstructure-sensitive model used to capture the first order effects on the macroscopic stress-strain response due to grain size, $\gamma^{'}$ precipitate size distribution and $\gamma^{'}$ precipitate volume fraction. These microstructure features all greatly affect the material and fatigue response of nickel-base superalloys. This model was calibrated to complex cyclic stress-strain data of multiple microstructure variations at an operating temperature of 650°C with and without hold times [30]. Physically-based hardening models are used based on dislocation/precipitate interactions evidenced from experiments.

The kinematics of deformation are based on the fundamental multiplicative decomposition of the deformation gradient, $\mathbf{F}$, into an elastic portion, $\mathbf{F^e}$, and a plastic portion, $\mathbf{F}^p$, i.e. $\mathbf{F} = \mathbf{F}^e \cdot \mathbf{F}^p$. The elastic portion, $\mathbf{F}^e$ takes into account the elastic lattice distortion and rotation and $\mathbf{F}^p$ addresses dislocation glide along crystallographic slip planes. The elastic Green strain and second Piola-Kirchhoff stress tensor are denoted by $\mathbf{E}^e = \frac{1}{2}\left(\mathbf{F}^{eT} \cdot \mathbf{F}^e - 1\right)$ and $\boldsymbol{\sigma}^{pk2} = \det\left(\mathbf{F}^e\right)\mathbf{F}^{e-1} \cdot \boldsymbol{\sigma} \cdot \mathbf{F}^{e-T}$, respectively. Assuming small elastic strains, ($\boldsymbol{\epsilon}^e \approx \mathbf{E}^e$), the linear hyperelastic relation is given by $\boldsymbol{\sigma}^{pk2} = \mathbf{C} : \mathbf{E}^e$, where $\mathbf{C}$ is the fourth rank anisotropic elasticity tensor of the crystal.

In the reference configuration, the slip plane unit normal vector $\mathbf{m}_o^{(\alpha)}$ and slip direction unit vector $\mathbf{s}_o^{(\alpha)}$ for each slip system (α) frame the plastic velocity gradient in the intermediate configuration via

$$\mathbf{L}^p = \dot{\mathbf{F}}^p \cdot \mathbf{F}^{p-1} = \sum_{\alpha=1}^{N_{slip}} \dot{\gamma}^{(\alpha)} \left(\mathbf{s}_o^{(\alpha)} \otimes \mathbf{m}_o^{(\alpha)}\right) \tag{2.1}$$

where $\dot{\gamma}^{(\alpha)}$ is the shearing rate for each slip system (α). The slip system normals and directions in the current configuration are respectfully related to that in the reference

configuration $\mathbf{s}^{(\alpha)} = \mathbf{F}^e \cdot \mathbf{s}_o^{(\alpha)}$ and $\mathbf{m}^{(\alpha)} = \mathbf{m}_o^{(\alpha)} \cdot \mathbf{F}^{e-1}$. Thus, the resolved shear stress on each slip system is $\boldsymbol{\tau}^{(\alpha)} = \boldsymbol{\sigma} : \left(\mathbf{s}^{(\alpha)} \otimes \mathbf{m}^{(\alpha)}\right)$, where $\boldsymbol{\sigma}$ is the Cauchy stress.

The shearing rate on each slip system is given by a two-term potential flow rule [33]

$$\dot{\gamma}^{(\alpha)} = \left[\dot{\gamma}_1 \left\langle \frac{\left|\tau^{(\alpha)} - \chi^{(\alpha)}\right| - \kappa^{(\alpha)}}{D^{(\alpha)}} \right\rangle^{n_1} + \dot{\gamma}_2 \left\langle \frac{\left|\tau^{(\alpha)} - \chi^{(\alpha)}\right|}{D^{(\alpha)}} \right\rangle^{n_2} \right] \operatorname{sgn}\left(\tau^{(\alpha)} - \chi^{(\alpha)}\right) \quad (2.2)$$

Here $\dot{\gamma}_1$ and $\dot{\gamma}_2$ are constants, n_1 and n_2 are flow exponents, $\kappa^{(\alpha)}$ is the threshold stress, and D^{α} is an average drag resistance. The first term in Equation 2.2 captures the dominant cyclic behavior with the threshold stress playing the role of yield strength. The second term incorporates the effect of thermally activated creep at lower stresses. At lower stresses, the first term may not be active, and the dominant flow mechanisms are controlled by heterogeneous partial dislocation dissociation and matrix faulting. The use of a two term flow rule is necessary to model complex cyclic stress-strain histories.

The anomalous yield behavior of nickel base superalloys can be attributed to the unique deformation mechanisms in its constituent phases. As mentioned previously, the γ matrix is an FCC crystalline lattice. At lower temperatures, dislocation motion within the matrix is often limited to planar slip along the 12 octahedral slip planes $\langle 110 \rangle$ $\{111\}$, which is typical for the FCC lattice structure. At higher temperatures, macroscopic slip traces have shown evidence of an additional activation of 6 "cube" slip systems $\langle 110 \rangle$ $\{001\}$. Upon further investigation through transmission electron microscopy (TEM), Bettge and Österle [34] discovered that this cube slip was actually due to thermal activation of "zig-zag" cross slip of screw dislocations (Fig. 2.4(a)). As the screw dislocations migrate through $\gamma^{'}$ precipitate channels, they are blocked at the $\gamma/\gamma^{'}$ interface causing the zig-zag cross slip mechanism (cf. Figure 2.4(b)). Thus, at higher temperatures, cross slip creates complicated forest dislocation interaction which increases the dislocation density and restricts further motion of mobile dislocations. Therefore, we employ two internal state variables (ISVs) to describe the microstructure evolution of IN100, namely dislocation density, $\rho^{(\alpha)}$, and the back stress, $\chi^{(\alpha)}$. Based on the above considerations, we model 12 octahedral slip systems $\langle 110 \rangle$ $\{111\}$ and 6 "cube" slip systems $\langle 110 \rangle$ $\{001\}$ in IN100.

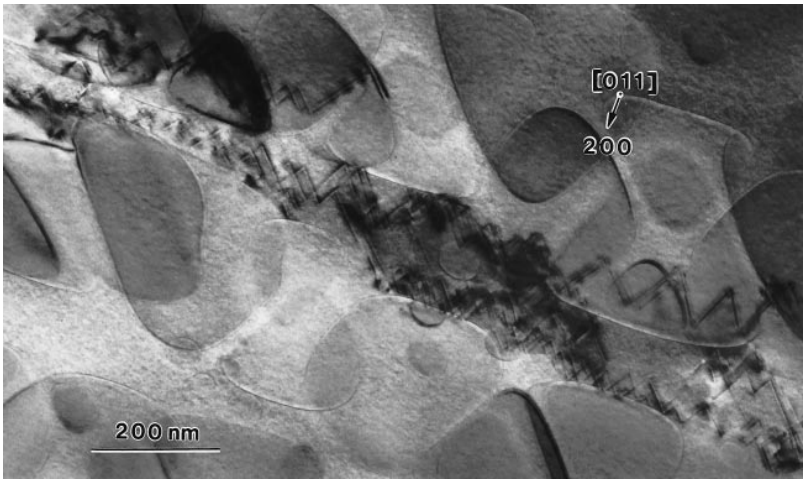

(a) TEM bright field micrograph showing zig-zag dislocation configuration in a single crystal Ni-base superalloy SC16 specimen deformed to 0.2% strain at 650° [34].

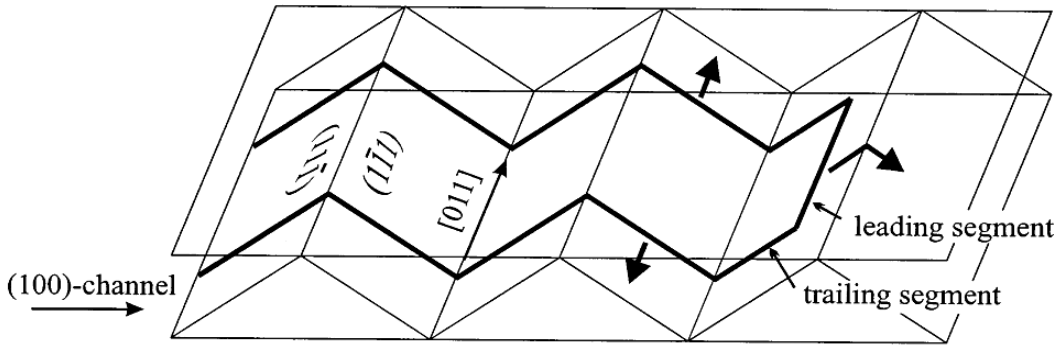

(b) Schematic of zig-zag {111} slip in the {100} γ' channels [34].

Figure 2.4: Illustration of zig-zag "cube" slip in a near-[111] oriented single crystal Ni-base superalloy SC16 [34].

The hardening of the threshold stress on each slip system is assumed to follow the Taylor relation

$$\kappa_{\lambda}^{(\alpha)} = \kappa_{o,\lambda}^{(\alpha)} + \alpha_t \ \tilde{\mu} \ \tilde{b} \ \sqrt{\rho_{\lambda}^{(\alpha)}} \tag{2.3}$$

In Equation 2.3, λ represents either octahedral or cube slip systems and $\rho^{(\alpha)}$ is the dislocation density on each slip system. The shear modulus $\tilde{\mu}$ follows a rule of mixtures $\tilde{\mu} = (f_{p1} + f_{p2} + f_{p3})\,\mu_{\gamma'} + f_m \mu_m$, where f_{p1}, f_{p2}, f_{p3}, and f_m are the volume fractions of the primary $\gamma^{'}$, secondary $\gamma^{'}$, tertiary $\gamma^{'}$ and matrix phases respectively, and $\mu_{\gamma'}$ and μ_m are the shear moduli of the precipitate and matrix phases. Similarly, an effective burgers vector is employed, $\tilde{b} = (f_{p1} + f_{p2} + f_{p3})\ b_{\gamma'} + f_m\ b_m$, where $b_{\gamma'}$ and b_m are the burgers vectors of the $\gamma^{'}$ precipitates and matrix, respectively. Also, α_t is a statistical coefficient that accounts for spatial arrangements of the dislocation population. The initial critical resolved shear stress (CRSS), $\kappa_{o,\lambda}^{(\alpha)}$ is based on the work of Reppich and co-workers [35, 36] and is given as:

$$\begin{aligned}
\kappa_{o,\text{oct}}^{(\alpha)} &= \left[\left(\tau_{o,\text{oct}}^{(\alpha)}\right)^{n_\kappa} + \Psi_{\text{oct}}\left(f_{p1}, d_2, f_{p2}, d_3, f_{p3}\right)^{n_\kappa}\right]^{1/n_\kappa} + (f_{p1} + f_{p2})\ \tau_{ns}^{(\alpha)} \\
\kappa_{o,\text{cub}}^{(\alpha)} &= \left[\left(\tau_{o,\text{cub}}^{(\alpha)}\right)^{n_\kappa} + \Psi_{\text{cub}}\left(f_{p1}, d_2, f_{p2}, d_3, f_{p3}\right)^{n_\kappa}\right]^{1/n_\kappa}
\end{aligned} \tag{2.4}$$

where

$$\begin{aligned}
\Psi_{oct} &= \Psi_{cub} \\
&= \left[c_{p1}\sqrt{\zeta\frac{f_{p1}^{'}}{d_1}} + c_{p2}\sqrt{\zeta\frac{f_{p2}^{'}}{d_2}} + c_{p3}\sqrt{\zeta\ f_{p3}^{'}\ d_3} + \frac{c_{gr}}{\sqrt{d_{gr}}}\right]
\end{aligned} \tag{2.5}$$

In this equation, $\zeta = \frac{\Gamma_{APB}}{\Gamma_{APB,ref}}$ where Γ_{APB} is the anti-phase boundary energy. Also, d_1, d_2, and d_3, are the sizes of the primary, secondary, and tertiary $\gamma^{'}$ precipitates, respectively, while d_{grn} is the grain size. The exponent n_κ ranges from 1-1.2, and c_{p1}, c_{p2}, c_{p3}, and c_{gr} are determined by fitting the initial yield strength to the experimental data. The non-Schmid stress dependence of the octahedral slip systems is given by $\tau_{ns}^{(\alpha)} = h_{pe}\tau_{pe}^{(\alpha)} + h_{cb}\left|\tau_{cb}^{(\alpha)}\right| + h_{se}\tau_{se}^{(\alpha)}$ [37–40], where $\tau_{pe}^{(\alpha)}$, $\tau_{cb}^{(\alpha)}$, and $\tau_{se}^{(\alpha)}$ are the resolved shear stresses on the primary, cube and secondary slip systems, respectively and h_{pe}, h_{cb}, and h_{se} are constants. The normalized precipitate volume fractions are defined by

$$f_{p1}^{'} = \frac{f_{p1}}{f_{p1} + f_m}, \qquad f_{p2}^{'} = \frac{f_{p2}}{f_{p2} + f_m}, \qquad f_{p3}^{'} = \frac{f_{p3}}{f_{p3} + f_m}. \tag{2.6}$$

During plastic deformation partial dislocations travel in pairs in order to retain order in the crystalline structure. When a pair of partial dislocations encounter a γ' precipitate obstacle, the dislocations can shear the obstacle, pile up at the obstacle, loop around the obstacle, or avoid the obstacle through cross slip. In Ni-base superalloys these precipitate dislocation interactions depend strongly on the precipitate size: (1) for underaged precipitates ($< 100\,\text{nm}$), shearing takes place by weakly coupled dislocation pairs and the CRSS increases with precipitate size, (2) for slightly larger particles ($100\,\text{nm} < d_p < 400\,\text{nm}$), shearing occurs by strongly coupled dislocation pairs and the CRSS decreases as a function of the precipitate size, and (3) for overaged particles ($> 400\,\text{nm}$), dislocation looping can occur depending on precipitate distribution, and is promoted by increasing temperature. The relationship between weak and strong dislocation pairs as a function of precipitate size is schematically shown in Figure 2.5.

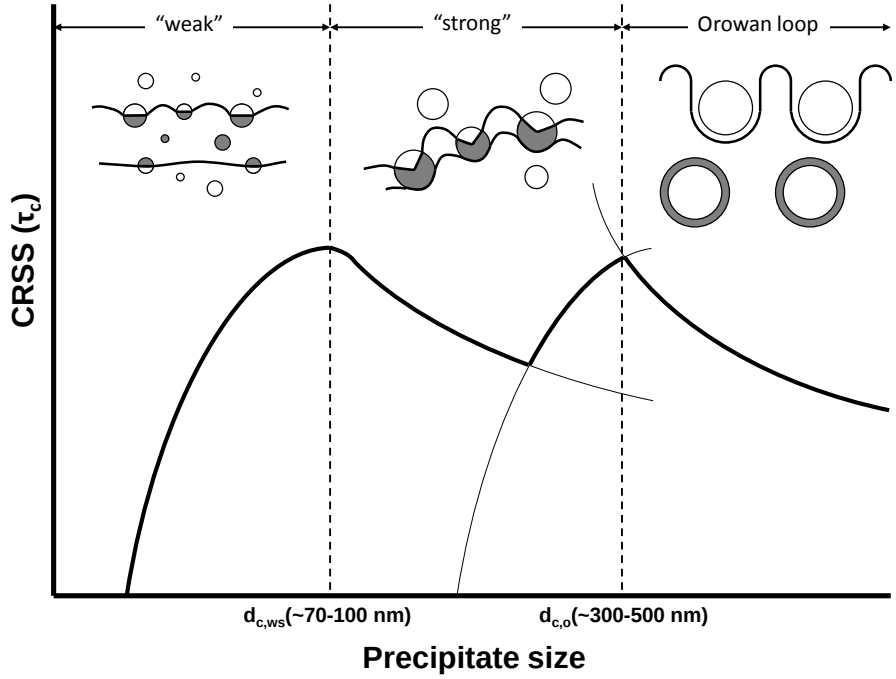

Figure 2.5: Schematic of theoretically expected CRSS as a function of particle size. After ref. [41].

The first two terms in Equation 2.5 account for increase of the CRSS by the shearing of the (small) primary and secondary precipitates by strongly coupled dislocation pairs and the third term represents shearing of tertiary precipitates by weakly coupled

dislocation pairs as evidenced by TEM observations of deformation of KM4, a similar Ni-base superalloy, at a temperature of 650°C [42]. The last term in Equation 2.5 is based on the Hall-Petch relationship in which the CRSS increases with decreasing grain size.

In this model, hardening is assumed to be a function of dislocation storage, dynamic recovery, and the size and spacing of $\gamma^{'}$ precipitates. Dislocation storage includes statistically stored dislocations (SSDs) and geometrically necessary dislocations (GNDs) [43]. Dynamic recovery is due to dislocation annihilation and rearrangement. The rate of dislocation recovery is assumed to be directly proportional to the dislocation density [44]. Thus, the evolution of dislocation density is given by

$$\dot{\rho}_{\lambda}^{(\alpha)} = h_o \left\{ Z_o + k_1 \sqrt{\rho_{\lambda}^{(\alpha)}} - k_2 \ \rho_{\lambda}^{(\alpha)} \right\} \left| \dot{\gamma}^{(\alpha)} \right| \tag{2.7}$$

and

$$Z_o = \frac{k_{\delta}}{\tilde{b} \ d_{\delta \text{eff}}}, \quad d_{\delta \text{eff}} \approx \left(\frac{2}{d_{2\delta}} \right)^{-1} \tag{2.8}$$

where the $k_1 \sqrt{\rho_{\lambda}^{\alpha}}$ represents dislocation storage and $k_2 \rho_{\lambda}^{\alpha}$ represents dynamic recovery. Also, k_1, k_2, and k_{δ} are constants and $d_{2\delta}$ and $d_{\delta \text{eff}}$ represent secondary and equivalent precipitate spacing, respectively. In Equation 2.7, the hardening coefficients for the octahedral and cube slip systems are $h_o = 4.8$ and $h_o = 2.4$, respectively.

To capture the Bauschinger effect, a back stress term, $\chi^{(\alpha)}$, is used. The evolution of back stress follows the form

$$\dot{\chi}_{\lambda}^{(\alpha)} = C_{\chi} \left\{ \eta \ \tilde{\mu} \ \tilde{b} \ \sqrt{\rho_{\lambda}^{(\alpha)}} \ \text{sgn} \left(\tau^{(\alpha)} - \chi_{\lambda}^{(\alpha)} \right) - \chi_{\lambda}^{(\alpha)} \right\} \left| \dot{\gamma^{(\alpha)}} \right| \tag{2.9}$$

and

$$\eta = \frac{\eta_o \ Z_o}{Z_o + k_1 \sqrt{\rho_{\lambda}^{(\alpha)}}} \tag{2.10}$$

where C_{χ} is a fitting parameter, and η reflects the relative proportion of GNDs to total dislocation density.

A summary of the constitutive equations are shown in Table 2.3. The above constitutive model is implemented as a user defined material (UMAT) subroutine in ABAQUS [45].

2.3.1 Model Calibration

Using the above framework, Shenoy et al. [30] used fully 3D finite element analysis to fit the above constitutive responses to very complex cyclic stress-strain behavior. Strain histories with and without hold periods at maximum strain were used to estimate the time-dependent behavior of the stress strain curve at a temperature of 650°C, the intended gas turbine disk operating temperature. See Shenoy et al. [30] for stress-strain response calibration of the coarse grain (super weak) IN100 microstructure used in the current study. The microstructure-sensitive crystal plasticity constants fitted through experiments are listed in Table 2.4.

Table 2.3: Microstructure-sensitive crystal plasticity constitutive equations for IN100.

Flow rule with back stress, threshold stress and drag stress

$$\dot{\gamma}^{(\alpha)} = \left[\dot{\gamma}_1 \left\langle \frac{\left|\tau^{(\alpha)} - \chi^{(\alpha)}\right| - \kappa_\lambda^{(\alpha)}}{D^{(\alpha)}} \right\rangle^{n_1} + \dot{\gamma}_2 \left\langle \frac{\left|\tau^{(\alpha)} - \chi^{(\alpha)}\right|}{D^{(\alpha)}} \right\rangle^{n_2}\right] \operatorname{sgn}\left(\tau^{(\alpha)} - \chi^{(\alpha)}\right)$$

Threshold Stress

$$\kappa_\lambda^{(\alpha)} = \kappa_{o,\lambda}^{(\alpha)} + \alpha_t\ \tilde{\mu}\ \tilde{b}\ \sqrt{\rho_\lambda^{(\alpha)}} \quad \text{for} \quad \lambda = \text{oct, cub,}$$

where $\quad \tilde{\mu} = (f_{p1} + f_{p2} + f_{p3})\ \mu_{\gamma'} + f_m\ \mu_m, \qquad \tilde{b} = (f_{p1} + f_{p2} + f_{p3})\ b_{\gamma'} + f_m\ b_m$

Initial Thresholds

$$\kappa_{o,\text{oct}}^{(\alpha)} = \left[\left(\tau_{o,\text{oct}}^{(\alpha)}\right)^{n_\kappa} + \Psi_{\text{oct}}\left(f_{p1}, d_2, f_{p2}, d_3, f_{p3}\right)^{n_\kappa}\right]^{1/n_\kappa} + (f_{p1} + f_{p2})\ \tau_{ns}^{(\alpha)}$$

$$\kappa_{o,\text{cub}}^{(\alpha)} = \left[\left(\tau_{o,\text{cub}}^{(\alpha)}\right)^{n_\kappa} + \Psi_{\text{cub}}\left(f_{p1}, d_2, f_{p2}, d_3, f_{p3}\right)^{n_\kappa}\right]^{1/n_\kappa}$$

where

$$\tau_{ns}^{(\alpha)} = h_{pe}\tau_{pe}^{(\alpha)} + h_{cb}\left|\tau_{cb}^{(\alpha)}\right| + h_{se}\tau_{se}^{(\alpha)} \quad \text{(non-schmid term)}$$

$$\Psi_{oct} = \Psi_{cub} = \left[c_{p1}\sqrt{\zeta\frac{f_{p1}^{'}}{d_1}} + c_{p2}\sqrt{\zeta\frac{f_{p2}^{'}}{d_2}} + c_{p3}\sqrt{\zeta\ f_{p3}^{'}\ d_3} + \frac{c_{gr}}{\sqrt{d_{gr}}}\right],$$

$$\zeta = \frac{\Gamma_{APB}}{\Gamma_{APB,ref}}, \quad f_{p1}^{'} = \frac{f_{p1}}{f_{p1} + f_m}, \quad f_{p2}^{'} = \frac{f_{p2}}{f_{p2} + f_m}, \quad f_{p3}^{'} = \frac{f_{p3}}{f_{p3} + f_m},$$

Internal State Variables

(a) Dislocation Density:

$$\dot{\rho}_\lambda^{(\alpha)} = h_o\left\{Z_o + k_1\sqrt{\rho_\lambda^{(\alpha)}} - k_2\ \rho_\lambda^{(\alpha)}\right\}\left|\dot{\gamma}^{(\alpha)}\right| \quad \text{(self-hardening)}$$

$$Z_o = \frac{k_\delta}{\tilde{b}\ d_{\delta\text{eff}}}, \qquad d_{\delta\text{eff}} \approx \left(\frac{2}{d_{2\delta}}\right)^{-1}$$

(b) Back Stress:

$$\dot{\chi}_\lambda^{(\alpha)} = C_\chi\left\{\eta\ \tilde{\mu}\ \tilde{b}\ \sqrt{\rho_\lambda^{(\alpha)}}\ \operatorname{sgn}\left(\tau^{(\alpha)} - \chi_\lambda^{(\alpha)}\right) - \chi_\lambda^{(\alpha)}\right\}\left|\dot{\gamma^{(\alpha)}}\right| \quad \text{(self-hardening)}$$

$$\eta = \frac{\eta_o\ Z_o}{Z_o + k_1\sqrt{\rho_\lambda^{(\alpha)}}}$$

Table 2.4: Parameters of the microstructure-sensitive crystal plasticity model of coarse grain IN100 at 650°C [46].

α_t	C_χ	$d_{1\delta}$(nm)	$d_{2\delta}$(nm)	$\dot{\gamma}_1(x10^{-10}s^{-1})$
0.1	2	-	15	0.417

$\tau^{(\alpha)}_{o,\mathrm{oct}}$(MPa)	$\tau^{(\alpha)}_{o,\mathrm{cub}}$(MPa)	c_{p1}	c_{p2}	c_{p3}	c_{gr}(MPa$\sqrt{\mathrm{mm}}$)	n_κ
85.1	170.2	1.351	1.351	1.22 x 10^5	9.432	1

$b_{\gamma'}$(nm)	b_γ(nm)	$\mu_{\gamma'}$(MPa)	μ_γ(MPa)	k_1(mm^{-1})	k_2	$\rho^{(\alpha)}_{\lambda,o}$(mm^{-2})	h_o
0.25	0.41	81,515	130,150	2.6 x 10^5	8.2	1.0 x 10^5	4.8(oct), 2.4(cub)

h_{pe}	h_{cb}	h_{se}	$\Gamma_{\mathrm{APB}}(=\Gamma_{\mathrm{APB,ref}})$ (J/m^2)	η_o	k_δ
0.8	0.0	-0.4	164 x 10^{-3}	2.82	2.5 x 10^{-3}

C_{11},γ'(MPa)	C_{12},γ'(MPa)	C_{44},γ'(MPa)	C_{11},γ(MPa)	C_{12},γ(MPa)	C_{44},γ(MPa)
135,000	59,210	81,515	158,860	73,910	130,150

n_1	n_2	$\dot{\gamma}_1$(s^{-1})	$\dot{\gamma}_1$(s^{-1})	$D^{(\alpha)}$(MPa)
15	9	8.7	3.9 x 10^{-11}	150(oct), 180(cub)

CHAPTER 3
SIMULATING THE EFFECT OF GB CHARACTER ON MSC PROPAGATION THROUGH A POLYCRYSTALLINE MICROSTRUCTURE

3.1 Introduction

Microstructurally small crack (MSC) growth is highly dependent on local microstructure. When plotted on a crack growth rate (da/dN) versus far field stress intensity range (ΔK) plot, MSCs typically display an oscillatory behavior. The oscillatory behavior is often attributed to the retardation of crack growth by grain boundaries [47–49]. The character of the grain boundary (eg. misorientation, tilt and twist angle, etc.) can have a significant effect on whether an MSC will accelerate, decelerate, or arrest at the grain boundary. The probability that an MSC will propagate past a grain boundary becomes very important for determination of MSC thresholds and for the accurate fatigue life prediction in the HCF to VHCF regimes. Previous experimental methods [49–51] indicate that GB character is the major driving force for fatigue crack propagation behavior. However, conclusions from such studies have been somewhat qualitative, i.e., higher angle grain boundaries tend to hinder or arrest fatigue crack propagation. Consequently, previous MSC growth analytical models have been phenomenological in nature. Many are fit to macroscopic mean fatigue crack growth behavior and are limited when trying to predict the amount of scatter in MSC growth behavior based on microstructural features. The incorporation of GB tilt angles and GB misorientation by Wen and Zhai [52] and Castellucio [53], respectively, show promise for more physically-based MSC growth models. To create a more physically-based MSC growth law, features such as (1) the current crack length, (2) the distance of the crack from the grain boundary, and (3) the tilt and twist angle of the crack path across the grain boundary should be accounted for. The objective of this work is to take into account the effect that these aforementioned microstructural features have on MSC growth rate to develop a more physically-based MSC growth

law that can account for the scatter in MSC growth rate and fatigue life response.

3.2 Multistage Fatigue Life Approach

Modeling and simulation of fatigue life using a hierarchical multistage approach has become very popular in recent years [4, 29, 54, 55]. Often the total fatigue life, N_T, of a component is decomposed into stages of fatigue crack formation and growth by [4, 29, 54, 55]

$$N_T = N_{inc} + N_{MSC} + N_{PSC} + N_{LEFM} = N_{inc} + N_{MSC/PSC} + N_{LEFM} \tag{3.1}$$

where N_{inc} is the number of cycles required to incubate or form a crack of initial length, a_i, on the order of microstructure scale (grain or phase size). In McDowell and Dunne [4], they further demarcate the incubation period as $N_{inc} = N_{nucl} + N^*_{MSC}$, where N_{nucl} is the number of cycles to nucleate (uncracked to cracked crystal lattice) a crack and N^*_{MSC} denotes the number of cycles required to propagate the crack beyond the influence of the nucleation site or beyond the first few microstructural barriers that resist crack advance. In Equation 3.1, N_{MSC} represents the number of cycles required for the incubated crack of length a_i to propagate through approximately 3-10 grain or second phase sizes/spacings [4, 29]. In the HCF and VHCF regimes, the propagation or non-propagation of MSC cracks past these first few microstructural barriers controls the fatigue limit and contributes to fatigue life scatter. For HCF and VHCF, a large portion of life ($\sim 90\%$ [56, 57]) is spent in the incubation and MSC growth regimes, $N_{inc} + N_{MSC}$.

Following MSC propagation, physically small crack growth (N_{PSC}) is considered up until the crack is of sufficient size so that linear elastic fracture mechanics (LEFM) is applicable. Physically small crack growth is characterized by the growth of a crack that is long compared to microstructure scale, yet does not conform to conditions for similitude because the cyclic crack tip plastic zone is on the order of grain/phase size. When the crack reaches a sufficient size (typically several hundred microns and above [4]) where the cyclic crack tip plastic zone and damage process zone are large compared to microstructure scale and the conditions of small scale yielding and

similitude are met, then long fatigue crack growth behavior is applicable. In this regime, LEFM can be used to determine the number of cycles, N_{LEFM}, required for the crack to grow from several hundred microns to failure.

Since the variation in MSC growth contributes to the marked variation in fatigue life in the HCF and VHCF regimes, the main focus of this work is to develop a MSC growth law that takes into account microstructural barrier (specifically, grain boundary) effect on MSC growth. In the next section, we review previous MSC growth laws developed.

3.3 MSC Growth Laws

Several different phenomenological crack growth rate equations have been proposed for MSC growth, many of which are based on microstructural small crack (MSC) growth mechanics and elastic-plastic fracture mechanics (EPFM). In the MSC growth regime, microstructure effects dominate small crack growth. As cracks grow, the effect of microstucture on fatigue crack growth decreases and the MSC and EPFM regimes tend to merge into the LEFM growth curve where a condition of similitude is reached [1, 2]. One form of an MSC growth equation was proposed by Hobson et al. [58, 59] via

$$\frac{da}{dN} = C(d-a)^{1-\alpha}a^{\alpha} \tag{3.2}$$

where d is a microstructural length scale parameter, a is the crack length, and C and α are constants. A similar equation for MSC growth was proposed by Miller [60] as

$$\frac{da}{dN} = A\Delta\gamma^{\alpha}(d-a) \tag{3.3}$$

where A and α are material constants and $\Delta\gamma$ is the cyclic shear strain range. Again the value of d depends on the dominant microstructural barrier resisting MSC growth. It should be noted that both Equations 3.2 and 3.3 contain the term $(d-a)$ that essentially accounts for the grain boundary effect on MSC propagation. As the crack length a approaches the microstructural parameter d (this parameter is often linked to the grain size), the MSC growth rate approaches zero. Following the propagation

of the crack past the grain (or other microstructural) boundary, a separate equation for elastic-plastic fracture mechanics can be used.

The growth of cracks under an elastic-plastic fracture mechanics condition has been described by multiple techniques. For example, Miller [60] used the form

$$\frac{da}{dN} = B\Delta\gamma^{\beta}a - D \tag{3.4}$$

where B and β are materials constants and D is an EPFM threshold value. Miller et al. [61] applied Equations 3.3 and 3.4 to the small crack growth of a 0.4% carbon steel and found that these two equations could estimate the mean small crack growth rate of this material. A similar approach for small fatigue crack growth was employed by Nisitani and Goto [62] on a mild steel and more recently by Goto et al. [63] on MSC growth in coarse-grained and ultrafine-grained copper via

$$\frac{da}{dN} = C\sigma_a^n a \tag{3.5}$$

where the applied stress amplitude is used as the EPFM crack extension driving force, rather than the shear strain component in Equation 3.4. Again, the constants C and n depend on the material tested. It should be noted that Frost and Dugdale [64] originally proposed Equation 3.5; they used it to describe the growth of large cracks in mild steels and aluminum alloys and found a good correlation with both materials for an exponent of $n = 3$. Regardless, Equations 3.4 and 3.5 seem to work well for a range of crack tip conditions including the large-scale yielding regime of EPFM (refs. [61,62]) in addition to the small-scale yielding condition representative of the LEFM regime (as evidenced by [64]) with separate experimental fitting constants required for both conditions. However, these models tend to predict the mean phenomenological small crack growth behavior and cannot predict the scatter in MSC growth evidenced in experiments.

A different grain boundary affected MSC growth law was proposed by Chan and Lankford [65]. In their approach, they assumed that a Paris-law approach could be applied to small cracks and accounted for crack tip/grain boundary interaction by

$$\frac{da}{dN} = C_1(\Delta K)^n \cdot \left[1 - \left(1 - \frac{\tau_B}{\tau_A}\right)\left(\frac{D-2X}{D}\right)^m\right] \tag{3.6}$$

where C_1 and n are typical Paris law constants, D is the grain diameter, X is the distance of the crack tip from the nearest grain boundary, m is a constant, and τ_A and τ_B are the resolved shear stresses in grains A (containing crack) and B (neighboring grain). It should be noted that the value of $2X$ varies from $2X = D$ to $2X = 0$ corresponding to the crack being furthest (a total grain diameter, D) from the next grain boundary to the crack being at the next grain boundary, respectively. In Equation 3.6, ΔK is the global stress intensity factor calculated as $\Delta K = \Delta\sigma\sqrt{\pi a/Q}$, where a penny-shaped crack (Q=2.26) was assumed. An exponent value of $m = 2$ was found to provide adequate correlation with experiments. In this equation, as the crack length distance from the grain boundary decreases to zero, the crack reaches the grain boundary and the effect of the grain boundary on crack propagation is maximized. Additionally, the authors do not place a restriction on the ratio of τ_B/τ_A. If $\tau_B/\tau_A > 1$, the resolved shear stress is larger in grain B (neighboring grain) than in grain A (containing crack) so crack growth rate increases as the crack approaches the grain boundary. Alternatively, if $\tau_B/\tau_A < 1$ the lower resolved shear stress in the neighboring grain causes the growth rate to decrease as the crack approaches the grain boundary. While it is noted that LEFM is not applicable in the small crack growth regime due to absence of similitude conditions [2], the means by which the authors used the crack tip distance to the grain boundary and the resolved shear stresses among neighboring grains to modify the LEFM driving force is intriguing. A similar, but different, formulation will be used in the current work to model the effect that the grain boundary has on the fatigue crack growth rate of MSCs.

Another method in which small crack growth can be characterized is based on the crack tip opening or sliding displacement. For example, for Stage I crack propagation a power law relationship between the range of crack tip sliding displacement and the fatigue crack growth rate can be assumed by

$$\frac{da}{dN} = C \cdot (\Delta CTSD)^m \tag{3.7}$$

where the constant C is an irreversibility factor that indicates the fraction of the $\Delta CTSD$ (range of crack tip sliding displacement) that contributes to crack growth.

Tanaka and coworkers [66] and Navarro and de los Rios [67] inferred this $\Delta CTSD$ value by imposing the theory of continuously distributed dislocations and the BCS solution [68] to model the interaction between growing cracks and grain boundaries. Kunkler, Christ and coworkers [56, 69] and Marx et al. [70, 71] have used Equation 3.7 in recent work to describe the transition from Stage I (single slip) to Stage II (double slip) dominated fatigue crack growth. Both groups were able to reproduce the transition from oscillatory MSC growth to that more closely related to LEFM.

MSC growth laws can be further enhanced with the crystal plasticity finite element method (CPFEM). Simonovski et al. [72–74] used 2D CPFEM simulations to determine the crack tip opening displacement (CTOD) ahead of the crack tip and found that crystallographic orientation has a significant effect on CTOD. Castelluccio and McDowell [53, 75] used CPFEM to simulate a crack within a single crystal Cu subjected to mixed loading. They found that computed multiaxial fatigue indicator parameters [55] (FIPs) were directly proportional to the crack tip displacement, and, hence, can be used as a local driving force for fatigue crack propagation. These nonlocal FIPs are preferred since they are easily computable within a CPFEM scheme.

Musinski and McDowell [76] used CPFEM to estimate fatigue crack initiation and early propagation within smooth and notched IN100 specimens. The total fatigue life was estimated as the summation of crack incubation life (N_{inc}), MSC propagation life ($N_{prop,MSC}$) and LEFM propagation life (N_{LEFM}). This hierarchical model [76] is modified here to include grain boundary effects on MSC growth.

Prior to presenting the overall hierarchical method in which fatigue life is estimated, a brief review of fatigue crack growth mechanisms in Ni-base superalloys is warranted. Therefore, the next section covers background information regarding failure mechanisms for Ni-base superalloys. This background information forms the basis for the way in which fatigue crack formation and early growth is modeled in this work.

3.4 Fatigue Crack Growth Mechanisms in Ni-base Superalloys

The mode in which Ni-base superalloys fail in fatigue is mainly determined by five key factors including the loading temperature, the grain size, the plastic zone size ahead of the crack tip, the environment, and the loading frequency at which tests are conducted. In general, the fracture surface will be more transgranular versus intergranular for lower temperatures, larger grain sizes, smaller plastic zone (or crack length) sizes, an environment that is more evacuated (lower oxygen partial pressure), and faster (or no hold time) testing frequencies. The reasons for these trends are further exemplified below.

3.4.1 Temperature effect

Failure in Ni-base superalloys tends to be transgranular from room temperature up to a temperature of about 700°C. At the lower end of this spectrum at temperatures below ~ 450°C, plastic deformation mainly occurs by planar slip along octahedral slip planes. As a result, small crack growth is dominated by faceted {111} crystallographic crack growth. As temperature increases to $\sim 450 - 700$°C, due to the potential for cross-slip, many superalloys can also deform macroscopically along cube slip planes. This mechanism is often attributed to zig-zag cross-slip through γ matrix channels [34]. For example, Phillips et al. [77] showed that in a supersolvus polycrystalline R104 Ni-base superalloy at both 427°C and 704°C deformation was due to wavy slip along two conjugate {111} planes. Experiments performed by Li et al. [78] on a coarse-grained IN100 showed that the IN100 Ni-base superalloy they tested failed crystallographically at room temperature and contained smoother transgranular fracture surfaces normal to the loading axis at 538°C. Ma and Shi [79] tested DS superalloy DZ4 and observed that the crack path was crystallographic at 25°C and 350°C whereas at 700°C the crack propagated by Mode-I propagation. Maier, Christ and coworkers [80, 81] reported a similar transformation from planar to a more wavy slip mechanism at test temperatures above 600°C for a high-temperature Ti alloy IMI 834. This was attributed to the CRSS for each slip system in their particular Ti alloy becoming more similar as temperature

was increased [80]. Therefore, it can be reasonably concluded that at intermediate temperatures ($\sim 450°C$ to $\sim 700°C$) multiple slip systems can be activated in Ni-base superalloys and MSC cracks tend to be oriented normal to the loading axis.

For temperatures above $\sim 700°C$, crack growth behavior can be influenced by creep deformation, fatigue, and oxidation simultaneously. Creep fracture involves void growth and coalescence at grain boundaries due to grain boundary sliding and vacancy diffusion towards the grain boundary during load application [82]. Oxidation also has a significant effect on crack growth at elevated temperatures. As Andrieu et al. [83] pointed out, oxidation can be characterized by short-range and long-range diffusion processes. The short-range diffussion comprises formation of an oxide layer at the crack tip, whereas long-range diffussion encompasses oxygen penetration deeper into the material through rapid diffusion paths, including slip planes and grain boundaries [83]. The oxidation of the crack tip may induce crack-tip shielding or oxidation-assisted enhancement of the crack growth rate depending on the applied stress. As such, oxidation-induced crack closure becomes influential at near-threshold loading [82, 84]. The formation of internal oxidation sites at grain boundaries hinders grain boundary sliding and migration which could result in buildup of internal stresses at the grain boundaries so that it makes crack propagation more preferable along the embrittled grain boundaries as opposed to transgranularly through the grains [82, 83]. Consequently, at elevated temperatures above $\sim 700°C$, intergranular fatigue crack growth can be activated in Ni-base superalloys due to the potential for the aforementioned void growth/coalescence and oxidation mechanisms at the grain boundaries. However, as discussed later, these high temperature fatigue cracking phenomena depend on load cycle type (with or without dwell) and testing frequency.

3.4.2 Grain size effect

Grain size also has an effect on the fatigue failure mechanism for Ni-base superalloys. Typically, at lower temperatures smaller grain sizes lead to higher strength and more fatigue-resistant microstructures. However, the higher fatigue resistance of these finer microstructures breaks down if they are exposed to higher temperatures; grain

boundary diffusional creep and intergranular oxidation can decrease the fatigue life of fine-grained Ni-base superalloys significantly at higher temperatures. As discussed in the previous section, oxygen and vacancies preferentially diffuse along/toward grain boundaries at these higher termperatures. Consequently, larger grain sizes tend to perform better at elevated-temperature and time-dependent fatigue conditions. This is due to there being less grain boundary area to oxidize and a larger mean distance for the vacancies to travel to reach the grain boundaries. Subsequently, engineers and designers have achieved major advancements in microstructure design through the advent of directionally solidified and single-crystal superalloys that greatly suppress or eliminate this grain boundary diffusional creep and intergranular oxidation mechanisms at higher temperatures. These types of casting processes also allow for preferential orientation of the crystals to maximize fatigue resistance in that orientation. Additionally, location specific design of components (e.g. dual or hybrid microstructures) can be used to produce an optimized microstructure based on the operational requirements (stress state, temperature, environment, etc.) at different locations of the component. An understanding of the dependence of grain size on fatigue failure mechanisms is crucial for the design and accurate modeling of these location specific microstructures. Here, we limit our brief discussion to the difference in fatigue behavior between fine-grained subsolvus and coarse-grained supersolvus Ni-base superalloys.

The mode of fatigue crack formation and growth in Ni-base superalloys at elevated temperatures ($\sim 600-700°\text{C}$) strongly depends on the grain size of the microstructure. For subsolvus, fine grain (average grain sizes $\sim 3-15$ μm) Ni-base superalloys, optical observation over somewhat coarser scales reveal a fracture surface that is relatively flat and featureless near the initiation feature [85]. This suggests a crack formation via a Stage II, non-crystallographic, transgranular quasi-cleavage mechanism near non-metallic inclusions (NMIs) or pores [12, 85, 86]. These fracture surfaces have not been investigated at a fine enough scale (e.g. using TEM) to determine whether this flat transgranular crack formation mechanism is due to cross slip on multiple slip planes. This transgranular fatigue crack growth mechanism transforms to intergranular

growth for surface cracks when the crack reaches a characteristic length ($\sim 50 - 100$ μm) [12, 85, 86] or when dwell periods occur [12]; for sub-surface cracks, intergranular cracking requires crack lengths greater than the characteristic length and exposure of the crack to the surface [12]. Alternatively, due to the planar slip mechanism in Ni-base superalloys [87,88], supersolvus, coarse grain (average grain sizes ≥ 15 μm) Ni-base superalloys favor Stage I crystallographic crack formation from inclusions, pores or large grains. This fatigue mechanism has been observed in Rene 88DT [89–91], IN100 [78], Waspoloy [85], N18 [92], and HIP Astroloy [85]. However, the early propagation of MSCs in coarse-grained Ni-base superalloys tends to be transgranular and normal to the loading axis [78, 79]. For example, Li et al. [78] conducted fatigue tests on a coarse grain IN100 microstructure (average grain size = 30 μm) at 538°C and reported that the early faceted MSC growth area extended to crack lengths on the order of ∼100-150 μm and was macroscopically normal to the loading axis (ref. Figure 3.1).

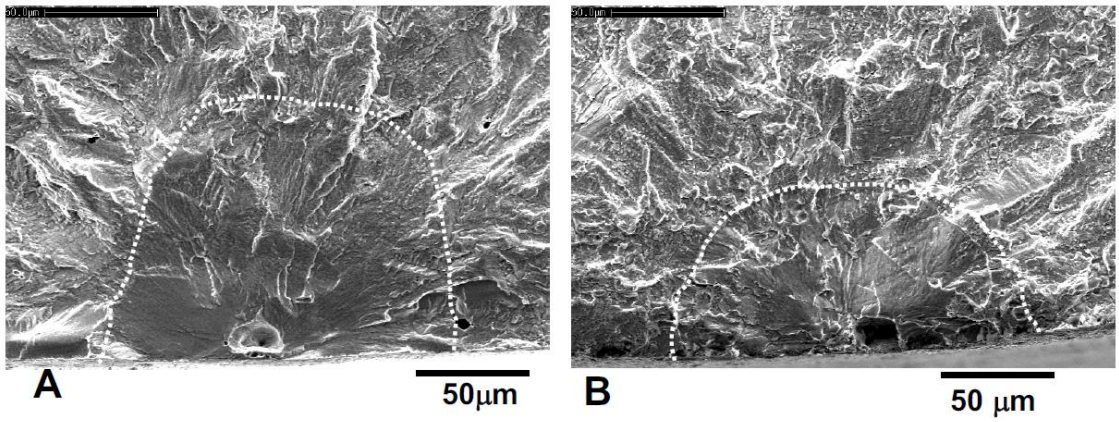

Figure 3.1: Fracture surface for two different specimens of coarse grain IN100 [78]. $T = 538$°C, $f = 0.5$ Hz, $R_\sigma = 0.05$, $\sigma_{max} = 1000$ - 1140 MPa. Faceted MSC growth region around crack formation is denoted by the white dotted lines in each SEM image. Faceted MSC growth extends to a crack lengths on the order of ∼100-150 μm.

Recent work by Sinha and coworkers [93] has characterized failure facets in a coarse grain IN100 fatigued at 650°C, $\sigma_{max} = 1100$ MPa, and $R_\sigma = 0.05$. The tilt fractography technique as outlined by Sinha et al. [94] was used to determine facet vector normals of the failure facets near fatigue crack formation. Sinha et al. [93] presented preliminary

results deduced from using OIM and SEM images at two different tilt angles for one facet feature near crack formation. For the case of the failed specimen presented, the orientation of the loading axis was given in Cartesian coordinate space by $\boldsymbol{L} = [001]$ and the crack facet normal near crack formation was $\boldsymbol{F} = \boldsymbol{i} - 0.14\boldsymbol{j} - 20.49\boldsymbol{k}$ [93]. This facet feature near crack formation had an orientation almost halfway between the [001] and [101] orientations (on an inverse pole figure plot). These results indicate that the transgranular facet near fatigue crack formation was not due to single slip along crystallographic planes; rather, it suggests that more than one slip system (i.e. zig-zag cross slip on multiple slip systems) could have contributed to the formation of the failure facet. Therefore, the driving force on multiple slip systems should be considered in MSC growth modeling and prediction.

3.4.3 Cyclic plastic zone size ahead of the crack tip

The cyclic plastic zone size ahead of a crack tip depends on both the crack length and the applied stress/strain range. At constant elevated temperature ($\sim$ 650°C for Ni-base superalloys), a higher plastic strain range or plastic zone size promotes intergranular over transgranular failure. This effect has been frequently observed for constant stress/strain fatigue loading of Ni-base superalloys with the transition from transgranular to intergranular failure mode with increasing crack length [12, 86]. For example, Caton and Jha [12] investigated the transition from transgranular to intergranular in a fine-grained IN100 cyclically loaded at a frequency of 0.33 Hz at 650°C and found that the transition to intergranular fatigue crack growth (and LEFM applicability) occurred for cracks on the order of $\sim 100\mu m$. Pang and Reed [86] studied a few microstructural variants of Udiment 720Li at 650°C in lab air. They noted that the crack growth changed from transgranular to intergranular when the length of the crack was four to six grains long.

3.4.4 Lab air versus vacuum effect

At higher temperatures, the existence of oxygen in lab air can promote oxidation within Ni-base superalloys at elevated temperatures. There have been many studies

showing that fatigue crack growth is much faster in lab air versus vacuum at elevated temperatures [95–97]. Dahal et al. [95] demonstrated this effect in the ranges of 650°C to 760°C for a ME3 superalloy with an average grain size of $44\mu m$. Pedron and Pineau [96] studied crack growth behavior in IN718 at 650°C in both lab air and vacuum environments. They found that at higher frequencies, there is not a significant difference in fatigue life between the lab air and vacuum experiments. On the other hand, lower frequencies significantly increased the fatigue crack growth rate in lab air relative to the vacuum experiments. A similar coupling effect between the frequency and environment was seen by Reger and Remy [97] in IN100 fatigued at 1000°C. This suggests that there is a significant coupling behavior between environment and testing frequency.

Although vacuum environments tend to prevent oxidation and intergranular failure, there are some cases in which intergranular failure can be seen in vacuum. For example, Everitt et al. [98] saw some cases at higher ΔK levels, high temperatures (725°), and under vacuum where intergranular failure occurred. This shows that there are multiple factors that can influence the mode in which fatigue cracks propagate at elevated temperatures.

3.4.5 Testing frequency and hold time effects

Testing frequency can have a significant effect on the failure mode of Ni-base superalloys. At elevated temperatures, lower testing frequency tends to promote intergranular failure. For example, Dahal et al. [95] studied the effect of loading frequency on the Ni-base superalloy, ME3, at temperatures of 650°C, 704°C, 760°C and found that there was a transition from transgranular-dominated to intergranular-dominated fatigue mode at a loading frequency of 0.1Hz. They attributed the intergranular cracking mechanism to grain boundary sliding.

For hold period testing, the overall fatigue cracking mode tends to be transgranular in fatigue (no-dwell) loading and intergranular in creep-fatigue (dwell) loading. This transition from transgranular to intergranular fatigue crack growth mechanism under tensile dwell periods has been seen in several Ni-base superalloys (cf. [12, 99–103]).

The transition from transgranular to intergranular is due to the formation of a brittle oxidation layer at the surface and the enhancement of oxygen diffusion along the grain boundaries near the surface at elevated temperatures. In addition to crack initiation from surface-connected embrittled grain boundaries, under tensile dwell creep-fatigue loading at elevated temperatures cavities/cracks can form along interior grain boundaries enhancing intergranular crack coalescence and reducing overall fatigue life (as exemplified for a Ni Alloy 617 subjected to 1.0% hold strain for 9000 seconds at 950°C in Carroll et al. [99]). This reduction in fatigue life due to enhanced intergranular fatigue crack growth can be significant, even by orders of magnitude [104, 105].

3.4.6 Assumed Failure Mechanism(s) for Current Work

As discussed in the sections above, there is a significant coupling effect of temperature, grain size, plastic zone size, environment, and testing frequency on the failure mechanisms in Ni-base superalloys. A good rule of thumb is that the fracture surface tends to be more transgranular over intergranular for lower (below ~ 450°C) temperatures, larger grain sizes, smaller plastic zone (or crack length) sizes, an environment that is more evacuated (lower oxygen partial pressure), and faster (or no hold time) testing frequencies. The computational studies performed here are mainly focused on fatigue loading of a supersolvus coarse-grained IN100 with average grain size of $34\mu m$ at an elevated temperature of 650°C subjected to quasi-static loading in an assumed lab air environment at a strain rate of $\dot{\varepsilon} = 1 \times 10^{-3}\text{s}^{-1}$ with no hold times. Based on these loading conditions and the discussion above, the failure mechanisms assumed for crack initiation, MSC growth, and LEFM propagation to final failure are as follows:

- **Crack Incubation:** For naturally-initiated cracks (i.e., no focused ion beam (FIB) notch), crack nucleation is assumed to be crystallographic. The incubated crack, a_{inc}, is assumed to be on the order of grain size.

- **MSC propagation:** Once a crack is formed on the order of grain size, MSC propagation is assumed to be planar and transgranular. The resultant contributions from multiple slip systems are assumed to make the MSC growth planes non-crystallographic.

- **LEFM propagation:** Once the crack is of sufficient length (3-10 grain diameters [4, 29]), LEFM propagation is assumed to be active and is applied via a typical Paris law equation.

3.5 Methodology

In this section a methodology is presented for a generalized, physically-based MSC growth law that accounts for grain boundary character, specifically tilt and twist angles. Before the MSC growth law is presented, definitions of tilt and twist angle and how they are calculated are discussed. Following this discussion, some background information is presented regarding fatigue indicator parameters (FIPs) and previous FIP-based MSC growth laws. Next, the MSC growth law incorporating crack distance from the grain boundary and tilt and twist angles is proposed. The FIP distribution as a function of crack length and microstructure is formulated using crystal plasticity finite element simulations of stationary cracks propagating through an ordered grain structure. Lastly, this framework is fitted to experimental MSC growth data and results are presented for an MSC growing from a FIB notch through a network of three-dimensional grains.

3.5.1 Definition of Grain Boundary Character

The grain boundary (GB) character has a significant effect on MSC growth behavior. Five macroscopic independent parameters or degrees of freedom are required to define a grain boundary, including three rotation angles that bring two misoriented crystals into coincidence, and two spherical angles that orient the boundary plane [106]. One way to describe the misorientation between two slip/crack planes of adjoining grains can be described by tilt and twist angles. Figure 3.2 shows what is meant by the tilt and twist angles between two crack planes at a grain boundary. A significant number of authors [49–51] point to the fact that the main parameters that control or inhibit MSC growth past a grain boundary is the magnitude of the twist and tilt angles between two slip/crack planes of adjoining grains. There is a general consensus that larger values of twist angle (α in Figure 3.2) prevent or slow down crack propagation.

However, it seems that these conclusions are generally qualitative, i.e., larger GB twist values inhibit MSC propagation to a greater degree than smaller GB twist values. The purpose of the work in this section is to quantitatively simulate the effect of GB character on the driving force for propagation past the grain boundary to develop a more physically-based MSC growth law.

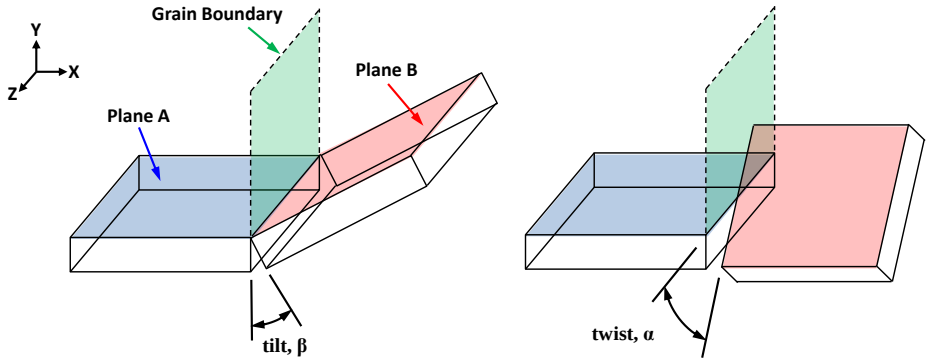

Figure 3.2: Definitions of tilt and twist angles between two crack planes at a grain boundary.

Another method in which researchers define the misorientation subset of the grain boundary character is to use the minimum misorientation (or disorientation) [107] between neighboring grains. Misorientation is the relative change in lattice orientation between neighboring grains and can be denoted by a rotation angle/axis pair; the minimum rotation angle among the set of all possible rotation angles that can be used to define the misorientation between to neighboring crystal lattices when crystal symmetry is considered is termed the disorientation [107, 108]. Grain boundaries with a high disorientation angle, often referred to as high angle grain boundaries (HAGBs), are typically more favorable locations for fatigue crack formation, whereas HAGBs tend to hinder or arrest MSC propagation [109]. Therefore, for purposes of modeling, researchers often use a threshold misorientation below which transmission of slip past the grain boundary is more favorable. These low angle grain boundaries (LAGBs) are often limited to grain boundaries with disorientation less than 15-30 degrees (cf. [53, 110–112]). However, the use of misorientation angle may not be the best measurement of grain boundary influence because twin boundaries that have

small twist angles but larger tilt angles (and therefore larger misorientation) have been shown to be able to allow slip transmission through the grain boundary (ref. [113,114]). Others researchers have indicated that the magnitude of the residual Burgers vector can be used as an indicator for slip transfer through grain boundaries, where higher residual Burgers vectors provide higher energy barriers for slip transmission [115, 116]. In the following, we proceed with using twist and tilt angles as key features of the grain boundary character.

Figure 3.3 establishes the coordinate system orientation, key feature orientation, and grain boundary orientation used for analysis of faceted MSC growth through grain boundaries. For the non-FIB studies covered in this Chapter, MSCs are assumed to grow into the depth (x-direction) of the material starting from the surface at $x = 0$. Each grain boundary normal vector, $\boldsymbol{n}_{GB}$, is oriented in the x-direction and the loading axis is in the y-direction. A schematic of MSC growth from the slip/crack plane in grain 1 to the slip/crack plane in grain 2 is shown in Figure 3.3. The faceted slip/crack planes can be assumed to be either crystallographic or non-crystallographic, without loss of generality, depending on the slip/failure mechanism assumed. For application to Ni-base superalloys, the slip/crack planes are assumed to be crystallographic for temperatures below ~ 450°C and non-crystallographic in the range of $\sim 450 - 700$°C, as per the previous discussion regarding temperature effect on failure mechanisms in Ni-base superalloys. The orientation of the slip/crack planes are chosen based on the plane that maximizes slip system driving force as informed by computed fatigue indicator parameters (FIPs).

Given two crack fracture surface planes with unit normal vectors defined by $\boldsymbol{n}_1$ and $\boldsymbol{n}_2$ that are separated by a grain boundary with unit normal vector $\boldsymbol{n}_{GB}$, as shown in Figure 3.3, the twist (α) and tilt (β) angles are found following the procedure outlined by Zhai et al. [49]. For the coordinate system displayed in Figure 3.3, the twist angle (α) is defined by the x-axis ($\boldsymbol{n}_{GB}$) rotation mifit of the two slip/crack planes and is given by [49]

$$\alpha = \cos^{-1}\left[(\boldsymbol{n}_{GB} \times \boldsymbol{n}_1) \cdot (\boldsymbol{n}_{GB} \times \boldsymbol{n}_2)\right] \tag{3.8}$$

Likewise, the tilt angle (β) is defined by the z-axis ($\boldsymbol{n}_Z$) rotation misfit of the two

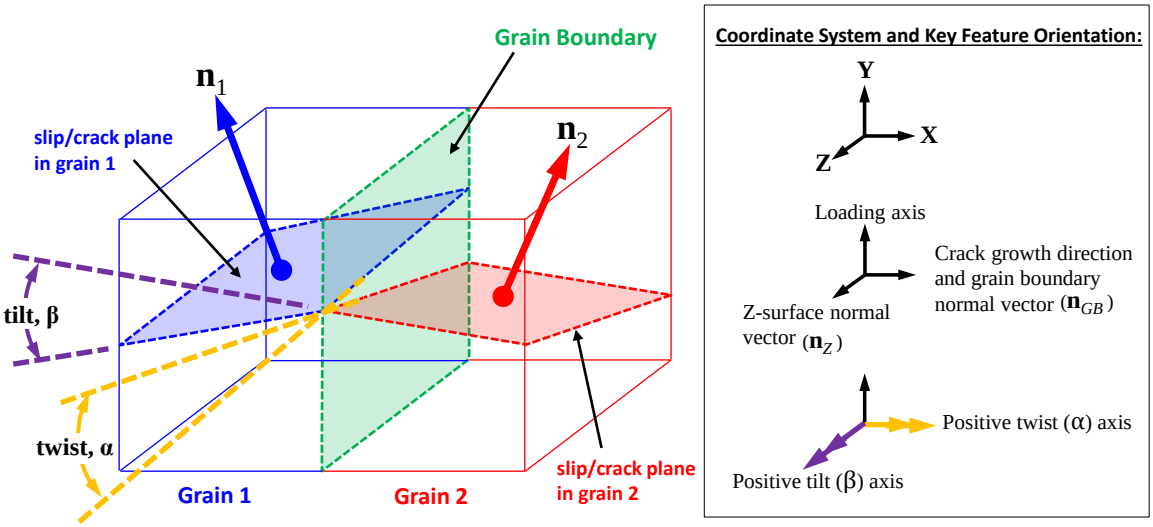

Figure 3.3: Schematic showing MSC growth along slip/crack plane in grain 1 to slip/crack plane in grain 2. After refs. [49, 52].

slip/crack planes as

$$\beta = \cos^{-1}\left[(\boldsymbol{n}_Z \times \boldsymbol{n}_1) \cdot (\boldsymbol{n}_Z \times \boldsymbol{n}_2)\right] \tag{3.9}$$

3.5.2 Fatigue Indicator Parameters (FIPs)

Multiaxial parameters have long been used to correlate fatigue damage to the cyclic stress-strain state [117–119]. Some of the earliest methods to correlate cyclic plastic strains to cycles to failure are from the works of Coffin [120] and Manson [121]. The multiaxial FIPs that are relevant to fatigue crack formation and small crack growth consider the combined effects of resolved shear stresses/strains and normal stresses/strains on a given plane. Theoretically, the normal stresses provide crack opening, reducing friction between crack surfaces, and resolved shear stresses support dislocation motion on the slip plane. The use of these multiaxial FIPs to correlate fatigue life with a given multiaxial stress/state can be summarized by

$$FIP(\boldsymbol{\sigma}(t), \boldsymbol{\varepsilon}(t), \boldsymbol{k}_i) = f(N_f) \tag{3.10}$$

where $\boldsymbol{k}_i$ are a set of material specific constants and $\boldsymbol{\sigma}(t), \boldsymbol{\varepsilon}(t)$ indicate stress and strain history dependence, respectively. What remains is the definition of the functional form of the left and right hand side of Eq. 3.10. In Kallmeyer et al. [119], they provide

a significant list of multiaxial parameter forms (cf. Table 4 in [119]) and investigated the ability of these multiaxial parameters to correlate well with experimental uniaxial and biaxial fatigue data for a Ti-6Al-4V alloy. Also, they defined the right hand side of Eq. 3.10 with a two term power law expression, $f(N_f) = A(N_f)^b + C(N_f)^d$ where A, b, C, and d are constants. They found that the Findley parameter [122] and the Fatemi-Socie parameter [117] provided the best correlation for both sets of data. These two parameters both take into account a combination of shear stresses/strains and normal stresses/strains, which supports the use of multiaxial FIPs for fatigue life estimation.

Regardless of method used, the driving force parameter used for estimation of fatigue failure should account for the means in which failure is produced. Since it is assumed that early growth of MSCs in Ni-base superalloys is along transgranular facets up to a given operating temperature, we characterize the driving force FIP for early MSC growth along a given transgranular facet via the Fatemi-Socie (FS) parameter [117, 123]. This FIP considers the combined effects of resolved plastic shear strains and normal stresses along a given facet plane ($\diamond$) and is given by:

$$FIP_{FS}^{(\diamond)} = \frac{\Delta\gamma_{max,(\diamond)}^{p*}}{2}\left(1 + K'\frac{\sigma_{n,(\diamond)}^{max*}}{\sigma_y}\right) \tag{3.11}$$

where $\Delta\gamma_{max,(\diamond)}^{p*}$ is the range of plastic shear strain on the facet plane and $K' = 1$ [123] accounts for the effect of stress $\sigma_{n,(\diamond)}^{max*}$ normal to the facet plane divided by the cyclic yield stress σ_y. The (*) symbol in Equation 3.11 indicates averaging over a nonlocal domain, and will be discussed further in Section 3.5.2.2.

3.5.2.1 Procedure for calculating crystallographic and maximum non-crystallographic FIP

In the following, we consider the calculation of FIP for proportional loading only. Two categories of facet planes are considered for the calculation of FIPs, namely, crystallographic and maximum non-crystallographic. Crystallographic FIPs correspond to FIPs calculated on each slip plane and non-crystallographic FIPs consider the maximum FIP on any given plane in 3D space. For both types, the calculation of FIP_{FS} for proportional loading follows previous techniques described in [46, 124, 125]

and begins with the calculation of the range of plastic strain tensor, $\Delta\varepsilon_{ij}^{p*}$, over a stabilized loading cycle at the FEM integration points, via $\Delta\varepsilon_{ij}^{p*} = \Delta\varepsilon_{ij}^{p*}\big|_A - \Delta\varepsilon_{ij}^{p*}\big|_B$. The plastic strain tensors at points A and B for R_ε = -1 and R_ε = 0.05 loading are calculated at points A and B in the third fatigue cycle as schematically shown in Figure 3.4.

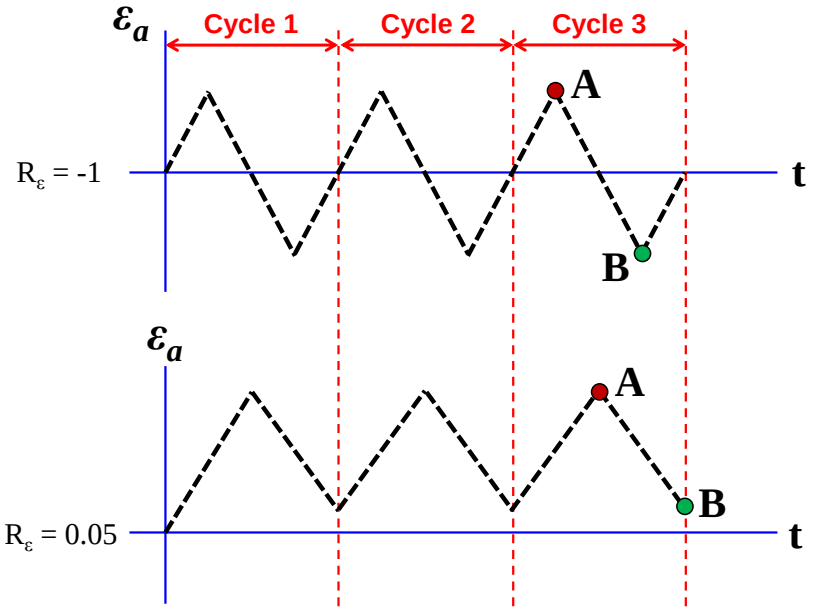

Figure 3.4: Schematic of R_ε = -1 and R_ε = 0.05 displaying loading points A and B used for FIP calculations. After ref [124].

For the crystallographic FIP_{FS}, the nonlocal range of plastic shear strain $\Delta\gamma_{(\alpha)}^{p}$ for each slip system (α) is calculated from the range of plastic strain tensor $\Delta\boldsymbol{\varepsilon}^{p*}$ by

$$\Delta\gamma_{(\alpha)}^{p*} = 2\boldsymbol{n}\cdot\Delta\boldsymbol{\varepsilon}^{p*}\cdot\boldsymbol{s} \tag{3.12}$$

where $\boldsymbol{n}$ and $\boldsymbol{s}$ correspond to unit vectors for each slip system normal and direction, respectively. The maximum stress normal to each slip system plane is then calculated via

$$\sigma_{n,(\alpha)}^{max*} = \boldsymbol{n}\cdot\boldsymbol{\sigma}\cdot\boldsymbol{n} \tag{3.13}$$

These values of $\Delta\gamma_{(\alpha)}^{p*}$ (Eqn. 3.12) and $\sigma_{n,(\alpha)}^{max*}$ (Eqn. 3.13) are then substituted into Equation 3.11 to find the crystallographic FIP.

For the maximum non-crystallographic FIP_{FS}, the maximum non-crystallographic range of plastic shear strain, $\Delta\gamma^{p*}_{(non-xtal)}$, is calculated by finding the eigenvalues of the range of plastic strain tensor and is given by

$$\Delta\gamma^{p*}_{(non-xtal)} = 2(\Delta\varepsilon_{p,1} - \Delta\varepsilon_{p,3}) \tag{3.14}$$

with the eigenvalues of the plastic strain tensor ranked in order of $\Delta\varepsilon_{p,1} > \Delta\varepsilon_{p,2} > \Delta\varepsilon_{p,1}$. The value of $\Delta\gamma^{p*}_{(non-xtal)}$ in Eqn. 3.14 and the maximum stress normal to this plane (calculated in same manner as Eqn. 3.13) are then substituted into Equation 3.11 to find the maximum non-crystallographic FIP.

3.5.2.2 Averaging domain for FIPs

The length scale at which FIPs are averaged should be chosen based on the physical fatigue/failure process of interest. Since we are interested in the driving force for fatigue crack formation and propagation at the scale of grains and the sub-grain evolution of FIP with MSC growth, we select the averaging volume to be sub-grain. This averaging domain of the FIP is chosen for two main purposes: (1) To regularize mesh size sensitivity and (2) to model the sub-grain crack extension (i.e., damage process zone) with the intent to develop a relationship between the nonlocally-averaged FIPs of uncracked and cracked simulations. Essentially, the goal is to use the FIPs from uncracked simulations to infer those from cracked simulations at the level of individual grains (grain-by-grain basis).

In recent work by Castelluccio and McDowell [126], they simulated multiple digitally-created polycrystalline microstructures to investigate the effect of FIP averaging volume selection on FIP variability. They considered the averaging of FIPs over (1) individual elements, (2) bands parallel to slip planes, and (3) the entire grain volume. They found that the FIP values were larger for slip band averaging regions that were located away from the center of the grains. However, when the distribution of FIPs in slip band averaging regions and whole grain averaging regions were regularized by grain size effects (band size and grain size, respectively), the distribution of regularized FIPs for slip band and grain averaging regions were very similar. There was only

a slight difference in the FIP extreme values. This analysis showed the importance of regularizing FIP driving force over the size of the slip band size or grain size for consideration of crack nucleation driving forces.

3.5.3 MSC Growth Law Formulation

In the prediction of fatigue life, the total fatigue life (N_T) is assumed to be decomposed into stages of fatigue crack incubation (N_{inc}) on the order of the size of microns, MSC/PSC propagation ($N_{MSC/PSC}$) through the microstructure, and LEFM propagation (N_{LEFM}), i.e., $N_T = N_{inc} + N_{MSC/PSC} + N_{LEFM}$ [29, 55]. The process of progressive cyclic damage until fatigue crack nucleation typically involves the localization of irreversible slip within persistent slip bands that either (1) form intrusions/extrusions at surface grains [127, 128] or (2) impinge on grain boundaries for non-surface grains [129, 130]. To model this dislocation-based fatigue crack nucleation process, many researchers have used various derivatives of the Tanaka and Mura [131] model which assumes an energy balance between cyclically formed dislocation dipoles (slip bands) and the required energy to form a crack. Once a crack has formed, an MSC/PSC propagation law is often assumed via a semi-empirical growth model (for example, Mikkola et al. [132] or Alexandre et al. [133]) or based on an average FIP at the grain scale (for example, Musinski and McDowell [76] or Castelluccio [53]).

Previous work on FIP-based MSC propagation laws used by McDowell and colleagues [53, 76, 134] can be generalized into two different methods: (1) A method in which the estimation of MSC growth is based on FIPs obtained from uncracked simulations, and (2) a method in which the estimation of MSC growth is based on FIPs computed from successive simulations of stationary cracks of progressively longer lengths, including effects of cyclic stress and plastic strain redistribution. The idea behind these models is that since the $FIP_{FS}^{(\alpha)}$ is directly related to the cyclic crack tip displacement (ΔCTD) for a crack growing within a single crystal [75], the local driving force for MSC propagation within a polycrystalline microstructure can be estimated from these computed FIPs. The two aforementioned MSC growth methods employed previously by McDowell and colleagues [134] can be generalized and summarized,

respectively, by

$$\left.\frac{da}{dN}\right|_{MSC,uncracked} = A_{FS,uncracked}\left(\tau_y \; FIP_{FS,uncracked}\right) a - \eta b \tag{3.15}$$

$$\left.\frac{da}{dN}\right|_{MSC,cracked} = A_{FS,cracked} \; FIP_{FS,cracked} \; \overline{d} - \eta b \tag{3.16}$$

where the A_{FS} constants are fit to experimental data, τ_y is the critical resolved shear stress on the slip plane, a is the current crack length, and $\overline{d}$ is a characteristic crack length on the order of the grain size. The second term of both equations, $\eta b \approx \Delta CTD_{th}$, designates the threshold range of crack tip displacement below which irreversible crack tip extension does not occur, with η on the order of unity and b equal to the magnitude of the Burgers vector. In the case of the uncracked simulations (Eq. 3.15), the crack length, a, is multiplied by the FIP obtained from uncracked simulations to estimate the increase in FIP with crack propagation.

The approach in Eq. 3.16 is more accurate, but it requires many successive stationary crack simulations or the use of a proper damage evolution/scaling relationship, which causes this model to be computationally prohibitive for large-scale finite element models and/or large-scale parametric studies. On the other hand, the approach in Eq. 3.15 is computationally faster and is better suited for larger-scale FEM simulations and parametric studies. However, the latter approach, in its current form, does not account for the intensification of cyclic stress and plastic strain ahead of the crack tip with crack advance.

This work seeks to enhance the approach in Eq. 3.15 and relate this growth law to actual MSC growth experiments. We accordingly propose a new MSC growth law as:

$$\frac{da_N^*}{dN} = A_{FS}^{env} \; FIP_{FS}^*(N) \; (a_N)^{n_{env}} - \eta b \tag{3.17}$$

where the parameters A_{FS}^{env} and n_{env} are meant to account for environmentally-assisted MSC growth of laboratory air versus vacuum experimental environments. An increase in the A_{FS}^{env} and n_{env} parameters in Eqn. 3.17 respectively increase the nominal "y-intercept" and "slope" of the power law expression (Eqn. 3.17) when plotted on log-log plot of da/dN versus computed ΔK. It is well known from post-test fractography

analyses of elevated temperature Ni-base superalloy tests (cf. [12, 85]) that cracks emanating from the interior or bulk of a specimen behave differently and grow at a different rate than cracks emanating from the surface due to two factors: (1) Interior MSCs are subject to more constraint from the surrounding material than cracks emanating from the surface [135] and (2) internal MSCs are more shielded from environmentally-assisted cracking. It should be noted that environmentally-assisted cracking within the bulk of the material can occur due to long-range oxygen diffusion along slip planes or grain boundaries [83]. However, the cyclic loading frequency considered for the current study ($f = 0.33$ Hz) is above the 0.1 Hz transition frequency below which there is a transition from transgranular-dominated to intergranular-dominated fatigue mode [95]. In fact, internal MSC growth in fine-grained Ni-base superalloys at 650°C and $f = 0.33$ Hz remains transgranular until the crack reaches the surface; once the crack is exposed to lab air there is a sharp transition to intergranular failure mode around the periphery of the crack when the crack length is above a transition crack length of ~ 100 μm [12, 85]. Hence, prior to breaking the surface of a specimen, internal MSCs grow under a pseudo-vacuum whereas cracks emanating from the surface are exposed to the external (air) environment. Therefore, we propose that the A_{FS}^{env} and n_{env}, where the env can be either lab air (air) or the vacuum (vac), are used to account for the difference in MSC growth rates for cracks emanating from the surface (lab air) and from the bulk (pseudo-vacuum). These two parameters are estimated using long crack growth experiments performed in vacuum [136] and small crack growth experiments performed in lab air [137, 138]. More details regarding these experiments will be covered later.

The purpose of $FIP_{FS}^{*}(N)$ in Equation 3.17 is to capture the increase in FIP_{FS}, cyclic stress, and plastic strain ahead of the crack tip with crack advance as a function of $FIP_{FS,uncracked}$. The value of $FIP_{FS}^{*}(N)$ is assumed to depend on many loading and microstructural parameters, as

$$FIP^{*}(N) = f(FIP_{FS,uncracked}, a_N, \overline{d}_{GB}, \alpha, \beta) \tag{3.18}$$

where the variables in the parentheses include the Fatemi-Socie FIP from uncracked

simulations, the current crack length at a given number of cycles, the distance of the crack tip from the grain boundary, and the twist and tilt angles of adjacent slip/crack planes. Implementation of such a model requires knowledge of how the FIP evolves with all these listed parameters. This is no small task to pursue. Determining the effect of every single combination of tilt and twist angles on the evolution of $FIP^*_{FS}(N)$ is impossible. As an example, Saylor et al. [106] state that between two cubic crystals there are 10^5 different GB character combinations, assuming 5° resolution for all 5 GB degrees of freedom. Therefore, in this work, a number of random grain orientation instantiations are simulated for a simple FEM model geometry. The assumption here is that fitting a functional form to these parameters for a number of FEM instantiations should suffice in the current framework and should be able to describe the evolution of FIP for the whole cornucopia of potential grain boundary character.

An extensive amount of analysis regarding the fatigue crack growth behavior as a function of grain boundary character has been done by Zhai and coworkers [49, 52, 139, 140] to characterize the effect of twist angle on crack growth past the grain boundary. In the Ph.D. work of Wen [141], a Paris-law-type crack growth rate was assumed to apply for small crystallographic cracks growing in a high-strength Al-Cu aluminum alloy AA2024-T351, i.e.,

$$\left.\frac{da}{dN}\right|_{GB} = C\left(\Delta K_{eff} - R(\alpha)\right)^m \tag{3.19}$$

where the range of effective stress intensity factor was calculated as $\Delta K = 2\Delta\sigma\sqrt{a/\pi}$ for the assumption of a semi-circular shaped crack, $\Delta\sigma$ was the far-field stress amplitude, and a was the crack half-length. The resistance of the grain groundary to crack propagation, $(R(\alpha))$, was assumed to be a function of the twist angle (α) of the grain boundary and was assumed to follow the form of a two-parameter Weibull cumulative distribution function, i.e.,

$$R(\alpha) = R_f\left[1 - \exp\left\{-(\alpha/\alpha_o)^n\right\}\right] \tag{3.20}$$

where values of R_f=0.9MPa$\sqrt{m}$, the Weibull scale α_o=20.1°, and Weibull shape $n = 4.2$ were found to fit the crack growth resistances measured from aluminum alloy

crack growth experiments, as shown in Figure 3.5. As can be seen from this Figure, the crack growth resistance is an "S-curve" shape that is minimal for smaller twist angles, reaches an intermediate inflection point at twist angle of approximately 20° and tends to plateau at twist angles above 30°.

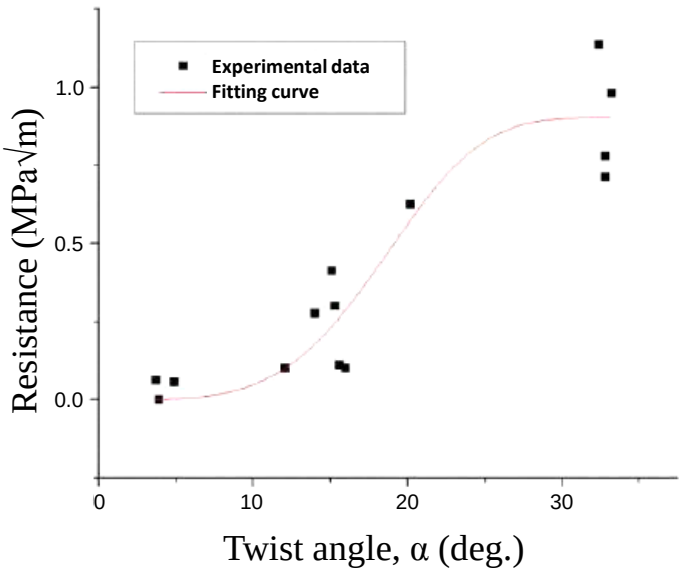

Figure 3.5: Experimental crack growth resistance versus grain boundary twist angle data for a single crack growth through 14 grain boundaries in a high-strength Al-Cu aluminum alloy AA2024-T351 [141].

One thing that should be noted about the previous work of Wen [141] and Wen and Zhai [52] is that they used the remote stress intensity factor, ΔK, as the driving force for microstructurally-small crack growth. It is well known that the applicability of ΔK as a unique identifier of crack growth da/dN breaks down for MSCs due to their lack of similitude [2] and the significant effect of microstructure heterogeneity in the MSC growth regime. Therefore, the application of the grain boundary resistance factor $R(\alpha)$ in Equation 3.20 to MSCs should be modified accordingly. In the current work, we adopt the essence of this Equation for estimating MSC growth resistance as the MSC approaches the grain boundary; the Weibull-distributed resistance to MSC growth will be used to modify the driving force (FIP) computed from CPFEM simulations.

To incorporate the effect of tilt angle on the resistance of the grain boundary to MSC propagation, a modification of Equation 3.20 is proposed. Some observations and assumptions must be stated. First, based on the limited number of data points in Figure 3.5, there seems to be a steady increase in the spread between the minimum and maximum grain boundary resistance values for a given twist angle with an increase in the twist angle. This increase in grain boundary resistance spread can be estimated to first order via

$$R_{max}(\alpha) - R_{min}(\alpha) = C_1 + C_2\alpha \tag{3.21}$$

where C_1 and C_2 are constants. Second, since there is no information about the experiments regarding the tilt angles of each data point in Fig 3.5, it is assumed that the spread in grain boundary resistance (Eq. 3.21) is due to differences in grain boundary tilt angle. It is assumed that smaller tilt angles will provide less crack growth resistance than larger tilt angles for the same twist angle. Combining these two observations/assumptions, a modified Weibull distribution equation is assumed for the contribution of tilt angle to grain boundary resistance via

$$R(\beta) = [R_{max}(\alpha) - R_{min}(\alpha)]\,[1 - \exp\{-(\beta/\beta_o)^m\}] \tag{3.22}$$

$$= (C_1 + C_2\alpha)\,[1 - \exp\{-(\beta/\beta_o)^m\}] \tag{3.23}$$

The first part of this Equation accounts for the increase in the spread of GB resistance values with increasing twist angles as observed in the experimental data in Figure 3.5; the second part of Equation 3.23 accounts for the increase in grain boundary resistance with increase in tilt angle, β. Combining Equations 3.20 and 3.23, the total grain boundary resistance factor, $R_{GB}(\alpha, \beta)$, is assumed to follow the form:

$$R_{GB}(\alpha,\beta) = R_f \cdot [1 - \exp\{-(\alpha/\alpha_o)^n\}] \quad + \quad (C_1 + C_2 \cdot \alpha) \cdot [1 - \exp\{-(\beta/\beta_o)^m\}] \tag{3.24}$$

An example of comparing the grain boundary resistance factor for different values of twist and tilt angles is shown in Figure 3.6. In this Figure, R_f=0.65, α_o=20°, $n = 8$, $C_1 = 0.25$, $C_2 = 0.0075$, $m = 2$, and β_o=15.0°. Also, note that the experimental data from Figure 3.5 are also re-plotted on Figure 3.6 solely for the purpose of a pseudo-comparison of the amount of scatter in the grain boundary resistance as a function

of tilt and twist angles. It must be emphasized that the experimental and proposed computational grain boundary resistances plotted on Figure 3.6 are in *different* units ($[MPa\sqrt{m}]$ versus [non-dimensional], respectively) and that these two data sets should only be compared *qualitatively* because the overriding purpose of the proposed grain boundary resistance functional form is to capture the *essence* of the experimental data. Better predictions of grain boundary resistance values as a function tilt and twist angle could be obtained via detailed in-situ loading stages (e.g. high-energy diffraction microscopy [142, 143]) that are able to resolve real-time cyclic crack tip opening displacement values and growth rates for MSCs growing past grain boundaries for the Ni-base superalloy IN100 of current interest. However, in the absense of such detailed experimental data, we make a conjecture that the grain boundary resistance function in Equation 3.24 which is depicted in Figure 3.6 is applicable for the current study of MSCs growing in Ni-base superalloy IN100.

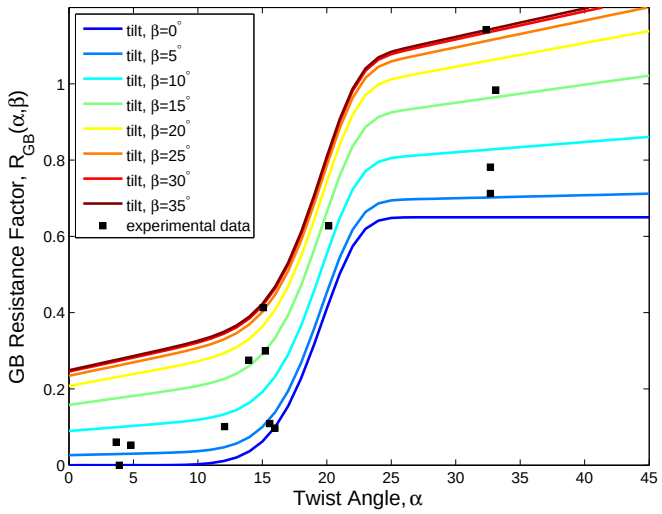

Figure 3.6: Experimental versus computationally-proposed crack growth resistance versus grain boundary twist and tilt angle. Computational values of resistance factor are non-dimensional and experimental values are in units of $[MPa\sqrt{m}]$.

MSC growth tends to display an oscillatory behavior in the da/dN versus remote ΔK curve with the crack growth rate slowing down as it approaches the grain boundary. Figure 3.7 shows a schematic of a transgranular MSC growing towards a grain boundary for uniaxial cyclic loading. The overall crack growth direction in this Figure is in the

x-direction. For modelling crystallographic/planar MSC growth, the crack is assumed to propagate along the plane with the highest driving force FIP (covered later). The MSC is assumed to propagate along this plane with no deflection, until it reaches the next grain boundary. Once the crack reaches the next grain boundary, the next MSC propagation plane is chosen, and so on, until the conditions of LEFM are met (crack length on the order of 3-10 grain sizes) and crack growth is estimated by a Paris law. The total crack length projected normal to the loading axis is the projected crack length, a_p. The length of the portion of the crack in the current cracked grain is given by a_g and the remaining ligament within the current cracked grain is given by B (ref. Figure 3.7). Based on these definitions, a normalized distance to the next grain boundary is given by $\overline{d}_{GB} = B/(\alpha_g + B)$.

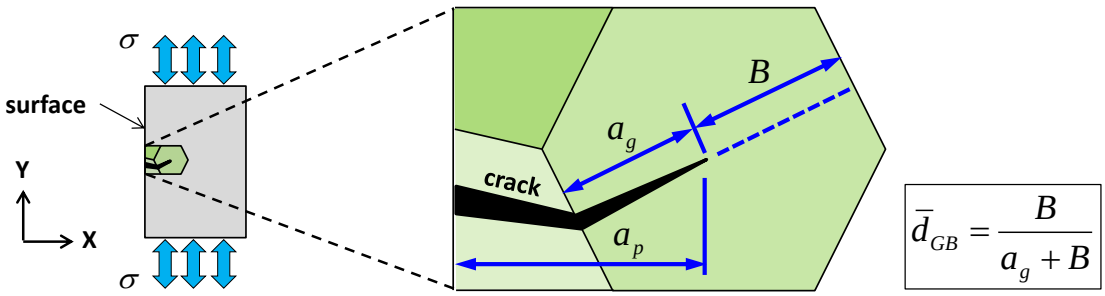

(a) Cyclically loaded component. Overall crack growth is in x-direction.

(b) Zoomed-in view to display crack and grain boundary distance definitions.

Figure 3.7: Schematic showing definition of projected crack length (a_p) and grain boundary distance ($\overline{d}_{GB}$) for the growth of a transgranular MSC due to cyclic uniaxial loading.

To account for the influence of the grain boundary on deceleration of the crack growth rate, a grain boundary distance function, $\eta(\overline{d}_{GB})$, is introduced via

$$\eta(\overline{d}_{GB}) = (1 - \overline{d}_{GB})^2 \tag{3.25}$$

This grain boundary function, inspired by the work of Chan and Lankford [65] (ref. Equation 3.6), is shown in Figure 3.8. Note that the grain boundary distance is normalized so that $(1 - \overline{d}_{GB})$ falls between the values of 0 (furthest from next grain boundary) and 1 (at next grain boundary), corresponding to the next grain boundary having a minimum and maximum grain boundary effect. The grain boundary

distance is normalized to account for differences in grain sizes when using a digitally-reconstructed microstructure that contains a grain size distribution.

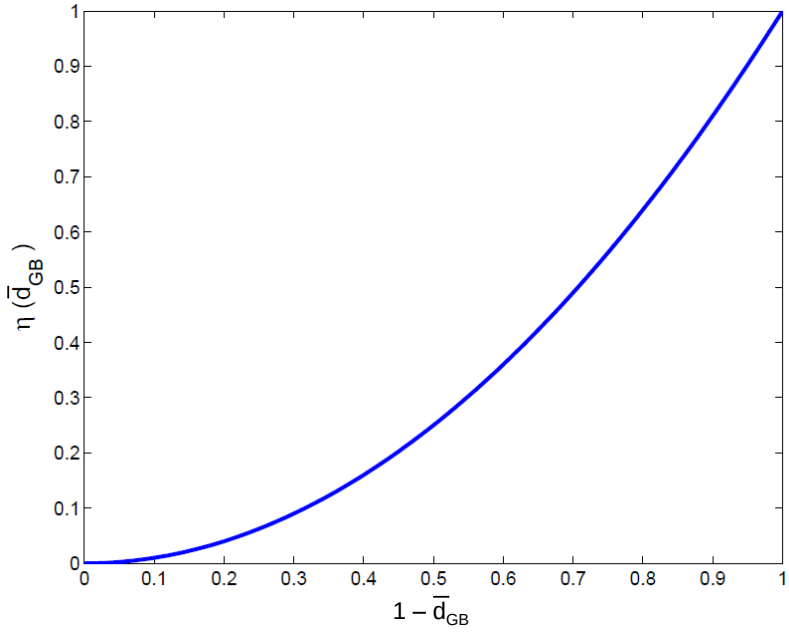

Figure 3.8: Grain boundary distance function, $\eta(\overline{d}_{GB})$, as a function of the distance to the next grain boundary, $\overline{d}_{GB}$, used to account for grain boundary influence on deceleration of the MSC growth rate.

Combining the effects of Equations 3.24 and 3.25, the proposed crack growth resistance as a function of tilt and twist angle and distance of the crack from the grain boundary is given as

$$\begin{aligned} R_{GB}(\alpha,\beta,\overline{d}_{GB}) = \{\ & R_f \cdot [1-\exp\{-(\alpha/\alpha_o)^n\}] \\ & +(C_1+C_2\cdot\alpha)\cdot[1-\exp\{-(\beta/\beta_o)^m\}]\ \}\cdot(1-\overline{d}_{GB})^2 \end{aligned} \tag{3.26}$$

An example of how the proposed MSC crack growth resistance curve evolves as a function of twist angles and crack distance from the next grain boundary for a constant tilt angle ($\beta = 0$) is shown in Figure 3.9. This proposed crack growth resistance curve modifies the MSC crack growth driving force, so that the MSC propagation law (Equation 3.17) now becomes

$$\frac{da_N^*}{dN} = A_{FS}^{env}\ FIP^*(N)\ (a_N)^{n_{env}}\left[1-R_{GB}(\alpha,\beta,\overline{d}_{GB})\right] - \Delta CTD_{th} \tag{3.27}$$

Now, what is left to be defined is how $FIP^*(N)$ changes with crack growth. This expression is developed through finite element simulations of stationary cracks of different lengths in the following section.

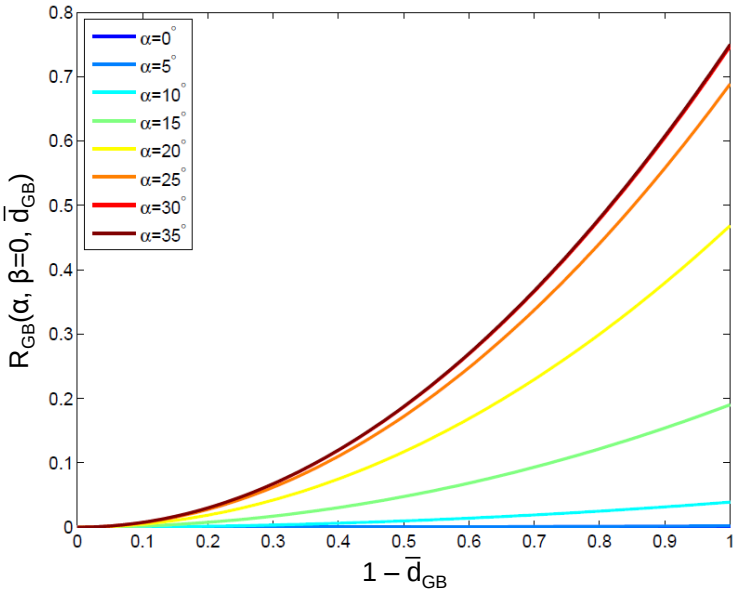

Figure 3.9: Proposed crack growth resistance versus grain boundary twist angle and crack distance from the next grain boundary for a constant tilt angle ($\beta = 0$).

3.5.4 FEM Simulation of Growth of a Stationary Crack

A finite element model is used here to model the evolution of fatigue crack driving force ($FIP^*(N)$) with crack growth. For this FEM simulation, a regular array of three rectangular-prism-shaped grains surrounded by a J2 plasticity matrix is modeled as shown in Figure 3.10. The dimensions of this model are $H = 500$ μm, $W = 500$ μm, and $B = 34$ μm. For each instantiation a random set of Euler angles was selected for each grain (G1-G3) according to the Bunge [107] convention from a uniform crystal orientation distribution via [32]

$$\phi_1 = 2\pi \cdot \xi_j, \quad \phi_2 = \cos^{-1}(2 \cdot \xi_{j+1} - 1), \quad \text{and} \quad \phi_3 = \pi \cdot \xi_{j+2} \tag{3.28}$$

where ξ is a random number from 0 to 1. To test out the validity of Equation 3.28 for generating random microstructures for cubic materials, a set of 100 random grain orientations was generated using Equation 3.28. The resulting pole figure and inverse

pole figure for this set of random grain orientations are shown in Figure 3.28. These pole figures were generated using the free MATLAB [144] plug-in MTEX [145]. As shown in Figure 3.11, Equation 3.28 is sufficient for generating random microstructural textures in cubic symmetry materials.

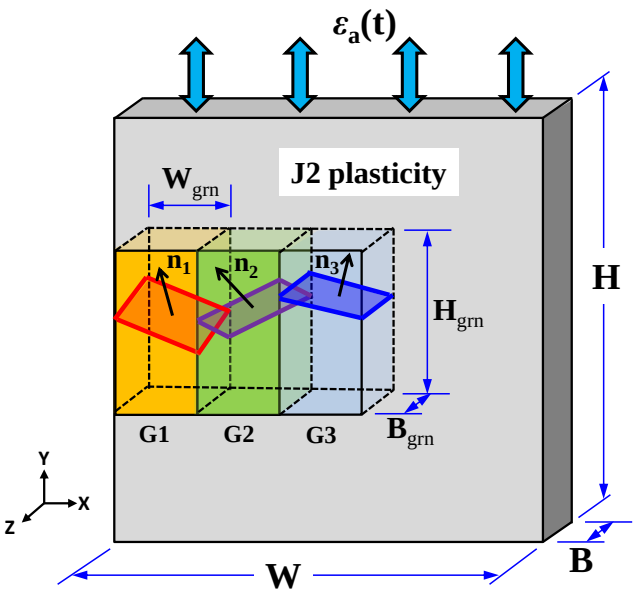

Dimension	Value (μm)
H	500
W	500
B	34
H_{grn}	136
W_{grn}	34
B_{grn}	34

Figure 3.10: Schematic of FEM model used to model MSC growth through three grains.

For the finite element arrangement displayed in Figure 3.10, the grain boundary normals are perfectly aligned along the x-direction and crack growth is assumed along the x-direction from the surface ($x = 0$) to the bulk of the material. This model was subjected to constant amplitude ($R_\varepsilon = 0.05$) strain-controlled loading with $\varepsilon_{max} = 1.5 * \varepsilon_y$, where $\varepsilon_y = 0.42\%$ is the yield strain (proportional limit) of the material, for the number of cycles that provided convergence of the FIP response. More details on how the FIP response converged with number of cycles will be covered later. To remove the effect of the top and bottom grain boundaries (in the y-dimension) on crack propagation and thereby isolate the effect of the grain boundary ahead of the crack tip on crack propagation along the x-axis, the grains were elongated along the y-axis so that the overall dimensions of each grain in the x, y, and z directions were $W_{grn} = 34$ μm, $H_{grn} = 136$ μm, and $B_{grn} = 34$ μm, respectively.

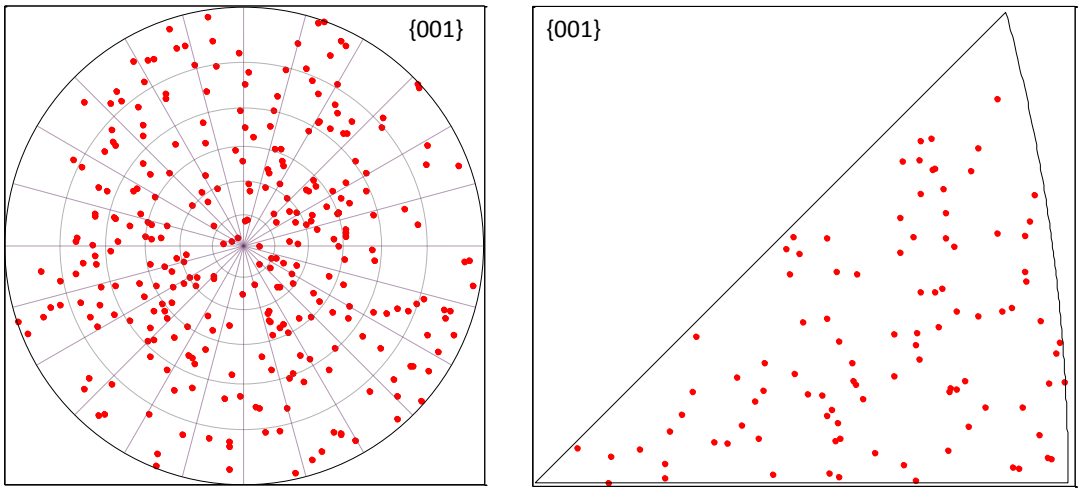

(a) [001] pole figure.

(b) [001] Inverse pole figure.

Figure 3.11: Example (a) [001] pole figure and (b) [001] inverse pole figure for 100 random grain orientations.

Crack propagation is limited to the crystallographic octahedral and cube slip planes for the current study. Once the crack plane corresponding to a particular slip plane is activated, it is "locked in" and assumed that the crack propagates along this plane throughout this grain. In other words, as shown schematically in Figure 3.10, the crack can only propagate along planes with normals $\boldsymbol{n}_1$, $\boldsymbol{n}_2$, and $\boldsymbol{n}_3$, for grains G1, G2, and G3, respectively; selection of these plane normals are described below. Experimentally, MSCs are observed to sometimes deflect onto other crystallographic planes within a grain so that multiple slip/crack planes are activated within a single grain. This phenomenon has been observed in Ni-base superalloys [89] and titanium alloys [142]; however, crack deflection onto other slip systems within grains is not accounted for in this work.

Several assumptions for the three-dimensional crack nucleation and MSC growth location and orientation are prescribed for this particular finite element configuration, as summarized in the 2D schematic shown in Figure 3.12. Figure 3.12(a) shows a side view of the full finite element model used for analysis. Each grain (G1, G2, G3 in Figure 3.10) is partitioned in the x-direction into 3 zones (z1, z2, and z3) that are used for tracking sub-grain FIP evolution with extension of the stationary crack front. The

naming convention used to identify each partition is G#z#, where the # numbers denote grain and partition zone numbers, respectively. To remove the influence of the J2 plasticity and CPFEM interface at the top and bottom of the grains on the overall crack propagation driving force, averaging of fatigue indicator parameters (FIPs) was done within the interior of the grain (vertically along the y-axis). The y-thickness of the "FIP non-averaging buffer zone" on the top and bottom of the grains used is 34 μm, as indicated by the cloudier-shaded regions in Figure 3.12 above and below the "FIP averaging region" in the center (vertically along the y-axis) of the grains.

Figures 3.12(b)-(e) show larger views of the 3 grain structure to display how crack nucleation and MSC propagation is applied in the finite element model. For crack nucleation (Figure 3.12(b)), averaging of the "uncracked FIP" is done within the whole grain, less the top and bottom non-averaging buffer zones. Thus, the averaging volume for fatigue crack nucleation is equal to 34 μm $\times$ 68 μm $\times$ 34 μm. The crack incubation plane, $\boldsymbol{n}_1$, is the crystallographic plane that contains the maximum of all slip system ($N_{\text{slip sys}} = 1$ to 18) ranges of plastic shear strain, i.e.,

$$\boldsymbol{n}_1 = \boldsymbol{n}\left(\max\left[\Delta\varepsilon_{ij}^p n_i s_j\big|_{\text{slip sys=1}} \;,\; \Delta\varepsilon_{ij}^p n_i s_j\big|_{\text{slip sys=2}} \;,\; \cdots \;,\; \Delta\varepsilon_{ij}^p n_i s_j\big|_{\text{slip sys=18}}\right]\right) \tag{3.29}$$

where the range of plastic strain $\Delta\varepsilon_{ij}^p$ is the range over the last cycle of a given finite element loading block [29, 55].

The imposed location for crack nucleation is shown in Figure 3.12(c). For numerical convenience, the crack incubation plane is centered vertically along the y-direction about the first grain boundary between grain #1 and #2. This restriction is applied so that the crack can remain more centered vertically (y-direction) within the model as it propagates through the second and third grains. For crack nucleation, a crack is induced where this crack incubation plane intersects the first partition zone in grain #1 (G1z1). The crack is assumed to go through the entire z-thickness of the grain as indicated in Figure 3.12(c).

The stationary crack is induced in the FEM simulation by "cutting away" material from the model where the "cutting blade" is the crystallographic crack plane plus/minus a small kerf of total thickness, $t = 2$ μm. This cutaway for subsequent FEM models

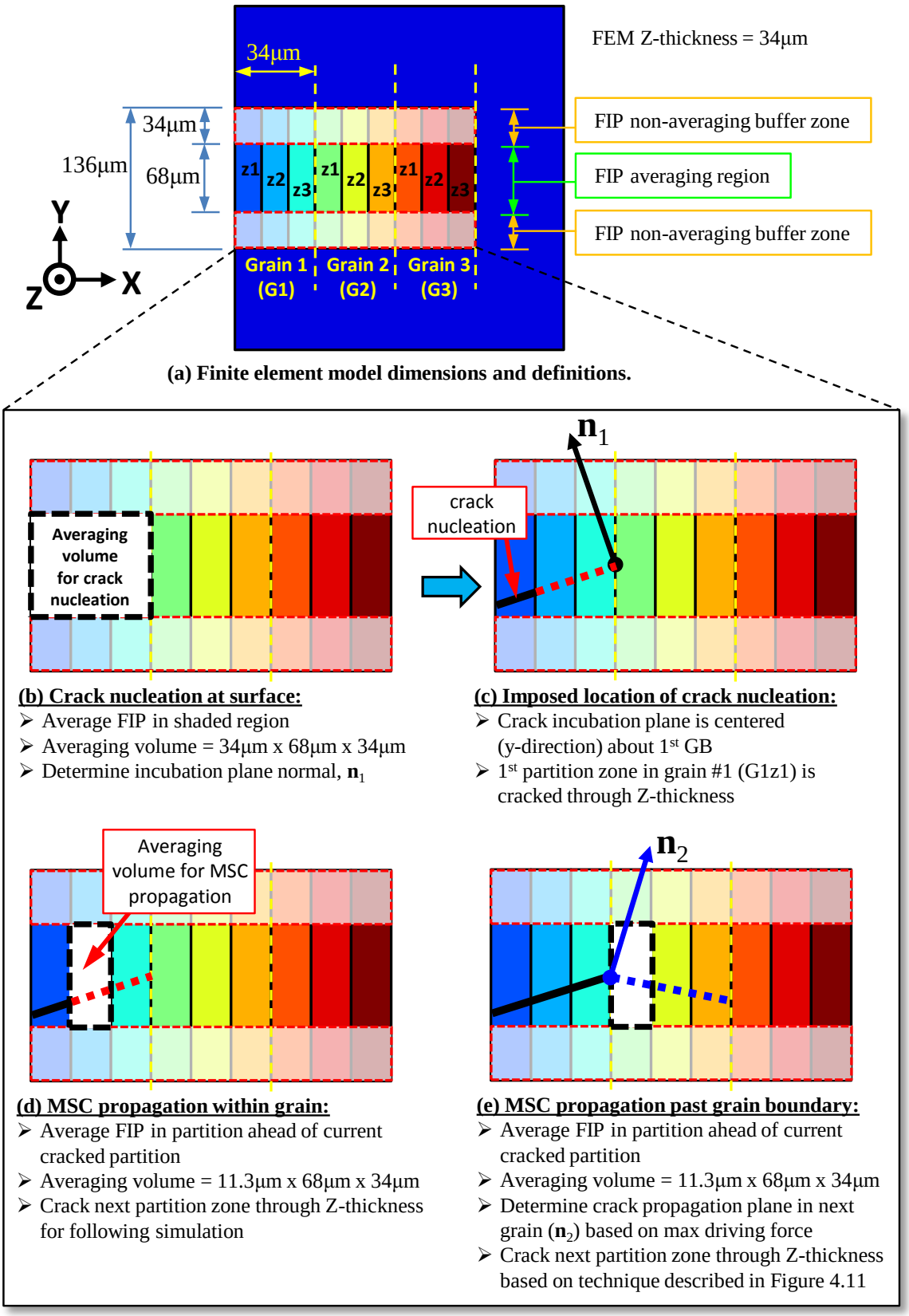

Figure 3.12: Two-dimensional schematic showing FEM definitions and technique for 3D MSC formation and propagation for 3 grain model.

is done using the Extrude/Cut command within the python scripting interface of ABAQUS [45]. The finite element model is then re-meshed for each simulation. This model employs second-order tetrahedral elements, C3D10, throughout all simulations. The length of the extension of the crack for each simulation is controlled by the partition zone thickness. For the current model, each grain is partitioned into three pieces, so each partition has an x-thickness of 11.3 μm.

Once a crack is incubated, MSC propagation is considered. As shown in Figure 3.12(d), for sub-grain MSC propagation, the driving force FIP is averaged within the partition ahead of (in the x-direction) the current cracked partition, less the non-averaging buffer zone. In the current case, the FIP averaging volume for MSC propagation is equal to 11.3 μ m $\times$ 68 μm $\times$ 34 μm. The crack growth is subsequently incremented by one partition x-thickness and remeshed for the next simulation. This process is continued until the MSC reaches the next grain boundary. For the current model, each grain is partitioned into three pieces, so there are three crack lengths simulated through each grain.

Once the crack is formed and propagates to the grain boundary, a criterion for MSC propagation past the grain boundary and into the next grain is required. Consider the propagation of an MSC from grain #1 (G1) to grain #2 (G2) as depicted in Figure 3.12(e). The average FIP located in the first partition of the next grain (G2z1) is used for assessing the next MSC propagation plane, $\boldsymbol{n}_2$. The orientation of the crack plane normal of the next grain, $\boldsymbol{n}_2$, is selected as the one that maximizes the MSC growth rate in Equation 3.27 of all slip systems ($N_{slip\ sys} = 1$ to 18), i.e.,

$$\begin{aligned}\boldsymbol{n}_2 = \boldsymbol{n}\,(\max[\ &\left\{A_{FS}^{env} FIP^{(k)} (a_N)^{n_{env}} \left[1 - R_{GB}(\alpha, \beta, \overline{d}_{GB})\right] - \Delta CTD_{th}\right\}|_{slipsys,k=1}\,, \\ &\left\{A_{FS}^{env} FIP^{(k)} (a_N)^{n_{env}} \left[1 - R_{GB}(\alpha, \beta, \overline{d}_{GB})\right] - \Delta CTD_{th}\right\}|_{slipsys,k=2}\,, \\ &\qquad\qquad\vdots \\ &\left\{A_{FS}^{env} FIP^{(k)} (a_N)^{n_{env}} \left[1 - R_{GB}(\alpha, \beta, \overline{d}_{GB})\right] - \Delta CTD_{th}\right\}|_{slipsys,k=18}\ ])\end{aligned} \tag{3.30}$$

This new crack plane in partition G2z1 is centered vertically (y-direction) according to where the crack in partition G1z3 is located at the grain boundary, as shown in Figure 3.12(e). The reason that the new plane is centered vertically relative to the

previous plane is because it is assumed that the crack path will follow the path of least resistance as it crosses the grain boundary; if there is no difference in the vertical translation of the crack between the two grains, the crack only has to tilt and twist its crack plane to propagate into the neighboring grain.

In most cases, when the two randomly oriented crack planes come together at the grain boundary, the coalescence between these two planes will not be a contiguous crack path. Fracture/slip steps can form [139] and/or propagation along two different slip planes can occur [146] to accommodate MSC propagation past grain boundaries that have slip/crack planes that do not intersect at the grain boundary. The formation of fracture/slip steps or propagation along two slip planes is not accounted for in this work. Instead, a numerical method to connect the crack plane from one grain to the next through the grain boundary is presented here by a simple example. Figure 3.13 shows an example of a bi-crystal with nonzero tilt and twist angles. The left hand side of this Figure shows the front face of the bi-crystal where, due to the twist angle of the grain boundary, the crack plane B is above crack plane A. For this case, the crack plane B is assumed to coalesce into crack plane A by carving out the yellow section of grain A as shown on the left hand side of Figure 3.13. Similarly, since the rear face has the crack plane A above crack plane B, crack plane A will carve into grain B along the yellow section shown on the right hand side of Figure 3.13. Therefore, this coalescence criteria allows the crack to tunnel through a little bit of each side of the grain boundary. In fact, since the two neighboring crack planes are centered vertically relative to each other at the grain boundary, the (yellow) volumes removed from grain A and B on each side of the grain boundary are exactly equivalent. For the cases where the tilt between the two crack paths is near zero and the twist is non-zero, the material is carved up to the face of the next partition zone.

It should be stressed that this coalescence criteria is merely used here as a numerical tool to avoid contact issues between the crack faces of different grains and to provide a contiguous crack path. The removed material within the crack zone has little effect on the stress distribution ahead of the crack tip, which is the most important zone for assessing MSC propagation in positive R-ratio loading. In other words, crack tip

closure is neglected for the loading conditions applied in these MSC growth simulations.

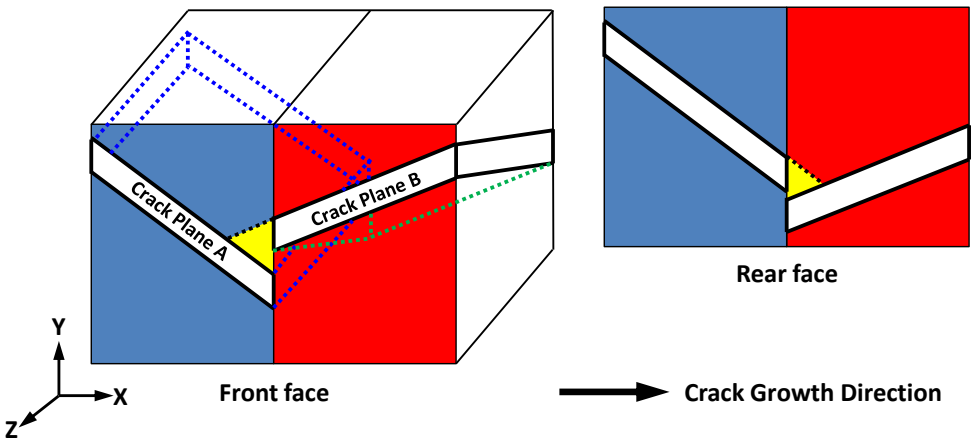

Figure 3.13: Example of prescribed condition for MSC growth across a Bi-crystal GB where the two crack planes have nonzero tilt and twist angles. Crack plane B normal vector is determined by Equation 3.30.

3.6 Results

3.6.1 Characteristics of MSC Growth Paths

The crystallographic and planar MSC growth process illustrated in Figure 3.12 was repeated for multiple instantiations. The contour plots of the Von Mises stresses for four different crack lengths (zero, one, two and three grains cracked) that were captured at the 3rd cycle at maximum tensile load are shown in Figure 3.14 for one instantiation. For each Von Mises plot, the contour plots are colored according to the color bar displayed in the upper left hand portion of the Figure. Also shown in this Figure are the three Euler angles used for each grain in the simulation. As expected, the higher stress lobes in front of the crack tip increase in overall size with crack growth due to the generation of a stress concentration at the crack tip. Also, it is apparent that the stresses decrease significantly in the wake of the crack tip. The existence of the crack prevents the material from carrying any load along the crack faces. A more quantitative assessment of the driving forces ahead of the crack tip and the crack path are covered in this section. This more quantitative characterization of how the stresses redistribute and evolve with MSC propagation will be used here to

help develop a more robust MSC growth prediction law.

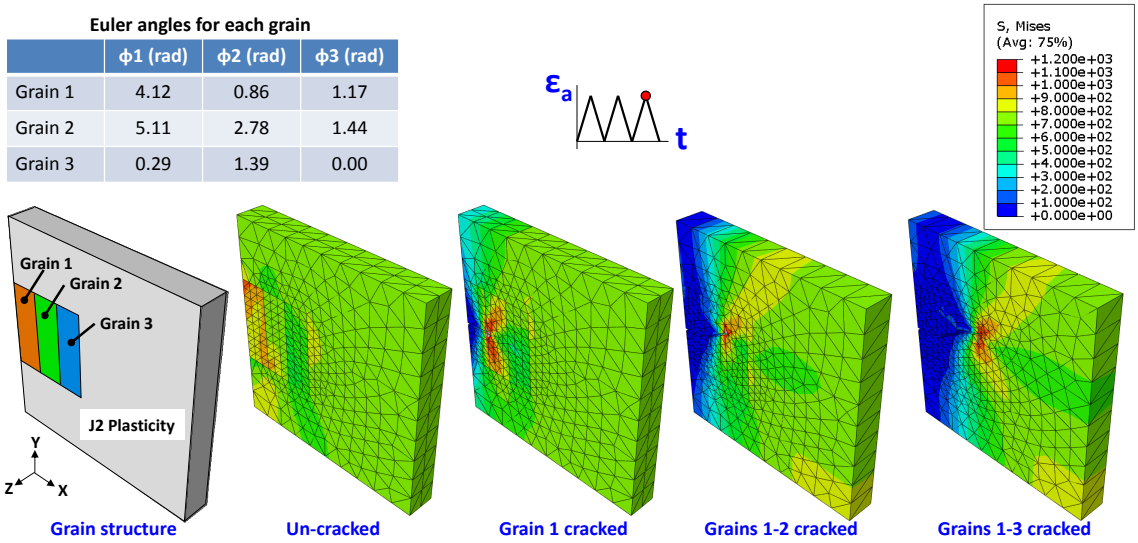

Figure 3.14: Contours of Von Mises stresses captured at the 3rd tensile maximum load for crack propagation through three grains.

Figure 3.15 shows the crack growth attributes of the MSC propagation example shown in Figure 3.14. The top and bottom left hand images in this Figure highlight the top and bottom portions of the induced crack path, respectively. The blue, red, and green fill colors in this Figure correspond to the crack planes in grains 1, 2, and 3, respectively. The calculated tilt and twist angles across each grain boundary are also displayed in this Figure. Note that the configuration of crack planes of the first grain boundary (1-2) are representative of the configuration shown previously in Figure 3.13. Since this first grain boundary has a positive tilt angle ($\vee-$shaped) and the second grain boundary is above the first grain boundary at the front face, the assumed growth across the GB results in the second grain carving into the first one towards the front face and the first grain carving into the second one towards the back face, which is consistent with the condition in Figure 3.13. The second grain boundary in this Figure shows the growth across the GB for a grain boundary with a negative tilt angle. In this second case, the carving out of grains 2 and 3 are performed on the bottom portion of the crack plane.

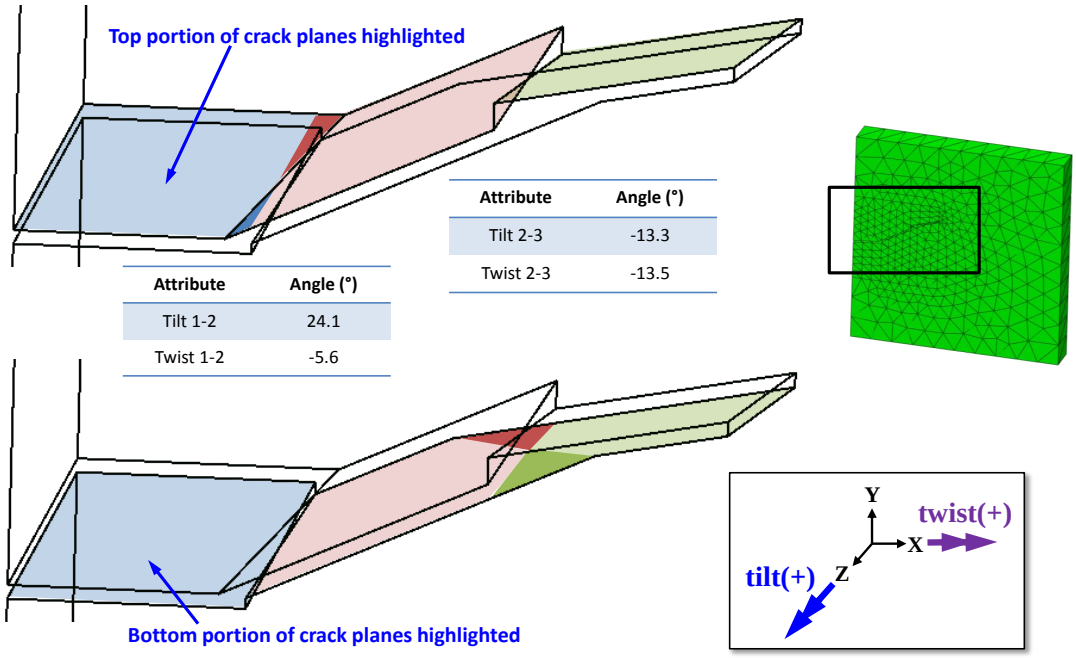

Figure 3.15: Example crack path attributes for the crack propagation through three grains shown in Figure 3.14.

3.6.2 Distribution of Tilt and Twist Angles for Example MSC Growth Paths

The grain boundary character has a significant effect on MSC growth behavior. The grain boundary character contains five degrees of freedom, including three rotation angles that bring two misoriented crystals into coincidence, and two spherical angles that orient the boundary plane [106]. One way to describe the misorientation between two slip/crack planes of adjoining grains is by tilt and twist angles. A significant number of authors [49–51] point to the fact that the main parameters that control or inhibit MSC growth past a grain boundary is the magnitude of the twist and tilt angles between two slip/crack planes of adjoining grains. It has been shown in previous FIB serial sectioning studies of MSCs in a directionally-solidified CMSX-4 [146] that the orientation of the grain boundary normal relative to the loading axis also has a significant effect on MSC growth resistance past a grain boundary. However, the current study is solely focused on the effect of tilt and twist angles on MSC growth across grain boundaries.

This section presents results from $N = 9$ instantiations of simulated MSC growth through three grains. For each instantiation, the Euler angles of each grain were randomly selected from a uniform orientation distribution function (Equation 3.28). A small sampling of example crack paths in three-dimensional space are shown in Figure 3.16. Again, the slip planes that were chosen to crack in grains 2 and 3 were the ones that maximized the MSC growth rate in Equation 3.30. The blue, red, and green planes in Figure 3.16 correspond to the crack planes in grains 1, 2, and 3, respectively. In these simulations, the crack path was assumed to start from the surface at x=0 and propagated through the depth of three grains to $x = 102$ μm. The grid spacing in this Figure matches the average grain size, $d_{grn} = 34$ μm.

For each instantiation and grain boundary, the tilt and twist angles were calculated and are listed in Table 3.1. It is easy to note that most twist and tilt angles in this Table are lower than 35°. As a comparison, the maximum twist angle possible between two $\langle 111 \rangle$ octahedral slip planes is 35.3°. The two main exceptions where the tilt and twist angles are above 35° are instantiations 4 and 9; instantiation 4 has a twist angle between grains 2 and 3 of 63.1° and instantiation 9 has a tilt angle of 67.6° degrees because it had a high Schmid factor along the failure plane. These two particular grain boundary crack paths have a lower twist angle when the tilt angle is higher and vice versa. It has been observed experimentally for a high-strength FCC aluminum alloy [139] that tilt and twist angles above 35° occur. However, these cases where high tilt or twist boundaries are observed are not seen as readily as grain boundaries with lower tilt and twist angles. The distribution of tilt and twist angles in Table 3.1 are compared to experimental values [139] next.

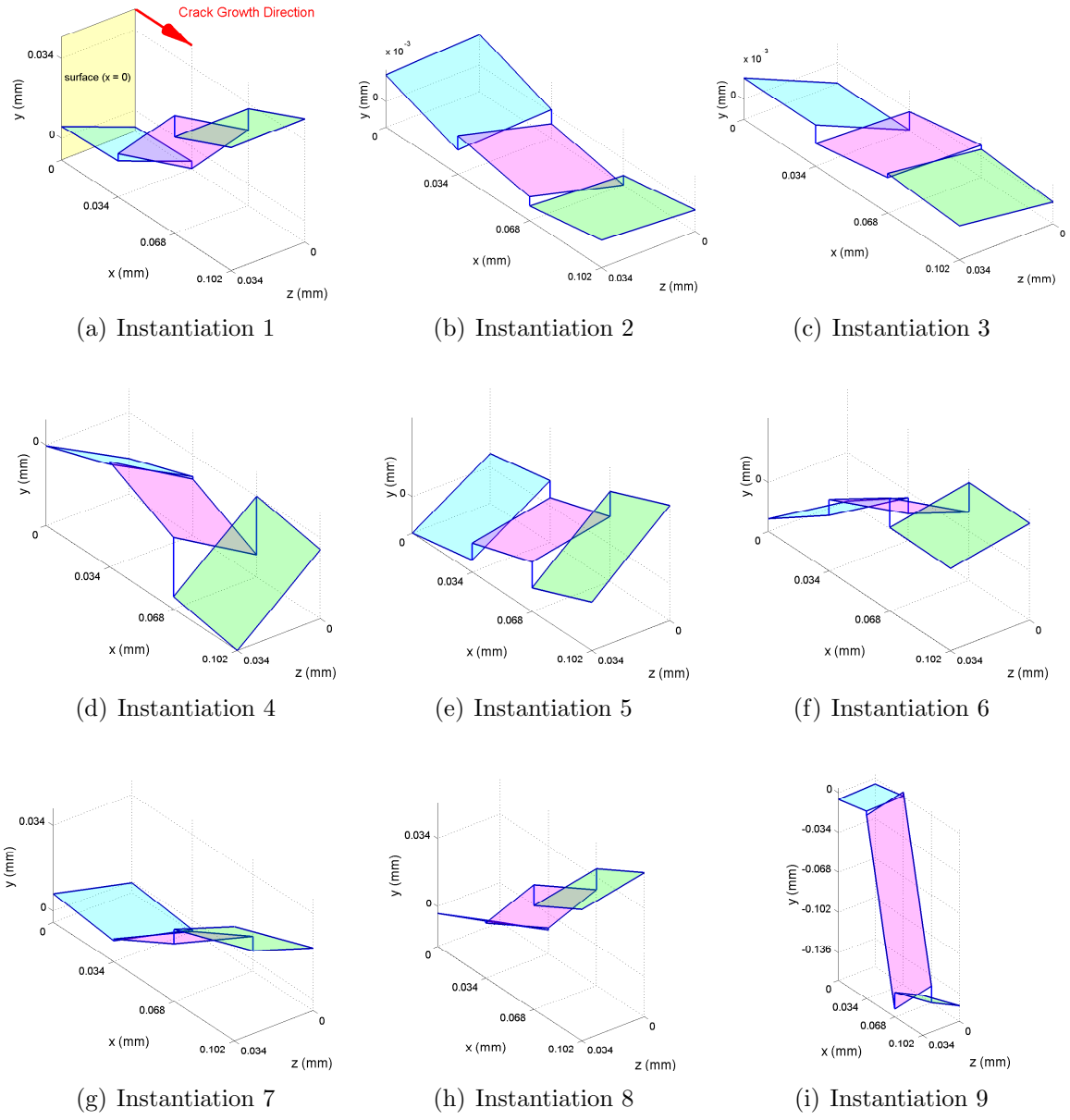

(a) Instantiation 1 (b) Instantiation 2 (c) Instantiation 3

(d) Instantiation 4 (e) Instantiation 5 (f) Instantiation 6

(g) Instantiation 7 (h) Instantiation 8 (i) Instantiation 9

Figure 3.16: Example MSC crack paths for different randomly oriented grains. The cracks are assumed to initiate at $x = 0$ and propagate along the x-axis. Each color corresponds to a different grain and crack plane.

Table 3.1: Tilt and Twist Angles for Crack Paths Displayed in Figure 3.16.

Instantiation	Twist12 (°)	Tilt12 (°)	Twist23 (°)	Tilt23 (°)
1	8.5	41.2	19.8	20.2
2	15.9	23.3	5.7	22.5
3	19.8	7.1	15.2	3.4
4	2.4	31.4	**63.1**	6.8
5	20.0	6.1	7.7	19.8
6	19.2	3.3	17.9	25.3
7	2.2	16.1	18.4	17.7
8	2.8	25.9	36.6	4.2
9	11.3	**67.6**	33.4	8.7

The importance of accounting for the tilt and twist angles when assigning MSC crack paths should be underlined further with comparisons to experimental crack path data. In the absence of available detailed MSC crack path data for Ni-base superalloys at elevated temperatures, comparison to other alloys with similar failure modes is necessary. Therefore, the crack path tilt and twist angles obtained computationally are compared to the experiments of Zhai et al. [49, 139] on an FCC aluminum alloy Al-Li 8090 fatigued at room temperature. The main failure mode experimentally observed in this alloy was crystallographic along octahedral slip planes [139], which is similar to the faceted {111} crystallographic crack growth mode in Ni-base superalloys at lower temperatures ($T < 450$°C) previously described in Section 3.4. Although these Al-Li 8090 experiments are from a different alloy than IN100, a qualitative comparison is made due to similar activation of octahedral slip/failure mode at lower temperatures. Thus, these Al-Li 8090 experiments are deemed comparable to the assumed failure mode in Ni-base superalloys at intermediate (T$\sim$450° and lower) temperatures where octahedral slip is the dominant slip mechanism active. Better comparisons can be made when more detailed investigations into characterizing MSC fracture surfaces for Ni-base superalloys fatigued at elevated temperatures become available (for example, by tilt fractography in [93, 94]). For the time being, there is merit in qualitatively comparing the distribution of tilt and twist angles in Table 3.1 found from the simulations depicted in Figure 3.16 to the distribution of tilt and twist

angles found in these aluminum alloy experiments.

There is a significant difference in the distribution of MSC crack path characteristics (tilt and twist angles) for multiple instantiations between (Case 1) accounting for and (Case 2) not accounting for the tilt and twist angles when using the FIP to assess the plane in which the crack will be extended past the grain boundary and into the next grain. To support this statement, 10 separate MSC growth model instantiations were simulated. In this second case where the tilt and twist angles were not accounted for, only the maximum crystallographic Fatemi-Socie parameter was used as the indicator for which slip plane was going to be cracked in the next grain. The resulting distribution of tilt and twist angles of the computational MSC growth models when the tilt and twist angle are (Case 1) accounted for and (Case 2) not accounted for are shown in Figure 3.17. In these two plots, the green filled diamonds represent the experimentally-observed [139] tilt and twist angles for N=13 grain boundaries for an aluminum alloy Al-Li 8090 fatigued at room temperature. Also in this Figure, each red "x" and blue "o" corresponds to the tilt/twist combination at the grain boundary between grain 1 and 2 and the grain boundary between grain 2 and 3, respectively, calculated for a single instantiation of a randomly-oriented set of 3 grains.

Several key points can be made regarding Figure 3.17. First, the experimental grain boundary tilt and twist angle data points are most densely populated within the window where the tilt and twist angles are less than 30°. There are a few outliers in the experimental data where the twist and tilt angles are above this 30° window, but these values tend to have only a larger twist *or* tilt angle. Comparing this experimental distribution to Case 1, where the tilt/twist behavior is accounted for in the MSC growth law, it is easy to see that the distribution of computational data for Case 1 qualitatively match that of the experimentally-observed data. On the other hand, when the tilt/twist behavior is not accounted for in the MSC growth law as in Case 2, the experimental and computational data have no correlation. In fact, it seems that higher twist angles promote a higher driving force for fatigue crack propagation as defined in Case 2 as the maximum crystallographic Fatemi-Socie parameter. Experimentally, it has been shown that high-angle grain boundaries tend to be more favorable for fatigue

crack formation [109]. Therefore, the tilt and twist angles should be used for assessing MSC growth propagation, and not fatigue crack initiation.

To further display the correlation between experimental data and the simulation data obtained for Case 1, the twist and tilt data in Figure 3.17 are re-plotted in Figure 3.18 as histograms containing 10° bin sizes. In this Figure, the left column contains the twist data and the right column contains the tilt data for the experimentally observed (top row) values [139] versus the computationally-predicted values for Case 1 (middle row) and Case 2 (bottom row) crystallographic MSC growth. Again, Case 1 accounts for tilt/twist behavior and Case 2 does not account for tilt/twist behavior within the MSC growth law. Figure 3.18 shows that the distribution of twist and tilt values of Case 1 (in the middle row) have a high frequency of values at tilt and twist angles less than 30 degrees and sparse tilt and twist values above 40 degrees, which correlates well with the experimental distribution of tilt and twist angles in the top row. On the other hand, the distribution of tilt and twist angles for Case 2 in the bottom row appear more evenly distributed and do not correlate well with the experimental distributions in the top row. Therefore, based on the limited number of experimental twist/tilt data points ($N = 13$ GBs) and computational twist/tilt data points (18 GBs for Case 1 and 20 GBs for Case 2), we conclude that Case 1 is more suited for MSC growth past grain boundaries than Case 2.

One last comparison that should be made between experiments and computations is the distribution of grain boundary resistance values used for the (Case 1) MSC simulations that took into account grain boundary tilt/twist character. Plotted in Figure 3.19 are the grain boundary resistance values for the simulations plotted in Figures 3.16 and 3.17(a) as a function of the twist values of the grain boundary. Just like in Figure 3.17, each red "x" and blue "o" corresponds to the GB resistance/twist combination at the grain boundary between grain 1 and 2 and the grain boundary between grain 2 and 3, respectively. Also plotted in Figure 3.19 is the minimum and maximum possible bounds on the grain boundary resistance values for the case when a tilt angle of 0° and 90° are assumed, respectively. Comparing the computational distribution of GB distribution values in this Figure to the S-curve distribution

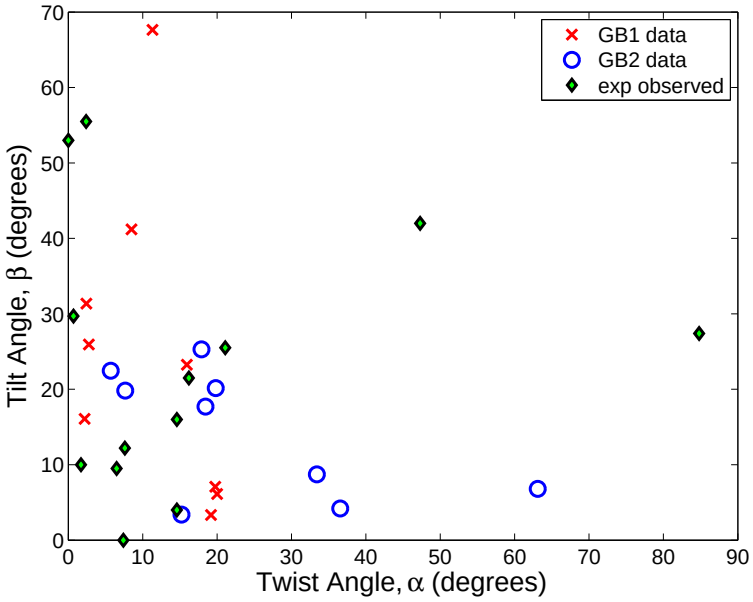

(a) Case 1: Accounting for tilt/twist behavior in MSC growth law.

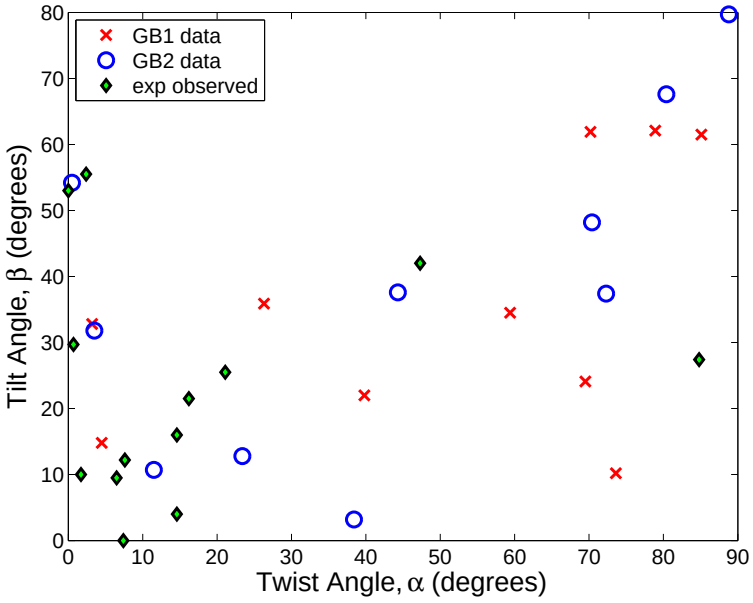

(b) Case 2: Not accounting for tilt/twist behavior in MSC growth law.

Figure 3.17: Tilt versus twist character values for example MSC crack paths with comparison to experimentally observed values [139]. The tilt and twist behaviors for Case 1 correspond to MSC crack paths displayed in Figure 3.16. The GB1 and GB2 values correspond to the grain boundary between grains 1 and 2 and grains 2 and 3, respectively.

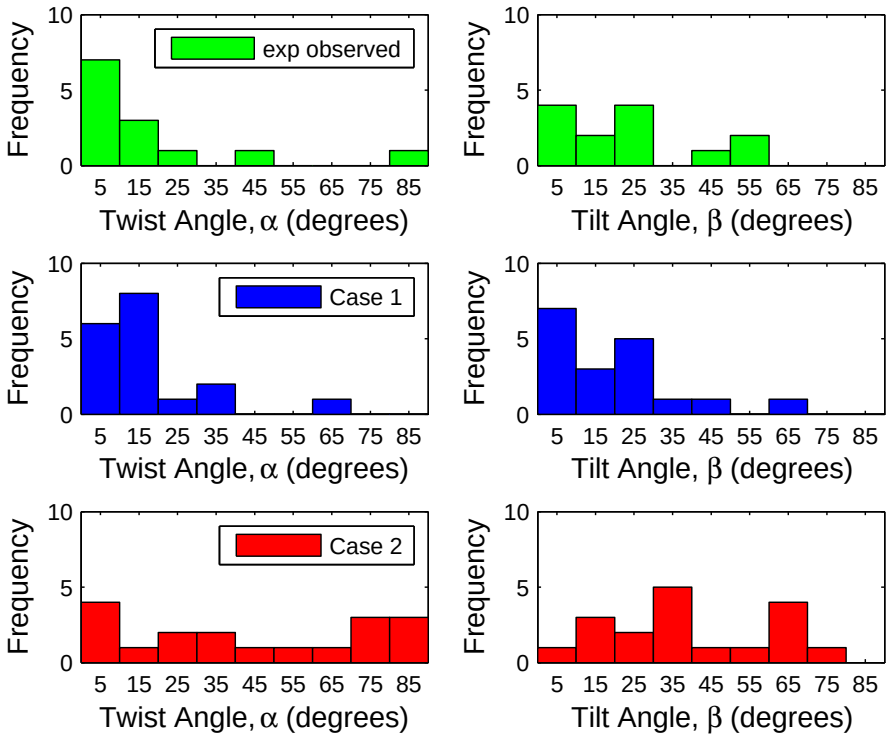

Figure 3.18: Histograms of twist (left column) and tilt (right column) angles for experimentally observed (top row) values [139] versus those computationally-predicted for Case 1 (middle row) and Case 2 (bottom row) crystallographic MSC growth. Case 1 accounts for tilt/twist behavior and Case 2 does not account for tilt/twist behavior within the MSC growth law.

of experimental GB resistance values in Figure 3.6 it can be seen that these two distributions are qualitatively very similar. Both distributions are relatively dense up to the inflection point of the S-curve. Also, both distributions have data points above the inflection point, but these are a small percentage of all data points recorded. Therefore, it can be concluded that the functional form for the grain boundary resistance as a function of tilt/twist angles presented in Equation 3.26 *qualitatively* reproduces the distribution of grain boundary resistances seen in experiments.

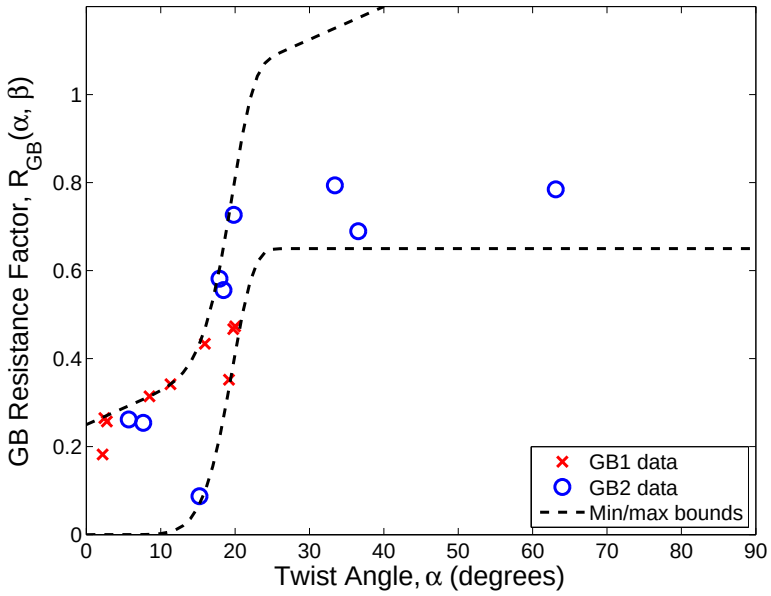

Figure 3.19: Grain boundary resistance values used for MSC simulations displayed in Figure 3.16. Distribution of GB resistance should be compared to Figure 3.6.

3.6.3 Applicability of MSC growth law incorporating tilt and twist angle

The MSC growth law developed in this section uses the tilt and twist angles and distance from the grain boundaries as indicators of resistance to crack growth propagation past the grain boundary. This growth law is predicated on the assumption of crystallographic crack growth. As such, for Ni-base superalloys, this law is applicable for MSC growth estimations at intermediate (T$\sim$450° and lower) temperatures where octahedral slip is the dominant slip mechanism active. For higher temperatures, multi-slip or wavy slip is more predominant resulting in Mode I crack propagation [78, 79].

Therefore, the meandering crack front can approach the boundary such that minimal resistance is encountered. However, oscillatory MSC growth behavior in Ni-base superalloys is still relevant at these higher temperatures (cf. [12]) and there is still a barrier to slip at grain boundaries. Therefore, a slight modification to the MSC growth law proposed in Equation 3.27 is used for higher temperature MSC propagation via:

$$\frac{da_N^*}{dN} = A_{FS}^{env}\ FIP^*(N)\ (a_N)^{n_{env}}\left[1 - R_{GB}\cdot(1-\overline{d}_{GB})^2\right] - \Delta CTD_{th} \tag{3.31}$$

where the grain boundary resistance, R_{GB}, is assumed to be a constant instead of varying with tilt and twist angle. Since the current work models MSC growth at 650° in a coarse-grained IN100, Equation 3.31 will be used for MSC growth computations.

3.6.4 Evolution of FIP with Number of Cycles

One question that needs to be addressed is the evolution of the FIP with number of cycles for a crack of a given length (for the FIP averaging regions shown in Figure 3.12). When a specimen is cycled in strain-controlled, positive R-ratio fatigue, the phenomenon of hardening and elastic/plastic ratcheting can cause the local stress/strain behavior near the crack tip to cyclically relax, such that the local mean stress and R-ratio near the crack tip is lower than the remotely applied mean stress. An example of this is shown in Figure 3.20 where the cyclic stress-strain response of the averaging region just ahead of the crack tip is plotted over 10 cycles for cracks of different lengths. It is apparent in this Figure that the initial first load induces a significant amount of plasticity in the microstructure. The cyclic relaxation of the local mean stress near the crack tip is also apparent in this Figure. This cyclic relaxation of the mean stress can cause the local driving force to decrease with number of cycles; this cyclic relaxation phenomenon should be addressed in MSC growth simulations.

For the same set of simulations shown in Figure 3.20, the FS FIP values for each averaging region are shown in Figure 3.21. In this case the maximum (*non-crystallographic*) FS FIP is shown as a function of number of cycles from cycles 1 to 10. As one can see, after the first cycle the FIP steadily decreases with each cycle and approaches a steady state change in FS FIP over each cycle ($\Delta \text{FIP}_{FS}/\Delta N$)

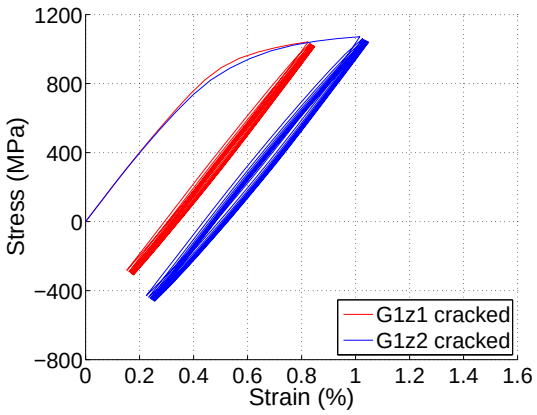

(a) Grain 1

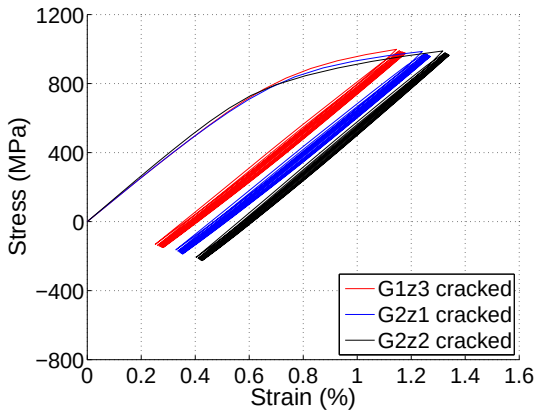

(b) Grain 2

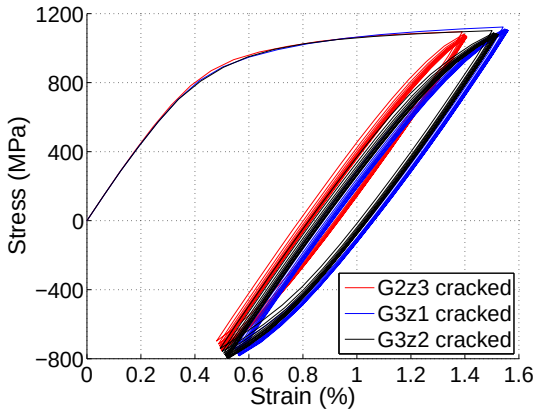

(c) Grain 3

Figure 3.20: Stress strain behavior of averaging regions for different crack lengths.

due to the ratcheting mechanism. The average percent change in FS FIP (given by Equation 3.32 below) with each cycle number is shown in Figure 3.22. As shown in this Figure, the percent change in FS FIP for the first cycle is ∼90% and steadily decreases with increasing cycle number. Therefore, a better estimation of the driving force parameter can be obtained with more cycles. However, simulating many cycles per each crack length can be computationally expensive. Therefore, a compromise between computational efficiency and solution accuracy must be reached. Since the percentage change in FIP between the third and fourth cycle is a small percentage of the FIP measured at the third cycle, i.e.,

$$\%\frac{\Delta FIP}{\Delta N} = \sum_{j=1}^{N\_crack\_lengths} \frac{1}{N\_crack\_lengths} \cdot \frac{\Delta FIP_j/\Delta N}{FIP_j} \times 100\% \approx 5\% \text{ for 3rd cycle,} \tag{3.32}$$

we assume that the driving force calculated at the third fatigue cycle is adequate for estimation of MSC growth. It should also be noted that there is virtually no difference in the trend of the FIP distribution for cycle numbers two and greater, minus a small decrease/translation in FIP values with increasing number of cycles. This small decrease in FIP values can be offset by adjusting the MSC growth law fitting parameters to account for these slightly higher FIP values for the third cycle versus cycles after the third cycle. In the end, as long as the methodology shows correlation with experiments and is used consistently throughout the estimation of fatigue life, than this small offset will not be a problem. Thus, averaging of the FIP over the third fatigue cycle will be employed subsequently.

To check how the *crystallographic* FIP changes with crack extension, Figure 3.23 shows the FIP values for all slip systems as a function of each cracked simulation for the crack path shown in the upper right hand corner of this Figure. The upper left hand corner of this Figure defines and labels each partition and assigns a given color for each partition zone. The bottom portion of Figure 3.23 is split into a 3×3 array of plots where the rows correspond to the grain numbers 1-3 and the columns correspond to averaging partition zones 1-3 (reference the upper left hand corner of this Figure for partition and grain number definitions). For each partition, FIP values

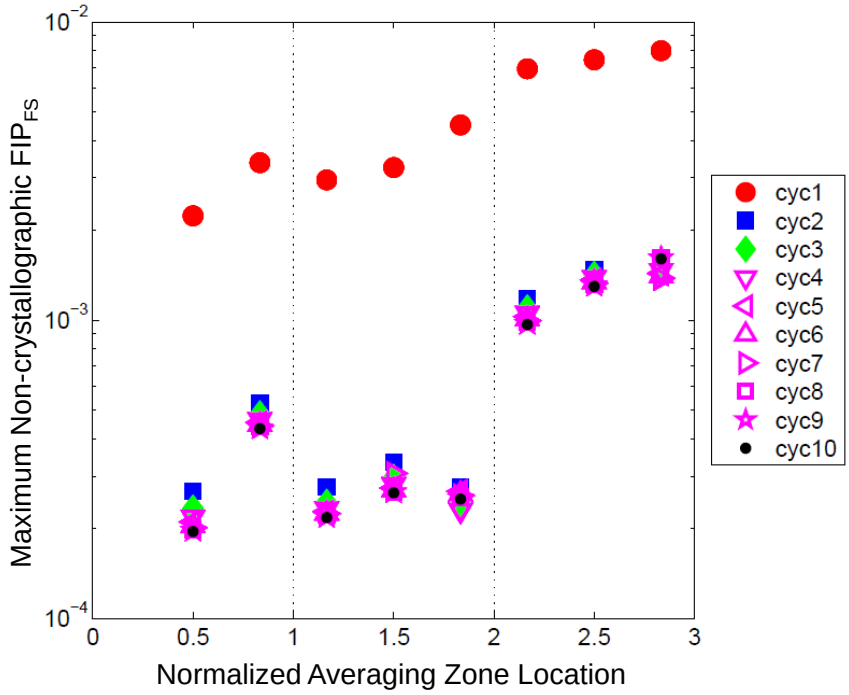

Figure 3.21: Evolution of FIP with crack length and number of cycles.

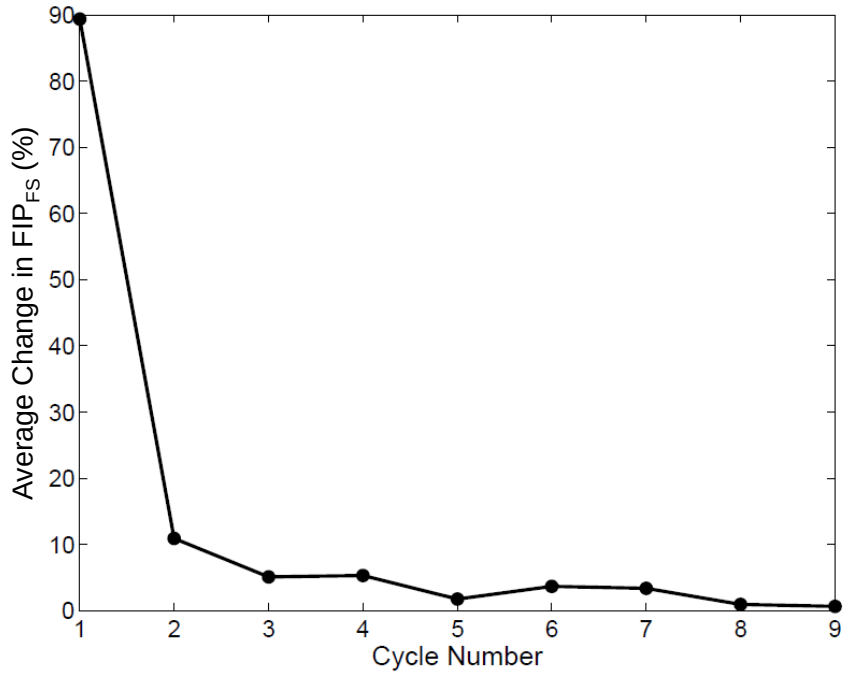

Figure 3.22: Average percent change in FIP with number of cycles.

are shown from the uncracked simulation up until the respective partition is cracked, which is denoted by a dashed red line in each case. As an example, the first partition zone has FIP values for the uncracked simulation and for the first partition being cracked as plotted in Figure 3.23(b). The second partition zone in Figure 3.23(c) has FIP values plotted for the uncracked simulation, the first partition cracked simulation, and the second partition cracked simulation. And so on. In each of the subplots (b) through (j), slip systems 1-12 correspond to octahedral slip and 13-18 correspond to cube slip systems. The red-filled black circle in each subplot indicates which FIP is the maximum FIP for that particular crack length and averaging region. For the MSC propagation case of Figure 3.23, the first grain favors slip along octahedral slip system 8, the second grain favors slip along cube slip system 16, and grain 3 favors slip along octahedral slip system 9. It is interesting to note that the slip system that contains the maximum crystallographic FIP for a particular grain does not change throughout crack propagation. Therefore, it can be reasonably assumed that the slip system with the highest FIP value for a grain when a crack reaches it can be inferred from the highest initial FIP within that same grain found from the uncracked simulation. The challenge with this approach is to estimate the *magnitude* of the cracked FIP distribution as a function of crack length and cycle number from the FIPs calculated in uncracked simulations. The next section sheds some more light on how this is done.

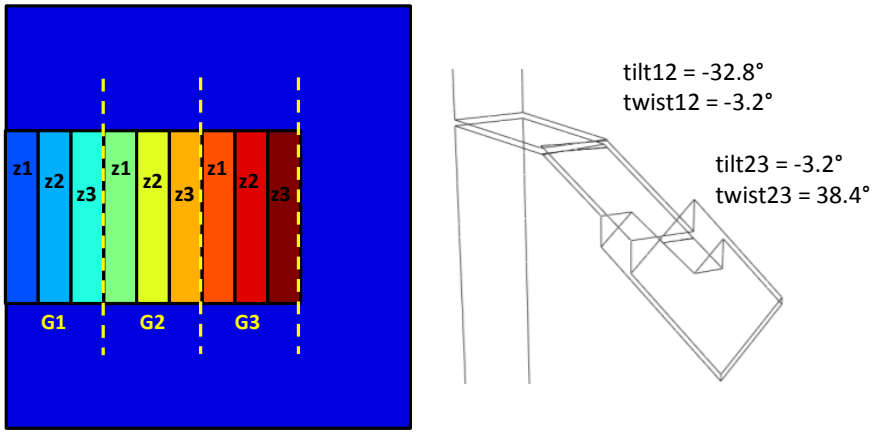

(a) Schematic showing different partition labels and crack path

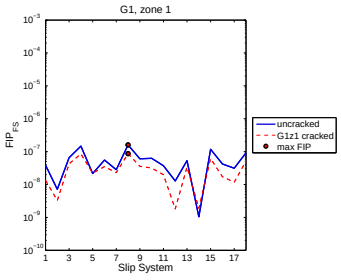

(b) Grain 1, partition zone 1

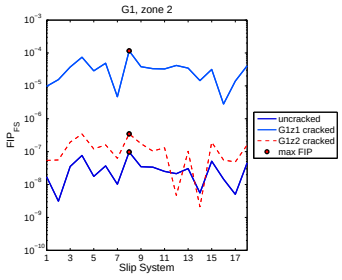

(c) Grain 1, partition zone 2

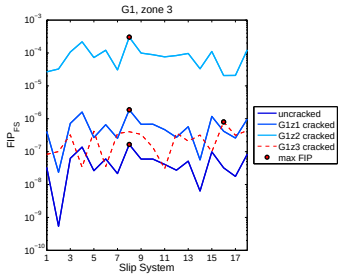

(d) Grain 1, partition zone 3

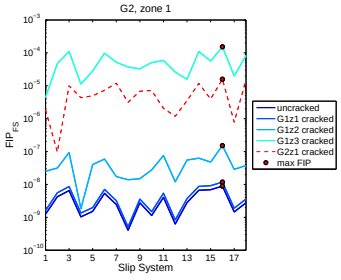

(e) Grain 2, partition zone 1

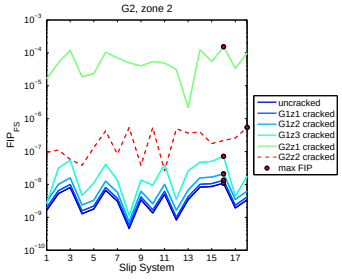

(f) Grain 2, partition zone 2

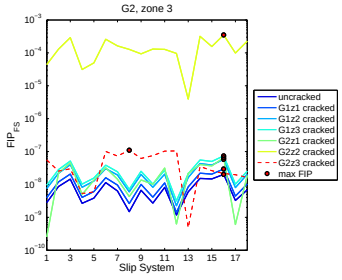

(g) Grain 2, partition zone 3

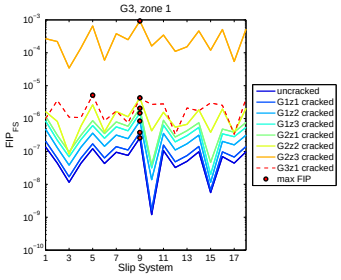

(h) Grain 3, partition zone 1

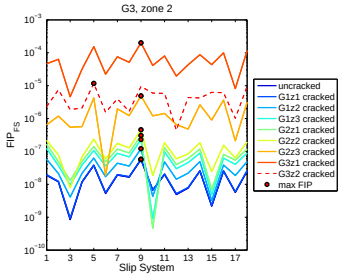

(i) Grain 3, partition zone 2

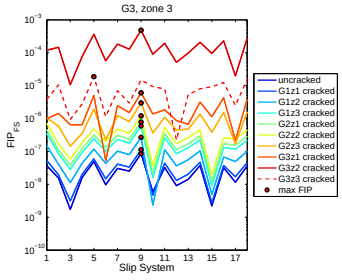

(j) Grain 3, partition zone 3

Figure 3.23: Crystallographic FIP values for all slip systems averaged within each partition as a function of simulation number.

3.6.5 Generalization of FIP Evolution Expression with MSC Growth

An expression to characterize how the FIP evolves with crack length is proposed in this section. As previously introduced in Equation 3.18, the evolution of the FIP with MSC crack length can be a function of a number of variables, i.e., $FIP^*(N) = f(FIP_{uncracked}, a_N, \overline{d}_{GB}, \alpha, \beta)$. To determine the effect of each individual parameter on the evolution of the FIP distribution would require an extensive parametric study effort. Instead of employing every single combination of tilt and twist angles at each grain boundary, a number of random orientation simulations are performed to generalize this expression for any combination of these attributes. The evolution of the FIP as a function of normalized crack length is assumed to follow

$$FIP^*(\overline{a}_N) = B_{MSC}(\Delta\varepsilon_a)^n(\overline{a}_N)^m \quad + \quad C_{MSC}\ \overline{a}_N \left[\Phi\left(\overline{X}\middle|\, \mu, \sigma\right) - 0.5\right] \ , \tag{3.33}$$

where $\overline{a}_N$ is the crack length normalized by the average grain size and B_{MSC} controls the rate at which the average FIP (of all instantiations) increases as a function of the applied strain range, $\Delta\varepsilon$, and the normalized crack length, $\overline{a}_N$. The exponents on the applied strain range (n) and normalized strain range (m) are fit to simulations for different applied strain ranges in the next section. The constant C_{MSC} controls the perturbation above or below the average FIP curve that a given FIP value will be according to the particular grain that the crack is currently contained in. The perturbation function, $\Phi\left(\overline{X}\middle|\, \mu, \sigma\right)$, is assumed to be in the form of a normal cumulative distribution function, via:

$$CDF = \Phi\left(\overline{X}\middle|\, \mu, \sigma\right) = \frac{1}{\sigma\sqrt{2\pi}} \int_{-\infty}^{\overline{X}} \exp\left[-\frac{(t-\mu)^2}{2\sigma^2}\right] dt \tag{3.34}$$

where μ and σ are the mean and standard deviation of the $\overline{X}$ variable. For this case, the $\overline{X}$ value is a normalized and lognormally-transformed function of the initial (uncracked) FIP value averaged within each grain and is given by

$$\overline{X} = \log_{10}\left[\frac{\overline{FIP}_o(G_j)}{\overline{FIP}_o(G_{All})}\right] \tag{3.35}$$

The $\overline{FIP}_o(G_j)$ is the initial (uncracked) average FIP value within the jth grain that the crack is currently in and $\overline{FIP}_o(G_{All})$ is the initial (uncracked) average FIP value

for *all* grains that contain a given macroscopic stress condition. What is meant by this given macroscopic stress condition is whether the macroscopic stress state is uniform or if there is a stress gradient due to a notch, inclusion, pore, or other stress concentrator. For the current situation, where a smooth specimen is simulated, the initial average FIP value for all grains ($\overline{FIP}_o(G_{All})$) is considered to be equal in all FEM locations, and is assigned a value of $\overline{FIP}_o(G_{All}) = 5.0 \times 10^{-7}$.

For FEM models that contain gradient stress conditions, such as notched components or inclusions, the initial average FIP value for all grains ($\overline{FIP}_o(G_{All})$ in Equation 3.33) is assumed to be spatially dependent on the distance from the stress concentration notch root. For example, one could employ the exponential FIP decay function that was introduced by Musinski and McDowell [76] and is given by:

$$\overline{FIP}_o^{notched}(G_{all}) = FIP_{max} \cdot \exp\left[-\xi(\rho) \cdot x\right] \tag{3.36}$$

where $\xi(\rho)$ controls the rate of FIP decay from the notch root as a function of different radii (ref. Fig 6. in [76] for the decay of the FIP from notch roots of different radii). This formulation for the analysis of FIP within notch roots will be further covered in Chapter 4 where MSC growth within notched components containing non-metallic inclusions will be considered.

The application and fitting of Equations 3.33 through 3.35 is shown in Figure 3.24. Plotted in Figure 3.24 are comparisons of predicted (from uncracked simulations and using Equations 3.33 through 3.35) versus actual (progressive stationary crack simulations) FIP values for 6 individual instantiations. The constants used for the prediction of the evolution of FIP versus crack length are shown in Table 3.2 below. In Figure 3.24, the values of minimum, mean (on logarithmic scale) and maximum (of all instantiations) initial uncracked FIP are plotted with blue, black, and red dashed lines. These dashed lines correspond to $\overline{FIP}_o(G_j)$ values equal to 1.3×10^{-8}, 4.66×10^{-7}, and 1.67×10^{-5}, respectively. The magenta solid lines are the initial (uncracked) average FIP values within each grain, $\overline{FIP}_o(G_j)$. These initial (uncracked) FIP values were used to construct the predicted FIP*($\overline{a}_N$) from Equations 3.33 through 3.35 and is depicted with the green lines in Figure 3.24. These predicted FIP values are

also compared to the actual FIP*($\overline{a}_N$) obtained from progressive stationary crack simulations and are denoted on this Figure as red 'x' markers. From this Figure it can be seen that there is reasonable agreement between the predicted and the actual FIP values as a function of the normalized crack length.

Table 3.2: Constants Used for Evolution of MSC FIP values versus Crack Length.

Variable	Value
B_{MSC}	1.2×10^{5}
n	4
m	1.5
C_{MSC}	1.0×10^{-3}
μ_{MSC}	0
σ_{MSC}	0.75
$\overline{FIP}_o(G_{All})$	5.0×10^{-7}

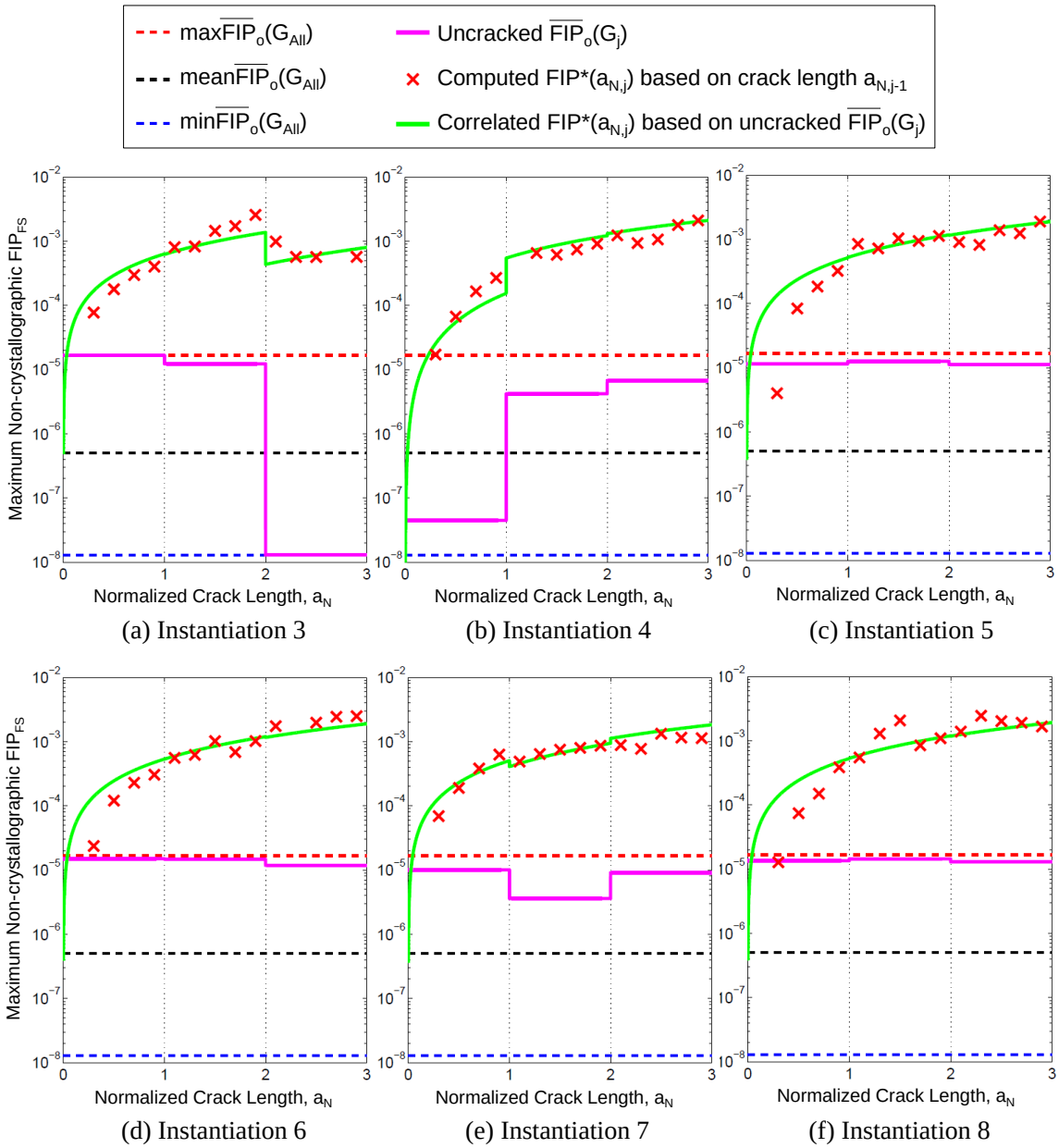

Figure 3.24: Computed $FIP^*(a_{N,j})$ values based on FEM simulations of crack length $a_{N,j-1}$ versus correlated $FIP^*(a_{N,j})$ values based on $\overline{FIP}_o(G_j)$ computed from uncracked FEM simulations.

3.6.5.1 Effect of applied strain amplitude on FIP evolution with crack extension

The current FIP evolution study was performed using only one applied strain amplitude, $\varepsilon_a = 1.5\varepsilon_y$, where ε_y=0.42% is the macroscopic proportional limit of the coarse grain IN100 modeled. To assess how this framework pertains to different applied strain amplitudes, the finite element procedure for determining the driving force for fatigue crack propagation ahead of the crack tip was repeated for three other strain amplitudes ($\varepsilon_{max} = \varepsilon_y$, $1.75\varepsilon_y$, and $2.0\varepsilon_y$) for instantiation #4 (ref. Figure 3.24) only. This instantiation was chosen at random for this study. For instruction, only a few different normalized crack lengths ($\overline{a}$ = 0.6, 1.2, 1.6, 2.2, and 2.6) were simulated at each strain amplitude. For these simulations, the maximum non-crystallographic FIP (ref. Section 3.5.2.1) averaged in the partition just ahead of the crack tip was computed for comparison among all strain amplitudes. These FIP values are displayed as a function of strain amplitude and normalized crack length in Figure 3.25. In this Figure, the dotted lines represent the mean FIP*($\overline{a}_N$) behavior (first term of Equation 3.33) and the solid lines represent the total FIP*($\overline{a}_N$) expression incorporating the pertubation about the mean (dotted) line. It should be noted that the value of $\overline{FIP}_o(G_{All})$ was different for each strain amplitude because the average FIP value changes with strain amplitude. It can be seen from this Figure that the estimated FIP*($\overline{a}_N$) correlates well with the actual FIP*($\overline{a}_N$) obtained from stationary crack simulations of different sizes. Therefore, this FIP*($\overline{a}_N$) is deemed applicable over a wide range of loading conditions as long as the initial FIP distribution is represented.

3.6.5.2 Discussion of FIP evolution with MSC growth

In this section, we discuss the increase in FIP as a function of MSC growth found in the current study and compare these results to previous CPFEM studies by Castelluccio and McDowell on polycrystalline RR1000 [147] and single crystal copper [75]. In the first study, Castelluccio and McDowell used 3D crystal plasticity models to assess the sub-grain evolution of the Fatemi-Socie FIP averaged along crystallographic slip bands with MSC extension. The crack was induced in the microstructure by degrading

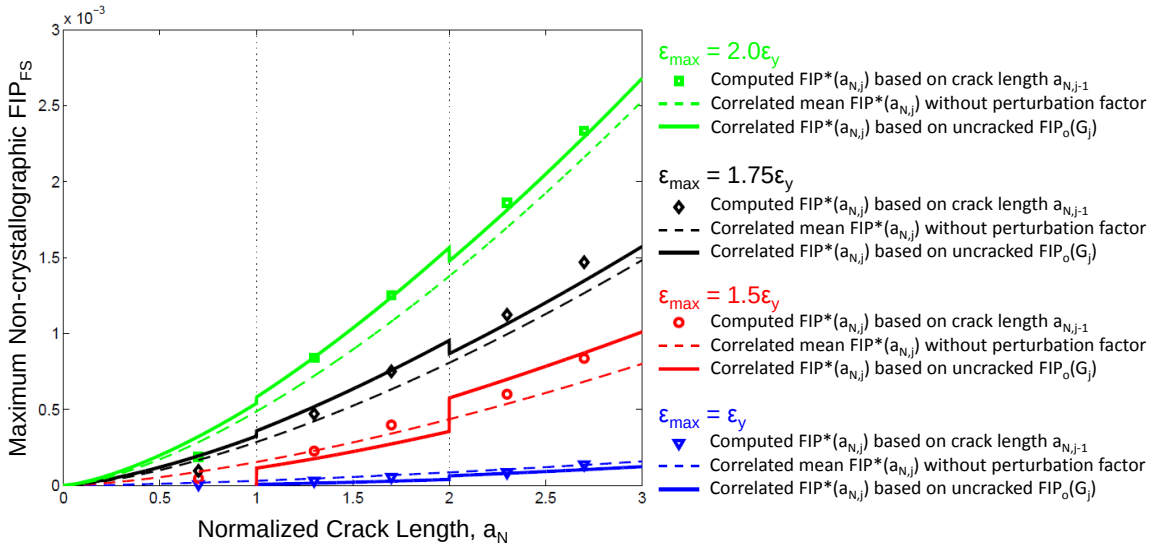

Figure 3.25: Predicted versus actual FIP*(N) values as a function of strain amplitude, $\Delta\varepsilon_a$, and normalized crack length, $\overline{a}_N$, for one MSC instantiation (#4).

the elastic stiffness in elements associated with the crack plane. They found that the slip-band-averaged FIP decreased with MSC growth within a grain. On the other hand, for single crystal copper, Castelluccio and McDowell [75] showed an overall increase in FIP driving force with successively larger stationary MSCs using different averaging volumes within different averaging volume shapes including a 3 μm sphere, a 5 μm sphere, a 1 μm thick band, a 2 μm thick band, and the entire single crystal. There are two main differences between these two studies by Castelluccio and McDowell [75, 147]. Obviously, one study investigated single crystals while the other investigated polycrystals. Depending on the grain boundary character, the grain boundary can act as a barrier to slip affecting the crack driving force FIP as an MSC approaches a grain boundary. Second, the FIPs for the single crystal copper studies [75] were assessed over the third fatigue cycle regardless of the stationary crack size. For each stationary crack size in the single crystal analysis, the initial material hardening state was identical. In other words, the larger MSC sizes simulated did not incur the material hardening/loading history from previous loading cycles of smaller MSC sizes. On the other hand, in the polycrystalline studies [147] the material hardening/loading history was carried over for successive MSC sizes as the crack propagated through the

polycrystalline microstructure. Therefore, the polycrystalline FIP values were able to cyclically relax more due to plastic strain redistribution resulting in a reduction of the FIP.

While the prediction of FIP reduction with MSC growth through each grain by the slip-band-averaging technique in Castelluccio and McDowell [147] is certainly noteworthy, the required element size refinement to account for variability in FIP [126] among multiple slip bands within a grain is too fine and computationally expensive for the relatively larger notched specimens simulated in Chapter 4. Therefore, a technique using coarser-scaled grain-averaged FIPs was presented here to establish a balance between computational efficiency of using coarser-scaled grain volume averaging and FEM solution accuracy of the finer scale slip-band averaging scheme. In the current work, the driving force FIP calculated over the third fatigue cycle was found to increase with increasing MSC size. This FIP value continues to decrease with more cycles (ref. Figure 3.21) due to cyclic stress application and plastic strain redistribution; however, a value of 3 cycles was shown to be a good compromise between computational efficiency and solution accuracy for the estimation of a stabilized FIP value. Subsequently, the decrease in FIP for MSC propagation as the MSC approaches the grain boundary is accounted for in this work by increasing the grain boundary resistance factor with decreasing distance to the next grain boundary (ref. Equation 3.25). In the end, the objective of this framework was to provide a means to infer/project cracked FIP values from uncracked simulations. In the following section, we fit the MSC growth law to experiments.

3.7 Application and Fitting of MSC Growth Law to Experiments

Having developed an expression for how the FIP changes with normalized crack length, we turn our focus on fitting/applying the previous MSC growth law in Equation 3.27 to experiments performed by AFRL researchers on a coarse-grained Ni-base superalloy [137, 138] and a fine-grained Ni-base superalloy [136]. The coarse grain Ni-base superalloy MSC growth tests were performed in laboratory air and the fine

grain Ni-base superalloy long crack growth tests were performed at different vacuum levels.

3.7.1 Laboratory air MSC growth experiments used for calibration

The coarse grain MSC growth tests in laboratory air were load-controlled with an R-ratio of 0.05 at 650°C on dog bone specimens with a nominal gage section of 4.6 mm × 4.6 mm × 25 mm. These specimens had two FIB notches machined at opposite surfaces near the middle of the gage section. Each FIB notch had length, width, and height dimensions of 40 μm × 20 μm × 3 μm and was oriented so that the length and width dimensions were normal to the loading axis. Surface crack growth was measured using a replica technique. The replicas were taken at a hold stress of 660 MPa, which was 60% of the maximum applied cyclic stress of 1100 MPa. Note that this replica technique measures surface crack length and assumes a semi-circular crack front geometry for da/dN versus ΔK measurements. The results from these tests [137, 138] are plotted in blue as $k_t = 1.0$ data in Figure 3.26. This Figure also displays long crack growth data in red for coarse grain IN100. Above the long crack growth threshold, $\Delta K_{th} \sim 10$ MPa, the LEFM behavior in laboratory air is represented by Paris law constants $C = 2.0{\times}10^{-8}$ and $m = 2.9$. The green dotted line in Figure 3.26 is a "mean fit" line used to calibrate the MSC growth law later in Section 3.7.3 and is characterized by the Paris law equation $da/dN = C_{air,MSC}(\Delta K)^{m_{air,MSC}}$ with $C_{air,MSC} = 4.25 \times 10^{-8}$ (mm/cycle) and $m_{air,MSC} = 2.85$.

3.7.2 Fatigue crack growth experiments for long cracks in vacuum used for calibration

Due to the absense of elevated temperature MSC growth experiments for Ni-base superalloys in vacuum, we use previous long fatigue crack growth experiments performed by Rosenberger [136] for calibration of the MSC growth law in vacuum. Rosenberger [136] investigated long crack growth of a fine grain IN100 microstructure (average grain size $\sim 3-5$ μm) at different vacuum levels using compact tension specimens in accordance with ASTM standard E647 [148]. A longer 30-second cycle time ($f = 0.033$ Hz) was used to augment the effect of vacuum level on long crack growth rate and long

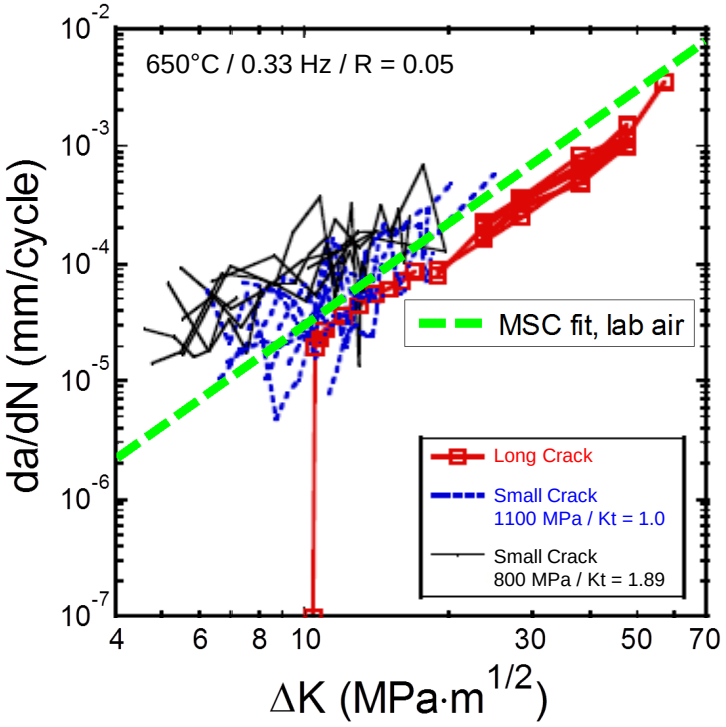

Figure 3.26: Experimental small crack growth data for a coarse grain Ni-base superalloy [137, 138] and MSC fit line overlaid on plot.

crack growth mechanisms. Figure 3.27 shows fatigue crack growth results for vacuum pressure levels 10^{-5} Torr, 100 mTorr, 450 mTorr and 1 atm and testing conditions (a) $T = 621°C$ and R = 0.3 and (b) $T = 657°C$ and R = 0.15.

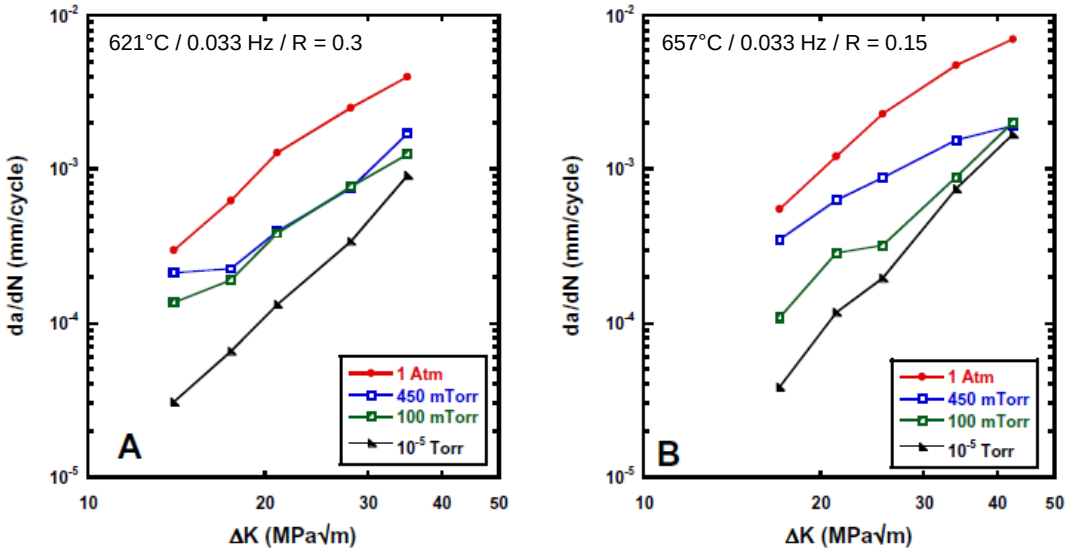

Figure 3.27: Experimental effect of different vacuum levels on the long fatigue crack growth rate in a fine-grained IN100 for a frequency of $f = 0.033$ Hz with (a) $T = 621°C$, R = 0.3, and (b) $T = 657°C$, R = 0.15 [136].

The long fatigue crack data in Figure 3.27(a) and (b) for vacuum pressure level 10^{-5} Torr and atmospheric air (1 atm) are replotted in Figure 3.28 on the same set of axes. The P = 10^{-5} Torr vacuum data are represented by filled symbols and the atmospheric (1 atm) lab air data are denoted by open symbols. Additionally, a best fit line for vacuum and lab air long crack data are represented via a green dashed line and a blue dash-dot line, respectively. For comparison, the MSC fit line from Figure 3.26 is also shown in Figure 3.28 via the solid magenta line. The Paris law constants for each fit line are listed in the legend of this Figure. It is interesting to note that the (magenta solid) MSC growth data in lab air has a similar slope, $m_{air,MSC} = 2.85$, as the (blue dash-dot) long crack growth data in lab air, $m_{air} = 2.81$, in spite of the differences in R-ratio, crack length, and load frequency applied.

The (green dashed) fit line for long crack growth data in vacuum in Figure 3.28 is assumed to be applicable to MSC growth in vacuum. The slope of this (green dashed)

vacuum fit line ($m_{vac} = 3.88$) is the average of the fit slopes for both sets of long fatigue crack data at $P = 10^{-5}$ Torr. Since MSCs tend to propagate faster than long cracks on a da/dN versus ΔK plot (ref. Figure 3.26), it is assumed that the average growth rate of MSCs in vacuum will be greater than or equal to the fatigue crack growth rate reported at $P = 10^{-5}$ Torr in Figure 3.28. In other words, the constant $C_{vac} = 1 \times 10^{-9}$ (mm/cycle) was selected so that the (dashed green) fit line was an upper bound on the long crack growth data in vacuum. A better mean fit line for MSC growth rate could be obtained when elevated temperature MSC growth rate data measured in vacuum (cf. experimental test rig development in [149]) are readily available.

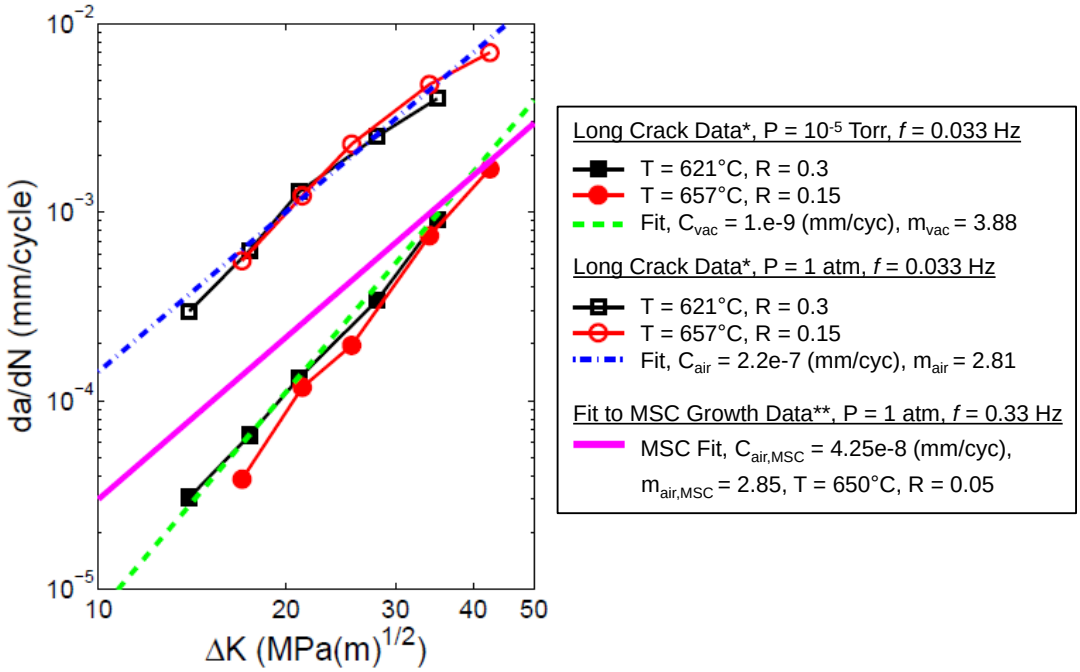

Figure 3.28: Experimental data showing effect of vacuum level on long fatigue crack growth rate. *The long crack growth experimental data is from Rosenberger [136]. **The MSC fit line was fitted to experimental MSC growth rate data for a coarse grain Ni-base superalloy [137, 138] as depicted in Figure 3.26.

3.7.3 Calibration of MSC model for 1D crack growth

To calibrate the MSC growth model for both laboratory air and vacuum experiments, a simple 1D model for crack growth was used. Several assumptions were used for fitting.

First, as depicted in the MSC growth experiments in Figure 3.26, there is a significant amount of scatter in small crack growth for the coarse grain IN100 microstructure [137, 138]. The scatter between the maximum and minimum crack growth rates is approximately an order of magnitude apart (cf. Fig. 3.26). Mathematically, this can be represented by $\log(\max\{da/dN\}/\min\{da/dN\}) \approx 1$. Therefore, for fitting, the MSC growth law is assumed to be bounded by the mean crack growth rate (da/dN_{mean}) plus or minus a half order of magnitude. The mean MSC growth rate lines for lab air and vacuum environments are given by the previously discussed green dashed lines in Figures 3.26 and 3.28, respectively.

The application of the MSC growth model to 1D MSC growth along the x-direction is shown in Figure 3.29. The 1D model is assumed to be composed of a chain of grains (G1, G2, ... , G(N-1), GN), each having a constant grain size, $d_{grn} = 34$ μm. Each grain is assumed to have a constant uncracked FIP value equal to the mean FIP of all grains, i.e.,

$$\overline{FIP}_o(G1) = \overline{FIP}_o(G2) = \cdots = \overline{FIP}_o(G(N-1)) = \overline{FIP}_o(GN) = \overline{FIP}_o(G_{All}) \tag{3.37}$$

The reason for this assumption is that we want to calibrate the MSC growth model to the mean behavior of the material. With all uncracked FIP values equal to the mean FIP of all grains (Equation 3.37), the second "perturbation about mean FIP behavior" term in the FIP^* Equation 3.33 is equal to zero. Subbing the first term from the FIP^* Equation 3.33 into Equation 3.27, the MSC growth law for 1D crack propagation can be expressed as

$$\frac{da_N^*}{dN} = A_{FS}^{env} \cdot \{B_{MSC} \cdot (\Delta\varepsilon_a)^n \cdot (\overline{a}_N)^m\} \cdot (\overline{a}_N)^{n_{env}} \cdot \left[1 - R_{GB} \cdot (1 - \overline{d}_{GB})^2\right] - \Delta CTD_{th}^{env} \tag{3.38}$$

The application and fitting of the MSC crack growth model to 1D crack propagation in both lab air and vacuum are displayed in Figures 3.30 and 3.31, respectively. The constants used for fitting are shown in the upper left hand corner of each Figure. There are a couple of things to note about these plots. First, the minimum and maximum crack growth rate spread is well represented by the constants chosen for

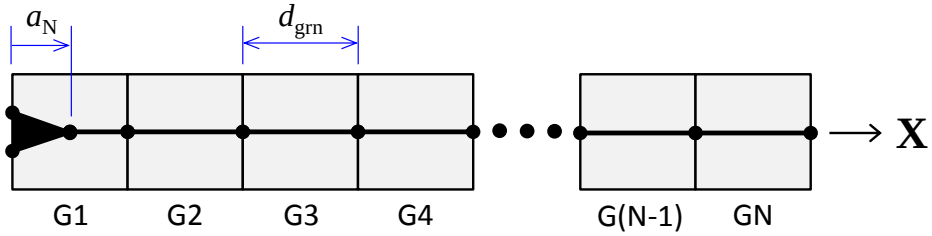

Schematic of 1D MSC growth model.

Assumptions:

- Constant grain size d_{grn} = 34 μm for all grains (G1, G2, … , G(N-1), GN)
- Each grain contains an uncracked FIP equal to the average uncracked FIP of all grains, i.e.,

$$\overline{FIP}_o(G1) = \overline{FIP}_o(G2) = \cdots = \overline{FIP}_o(G(N-1)) = \overline{FIP}_o(GN) = \overline{FIP}_o(G_{All}) \quad \text{Eqn. (3.37)}$$

- Crack growth is 1D along x-direction

Application of MSC law to 1D crack growth:

- MSC growth law:

$$\frac{da_N^*}{dN} = A_{FS}^{env}\left\{FIP^*(N)\right\}(\bar{a}_N)^{n\_env}\left[1-R_{GB}(1-\bar{d}_{GB})^2\right]-\Delta CTD_{th} \quad (3.31)$$

$$\hookrightarrow FIP^*(N) = \underbrace{B_{MSC}(\Delta\varepsilon_a)^n(\bar{a}_N)^m}_{\text{Mean FIP behavior}} + \underbrace{C_{MSC}\,\bar{a}_N\,[\Phi(\bar{X}|_{\mu,\sigma})-0.5]}_{\text{Perturbation about mean FIP behavior}} \quad (3.33)$$

- With $\overline{FIP}_o(G_j) = \overline{FIP}_o(G_{All})$:

$$\hookrightarrow \bar{X} = 0 \quad (3.35)$$

$$\hookrightarrow \Phi(\bar{X}|_{\mu,\sigma}) = 0.5 \quad (3.34)$$

$$\hookrightarrow \text{Eqn. (3.33)} \quad \textit{becomes} \quad FIP^*(N) = B_{MSC}(\Delta\varepsilon_a)^n(\bar{a}_N)^m$$

- Subbing FIP*(N) expression into Eqn. (3.31), 1D MSC growth model is given by

$$\Rightarrow \frac{da_N^*}{dN} = A_{FS}^{env}\left\{B_{MSC}(\Delta\varepsilon_a)^n(\bar{a}_N)^m\right\}(\bar{a}_N)^{n\_env}\left[1-R_{GB}(1-\bar{d}_{GB})^2\right]-\Delta CTD_{th} \quad (3.38)$$

Figure 3.29: Application of MSC growth model to 1D MSC growth for calibration to experiments.

each environment condition. Also, since these are only 1D simulations, the amplitude of the fluctuations in the crack growth rate remain constant over all crack lengths. In reality, as the crack length increases, the crack front will sample more grains and the MSC growth will tend to smoothen out so that the effects of individual grain boundaries and microstructure are less pronounced for larger crack sizes. This will be shown to be the case for the FIB notch simulations covered in the next section.

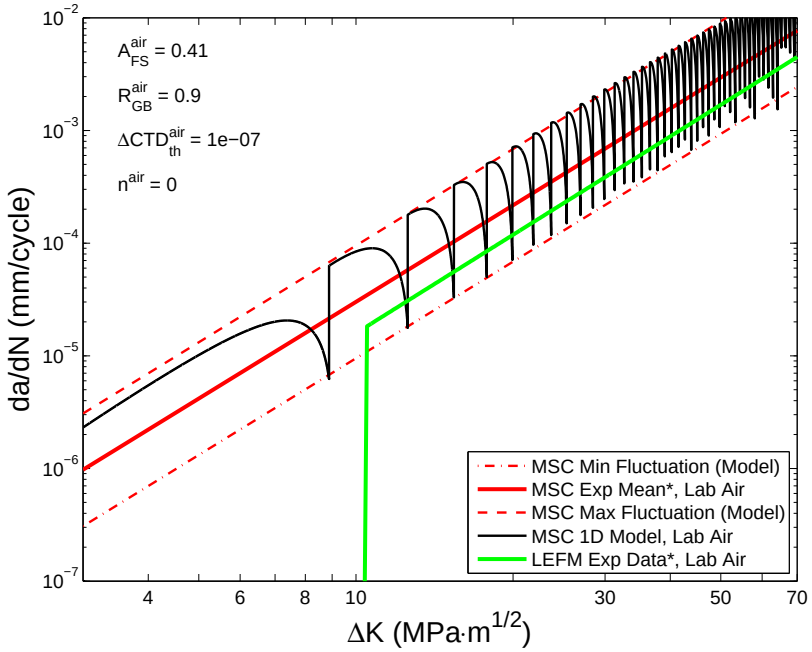

Figure 3.30: 1D MSC model for crack growing in lab air. *MSC mean and LEFM lines were fit to experimental data [137, 138] depicted in Figure 3.26.

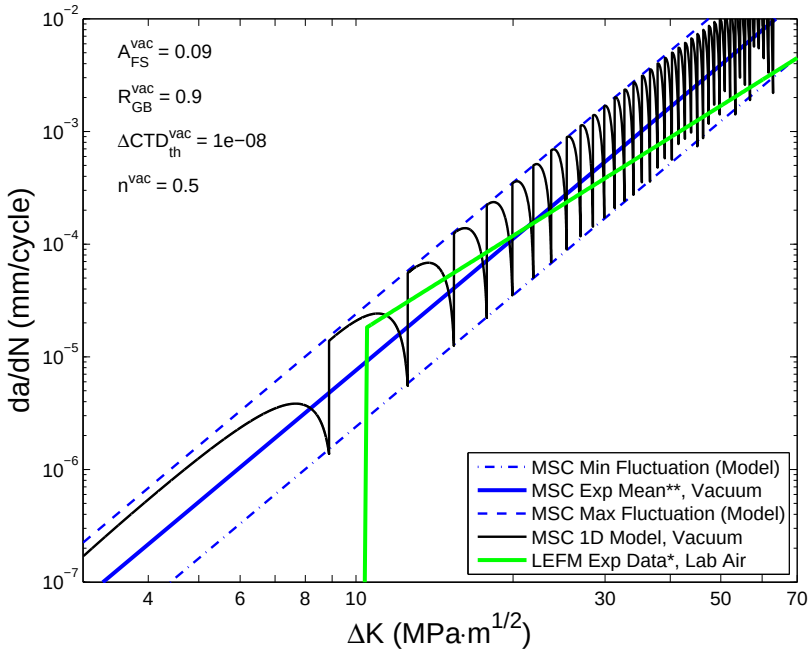

Figure 3.31: 1D MSC model for crack growing in vacuum. *LEFM lines were fit to experimental data [137, 138] depicted in Figure 3.26. **MSC mean data line in vacuum was fit to LEFM vacuum data [136] as depicted in Figure 3.28.

3.7.4 FEM Model for MSC Crack Growing from FIB Notch

A polycrystal plasticity finite element model was created to estimate the MSC growth ahead of a rectangular FIB notch in both vacuum and lab air environments. Where plausible, the FEM model mimicked the geometry and loading conditions of experiments [137, 138]. The FEM model FIB notch had the same dimensions as the experimental one [137, 138] with length, width, and height dimensions of 40 μm × 20 μm × 3 μm. A smaller piece of material than the experimental gage section was employed to make the simulations less computationally expensive. The overall dimensions of the FEM model were 170 μm × 250 μm × 250 μm which correlated to approximately 5 × 7.3 × 7.3 grains through the thickness in the x, y, and z dimensions, respectively. The FEM model was constrained from normal movement (on rollers) along the bottom ($y = 0$) face, the back ($z = 0$) face, and the right ($x = 170$ μm) face. The FIB notch was centered about the left ($x = 0$) face and was oriented with the length and width dimensions normal to the y loading axis. A multi-point constraint

was applied to the top ($y = 250\ \mu m$) face so that all nodes on this face had the same displacement. The top face was subjected to load-controlled cyclic loading at a maximum stress of 1100 MPa, an R-ratio of 0.05, and a frequency of 0.33 Hz for three cycles. The macroscopic strain range (due to cyclic ratcheting) and the distribution of FIPs were calculated over the third fatigue cycle and used to estimate 3D MSC growth through the microstructure from the FIB notch. An example of one of the finite element meshes used in this study is shown in Figure 3.32. In this Figure, each color represents a different grain; the FIB notch is represented by the yellow box on the right hand side of this Figure and the depth in which this FIB notch penetrates into the grain structure is schematically shown with the dotted lines connected to this yellow box.

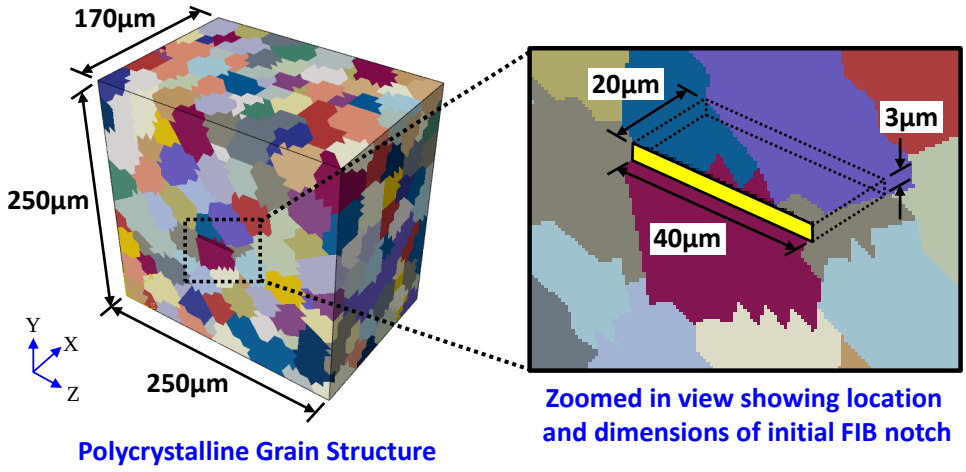

Figure 3.32: Example FEM model containing FIB notch used for calibration of MSC growth model.

Figure 3.33 shows the means in which MSC growth from the FIB notch is estimated. A two-dimensional schematic is used in Figure 3.33 for ease of explanation of the crack growth process; however, the crack growth from the FIB notch is three-dimensionsal. The method of MSC extension from the FIB notch can be summarized by:

1. **Construct radial lines:** First, imaginary radial lines emanating from the center of the FIB notch are created; these radial lines are separated by $d\theta = 2°$. This value of $d\theta$ was chosen because it provided good resolution of the crack front

without making the MSC growth calculations too computationally expensive.

2. **Discretize crack front:** Next, the crack front for a given cycle number in time is discretized using many different crack front points (green dots in Figure 3.33) corresponding to where the dotted radial lines from the previous step intersect the current crack front.

3. **Determine crack plane normal:** If the current grain that the crack front is in is already cracked, then the previous crack plane is used. Otherwise, the crack plane unit normal is determined by Equation 3.39. This equation accounts for the multi-slip mechanism of Ni-base superalloys on discrete crystallographic planes at elevated temperatures by finding a "FIP-weighted" average plane as the cracked plane. To mimic the resultant plane of zig-zag cross slip, only the two planes with the largest FIP value are used for averaging, i.e., $N_{\_slip} = 2$ for Equation 3.39.

$$\underset{\sim}{n}_{multi\text{-}slip} = \frac{\sum_{m=1}^{N\_slip} FIP^{(\alpha)} \cdot \underset{\sim}{n}^{(\alpha)}}{\left|\left|\sum_{m=1}^{N\_slip} FIP^{(\alpha)} \cdot \underset{\sim}{n}^{(\alpha)}\right|\right|} \tag{3.39}$$

4. **Determine radial direction along crack plane:** The radial direction projected into the crack plane is determined by crossing the unit normal along the theta direction, $\underset{\sim}{e}_{\theta}$, with the crack plane normal found in the previous step, $\underset{\sim}{n}_{multi\text{-}slip}$. This is denoted in Figure 3.33 by the red vector emanating from the top green dot along the crack front.

5. **Find crack growth rate for each crack front point:** The crack growth rate for each crack front point is determined using Equation 3.31, which is shown again in the upper right hand side of Figure 3.33.

6. **Nonlocal averaging of crack growth rate:** The crack growth rates from the previous step are normalized by multiplying by a discretized Gaussian, or normal PDF, bell curve weighting function. For the current study, only the next two neighbors on each side of the current crack front point are used for averaging; for a radial line division value of $d\theta$, the crack growth rate is averaged over an

approximate crack front arc length of $dS \approx \overline{a} * 5d\theta$, where $\overline{a}$ is the current radial crack length. The nonlocal averaging scheme can be represented mathematically by the following:

$$\left.\frac{da_{N,j}}{dN}\right|_{nonlocal} = \frac{\sum_{k=-2}^{k=2}\left[(w_{j+k})\cdot\frac{da^{*}_{N,j+k}}{dN}\right]}{\sum_{k=-2}^{k=2}\left[w_{j+k}\right]} \tag{3.40}$$

where the weighting function w_j is a normal probability distribution function (ref. Equation 3.34) with mean value $\mu = 0$ and standard deviation $\sigma = 1.1$. This standard deviation function corresponds to weighting factors of approximately 1, 4, 6, 4, and 1 for crack front points $\boldsymbol{x}_{j-2}$, $\boldsymbol{x}_{j-1}$, $\boldsymbol{x}_{j}$, $\boldsymbol{x}_{j+1}$, and $\boldsymbol{x}_{j+2}$, respectively.

7. **Increment crack extension:** Each crack front point is incrementally extended in the radial direction projected into the crack plane by an amount $\Delta a = da/dN \times \Delta N$, where $\Delta N = 10$ cycles was used for this study. This value of ΔN provided computationally efficient crack growth calculations with adequate resolution for the crack front growth.

This procedure is repeated until an arbitrary ΔK value is reached. The methods by which the crack length and ΔK are calculated are covered in the next section.

3.7.5 Crack length and stress intensity factor definitions

There are two methods by which crack length is computationally measured in the current study. First, since the experiments [137,138] measure surface crack length, the surface crack length ($2a$) from the computational crack is the distance between the two crack front points located at the surface ($x = 0$). The geometry of this crack front is assumed to be semi-elliptical through the whole MSC growth regime. Note, that there will be a small amount of error induced by assuming that the initially rectangular-shaped FIB notch is semi-elliptical; however, as the crack grows, the rectangular crack front transforms to a more semi-elliptical crack front, so the error associated with the initially different geometry reduces toward zero with crack extension. Based on the geometric assumption of a semi-elliptical crack front the stress intensity factor is found by means of the Raju and Newman [150] K solution. The reason that the Raju

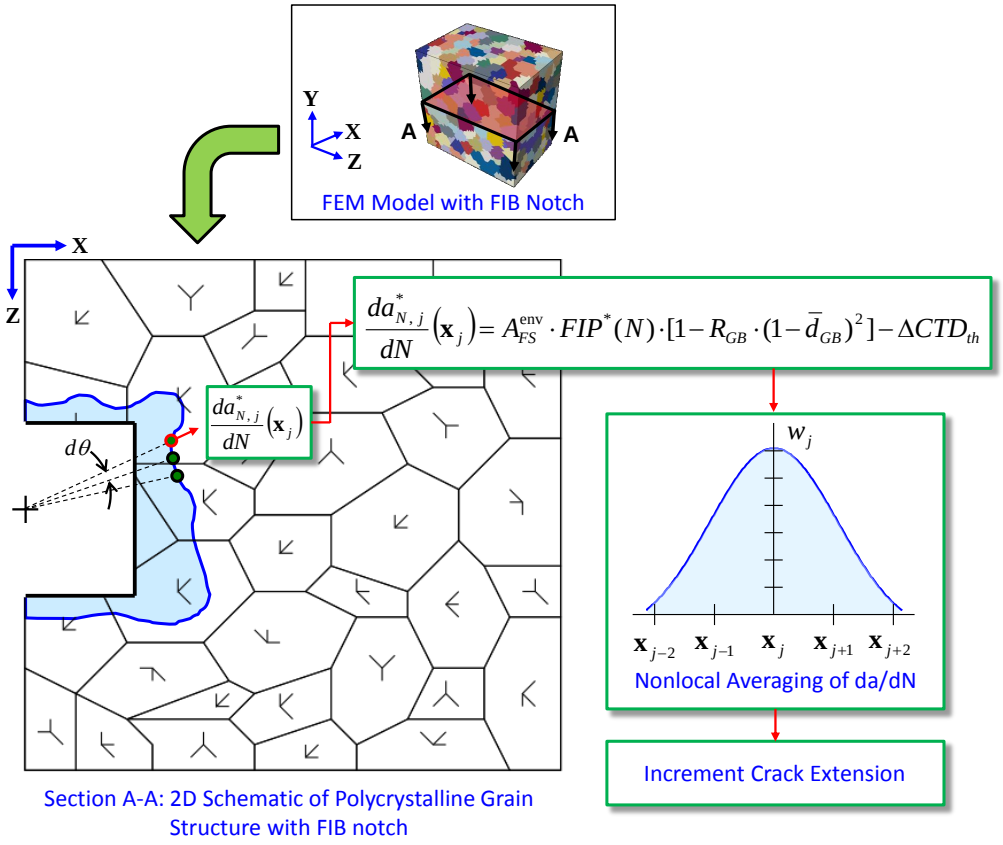

Figure 3.33: Schematic showing how MSC growth from a FIB notch is estimated.

and Newman solution is used is to maintain consistency with the experimental ΔK calculations [151].

The other way in which the crack length is tracked is by using the square root of the projected area method proposed by Murakami et al. [152–154]. To compute the projected area of the crack front, built-in MATLAB [144] functions are used. First the crack front points are triangulated using a Delaunay Triangulation ("*delaunay*"). The area of each triangle is then computed using the convex hull ("*convhull*") function. The square root of the summed up triangular areas are then used as the current crack length. Finally, this equivalent crack length is used in the previously described Raju and Newman K solution [150] to determine the current range in stress intensity factor. The resulting differences between the two means of calculating the crack length and stress intensity factor range are described next.

3.7.6 Results from FIB Notch MSC Growth Studies

Figure 3.34 shows the polycrystalline grain structure that the simulated MSC propagates through viewed normal to the y loading axis for instantiation #1. The MSC propagation starts from the FIB notch which is denoted by the white rectangular region in the center of this Figure. Each crack front point is color-coded by the grain number it is currently in according to the color bar shown in this Figure. Smaller grain numbers correspond to larger grain sizes. Additionally, solid lines representing the full crack front at a given cycle number are superimposed on the grain structure in this Figure to show how the crack growth evolves according to the location within the grain. These crack front isolines are shown for every $\Delta N_{isolines} = 50$ cycles. The same crack front isolines in Figure 3.34 are shown without the grain structure in Figure 3.35. It is easy to see in Figure 3.35 how the crack front evolves from a rectangular-shaped FIB notch to a more semi-elliptical-shaped crack front with crack extension.

A three-dimensional rendering of the crack path shown in Figures 3.34 and 3.35 is displayed in Figure 3.36. This meshed surface patch was created using the "*surf*" command in MATLAB [144]. In this Figure the color of the surface patch indicates the vertical elevation (y-direction) of the crack path; the dark blue surface patches

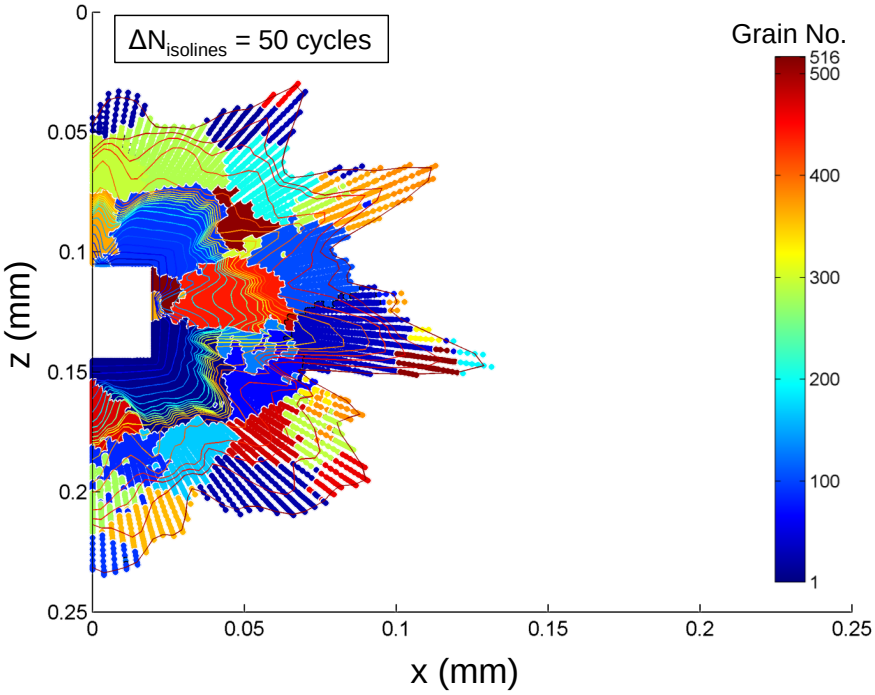

Figure 3.34: Polycrystalline grain structure and MSC growth from FIB notch isolines for instantiation #1.

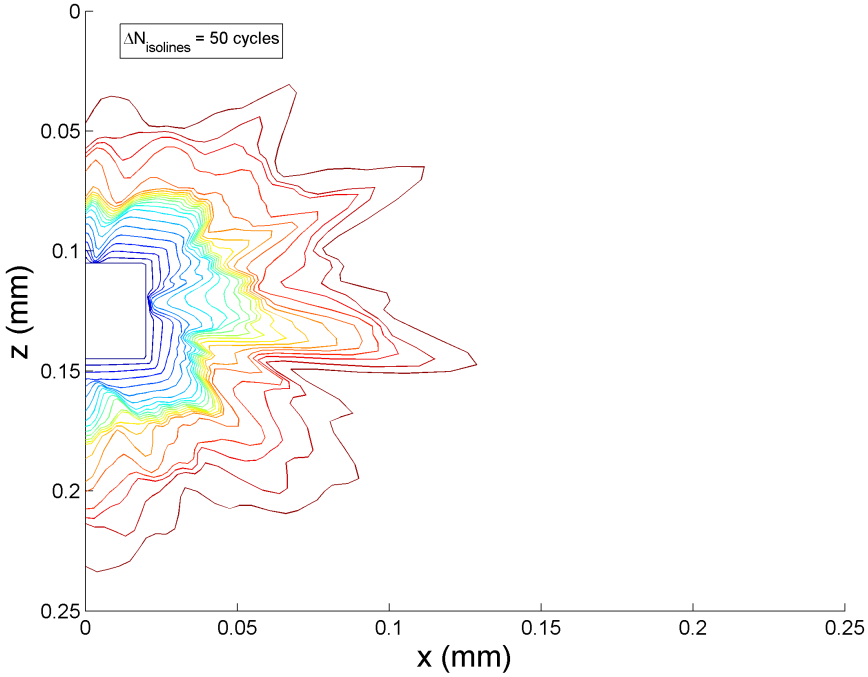

Figure 3.35: MSC growth from FIB notch isolines for instantiation #1.

are the lowest elevation whereas the bright red are the highest. The overall shape of the crack path is relatively flat, with the difference between the minimum and maximum elevation of the crack path being approximately 15 microns. This value of 15 microns is below the average grain size of 34 microns for this coarse grain IN100 microstructure. As stated previously, experimental fractography studies on Ni-base superalloys that were fatigued at elevated (538-700°C) temperatures showed that these fracture surfaces tended to be relatively flat and normal to the loading axis [7,78,79].

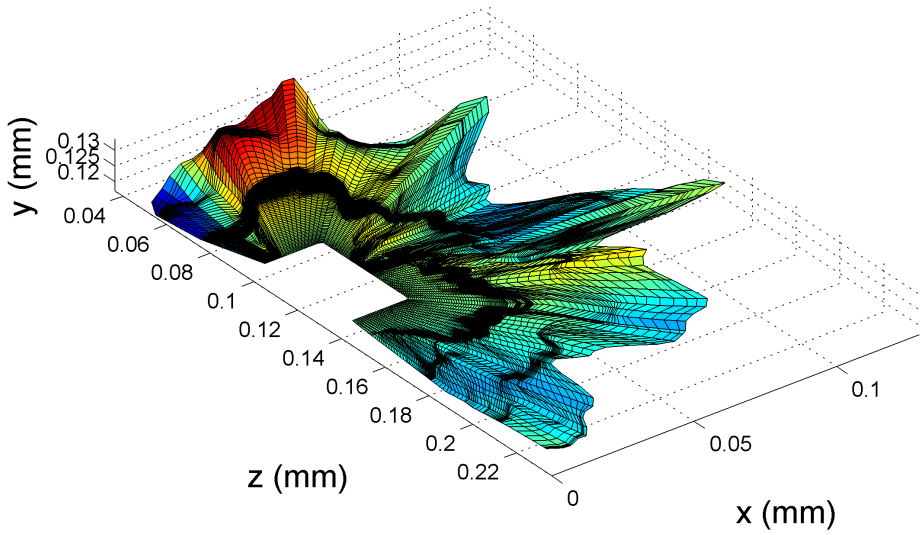

Figure 3.36: 3D rendering of MSC growth from FIB notch for instantiation #1. Color of surface patch indicates vertical elevation (y-direction) of crack path.

The surface roughness of the crack front requires more investigation. In previous work by Porter III et al. [7], they reported surface roughness values for cracks initiating in Rene' 88DT specimens subjected to load-controlled fatigue loading at 593°C with maximum stress, $\sigma_{max} = 1250$ MPa, a frequency of 0.33 Hz, and a stress ratio of 0.05. The average grain size of this microstructure was 30 microns. The average root mean square (RMS) value of the fracture surface roughness for three Rene' 88DT specimens was reported to be $\sim$2.6 μm for cracks with an average square root of the projected

area normal to the loading axis of ∼137 μm. For comparison, the surface heights of the crack front shown in Figure 3.36 were determined through linear interpolation into a regular 2 μm x 2 μm square grid as shown in Figure 3.37. These interpolated values were used to find the RMS surface roughness (h_{RMS}) via:

$$h_{RMS} = \sqrt{\frac{1}{N\_grid\_pts} \sum_{j=1}^{N\_grid\_pts} (y_j - \overline{y})^2} \tag{3.41}$$

where N_grid_pts is the total number of grid squares containing surface height data and $\overline{y}$ is the average surface height of the simulated (and interpolated) fracture surface. The square root of the projected area is determined by taking the square root of the total area encompassing grid squares containing surface height data. The values of projected area and surface roughness obtained for the simultated crack path in Figure 3.37 are 134 μm and 2.4 μm, respectively. This process was repeated for 5 different instantiations resulting in square root of the projected area mean and standard deviation values of 136 μm and 1.2 μm and RMS height mean and standard deviation values of 1.8 μm and 0.7 μm. These values of square root of the projected area and crack front RMS height correlate well to the experimental values (137 μm and 2.6 μm). Therefore, the use of the multislip assumption (ref. Equation 3.39) for determining the crack plane normal seems to provide a good representation of the failure mode seen in experiments [7, 78, 79].

The fatigue crack growth rate versus stress intensity factor for MSC growth from the FIB notch in lab air is displayed in Figure 3.38. In this plot, the results from assuming that the crack is defined by its surface crack length versus using the projected area approach are shown. These are compared to experimental LEFM data [137, 138] for coarse grain IN100 in lab air at the same temperature and loading conditions. There are a few key results that need to be pointed out regarding this Figure. Firstly, the average crack propagation rate for the surface crack measurement is higher than that for the projected area crack measurement. This effect is most likely due to less kinematic constraint in surface grains versus grains located in the bulk. With less constraint, the grains are allowed to plastically deform more. This, in turn, increases the FIP and the driving force for MSC propagation leading to a higher MSC

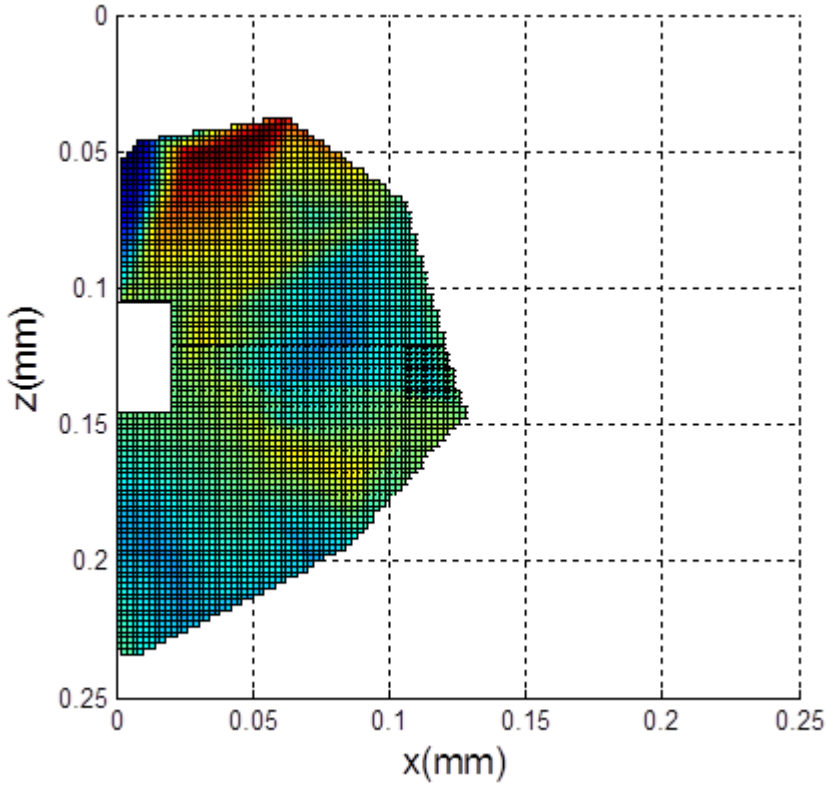

Figure 3.37: Example interpolation of crack front height into $2\mu m$ x $2\mu m$ regular grid spacing. Grid color indicates vertical elevation (y-direction) of crack path.

growth rate. Secondly, the amplitude of the oscillations of the da/dN versus ΔK curve for the surface crack measurement are approximately two times higher than the oscillations found using the projected area approach of crack measurement. Lastly, the amplitude of the oscillations in the fatigue crack growth rate for the projected area crack measurement tend to decrease with increasing crack length or range of stress intensity factor, ΔK, whereas the amplitude of oscillations for the surface crack measurement stay the same.

The reason for differences and changes in the amplitude of the oscillations of the da/dN versus ΔK curve for the surface versus projected area crack measurement approaches is directly related to the effect of microstructure and crack size. The da/dN oscillations at the surface are more pronounced because the surface crack only samples the crack growth locally at the surface. Therefore, since the surface crack is only sampling a few grains on either side of the semi-elliptical crack tip, the effect that the grain boundary has on propagation is much more prominent. The projected area crack, which accounts for the whole crack front, has more grains to sample along the crack front as opposed to the surface crack measurement. Depending on the local crack front location relative to the next grain boundary, there can be portions of the crack front that are propagating faster (within the grain) or slower (near the grain boundary). As the number of grains that the crack front touches increases, the local peaks and valleys of the local crack growth rates tend to average themselves out. Therefore, as one would expect, the oscillations both in experiments and within the current computational work decrease with crack length. Indeed, it is very interesting to note in Figure 3.38 that as the projected area MSC crack grows in length, it appears to be approaching the LEFM solution. In fact, the current FIB notch work predicts that this transition from MSC to LEFM is at a crack length of $2a \sim 250$ μm, which is on the order of the transition crack length seen in experiments ($a \sim 100$ μm) for a fine-grain IN100 microstructure [12]. Thus, this framework is very appealing in the aspect that it could help predict when an MSC crack is of sufficient length that a condition of similitude is reached and LEFM can be applied.

The simulation of MSC growth was repeated for five different randomly created

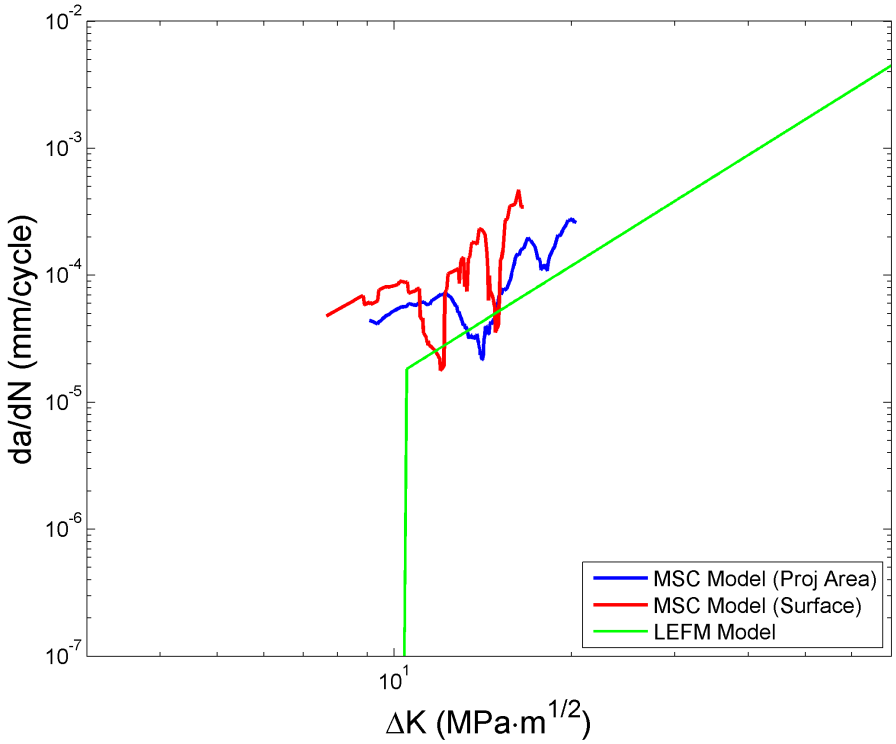

Figure 3.38: Example fatigue crack growth rate versus stress intensity factor for MSC growth from FIB notch in lab air. LEFM lines were fit to experimental data [137, 138] depicted in Figure 3.26.

digital microstructures for crack growth in both lab air and vacuum. In this case, the same microstructural instantiation was used for both environments. For example, the polycrystalline grain structure used for MSC Instantiation 1 was the same for both lab air and vacuum computations; the difference came in the MSC growth law that was applied (cf. Figures 3.30 and 3.31) for each environment condition. The polycrystalline grain structure and simulated fatigue crack growth for instantiations 2 through 5 are shown in Figure 3.39 for the lab air case. It is interesting to note the effect of different polycrystalline microstructures on the overall crack front shape. For the current case, nonlocal averaging of the crack growth rate was performed over the first two nearest neighbor crack front points. Increasing the number of nearest neighbor averaging crack front points further decreased the overall waviness of crack front so that it became more semicircular in shape. Experimental techniques such as in-situ high energy diffraction microscopy [142] could help determine the proper

number of crack front points that should be used in nonlocal averaging of the driving force for MSC propagation.

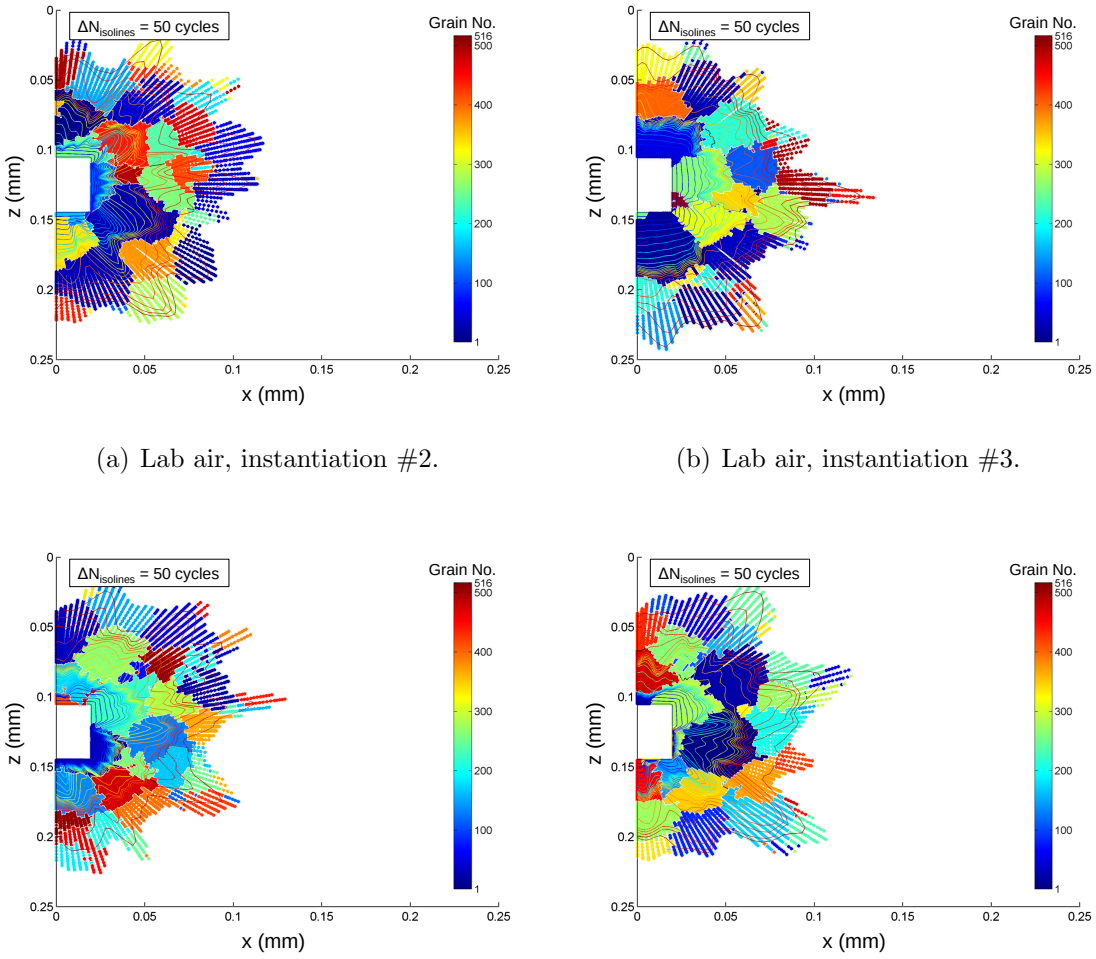

(a) Lab air, instantiation #2.

(b) Lab air, instantiation #3.

(c) Lab air, instantiation #4.

(d) Lab air, instantiation #5.

Figure 3.39: Comparison of MSC growth paths through polycrystalline microstructures for four different FIB notch instantiations.

Figure 3.40 shows a comparison of MSC growth rates for the five instantiations in lab air versus vacuum for the assumptions of a surface crack measurement versus projected area crack measurement. Similar conclusions can be reached with regards to the amplitude and convergence of the da/dN oscillations as those that were described for Figure 3.38. Additionally, it can be concluded that the MSC models used here for both vacuum and lab air surface crack growth simulation do a reasonable job

at mimicking the actual trends seen in experiments. It is hard to confirm that the projected area crack growth data is modeling experiments without more detailed techniques capable of measuring the full crack front at given time intervals, such as high energy diffraction microscopy techniques (cf. Herbig et al. [142] for example). However, since the computational MSC da/dN versus ΔK curve is approaching the LEFM solution, it appears that this computational technique is not too far off. Therefore, this MSC growth model is assumed to be sufficient for the fatigue life estimation employed in this work.

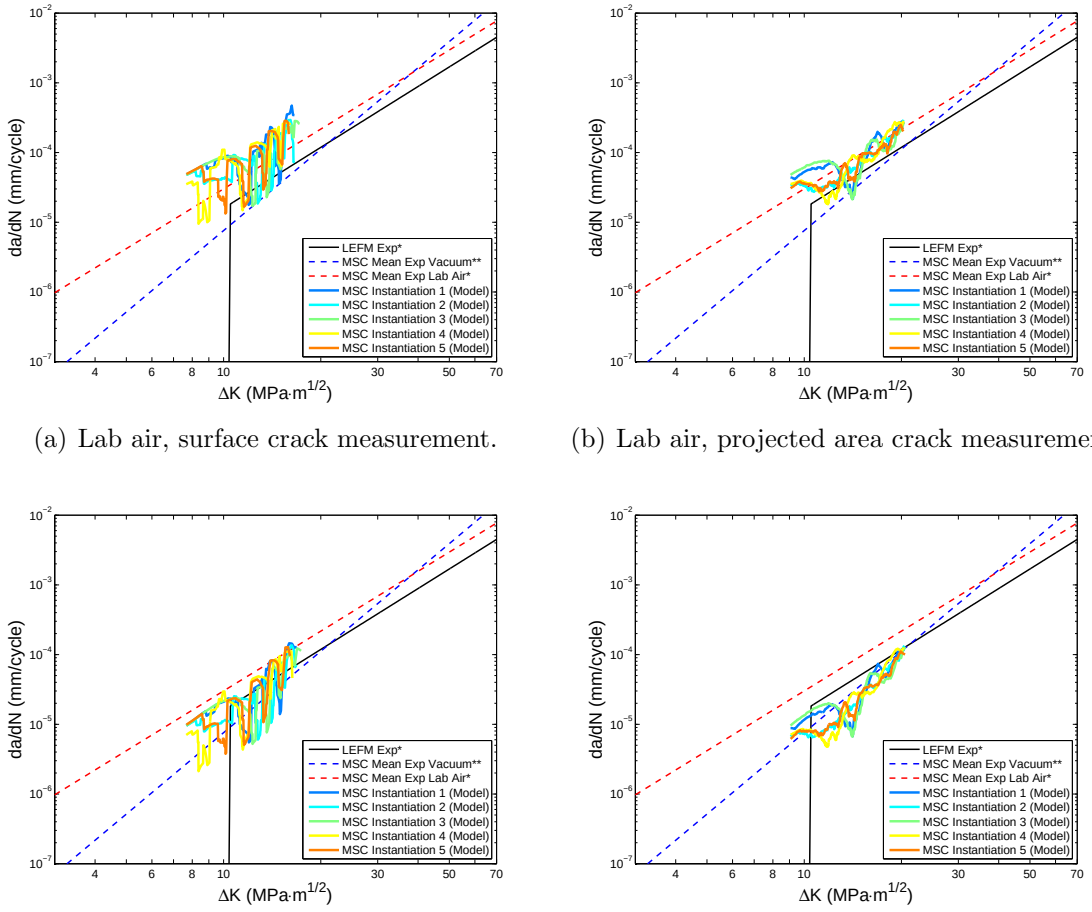

(a) Lab air, surface crack measurement.

(b) Lab air, projected area crack measurement.

(c) Vacuum, surface crack measurement.

(d) Vacuum, projected area crack measurement.

Figure 3.40: Comparison of MSC growth rate results for FIB notch simulations. *MSC mean and LEFM lines were fit to experimental data [137, 138] depicted in Figure 3.26. **MSC mean data line in vacuum was fit to LEFM vacuum data [136] as depicted in Figure 3.28.

3.8 Conclusions

In this section an MSC crack growth equation was proposed that takes into account the grain boundary character and distance of the crack tip to the next grain boundary. To be able to run this MSC growth model from uncracked simulations, an expression for the evolution of the crack extension driving force FIP was proposed based on a sequence of stationary crack propagation simulations. This FIP evolution expression allows for the projection of crack driving force for a crack of any length from the uncracked simulations. This MSC growth model was fit to experiments for the case of 1D crack growth and then computationally applied to 3D crack growth from a FIB notch. The computational MSC growth law effectively portrays the scatter in experimental MSC da/dN versus ΔK measurements for both lab air and vacuum environments. It was shown that since the bulk (projected area) crack samples more grains than the surface crack measurement, the crack growth rate becomes less oscillatory for the projected crack growth rate with crack extension. Additionally, the bulk MSC growth rate in lab air converged to the LEFM response. The MSC growth model developed in this Chapter was calibrated for uniaxial, proportional, cyclic (no dwell periods), and isothermal loading, so this MSC growth model should be only used within the confines of uniaxial, proportional, cyclic and isothermal loading. Extrapolation capabilities of this MSC framework to other finite element geometries will be studied in the following Chapters. The next section uses the calibrated lab air and vacuum MSC growth models to study the effect of inclusion depth on MSC growth in notched components.

CHAPTER 4
CONSIDERING THE EFFECT OF INCLUSIONS ON FATIGUE LIFE OF NOTCHED COMPONENTS

4.1 Introduction

One of the limiting factors of fatigue performance in PM Ni-base superalloys is the presence of processing-induced nonmetallic inclusions (NMIs) that serve as crack initiation sites [23, 24, 155, 156]. In the absence of a NMI, cracks can be initiated at pores located near the surface [7]. There have been many experimental studies to investigate the effects of inclusions [6, 7, 12, 20, 23, 24, 85, 86, 133, 155–159]. Since inclusions have a low probability of occurrence in commercial Ni-base superalloys, most of these experimental studies involve seeding, or introducing, NMIs into the powder metal so that they can be studied. The key conclusions from these studies are summarized by:

1. There exists a transition of fatigue crack initiation site from surface to subsurface/bulk with decreasing stress amplitude [23, 24, 157]. This leads to so-called "competing failure modes" [160–163] in the HCF/VHCF regimes.

2. Typically with a decrease in stress amplitude, the crack initiation location changes from inclusion-dominated to crystallographic type. In this transitional regime, the inclusion-dominated failure is usually life-limiting [157, 158].

3. Smaller grain size favors inclusion dominated initiation whereas larger grain size favors crystallographic crack initiation [6, 133, 159].

These inclusions are often introduced to the molten metal, due to erosion or spalling of the crucible, tundish or nozzle, prior to the gas atomization process used to create the powder [13, 25]. Two types of ceramic inclusions are typically introduced during the powder atomization process [155, 164]: (1) a blocky, non-deforming Al_2O_3/MgO ceramic due to the breakage of the ceramic crucible and (2) agglomerate and reactive

inclusions originating from patching putties (Al_2O_3 with silicon traces). As the PM processing techniques improve, cleaner Ni-base superalloys are being developed with reduced number densities of inclusions. However, proper probabilistic modeling of PM Ni-base superalloy components should take into account the probility of occurrence of a life-limiting NMI and the effect of the inclusion on the overall probability of failure. This approach should also consider the size effects associated with testing specimen-sized versus component-sized volume domains, since the statistically weakest "defect" size within a volume can change with the size of the volume [13, 165]. Thus, the purpose of this investigation is to computationally determine the relative effect of inclusions on the overall fatigue response and incorporate these effects in a probabilistic scheme to estimate the overall probability of failure of gas turbine engine components. We limit the current focus to single inclusions located within the damage process zone of notched specimens. Prior to presenting the simulation methodology, we present a review of relevent probabilistic approaches in HCF prediction/characterization and incorporation of inclusions in such probabilistic approaches.

4.1.1 Probabilistic approaches used in HCF prediction and characterization

Several probabilistic approaches have been developed to account for the effect of defects in HCF scatter. Most probabilistic approaches in HCF are based on weakest link theory and use probability distributions such as the two parameter Weibull distribution, three parameter Weibull distribution [166], or a Gumbel distribution [167] to describe the distribution of defects such as inclusions, pores, or microcracks that contribute to failure [168–170]. Other approaches consider the distribution of microvoids [171] or microplasticity [172].

In the high cycle fatigue (HCF) regime, cyclic plastic strain is often limited to a few fatigue critical hot spots where microstructure flaws (inclusions, pores, larger and/or favorably oriented grains, etc.) promote localized plastic slip intensification, fatigue crack formation and early growth. McDowell and coworkers [46, 134, 135, 173–175] have used crystal plasticity finite element modeling extensively to simulate the formation of

these HCF hot spots in multiple engineering alloys. Przybyla and McDowell [46, 173] computed nonlocal maximum FIP values for a large number of periodic statistical volume elements (SVEs) of realistic microstructures (Ni base superalloy IN100 [46] and a dual phase Ti-6Al-4V [173]) and fit these FIP values to a Gumbel extreme value distribution. This type of framework has subsequently been applied to simulate fatigue hot spot formation in two Widmanstätten Ti microstructures [174], to simulate effects of inclusions and pores in a martensitic gear steel [175], and to study the transition from surface to subsurface fatigue crack formation with decrease in applied stress/strain amplitude in Ti-6Al-4V [134] and Ni-base superalloy IN100 [135].

In weakest link theory a volume (V) is divided into j number of subvolumes (V_j). Each volume has a given density per unit volume of active fatigue critical sites, ϕ_j, which depends on many factors including applied stress amplitude, stress ratio, grain size, internal defect size, local anisotropy, and location within a component. The density factor ϕ_j follows a power law of the the stress amplitude and can take various forms. Typically, for three-parameter Weibull statistical analyses,

$$\phi = \frac{1}{V_o} \left\langle \frac{\sigma - \sigma_L}{\sigma_o} \right\rangle^m \tag{4.1}$$

where σ_L is the loacation parameter, σ_o is the scale parameter, m is the shape paramter (or Weibull slope), and V_o is a reference volume. For a given value of a, the Macauley brackes $\langle \cdot \rangle$ indicate that $\langle a \rangle = a$ for $a > 0$ and $\langle a \rangle = 0$ for $a \leq 0$.

The highly stressed volume of interest depends on the specimen geometry. For a smooth uniaxial specimen, the highly stressed volume encompasses the entire gauge section, whereas in a notched specimen it would only comprise the highly stressed volume at the notch root. For surface-dominated crack formation, the highly stressed volume of the smooth specimen would comprise the volume that is less than a given depth from the surface of the specimen. Therefore, the volume (V) in this case pertains to the highly stressed volume of interest. Using the above density factor ϕ (Eqn. 4.1, the probability of failure of the j^{th} infinitesimal volume is given as $dP_{f,j} = \phi_j dV_j$. Following weakest link theory [176], where an entire chain is only as strong as its weakest link, the probability of survival of volume (V) is equivalent to the probability

that all subvolumes dV_j within V simultaneously survive, determined by the product of survival probabilities, i.e.,

$$P_s = \prod_{j=1}^{m}(1 - \phi_j dV_j) \tag{4.2}$$

where m is the number of subvolumes ($m = V/dV_j$). Equation 4.2 assumes that there is no interaction between critically-stressed subvolumes. In other words, the distance between critical "defects" is sufficiently large that there is no interaction between defects. This assumption holds true in the HCF regime, where heterogeneous microplasticity is sparsely scattered throughout the fatigue specimen. If the subvolume size is very small compared to volume V and the density of sites ϕ is relatively low for low probabilities of failure, Equation 4.2 can be rewritten as

$$P_s \approx \lim_{dV_j \to 0}\left[\prod_{j=1}^{m}(1 - \phi_j dV_j)\right] = \exp\left(-\int_V \phi_j dV_j\right) \tag{4.3}$$

Combining Equations 4.1 and 4.3, the probability of failure of the volume V of a specimen becomes

$$P_f = 1 - \exp\left(-\int_V \phi_j dV_j\right) = 1 - \exp\left\{-\frac{1}{V_o}\int_V \left\langle \frac{\sigma - \sigma_L}{\sigma_o} \right\rangle^m dV\right\} \tag{4.4}$$

This equation is the three-parameter Weibull cumulative distribution function (CDF) and has been used extensively to model variability in fatigue strength.

4.1.2 Probabilistic approaches incorporating inclusion effects

Various researchers have used variant forms of the weakest link theory in Equation 4.2 and the Weibull fatigue strength CDF in Equation 4.4 to model inclusion/matrix effects and inclusion proximity to the surface effects in Ni-base superalloys. Figure 4.1 introduces a few dimension definitions to maintain consistency for the following description of different inclusion/matrix and inclusion/surface probabilistic approaches. As illustrated in this Figure, the diameter (or equivalent diameter for non-spherical particles) of a spherical inclusion is D and the distance that the inclusion is embedded in the matrix relative to the surface is denoted as d. For a fully embedded inclusion, the depth of the inclusion relative to the free surface is h.

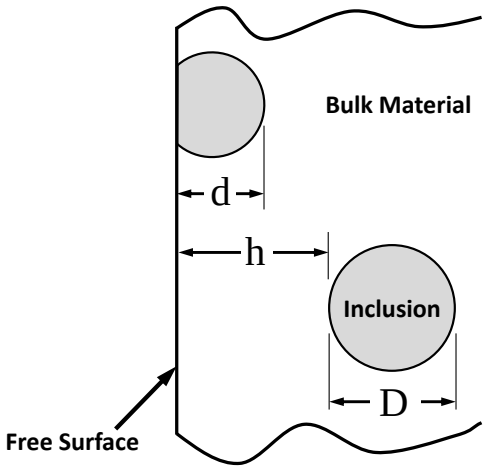

Figure 4.1: Definition of inclusion dimensions relative to the free surface.

The statististical distribution of inclusion sizes present in a PM Ni-base superalloy was considered by Pineau [165] in concert with a Paris law to determine the probability of failure of different sized components. This model considered both surface/volume effects and the formation and propagation of cracks from an inclusion to a critical size. The inclusions were assumed to be randomly distributed throughout the matrix and observed a known size probability distribution function. The inclusion sizes were divided into k number of bins. The probability of any one inclusion of a given bin size (k) intersecting the free surface was given as [165]

$$P_{k,surf}(D_k, n_k, S, V) = 1 - \left(1 - \frac{DS}{V}\right)^{nV} \tag{4.5}$$

where D_k is the inclusion diameter, n_k is the number of inclusions per unit volume, and S and V are the highly stressed surface area and volume of the specimen, respectively. To incorporate the extent (depth) in which the inclusion is embedded in the material relative to the surface, Equation 4.5 can be modified as

$$P_{k,surf}(D_k, n_k, S, V) = \left\{1 - \left(1 - \frac{DS}{V}\right)^{nV}\right\} \left[\frac{d}{D_k}\right] \tag{4.6}$$

where d is the depth in which the inclusion is embedded with respect to the surface (Fig. 4.1) and $D_k \geq d$ is assumed. Equation 4.6 ensures that inclusions that intersect the surface and are embedded further into the matrix will have a higher probability of failure than those that are less embedded by virtue of fatigue crack formation and

propagation process physics. The major and minor axes of the initial semi-elliptical crack (cf. Figure 3 in [165]) for LEFM analysis was assumed to be controlled by d and was assumed to evolve based on a Paris fatigue crack growth law. Instilling weakest link statistics, the total probability of failure as a function of all inclusion bin sizes (k) was given as

$$P_f = 1 - \prod_{k=1}^{N_{bins}} \left[1 - \left\{ 1 - \left(1 - \frac{DS}{V} \right)^{nV} \right\} \left[\frac{d}{D_k} \right] \right] \tag{4.7}$$

Using this approach, Pineau [165] estimated the probability of failure of three different sized components made from Rene' 95, corresponding to a large disc size, a small disc size, and a specimen size, and showed that the life-limiting inclusion size causing crack initiation increases with the size of the component.

The micro-mechanics of inclusion/matrix deformation was investigated by Deyber et al. [177] for a DA718 Ni-base superalloy fatigued at 450°C and 600°C. In addition to using the statistical distribution of particle size [165], Deyber et al. [177] estimated the probability of failure based on deterministic inclusion/matrix micro-mechanics. For the formation of cracks at particle/matrix interfaces, an equivalent Weibull stress function was proposed [177] as

$$P_f(\sigma_d) = 1 - \exp\left(- \left[\frac{\Sigma_1 + \beta \left\langle \sigma_{eq} - \sigma_y \right\rangle}{\sigma_o} \right]^m \right) \tag{4.8}$$

where Σ_1 is the maximum principal stress, β is the particle shape factor, σ_{eq} is the equivalent Von Mises stress, σ_y is the yield stress, and σ_o is a scaling parameter. Failure was considered when the numerator in Equation 4.8 reaches a critical decohesion stress, i.e., $\sigma_d = \Sigma_1 + \beta \left\langle \sigma_{eq} - \sigma_y \right\rangle$. Following crack formation, a micro-crack propation law based on the Tomkins model [178] was used. The probability of failure was based on the probability that a particle of a diameter D_o would propagate after a given number of cycles (N_o). The product of probabilities of survival of particles at the surface ($surf$), subsurface ($subsurf$), and within the bulk ($bulk$) was used to find the

overall probability of failure ($P_f = 1 - \prod_{k=1}^{3} P_{k,survival}$) as

$$P_f = 1 - \left\{ \prod_{n=1}^{N_{el,surf}} \left[(1 - P_f(\sigma_d) P(D \geq D_o))^{N_{part,surf}} \right] * \prod_{n=1}^{N_{el,subsurf}} \left[(1 - P_f(\sigma_d) P(D \geq D_o))^{N_{part,subsurf}} \right] * \prod_{n=1}^{N_{el,bulk}} \left[(1 - P_f(\sigma_d) P(D \geq D_o))^{N_{part,bulk}} \right] \right\} \tag{4.9}$$

where $P_f(\sigma_d)$ is given by Equation 4.8, N_{part} and N_{el} are the number of particles contained in the computational mesh elements, respectively, in each location (surface, subsurface, and bulk).

Inclusion/surface interactions were also investigated by de Bussac and Lautridou [25] and de Bussac [179]. They considered particles of different size bins (much like that described above) and the probability for an individual particle to have a depth greater than a critical depth d_c, i.e., $P(d > d_c) = S(D - d_c)/V$. Imposing weakest link statistics over each bin size, the total probability of failure was proposed as

$$P_f = 1 - \prod_{k=1}^{N_{bins}} \left[\exp \left\{ -n_k S(D_k - d_c) \right\} \right] \tag{4.10}$$

where n_k was the density is the number of inclusions per unit volume. Later, de Bussac [179] proposed a probability of failure function that considered the competition between the largest defect at the free surface and the largest defect within the bulk of the material, i.e.,

$$P_f = 1 - \left\{ \left[1 - P_S \right] \left[1 - P_V \right] \right\} \tag{4.11}$$

where P_S and P_V are the probabilities of surface and bulk volume failure, respectively. This model was evaluated using a large set of LCF data of N18, a PM Ni-base superalloy used for high-temperature jet engine disk applications. SEM analysis was used to characterize the size of the life-limiting defect as a function of the depth (h) of the defect from the free surface (cf. Fig 4.2). Figure 4.2 shows that near-surface crack formation ($h \sim 3 - 5$ μm) is more damaging than surface crack formation ($h = 0$) due to the fact that a crack formed beneath the surface will propagate through the

surface and effectively introduce a larger initial surface defect. Also, the life-limiting defect size increases as a function of depth from a minimum size of $\sim$ 30 μm at a depth of $\sim$ 4 μm up to a plateau value of $\sim$ 60-80 μm at a transition depth, h_t $\sim$100 μm. This indicates that there is a significant surface/inclusion size interaction effect on the probability of forming a crack in this PM Ni-base superalloy.

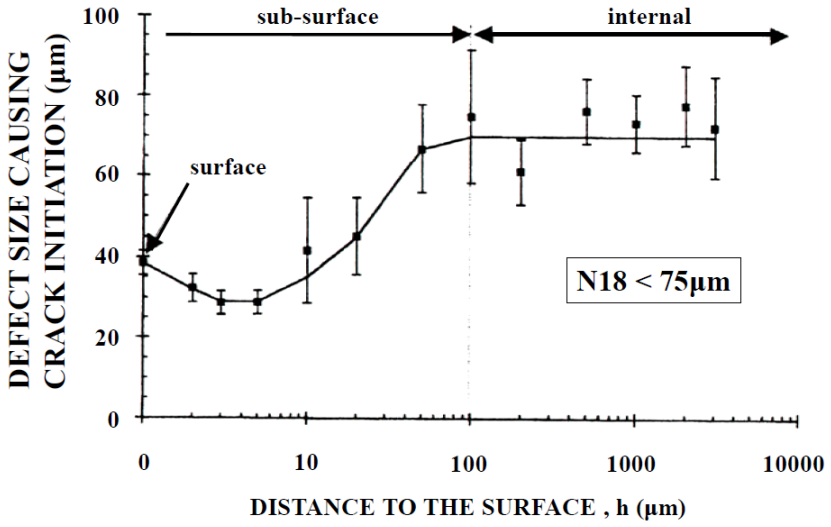

Figure 4.2: Fatigue critical crack initiation size versus distance from the surface for a PM Ni-base superalloy N18 [179].

Similarly, multiple papers from AFRL researchers [5, 18, 157, 180–183] have demonstrated a general framework for a physics-based understanding of fatigue life variability in a Ni-base superalloy IN100 [18,157,180,181], Rene' 88DT [91], and an $\alpha+\beta$ titanium alloy Ti-6Al-2Sn-4Zr-6Mo (Ti-6246) [5, 181, 183] based on a number of fatigue life experiments. They categorized the total fatigue lifetime probability density function (f_t) as a superposition of life-limiting, crack-growth-dominated (Type I) and mean-controlling, crack-initiation-dominated (Type II) mechanisms in fatigue, i.e.,

$$f_t = P_I f_I(x) + P_{II} f_{II}(x) \tag{4.12}$$

where $f_*(x)$ is the probability density function of each failure mechanism ($*$) and P_* is the weighted probability of occurrence of each individual response. Note that in Equation 4.12, $P_I + P_{II} = 1$. An example of bimodal fatigue showing Type I, Type II

and transition from Type I to Type II fatigue regimes is shown in Figure 4.3 for a Ti-6246 alloy [182]. For Ni-base superalloy IN100, the life-limiting fatigue mechanism was dominated by crack formation and early propagation from near-surface non-metallic inclusions, whereas the mean-controlling fatigue mechanism was due to near-surface pores and non-metallic inclusions within the bulk of the material [18, 157, 180, 181]. Additionally, there is an increased separation between the life-limiting and mean-controlling populations with decreasing applied stress/strain amplitude contributing to increased fatigue life variability. A probability plot of fatigue life data for a fine-grained IN100 with mean grain size of 4 μm is shown in Figure 4.4. This Figure displays the transition from Type I (life-limiting) to Type II (mean-controlling) fatigue failure mode in Ni-base superalloy IN100 at different maximum applied stress levels.

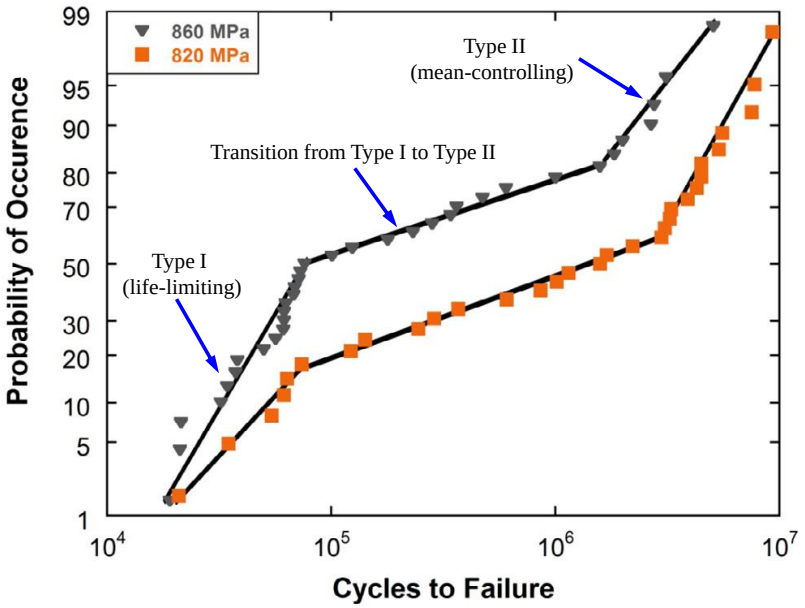

Figure 4.3: Lognormal probability plot for a Ti-6246 alloy displaying bimodal fatigue lifetime data [182].

Salajegheh and McDowell [135] considered the effect of inclusions on surface versus bulk fatigue crack formation and early growth in a fine-grained IN100 Ni-base superalloy. They proposed that the number of fatigue critical hot spots (Ψ) producing fatigue crack formation and early growth in the surface region followed a binomial

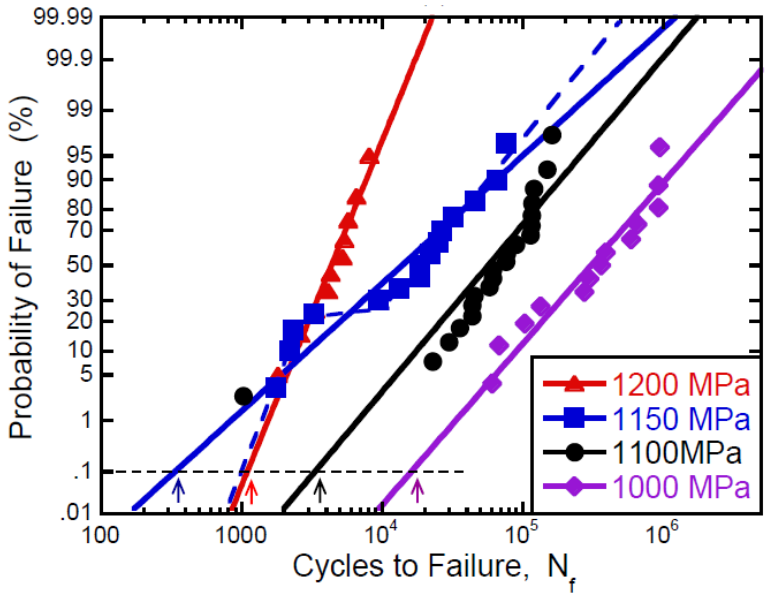

Figure 4.4: Probability plot of fatigue life data for a fine-grained IN100 Ni-base superalloy [18]. Mean grain size = 4 μm, $R_\sigma = 0.05$, T = 650°C, and $f = 0.33$ Hz [18].

distribution and was given by [135]

$$g(k) = \binom{\Psi}{k} \binom{V_s}{V_t}^{k} \left(\frac{V_t - V_s}{V_t}\right)^{\Psi - k} \tag{4.13}$$

where k is the number of successes in Ψ number of fatigue critical hot spot trials, and V_s and V_t are the volume of the surface region and the total volume of the specimen, respectively. The probability of having at least one fatigue hot spot in the surface region was given by [135]

$$p_s = 1 - g(k = 0) = 1 - \left(\frac{V_t - V_s}{V_t}\right)^{\Psi} \tag{4.14}$$

Owing to the fact that bulk fatigue critical hot spots usually have longer fatigue lives than surface ones [18, 157, 180, 181], it was assumed that bulk fatigue hot spots were critical only when surface hot spots were absent. Hence, Salajegheh and McDowell [135] assumed that the probability of bulk fatigue crack hot spots causing failure, p_b, was

$$p_b = 1 - p_s = \left(\frac{V_t - V_s}{V_t}\right)^{\Psi} \tag{4.15}$$

The value of Ψ in Equations 4.13 through 4.15 was estimated as a function of inclusion size (radius, R) and applied normalized strain amplitude ($\varepsilon_a/\varepsilon_y$) based on

the generalized extreme value (GEV) distribution of fatigue indicator parameters for "2.5D" CPFEM simulations of bonded and partially-debonded isotropic linear elastic inclusions. For interfacial debonding, they considered the maximum interface traction, $T_{int} = max(\boldsymbol{n}^{incl} \cdot \boldsymbol{\sigma}^* \cdot \boldsymbol{n}^{incl})$, where $\boldsymbol{n}^{incl}$ is the unit vector normal to the grain/inclusion interface and $\boldsymbol{\sigma}^*$ is the Cauchy stress tensor averaged over the grain. For partially-debonded inclusions, the Fatemi-Socie (FS) parameter was considered. Using this framework, Salajegheh and McDowell [135] showed trends of increasing probability of surface crack formation and early growth with increasing specimen size, increasing inclusion number density, increasing inclusion radius distribution, and decreasing inclusion/matrix interface strength.

4.1.3 Grain size effects (relative to inclusion size)

The size of the inclusion relative to the statistically largest grain size requires further discussion. In Gabb et al. [6], they investigated the fatigue mechanisms of a graded, dual-microstructure LSHR Ni-base superalloy used for a dual microstructure disk. They tested specimens from the inner ring (fine-grained), outer ring (coarse-grained), and the transition zone (contained both fine and coarse grains). They found that fine grain inner ring specimens predominantly failed due to internal NMIs that were larger than the average grain size, whereas the coarse grain outer ring and the transition zone failed from coarse grain facets. A similar conclusion was reached by Findley and Saxena [159] who studied LCF crack nucleation in Rene' 88DT and found that nucleation around inclusions is more prevalent for smaller grain sizes, whereas larger grain sizes favor slip band crack nucleation. Moreover, if the inclusion is smaller than the grain size, it seems to have little effect on the amplification of driving force for fatigue crack initiation and early growth as compared to the statistically largest grain in the microstructure. On the other hand, for inclusions that are larger than the average grain size, these inclusions will most likely be the fatigue-critical hotspot in the microstructure. Thus, the size of the largest inclusion as compared to the largest grain size, often referred to as the ALA (as large as) grain size, is a very important attribute to control during processing. This is the reason why control of inclusion

(and pore) size is very crucial in fine grained Ni-base superalloy microstructures, which have average grain sizes $\sim 3 - 15$ μm; cracks tend to form in these fine grained microstuctures via a Stage II, non-crystallographic, transgranular cleavage mechanism near non-metallic inclusions (NMIs) or pores [12, 85, 86].

The effect of inclusion size and strain amplitude on strain-life estimation was simulated for smooth specimens made of a coarse grain IN100 in previous work by Musinski and McDowell [184]. Example results [184] of the simulation of a single debonded Al_2O_3 inclusion at a distance of $h = 100$ μm from the surface are shown in Figure 4.5. As shown in Figure 4.5(b), there is a large amount of localization of the effective plastic strain and the maximum Fatemi-Socie (FS) parameter [123] near the debonded inclusion/matrix interface. As expected, the driving force for fatigue crack propagation, the FS parameter $\Delta\Gamma$, increases with increasing inclusion size and increasing strain amplitude. Also, the width of the maximum $\Delta\Gamma$ spike is larger for the larger inclusion size, indicating a larger plastic zone size at the crack tip. Following the hierarchical fatigue life estimation approach outlined in Musinski and McDowell [76], Figure 4.5(c) shows the predicted strain-life for inclusion diameter sizes $\phi = 20$ μm and $\phi = 50$ μm at strain amplitudes of $\varepsilon_a = 0.5\varepsilon_y$, $0.6\varepsilon_y$, $0.7\varepsilon_y$, and $0.8\varepsilon_y$ with $\varepsilon_y = 0.42\%$ being the proportional limit. Twenty different microstructural instantiations were simulated per each perturbation of inclusion size and strain amplitude. The predicted strain-life values are compared to seeded and unseeded experimental data [185,186] and the calibrated fatigue-life estimation computational model without inclusions [76]. It is interesting to note that the median strain-life behavior of the $\phi = 20$ μm inclusions, which is smaller than the average grain size of $d_{grn} = 34$ μm, follows closely to that of the smooth specimen without inclusions whereas the $\phi = 50$ μm inclusions display a knock-down effect on the strain-life plot. Hence, if the inclusion is smaller than the average grain size, it seems to have little effect on the amplification of driving force for fatigue crack initiation and early growth as compared to the statistically largest grain in the microstructure. On the other hand, inclusions that are larger than the average grain size will most likely be the fatigue-critical hot spot in the microstructure. Thus, the size of the largest inclusion as compared to the largest grain size, often referred

to as the ALA (as large as) grain size, is an important attribute to control during processing.

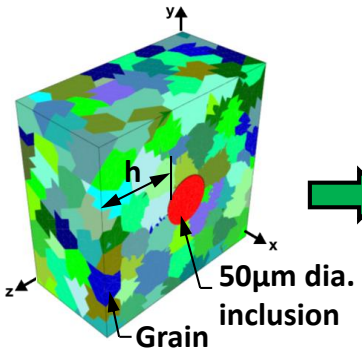

(a) Partially-debonded Al_2O_3 inclusion in IN100 matrix.

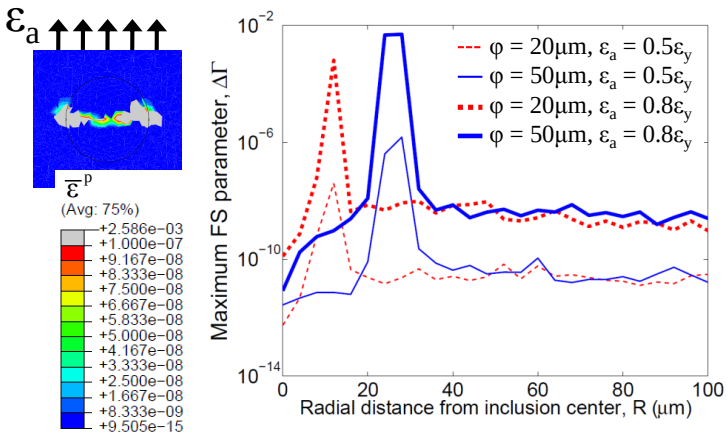

(b) Localization of effective plastic strain and maximum FS parameter near inclusion/matrix interface.

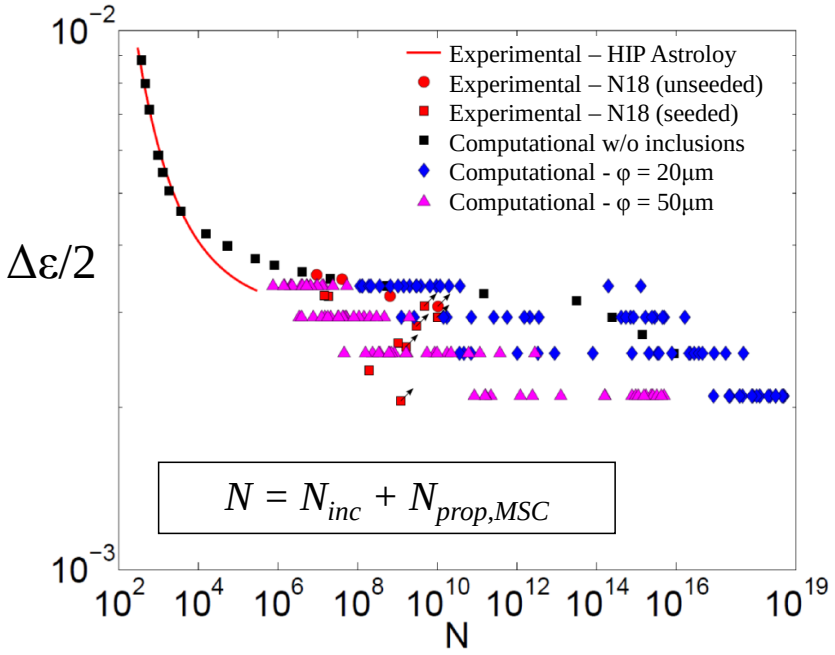

(c) Variability in strain-life due to debonded inclusion.

Figure 4.5: Example results of debonded inclusion study [184].

4.1.4 Notch and inclusion interaction effects

Most of the previous work involving characterization or simulation/prediction of inclusions/surface effects investigated smooth specimens under uniaxial (macroscopically uniform state of stress) fatigue conditions. However, the potential for competition between surface and internal initiation still exists in notched components [162, 164, 177, 187]. Figure 4.6 shows stress-life results for notched Ni-base superalloy specimens with stress concentration factor $k_t = 1.7$ fatigued under stress-controlled $R_\sigma = 0$ loading at 399°C. According to Cashman [162], these internal initiation sites "were just slightly below the surface." As evidenced from Figure 4.6, there is a clear transition from surface initiated to internal initiated cracks as the number cycles to failure increases from $\sim 10^4$ to 10^5.

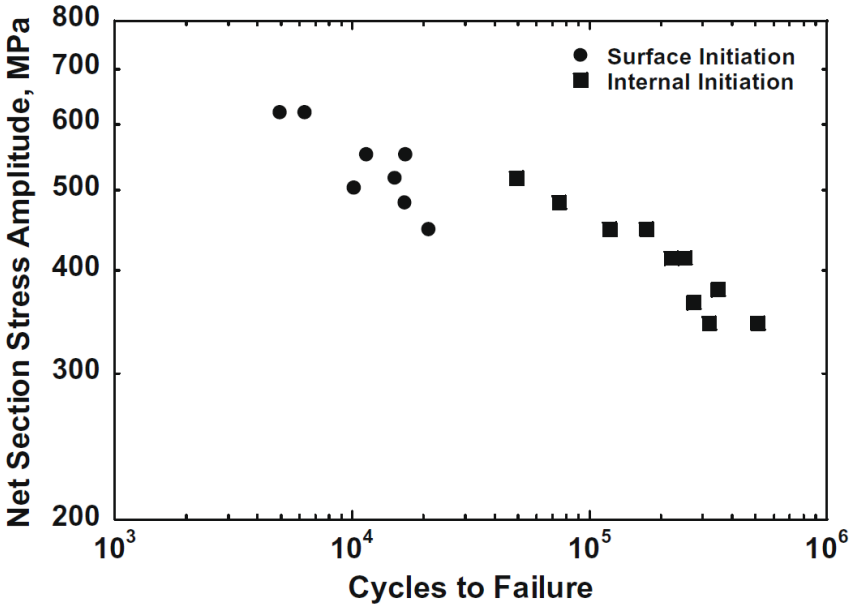

Figure 4.6: Experimental fatigue life results for notched Ni-base superalloy specimens ($k_t = 1.7$, $R_\sigma = 0$, and T = 399°C) [162, 187].

Figure 4.7 shows the LCF to HCF transition fatigue stress-life data for notched DA 718 Ni-base superalloy specimens with two different stress concentration factors, $k_t = 1.3$ and $k_t = 2.5$, at two different temperatures, 450°C and 600°C [177]. This Figure was recreated from ref. [177] to more clearly display the origin of failure for each data

point; open symbols indicate surface fatigue crack initiation and filled symbols indicate subsurface fatigue crack initiation. The stress amplitude value for each data point in Figure 4.7 was not recorded in [177]. However, qualitavtive experimental trends can be deduced from this data without knowing the exact stress amplitude values for the notched specimen experiments. As indicated by the blue dashed lines, there are three fatigue life regimes dominated by surface fatigue crack initiation ($N < 10^4$), subsurface fatigue crack initiation ($N > 5 \times 10^5$), and a transition fatigue regime that has both surface and subsurface fatigue crack initiation ($10^4 < N < 5 \times 10^5$).

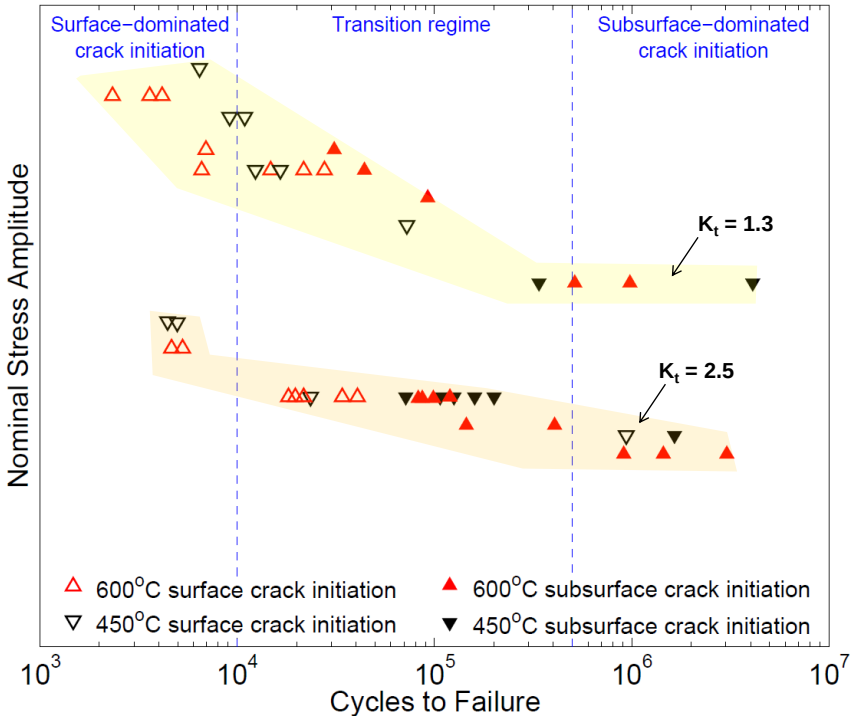

Figure 4.7: Notched specimen DA718 Ni-base superalloy fatigue life data. Recreated from data in [177]. (1Hz, average grain size 5-10 μm).

Another example of surface to sub-surface (internal) fatigue crack initiation for notched components is shown in Figure 4.8. This Figure displays fatigue life data for un-peened notched IN100 specimens tested between 538°C and 621°C, with stress concentration factor $k_t = 2.5$, test frequency $f = 0.5$-1.0 Hz, and stress-controlled loading $R_\sigma = 0.05$ [164]. The microstructure was processed using a subsolvus heat treatment resulting in an average grain size of 5 μm. In Figure 4.8, the filled data

points indicate surface fatigue crack initiation and the unfilled data points indicate internal fatigue crack initiation. The internal inclusions failed at a depth of 70 μm or more from the specimen surface for lower maximum applied stress levels, $\sigma_{max} = 595$ MPa and $\sigma_{max} = 568$ MPa [164]. Figure 4.8(a) displays the fatigue life data versus the critical equivalent inclusion diameter causing crack initiation and Figure 4.8(b) shows S-N data for the same data set as in Figure 4.8(a). Figure 4.8(b) illustrates a clear transition from surface initiated to internal initiated cracks as the number cycles to failure increases from $\sim 10^4$ to 10^5.

The critical inclusion size versus number of fatigue life cycles and maximum applied stress level in Figure 4.8(a) requires more discussion. Based on the limited number of data points at each maximum applied cyclic stress value, there is a slight correlation between increasing critical inclusion size and decreasing number of cycles to failure for a given stress amplitude and failure site (surface or internal). It is also interesting to note that for the highest applied stress amplitude ($\sigma_{max} = 811$ MPa), critical inclusion sizes within the interior of the specimen were larger than the critical inclusions at the surface. This surface effect is due to the combined effects of (1) incompatibility in deformation between the stiffer inclusion and the matrix and (2) the lack of constraint near the surface. These combined effects promote enhanced cyclic slip at the inclusion/matrix interface and fatigue crack formation at the surface [188]; therefore, smaller inclusions near the surface can be just as detrimental to the fatigue life as larger inclusions located within the bulk of the material. Thus, a probabilistic formulation for inclusion-dominated fatigue should consider both the inclusion size *and* depth relative to the surface.

One key reason why experimental notch and inclusion depth interaction studies are not more prevalent is due to the low probability of occurrence that inclusions exist in the damage process zone near the notch root. It would be very expensive and time consuming to study "naturally-occuring" inclusions at different surface depths within the notch root damage process zone. Seeding of the inclusions could be done to increase the probability of occurrence of inclusions within the damage process zone near the notch root. However, to parametrically study the effect of

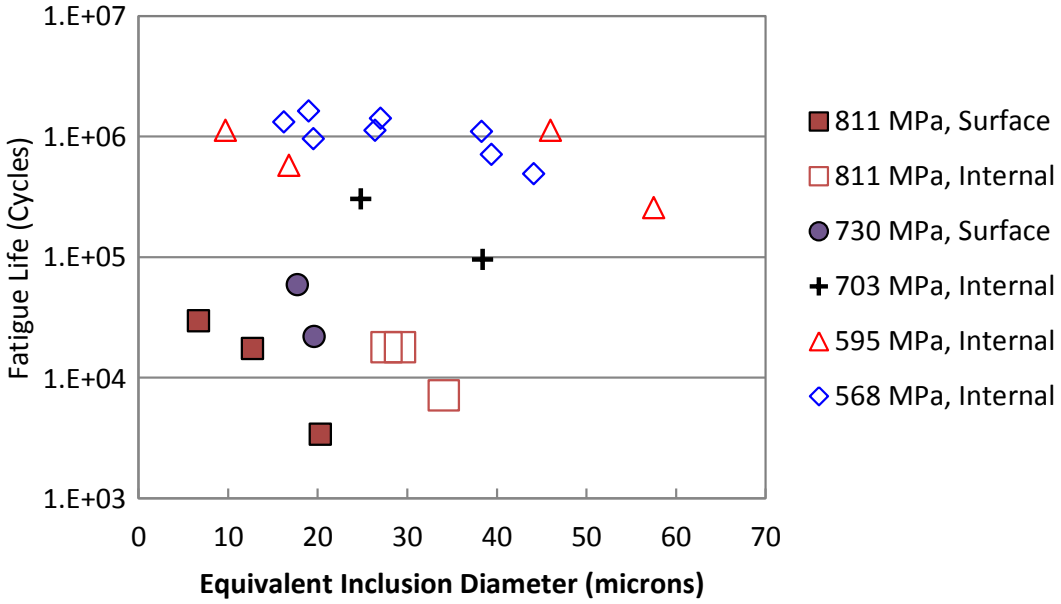

(a) Fatigue life as a function of equivalent inclusion diameter.

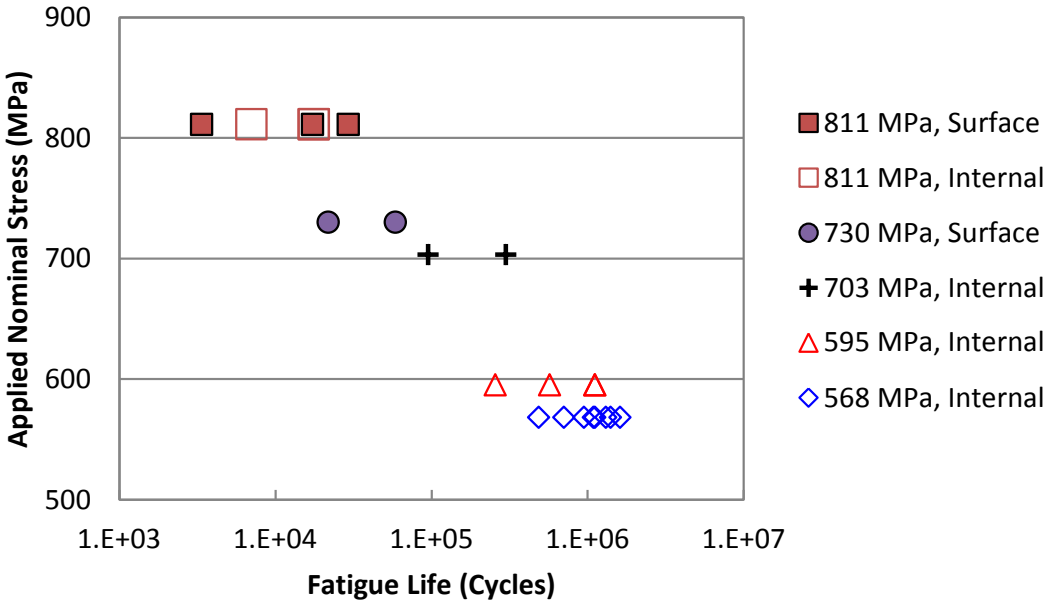

(b) S-N plot for data in part (a).

Figure 4.8: Fatigue life data for un-peened notched IN100 specimens tested between 538°C and 621°C, $k_t = 2.5$, $f = 0.5{-}1$ Hz, $R_\sigma = 0.05$, and average grain size of 5 μm [164]. Filled data points indicate surface crack initiation and open data points indicate internal crack initiation. Plots recreated from [164].

inclusion depth on notch fatigue would require a two-step process: (1) a pre-test non-destructive evaluation technique such as x-ray microtomography to determine the spatial distribution of inclusions and (2) "cookie cutting" specimens so that these inclusions are located at different depths within the notch root zone. Obviously, this experimental technique is wasteful, expensive, and prohibitive for inclusion depth parametric studies. Additionally, due to the low probability of occurrence of surface fatigue crack initiation in the HCF regime, a large number of experiments (~ 100) are required to accurately describe the life-limiting surface failure distribution at a high confidence level (95%) [135]. Computational CPFEM studies are a low-cost alternative that can be used to simulate the effect of inclusions on notch fatigue.

Simulation of the interaction between notches and inclusions has received little attention in the literature thus far, specifically with respect to the effect of depth of the inclusion relative to the notch root. To determine the effect of local grain structure on near-inclusion stresses/strains a computational crystal plasticity constitutive model is adopted. Previous simulation of fatigue at notches using 3D crystal plasticity constitutive relations has been done by Owolabi et al. [189] and Musinski and McDowell [76]. Both approaches considered inclusion-free microstructures. Recently, Owolabi and Whitworth [190] used the probability of fatigue crack formation approach outlined by Owolabi et al. [189] and the transition crack length approach developed by Musinski and McDowell [76] to estimate MSC formation and early growth within double-edge notched specimens that contained a single, fully-bonded inclusion at a given distance from the notch root. The inclusion was assumed to be ellipsoidal with the major principal axis $2a = 30$ μm, the minor principal axes $2b = 2c = 10$ μm, and was oriented so that the major principal axis was in the direction of the notch root gradient field and perpendicular to the loading axis. A single inclusion depth (1 mm, 0.6 mm, and 0.3 mm) was simulated per notch radius size (0.2 mm, 0.6 mm, and 1.0 mm), respectively. Owolabi and Whitworth [190] estimated the combined knock-down effect of the notch/inclusion on the strain-life plot and the probabilty of formation and early growth of MSCs. While this approach considering a single inclusion/notch effect is a natural extension to previous work [76, 189], it does not fully estimate

the combined effect of microstructure variability (grain size, shape and orientation), inclusion depth, and notch size on fatigue life scatter. In the following section, we present a methodology for studying the aforementioned microstructural effects on fatigue life variability.

4.2 Methodology

Modeling the effects of inclusions has been undertaken by many researchers. Murakami and coworkers [152–154, 191] have demonstrated a robust correlation between the square root of the projected area normal to the maximum tensile loading direction of the statistically most extreme inclusion size in steels to both (1) the fatigue limit and (2) the maximum stress intensity factor in front of the inclusion crack front. When modeling the inclusion/matrix interfacial characteristic, three different assumptions are usually considered: the inclusion is completely intact with the matrix, the inclusion is cracked, and the inclusion is partially debonded from the matrix. Of these, the worst case condition for fatigue crack initiation and propagation is the debonded inclusion, as shown for a martensitic gear steel [125], a directionally solidified Ni-base superalloy [188], a polycrystalline Ni-base superalloy [124], and a cast A356-T6 aluminum alloy [54,192]. Therefore, modeling inclusions as debonded can be considered applicable for minimum life designs. However, the debonded interface assumption may be overly conservative depending on the loading condition, location of the inclusion, and surface treatment. In the following section, a debond law is proposed based on in-situ experimental observations of inclusion/matrix interfacial separation in a Ni-base superalloy.

4.2.1 Proposed Debond Law for Inclusion/Matrix Interfacial Separation

The process of debonding of inclusions was experimentally studied by Xie et al. [20] for an Al_2O_3-seeded PM Rene'95 Ni-based superalloy with an average grain size of 8-10 μm. In Xie's work, specimens were machined so that the inclusions were located at the surface within the gauge section of the specimens. These specimens were subjected to monotonic and cyclic $R_\sigma = 0.1$ loading to study debonding behavior at room

temperature. For monotonic loading, the debonding of a ~ 50 μm inclusion from the matrix was observed at a stress level of approximately $0.8\sigma_{y,0.2\%}$, where $\sigma_{y,0.2\%}$ is the 0.2% offset yield strength of the material. For cyclic loading, two inclusion debonding instantiations were presented, one at $\sigma_{max} = 1000$ MPa and the other at $\sigma_{max} = 600$ MPa. The resulting SEM images from these studies are shown in Figure 4.9. As shown in these SEM images, the debonding process for a ~ 60 μm $\times$ 70 μm inclusion at $\sigma_{max} = 1000$ MPa occurred in between 5,000 and 7,000 cycles and the debonding process for a ~ 60 μm at $\sigma_{max} = 600$ MPa occurred in between 101,335 and 116,316 cycles. While these two data points are for slightly larger inclusions ($\sim$60 μm) than the 50 μm inclusions modeled in the current study, these data points combined with the monotonic debonding at $\sigma_{max} = 0.8\sigma_{y,0.2\%}$ are used to construct an approximate debond law for perfectly bonded inclusions. It should be stressed that these in-situ debonding experiments were performed at room temperature, and are considered to be applicable for the current study of the simulation of elevated temperature fatigue from inclusions. When in-situ observations of debonding inclusions at elevated temperature become available in the literature, the proposed debond law for perfectly bonded inclusions can be adjusted accordingly.

The proposed debond law for a single Al_2O_3 inclusion in a Ni-base superalloy matrix is shown in Figure 4.10. The five data points in this Figure correspond to the aforementioned experimental studies performed by Xie et al. [20], normalized by the 0.2% offset, $\sigma_{y,0.2\%} = 1400$ MPa, of the material at room temperature. Because of the limited number of experimental data points, a conservative debond curve limit was assumed to be composed of two piecewise smooth curves. First, a quadratic Bezier curve [193] was constructed using the three control vertices at $\boldsymbol{P} = \{(1, 0.8), (5000, 0.71), (101335, 0.43)\}$, corresponding to the normalized experimental debond data from Xie et al. [20]. Second, a linear decay (on a linear-log plot of normalized maximum stress versus number of cycles to debond) was assumed from the (101335, 0.43) data point to $\sigma_{max}/\sigma_{y,0.2\%} = 0$ with a slope equal to the slope of the Bezier curve at (101335, 0.43). As shown in Figure 4.10, the inclusion is assumed to be intact (perfectly bonded) below and to the left of the debond curve limit, whereas the

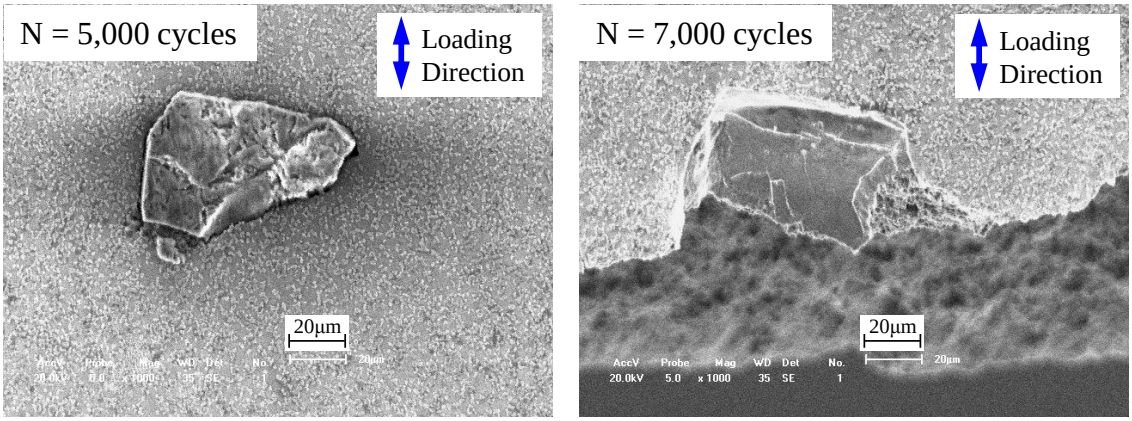

(a) In-situ SEM observation of ~60 µm x 70 µm inclusion at σ_{max} = 1000 MPa, R_σ = 0.1.

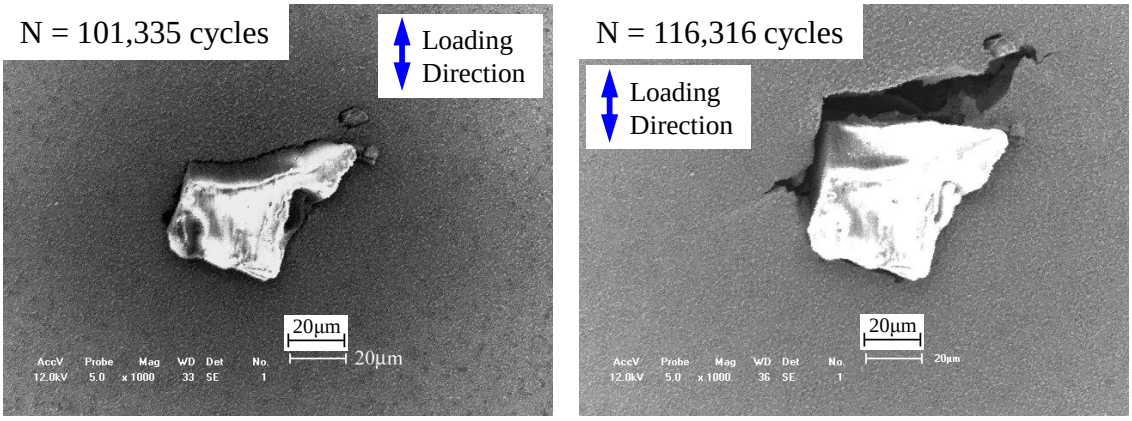

(b) In-situ SEM observation of ~60 µm inclusion at σ_{max} = 600 MPa, R_σ = 0.1.

Figure 4.9: In-situ SEM observation of the debonding process of a surface Al_2O_3 inclusion in a Rene'95 Ni-base superalloy fatigued at room temperature [20].

inclusion is assumed to be debonded in the zone above and to the right of the debond curve limit. For compressive applied stresses (maximum normalized stress values below zero), the number of cycles to debond the inclusion is assumed to be infinite. For the time being, this debond law is assumed to be applicable to the debonding of a single inclusion in a coarse grain IN100 matrix at $T = 650°C$. Again, when more detailed studies regarding debond behavior at elevated temperatures are available in the literature, the proposed debond law can be adjusted accordingly.

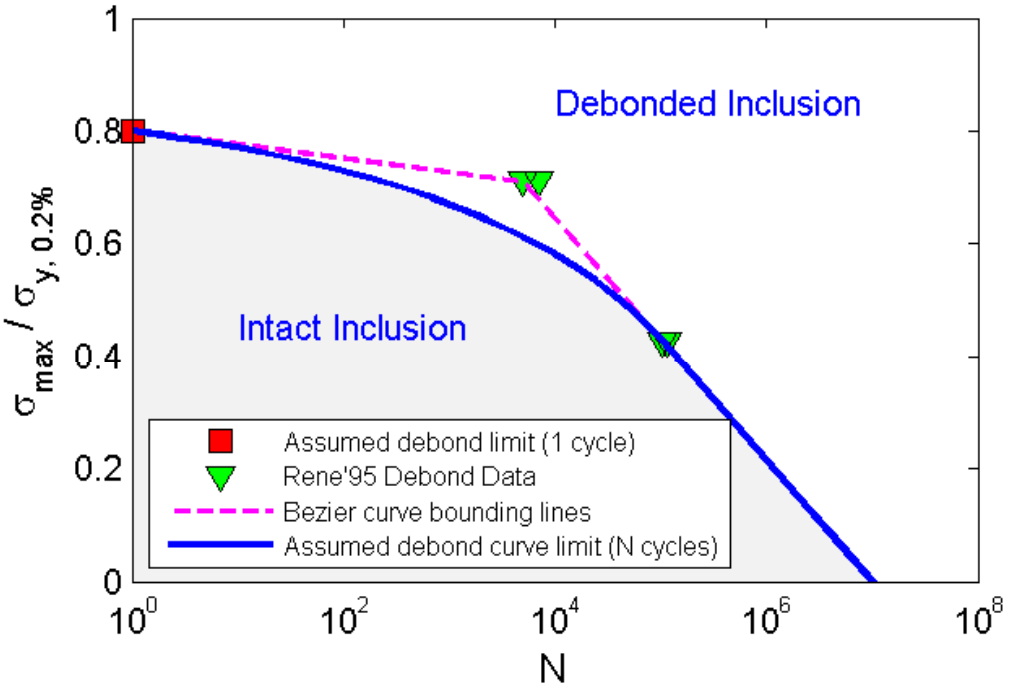

Figure 4.10: Proposed debond law for a single Al_2O_3 inclusion in a Ni-base superalloy matrix. Experimental data points are from Xie et al. [20].

4.2.2 Multistage Fatigue Life Prediction Incorporating Inclusion/Matrix Interfacial Separation

The multistage fatigue life approach [4, 29, 54, 55] introduced in Section 3.2 is modified here to incorporate inclusion/matrix interfacial separation. The process of debonding is assumed to precede the fatigue crack incubation period, so that the total fatigue life, N_T, of a component is decomposed into stages of interfacial/matrix debonding, fatigue crack formation, early MSC/PSC growth, and long crack growth by

$$N_T = N_{DB} + N_{inc} + N_{MSC/PSC} + N_{LEFM} \tag{4.16}$$

where N_{DB} is the number of cycles required to partially debond the inclusion from the matrix. For the case of a spherical inclusion, the matrix is assumed to debond from the spherical inclusion (centered vertically about $y = 0$) along the northern hemisphere defined by $y \geq 0$. For estimation of inclusion/matrix interfacial debonding, the maximum stress component along the y-axis (applied loading direction) is averaged within the polycrystalline matrix over a volume defined by a cylinder with diameter 100

μm and height 150 μm elongated along the loading y-axis and centered vertically along the y-axis as shown in Figure 4.11. This averaging volume encompassed approximately 30-50 grains for each instantiation. This nonlocal average stress value in the y-direction is used to determine the number of cycles to debond the inclusion from the matrix, N_{DB}, based on the debond law illustrated in Figure 4.10.

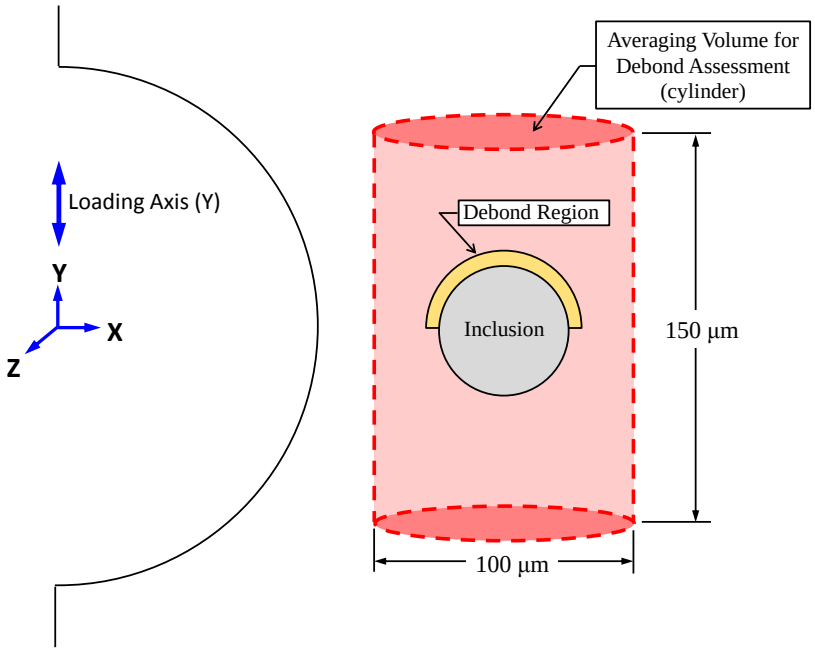

Figure 4.11: Schematic of cylindrical averaging volume used to assess debonding of inclusion/matrix interface within the notch root zone.

For the notch sizes, inclusion depths, and maximum applied strain values considered in this Chapter, the application of the debond law in Figure 4.10 results in the inclusion debonding from the matrix within the first simulated fatigue cycle, i.e., $N_{DB} = 1$ for Equation 4.16. The only exception to this was for the smallest notch root radius $\rho = 0.2$ mm and the inclusion located within the depth at $h = 100$ μm. For this exception, the estimated number of cycles to debond the inclusion from the matrix, $N_{DB} < 20$ cycles. Since this number of cycles to debond the inclusion from the matrix is very small compared to the other hierarchical regimes ($N_{DB} << \{N_{inc}, N_{MSC/PSC}$, and $N_{LEFM}\}$), the debond regime, N_{DB}, was neglected in Equation 4.16 for the notched simulations performed in this Chapter. Therefore, the FEM model for the notched components consisted of an initially debonded inclusion for estimation of fatigue life

incubation and early growth from the debonded inclusion. The number of cycles to debond the inclusion from the matrix becomes significant when initial compressive residual stresses exist (e.g., due to shot-peening) within the microstructure; inclusion debonding within a compressive residual stress field is covered further in Chapter 6.

Following debonding, crack incubation is considered in grains adjacent to the debonded region. A simplified form of the Tanaka and Mura [131] crack incubation model was extended to microplasticity by Shenoy et al. [194] to estimate the incubation life for IN100 for a crack on the order of grain size. In this study, the number of cycles to incubate a crack from the debonded inclusion region ($a = a_{DB}$) into polycrystalline matrix ($a = a_{DB} + a_{grn}$) is estimated via [194]

$$N_{inc} = \frac{\alpha_g}{d_{grn}} \left(\frac{(\Delta\gamma^p_{grn})_{max}}{2} \right)^{-2} \tag{4.17}$$

where $\alpha_g = 0.056$ μm-cycle is a parameter fit to IN718 experimental data [133] in the work of Shenoy et al. [194] and d_{grn} is the grain size of the grain where crack incubation occurs. For crack incubation, the grain-averaged maximum range of plastic shear strain, $(\Delta\gamma^p_{grn})_{max}$, is computed over the third simulated fatigue cycle. Of the grains adjacent to the debonded region, the grain with the lowest computed value of N_{inc} in Equation 4.17 is assumed to incubate the crack.

Once a grain-sized crack is incubated from the debonded region into the surrounding matrix, MSC propagation is considered. The application of the MSC propagation law is covered in Section 4.3.3 after presenting FIP_{FS} distributions within the notch root zone for different notch sizes.

4.2.3 Finite element model of an inclusion located at a surface notch

The modeling of fatigue crack formation and early growth from a single subsurface debonded inclusion within a notched component used here is an extension of previous debonded inclusion simulation work [184] and other similar mesoscale modeling approaches of crack initiation and early growth from defects performed by [54,132,188]. The use of 3D CPFEM in this work offers a benefit over previous 2D work [54,132,188] because it can account for statistical fatigue scatter due to variance in 3D size, shape,

and orientation of grains located near the debonded inclusion. The MSC growth model detailed in Chapter 3 is adopted here to account for (1) grain boundary effects on MSC growth and (2) the difference in behavior between surface versus bulk MSC growth. The next section describes the FEM model used for simulating a single inclusion within the notch root zone.

4.2.3.1 Schematic of input parameters/variables

In this study, we simulate the effect of a single Al_2O_3 spherical inclusion located within the notch root zone of a double edge-notched specimen as summarized in Figure 4.12. The total length, width, and thickness of the double edge-notched specimen is $H = 10$ mm, $W = 10$ mm, and $t = 0.34$ mm, respectively. Due to symmetry conditions, only one half of the width ($W/2$) of the double-edge notched component is constructured and symmetric displacement boundary conditions are imposed at the half width ($x = W/2$). The notch with radius ρ and inclusion with diameter ϕ are assumed to be centered along the vertical y-axis at $y = H/2$. Notch radii ranging from 0.2 mm to 1.0 mm were used to maintain consistency/comparison with previous notch simulations performed on coarse grain IN100 [76]. The spherical inclusion is centered about the z-axis at $z = t/2$ and assumed to be partially-debonded along the top hemisphere, representing the worst case scenario for crack formation from the inclusion. Inclusion depths of $h = 25$ μm, 50 μm, and 100 μm were chosen because they correspond to the simulated inclusion radius, inclusion diameter, and sub-surface/internal transition depth (ref. Fig. 4.2), respectively. To simulate the "debond material" a **UHypel* subroutine in ABAQUS [45] is used and will be further detailed later. The debond material thickness was selected based on the minimum element thickness for each FEM mesh; therefore, the debond material thickness was in the range of ~2-6 μm.

The boundary and loading conditions applied to the notched specimen are shown on Section A-A of Figure 4.12. The bottom face located at $y = 0$ and the right hand face at $x = W/2$ are constrained from displacement in the y-direction and x-direction, respectively. Four points located at (x,y,z) = {(0,0,0),(W/2,0,0),(0,H,0),(W/2,0,0)}

are constrained from displacement in the z-direction to eliminate rigid body translation/rotation. With these boundary conditions applied, the top face is subjected to strain-controlled $R_\varepsilon = 0.05$ loading with a maximum strain $\varepsilon_{max} = 0.6\varepsilon_y$, where $\varepsilon_y = 0.42\%$ is the proportional limit of the coarse grain IN100 modeled in this work.

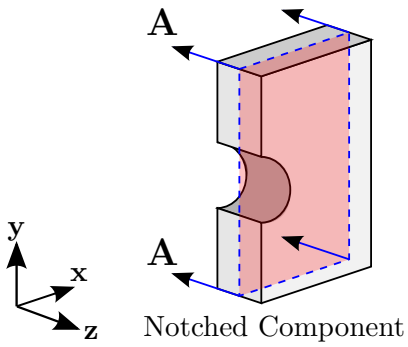

Notched Component

Variables	
Notch Radius, ρ (mm)	0.2, 0.4, 0.6, 0.8, 1.0
Inclusion Distance to Surface, h (μm)	25, 50, 100
Constants	
Inclusion Diameter, ϕ (μm)	50
Strain Amplitude ($\varepsilon_a/\varepsilon_y$)	0.6
Proportional Limit	$\varepsilon_y = 0.42\%$
Strain Rate (s^{-1})	$\dot{\varepsilon} =$ 1e-3
R-Ratio (strain-controlled)	$R_\varepsilon = 0.05$
Temperature (isothermal)	T = 650°C

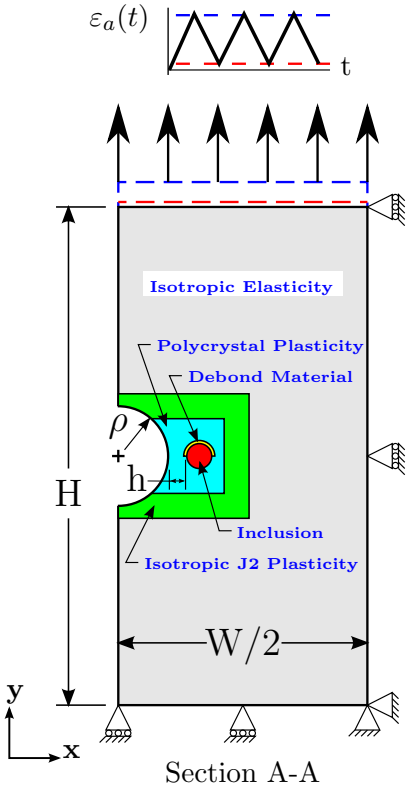

Section A-A

Figure 4.12: Schematic for simulation of an inclusion within the notch root field showing loading conditions, boundary conditions, and domain decomposition of material behavior.

4.2.3.2 Material models used for notched FEM simulations

The finite element model of a notched component is decomposed into multiple constituents each containing a different material behavior (cf. Fig. 4.12). The zone located furthest from the notch root is assigned isotropic, linear elastic properties with $E = 179$ GPa and $\nu = 0.33$. The polycrystal plasticity model outlined in Chapter 2 is assigned to the elements within the notch root zone minus the region where the spherical inclusion and debond material occupy. An isotropic J2 plasticity material behavior is used in the intermediate regime between the polycrystal plasticity zone and

the isotropic elastic outer zone to minimize the effect of different material behavior between these two zones. The dimensions of the polycrystal plasticity an J2 plasticity regions were selected so that there were no severe discontinuities in stress/strain response at the boundary of each region due to differences in material constitutive response.

The J2 plasticity model employed is an existing ABAQUS [45] material model that employs the Von Mises yield surface $F = f(\underset{\sim}{\sigma} - \underset{\sim}{\alpha}) - \sigma_{ys} = 0$, where $F = 0$ during plastic flow, $\underset{\sim}{\sigma}$ and $\underset{\sim}{\alpha}$ are the stress and back stress tensors, respectively, and σ_{ys} is the Von Mises equivalent yield strength. The function f is given by $f(\underset{\sim}{\sigma} - \underset{\sim}{\alpha}) = \sqrt{\frac{3}{2}(\underset{\sim}{S} - \underset{\sim}{\alpha}) : (\underset{\sim}{S} - \underset{\sim}{\alpha})}$ where $\underset{\sim}{S}$ is the deviatoric portion of the stress tensor. An associated flow rule is assumed and takes the form $\dot{\underset{\sim}{\varepsilon}}^p = \dot{\bar{\varepsilon}}^p \frac{\partial F}{\partial \underset{\sim}{\sigma}}$. Here, $\dot{\underset{\sim}{\varepsilon}}^p$ is the rate of plastic flow tensor and $\dot{\bar{\varepsilon}}^p = \sqrt{\frac{2}{3}\dot{\underset{\sim}{\varepsilon}}^p : \dot{\underset{\sim}{\varepsilon}}^p}$ is the equivalent plastic strain rate. Cyclic hardening of the yield stress is accounted for by the evolution of isotropic hardening [33, 195], via $\sigma_{ys} = \sigma_o + \kappa_s \left[1 - \exp\left(-b\bar{\varepsilon}^p\right)\right]$ where σ_o is the yield stress at zero plastic strain, κ_s is the maximum change in the size of the yield surface, and b defines the rate at which cyclic hardening occurs. The evolution of the back stress tensor is characterized by [45, 125] $\dot{\underset{\sim}{\alpha}}_k = \frac{c_k}{\sigma_{ys}}(\underset{\sim}{\sigma} - \underset{\sim}{\alpha})\dot{\bar{\varepsilon}}^p - r_k \underset{\sim}{\alpha}_k \dot{\bar{\varepsilon}}^p$. The first term in this equation represents purely kinematic hardening (linear Ziegler hardening law) and the second is a recall term depicting dynamic recovery. For this study, we employ $k = 2$ backstress terms ($c_1 = 280900$, $c_2 = 10178$, $r_1 = 1163.8$, $r_2 = 55.65$) to facilitate better stress-strain fitting at lower ($k = 1$) and higher ($k = 2$) strains. This computational model was matched to experimental stress-strain data of a coarse-grained IN100 Ni-base superalloy microstructure (Ref. Figure 4 in [30]).

Since the stress-strain relationship for the Al_2O_3 inclusion at elevated temperatures (650°C) is not readily available in the literature, isotropic elastic-perfectly plastic properties are assumed for the inclusion with $E = 360$GPa, $\nu = 0.24$ [196], and $\sigma_y^{inc} = 1345$MPa [197]. The importance of incorporating plastic yield for equivalent stress levels above $\sigma_y^{inc} = 1345$MPa will become apparent when considering inclusion/residual stress effects as illustrated in Chapter 6.

To model the debonded area of the spherical inclusion, the *UHypel subroutine is used in ABAQUS [45]. This *UHypel technique was preferred over using master/slave contact interations between the inclusion and matrix because it was more numerically stable for cyclic loading of notched components. The *UHypel subroutine allows for user-specified isotropic, hyper-elastic properties. This subroutine is used to model a "no tension" interface between the inclusion and matrix. In other words, in tension, the component is completely compliant, i.e., there is no stress allowed. In compression, the entire stiffness of the material is retained, which simulates the contact between the debonded inclusion and the matrix. To render the simulations more numerically stable, a functional form for the elastic modulus (isotropic elasticity) is chosen so that "no tension" is simulated via

$$E = \frac{E_{ref}}{1 + \exp(A \cdot \overline{\varepsilon})} \tag{4.18}$$

where $E_{ref} = 179\,\text{GPa}$ is the elastic modulus of the bulk matrix material. The variable A is used as a rate of smoothing constant. Larger values of A will lead to sharper cutoffs between the fully compliant material in tension and the stiffness tensor in compression. Lower values of A make the modulus, and hence the simulations, more "numerically stable." The effect of the value of A on the tension/compression assymmetry behavior of the stress strain diagram is shown in Figure 4.13. A value of $A = 1000$ was chosen for subsequent simulations.

4.2.4 Application of the *UHypel Subroutine

Multiple measurements of strain were tested for the value of $\overline{\varepsilon}$ in Equation 4.18 in the *UHypel subroutine including the maximum principal strain, the component of strain that is normal to the inclusion surface, equivalent strain, and hydrostatic strain. The selection of the particular value of strain measurement did not make much difference for the uniaxial cyclic loading conditions, because once the strain became tensile all the values of strain yielded essentially equivalent stress results. In the end, the purpose of the *UHypel subroutine was to simulate a debonded inclusion in tension and retain the stiffness matrix in compression. Therefore, for simplicity $\overline{\varepsilon} = \varepsilon_{yy}$ was used in Equation 4.18 for this study.

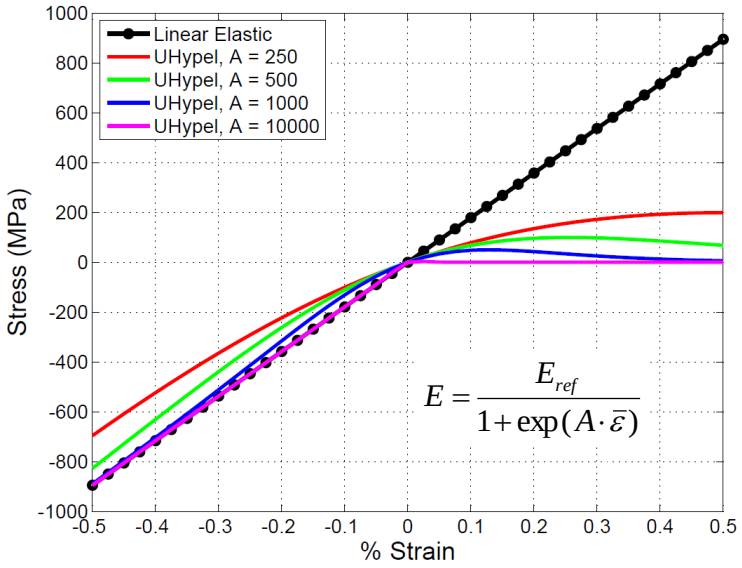

Figure 4.13: Example tension/compression asymmetric behavior of the stress strain diagram comparing different values of the amplification factor, A, within the **UHypel* subroutine in ABAQUS [45].

To test the *UHypel subroutine, a notched component with $\rho = 200$ μm was simulated as shown in Figure 4.14. This FEM model conforms to the schematic in Figure 4.12 for a notch radius of $\rho = 200$ μm and inclusion distance to the surface, $h = 25$ μm. The only exception was that R_ε = -1 loading was used to ensure that "crack closure" and retainment of the full stiffness matrix could be accounted for with the *UHypel material model.

Figure 4.14(a) shows the whole finite element mesh (3D C3D4 linear finite elements) that was subjected to strain-controlled R_ε = -1 cyclic loading for 3 cycles and a strain amplitude of $\varepsilon_a = 0.6\varepsilon_y$. Figures 4.14(b)-(e) show zoomed-in images of the notch root region that have been sectioned through the half-thickness of the specimen at $z = 0.17mm$ (similar to Section A-A in Figure 4.12). Figure 4.14(c) shows the polycrystalline grain structure, where each color represents a different grain. The bottom left Figure 4.14(d) shows the Von Mises stress at maximum tension for the third fatigue cycle and the bottom right Figure 4.14(e) shows the Von Mises stress at maximum compression. As shown in these Figures, the *UHypel material model for the debonded region heuristically mimics the debonded material response, with it being fully compliant (less than $\sim$ 100 MPa) in tension and retaining full material

stiffness in compression. Therefore, we proceed with this material model for parametric studies of notched components containing debonded inclusions at different depths.

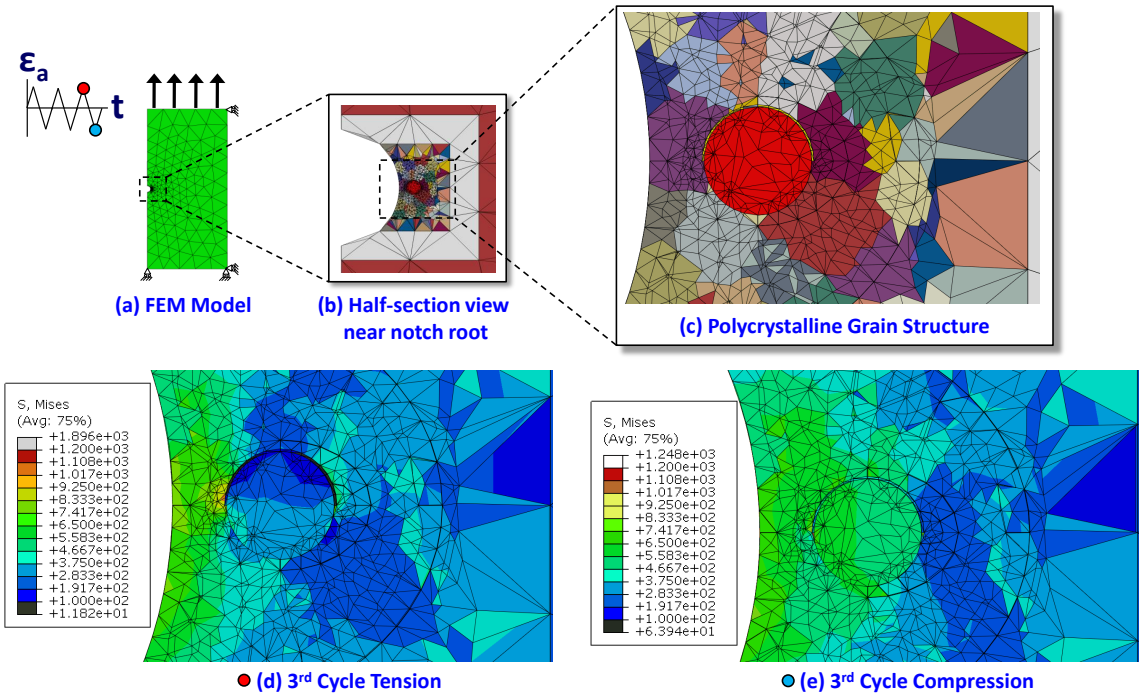

Figure 4.14: Distribution of Von Mises stresses during the 3rd cycle at maximum tension and compression loading for a notch root radius of $\rho = 200$ μm, $R_\varepsilon = -1$, and $\varepsilon_a = 0.6\varepsilon_y$.

4.2.5 Meshing technique for notched components

Three-dimensional C3D8 finite elements were used to mesh all notched components used for parametric studies. These brick elements were used over 3D tetrahedrons (linear C3D4 or quadratic C3D10) because they provided better numerical stability/convergence. The free meshing technique of tetrahedron finite elements in ABAQUS sometimes created elements with bad aspect ratios within the notch root zone. These bad aspect ratio elements caused negative eigenvalues to occur during the numerical analysis and caused the solution to diverge. Therefore, a structured brick finite element discretization was used instead. The generated mesh had a fine mesh seed size ($\sim$5 μm) near the notch root and center of the specimen thicknees in the z-direction. This mesh coarsened out with distance from the notch root to a maximum size of 0.5 mm in the elastic region. The technique used to bias the mesh seed size within the notch

root CPFEM zone is summarized in Figure 4.15. In this Figure, single arrowheads indicate single edge mesh size biasing and point to the direction in which element seed size increase. Likewise, double arrowheads indicate double edge mesh size biasing where the smallest seed size is in the center and increases in both directions. The Table in Figure 4.15 shows the local mesh seed size biasing used within the notch root zone as a function of notch root radius.

Figure 4.16 shows an example finite element mesh used for notch root radius $\rho = 600$ μm. The left hand side of this Figure shows a 2D side view of the entire FEM mesh and the right hand side of this Figure shows a 3D zoomed-in view of the FEM mesh displaying the polycrystalline grain structure; colors indicate different grains.

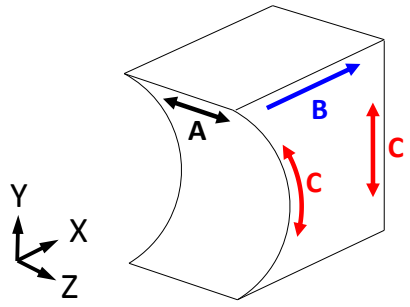

Polycrystal Plasticity Zone Mesh Seed Size Bias:

- Single arrowheads indicate direction in which element seed size increases.
- Double arrowheads have smallest seed size in center and increases in both directions.

Notch Radius, ρ	A min size	A max size	B min size	B max size	C min size	C max size
200	5	15	8	10	5	10
400	5	15	10	20	5	20
600	5	15	10	25	5	25
800	5	15	10	30	5	30
1000	5	15	20	34	5	34

*All values in table are in units of μm.

Figure 4.15: Mesh size bias imposition as a function of notch root radii. All dimensions in table are in units of μm.

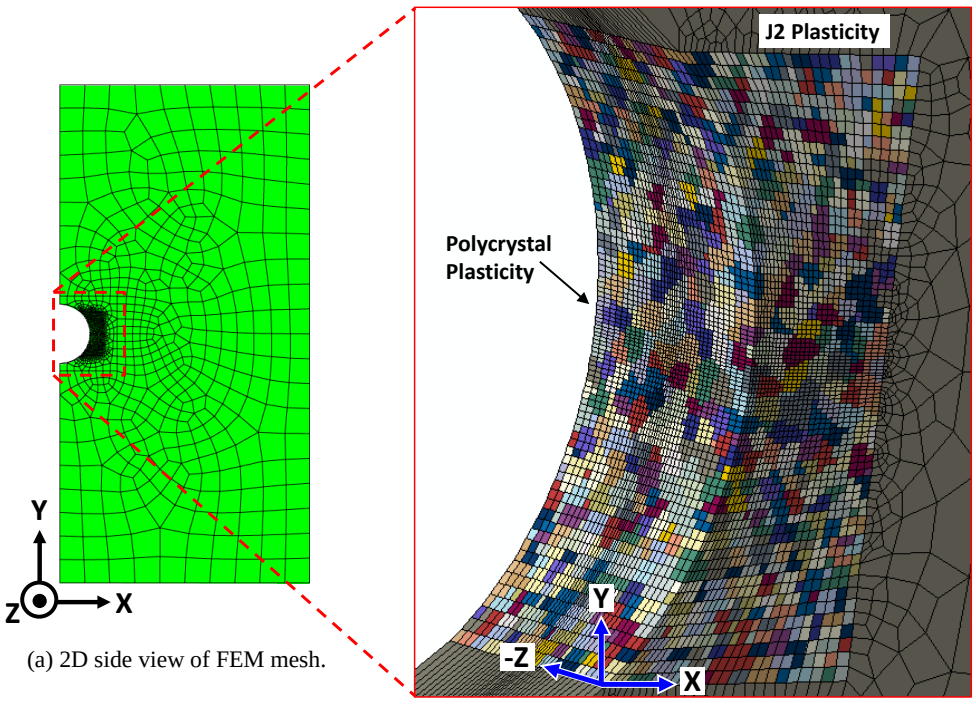

(a) 2D side view of FEM mesh.

(b) Zoomed-in 3D view of FEM mesh near notch root. Colors denote individual grains.

Figure 4.16: Schematic of finite element mesh for notch root radius, $\rho = 600$ μm. (a) 2D side view of entire finite element model and (b) 3D zoomed-in version showing grain structure.

4.2.6 Stress intensity factor (SIF) solution for MSCs growing in notch root zone

The weight function method was used to determine the stress intensity factor K for cracks emanating from the notch root zone. The weight function method provides a means to determine the stress intensity factor for any arbitrary loading via [198, 199]

$$K = \int_0^a h(x, a, a/c)\sigma_{yy}(x)dx \tag{4.19}$$

where $\sigma_{yy}(x)$ is the component of stress in the y-direction as a function of depth x. The weight function $h(x, a, a/c)$ is a function of x depth, and depends on crack dimensions. For the current case, a semi-elliptical surface crack is considered with crack surface length $2c$ and crack depth a. The weight function at the free surface (h_{0°) and the deepest point (h_{90°) can be represented by [198, 200]

$$h_{0^\circ} = \frac{2}{\sqrt{\pi x}}\left[1 + N_1\left(\frac{x}{a}\right)^{1/2} + N_2\left(\frac{x}{a}\right) + N_3\left(\frac{x}{a}\right)^{3/2}\right] \tag{4.20}$$

$$h_{90^\circ} = \frac{2}{\sqrt{2\pi(a-x)}}\left[1 + M_1\left(1-\frac{x}{a}\right)^{1/2} + M_2\left(1-\frac{x}{a}\right) + M_3\left(1-\frac{x}{a}\right)^{3/2}\right] \tag{4.21}$$

The MATLAB implementation of the stress intensity factor solution for a semi-elliptical surface crack subjected to an arbitrary stress distribution $\sigma_{yy}(x)$ from Golden and Grandt Jr. [199] was used to assess the stress intensity factor of a crack growing in a notch root region. Details regarding the derivation of the weight coefficients M_1, M_2, M_3, N_1, N_2, and N_3 in Equations 4.20 and 4.21 based on the Newman and Raju [201] K solution of a semi-elliptical surface crack subjected to an arbitrary stress distribution $\sigma_{yy}(x)$ can be found in Golden [202]. This method of estimating a SIF solution is predicated on the ability to determine an equivalent semi-elliptical surface crack shape, which is discussed next.

Because there is a potential for an irregular-shaped crack front and a closed-form K solution does not exist for irregular crack shapes, an equivalent ellipse crack front was assumed. For MSC growth growing in the notch root zone, the K solution for the projected crack area normal to the y-loading axis is assessed. Due to the stress gradient

effect of the notch, the size and depth of the crack front are both important. Two key assumptions were made to create an equivalent ellipse crack front. First, to account for the stress gradient and crack depth effect, it was assumed that the irregular-shaped crack front and the calculated equivalent ellipse crack front shared the same centroid in the x (depth) direction. Second, it was assumed the irregular-shaped crack front and the equivalent ellipse both encase the same area. The process of determining an approximate enveloped area for the irregular crack front and an equivalent ellipse follows:

1. A regular mesh grid was created.

2. To find the mesh points within the irregular crack front, the *griddata* interpolation function in MATLAB was used followed by a secondary operation to determine whether all points found from the *griddata* interpolation function were within the irregular crack front.

3. The area centroid of the mesh points within the irregular shape was determined based on results from the previous step.

4. The surface crack length $2c$ and crack depth a axes of the equivalent ellipse were found based on the equation of the centroid ($\overline{x}$) and area (A) of the semi-ellipse by:

$$a = \frac{3}{4}\pi\overline{x}, \qquad c = \frac{2A}{\pi c} \tag{4.22}$$

An example of the results of this equivalent ellipse procedure are shown for 3 arbitrary parametric curves in Figure 4.17. In each subfigure, the radius $R(\theta)$ as a function of angle θ, mesh size used, and calculated c and a ellipse axes values are listed for each arbitrary irregular curve. The resulting c and a axis values calculated from this equivalent ellipse method are used with the aforementioned weight function technique to find the estimated stress intensity factor of the irregular crack at a given number of cycles.

The equivalent ellipse technique was extrapolated to internal cracks to display a smooth transition from internal to surface crack stress intensity factors. In reality,

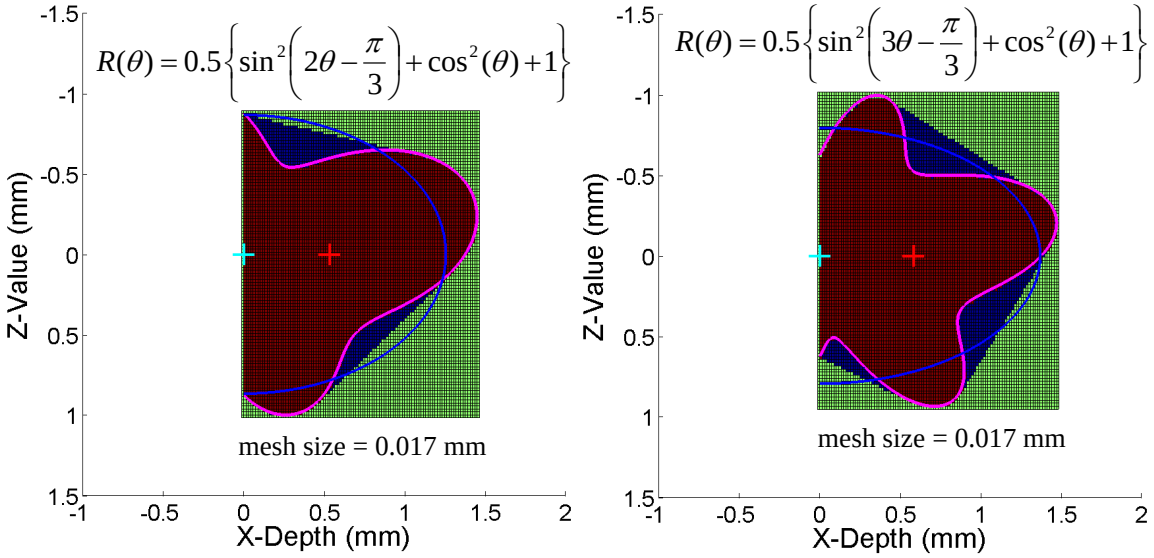

(a) Crack shape #1 (a = 0.87, c = 1.26)

(b) Crack shape #2 (a = 0.79, c = 1.37)

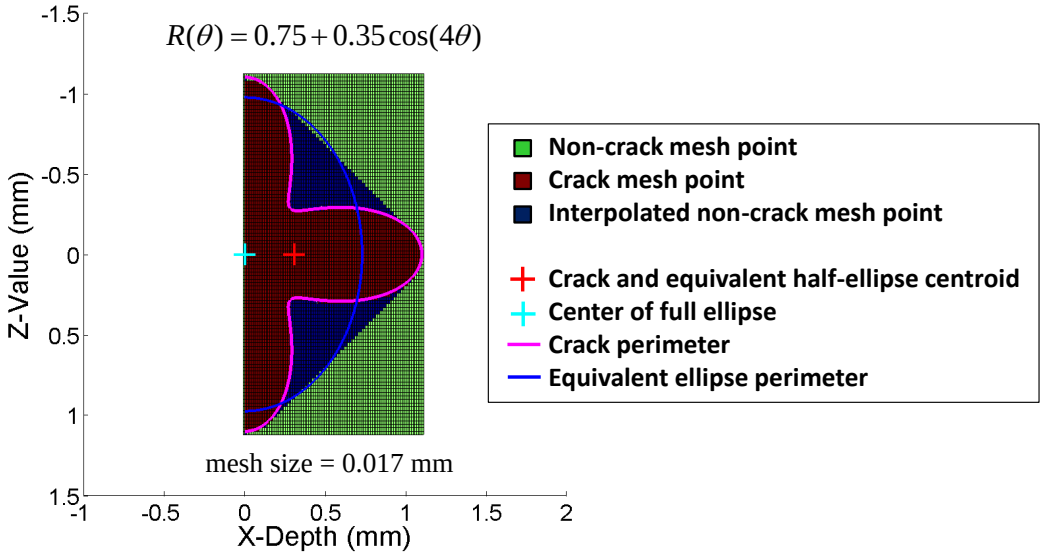

(c) Crack shape #3 (a = 0.97, c = 0.73)

Figure 4.17: Method to determine equivalent surface half-ellipse for an irregulary-shaped crack used to determine stress intensity factor, ΔK, solution.

as an internal crack approaches and breaks through the surface, there is a spike in the stress intensity factor near the surface in the remaining ligament of the material between the internal crack and the surface. However, the internal crack ΔK solution is not used to estimate fatigue life in the current study. It is merely used here to frame/communicate internal versus surface MSC growth in a traditional crack growth rate (da/dN vs. ΔK) plot and to ensure that there is a distinct transition between the two.

The gradient stress value, $\sigma_{yy}(x)$, for the calculation of SIF was determined from the FEM simulations performed in this study. Figure 4.18 shows the $\sigma_{yy}(x)$ values as a function of x-distance from the notch root at the maximum applied stress level during the third fatigue cycle. The data points in this Figure represent the average $\sigma_{yy}(x)$ values calculated within an x bin size of 0.1 mm. To ease calculation of the SIF, the decay of the stress value with x-depth was parameterized by

$$\sigma_{yy}(x) = S_{applied} + (K_{t,gross} S_{applied} - S_{applied}) \exp(-\xi_S \; x) \tag{4.23}$$

The values used for each parameter in Equation 4.23 are displayed in Table 4.1 as a function of notch root size. The resulting fit lines of the $\sigma_{yy}(x)$ function are displayed in Figure 4.18 as solid lines.

Table 4.1: Variables used in Equation 4.23 to describe gradient stress distribution $\sigma_{yy}(x)$ as a function of notch root size.

Notch radius, ρ (mm)	$S_{applied}$ (MPa)	$K_{t,gross}$	ξ_S
0.2	450	2.2	4.5
0.4	450	2.3	4.0
0.6	450	2.4	3.5
0.8	450	2.5	3.0
1.0	450	2.6	2.5

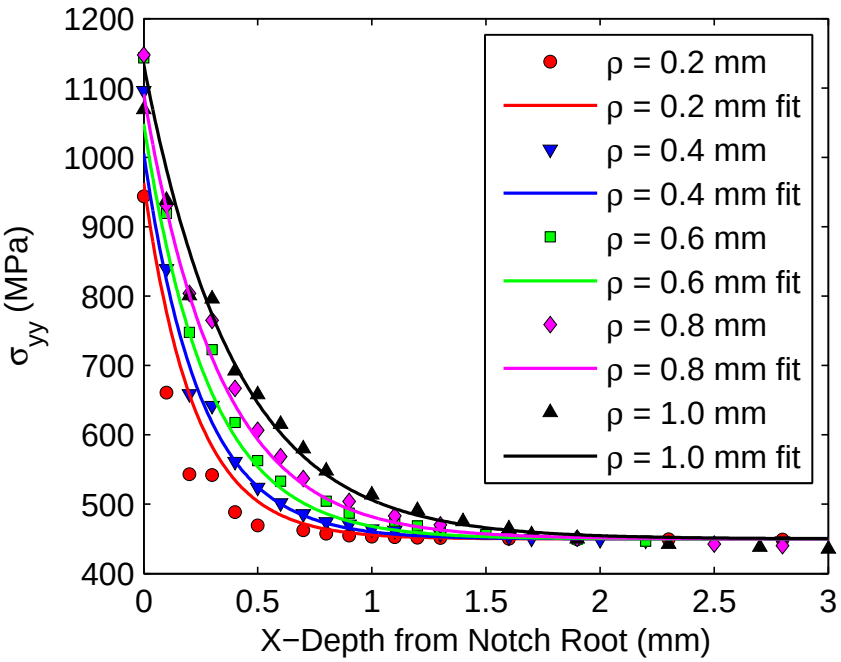

Figure 4.18: Stress distribution $\sigma_{yy}(x)$ at maximum applied stress as a function of x-depth from the notch root for different notch root radii. The fit lines are given by Equation 4.23.

4.3 Results and Discussion

4.3.1 Contours of Von Mises stress and equivalent plastic shear strain

Figure 4.19 shows example contour plot results for a notched specimen with $\rho = 600$ μm and an inclusion depth of 25 μm. All subplots in this Figure display the notched specimen sectioned halfway through the z-thickness so that the inclusion is visible. The right hand column of Figure 4.19 are zoomed-in versions near the notch root zone of the left hand column images. Figures 4.19(a) and (b) show the ensemble of polycrystalline grains (indicated by different colors) within the notch root zone. As indicated in Figure 4.19(b) the red elements represent the inclusion and the yellow elements are the debonded region elements. Figures 4.19(c) and (d) are contour plots of Von Mises equivalent stress at maximum applied strain during the third fatigue cycle. Figures 4.19(d) shows that the elements constituting the debonded region are not permitted to carry any stress (by design). Figures 4.19(e) and (f) show the equivalent plastic shear strain $\overline{\varepsilon}^p = \sqrt{2/3\boldsymbol{\varepsilon}^p : \boldsymbol{\varepsilon}^p}$ at maximum applied strain during

the third fatigue cycle. Values above $\overline{\varepsilon}^p = 1 \times 10^{-2}$ are denoted in light gray and values below $\overline{\varepsilon}^p = 1 \times 10^{-7}$ are displayed in dark gray to better view the heterogeneity in plastic strain within the notch root zone. The localization of plastic strain near the inclusion and surface of the notch are evident in Figure 4.19(f).

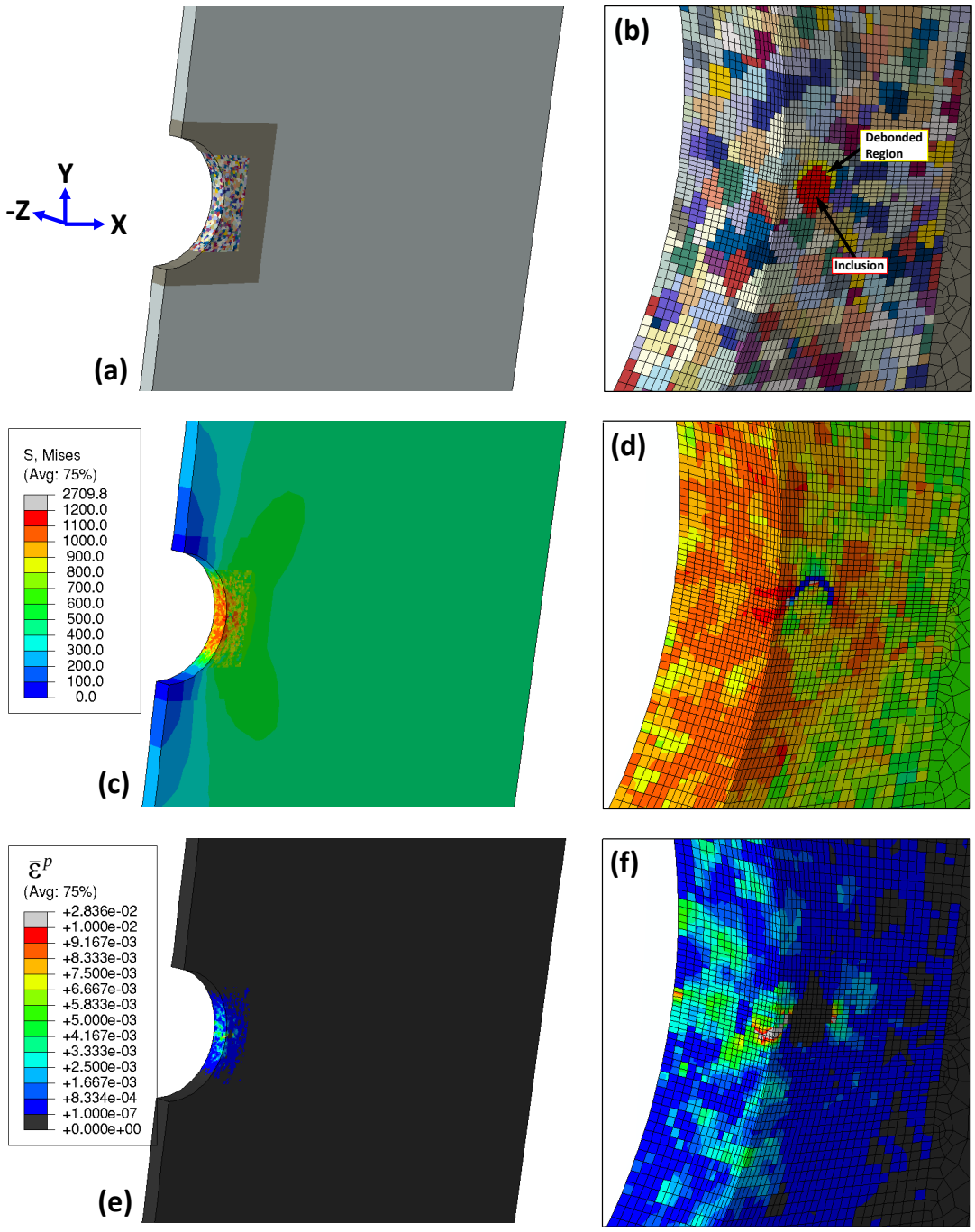

Figure 4.19: Comparison of (a)-(b) grain stucture, (c)-(d) Von Mises equivalent stress and (e)-(f) equivalent plastic shear strain values at maximum applied strain during the third fatigue cycle for a notch root radius of $\rho = 600$ μm and inclusion depth $h = 25$ μm. Right column contains zoomed in versions of left column.

The effect of inclusion depth on plastic strain localization is displayed in Figure 4.20. This Figure illustrates half-sections of the notched component of the polycrystalline grain structure (left column) and resulting equivalent plastic strain (right column) at maximum applied strain during the third fatigue cycle for inclusion depths of (a) $h = 25$ μm, (b) $h = 50$ μm, and (c) $h = 100$ μm. Note that Figure 4.20(a) and Figure 4.19(b) and (f) show results from the same instanstiation. To facilitate better comparison, the scale for each equivalent plastic strain contour plot are identical. Again values above $\overline{\varepsilon}^p = 1e-2$ are denoted in light gray and values below $\overline{\varepsilon}^p = 1e-7$ are displayed in dark gray to better view the heterogeneity in plastic strain within the notch root zone. As expected, there is an increase in equivalent plastic strain, and, subsequently, higher driving force for fatigue crack formation and early MSC propagation as the inclusion is located closer to the surface.

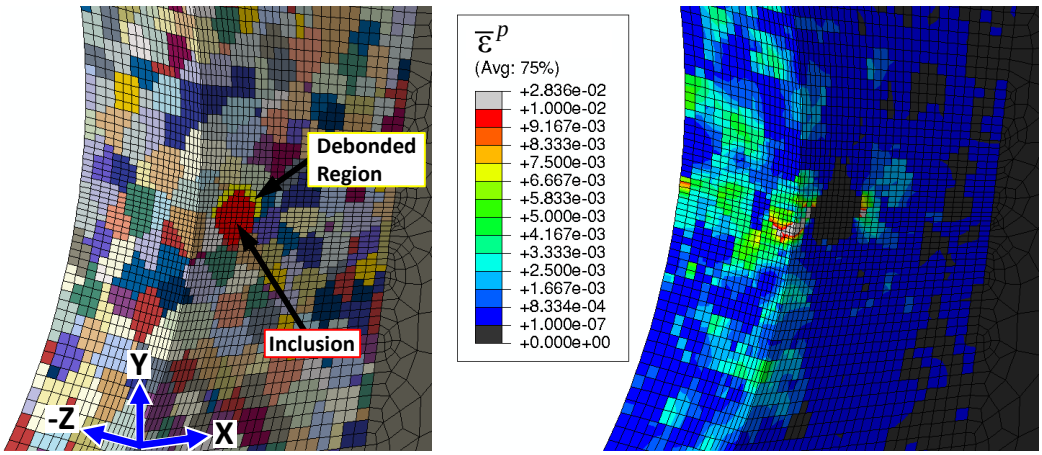

(a) Inclusion depth h = 25 µm.

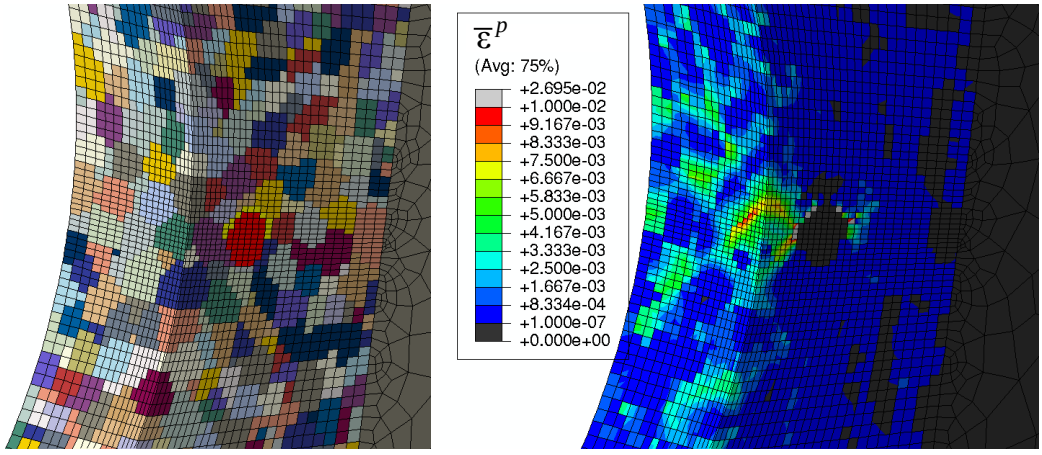

(b) Inclusion depth h = 50 µm.

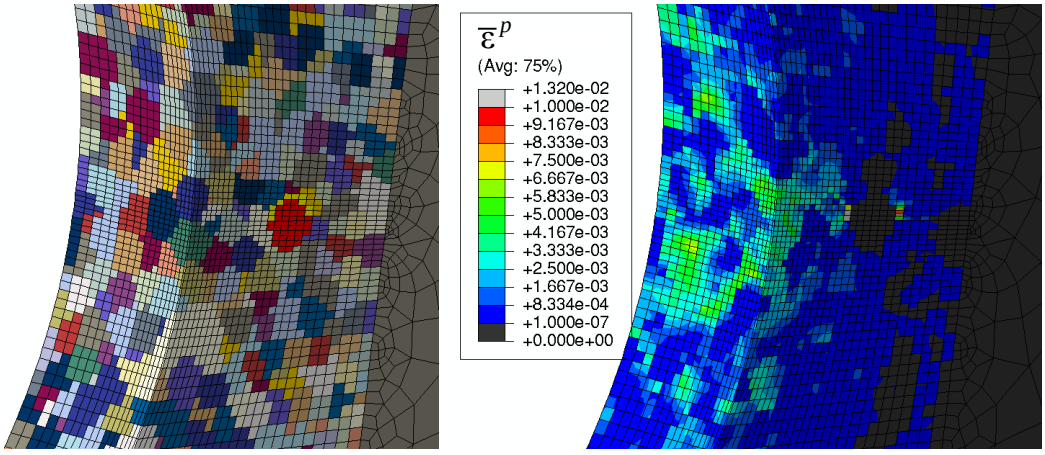

(c) Inclusion depth h = 100 µm.

Figure 4.20: Comparison of equivalent plastic shear strain values at maximum applied strain during the third fatigue cycle for a notch root radius of $\rho = 600$ μm and inclusion depths (a) $h = 25$ μm, (b) $h = 50$ μm, and (c) $h = 100$ μm. Left hand images show corresponding grain structure.

4.3.2 FIP distribution in notch root zone

The distribution of maximum non-crystallographic uncracked FIP_{FS} as a function of x-value for all notch root sizes (ρ = 0.2 mm, 0.4 mm, 0.6 mm, 0.8 mm, and 1.0 mm) and inclusion depths of (a) $h = 25$ μm, (b) $h = 50$ μm, and (c) $h = 100$ μm are shown in Figure 4.21. Each data point in Figure 4.21 indicates the maximum FIP value binned (x bin size = 17 μm) for a single instantiation. Thus, since 20 instantiations were simulated per each notch radius size and inclusion depth, each x bin value contains 20 FIP data points (one per instantiation). Since all notches are centered about $x = 0$, the notch root surface at $y = 0$ for each notch root size is located at $x = \rho$.

Comparing the maximum non-crystallographic FIP_{FS} values of all subplots in Figure 4.21, it is easy to see that the maximum FIP values increase as the inclusion gets closer to the surface. For the maximum inclusion distance simulated in this work ($h = 100$ μm), there is a slight increase in the FIP located at $x = \rho + h$ due to existence of the debonded inclusion within the notch root zone. However, the maximum FIPs at $x = \rho + h$ for most instantiations (minus the one outlier for ρ = 1.0 mm) are on the order of (or less than) the maximum FIP value at the surface $x = \rho$. Therefore, for an inclusion depth of $h = 100$ μm, the chance that another feature such as a surface grain/pore causes the failure initiation location versus the inclusion at $h = 100$ μm seem to be quite similar. This suggests that there will be competition between surface fatigue crack initiation and bulk fatigue crack initiation for inclusions located at $h = 100$ μm. For the inclusion located at $h = 50$ μm and simulated notch sizes above ρ = 0.2 mm, the interaction between the notch stress gradient, the surface, and the debonded inclusion cause the FIP to intensify near the inclusion on the order of $\sim$10-50 times the maximum FIP simulated for $h = 100$ μm. The number of instantiations with this level of FIP intensification further increases for $h = 25$ μm as indicated in Figure 4.21(a). These FIP results displayed in Figure 4.21 quantitatively display the probabilistic increase in fatigue crack driving force as the inclusion is located closer to the notch surface.

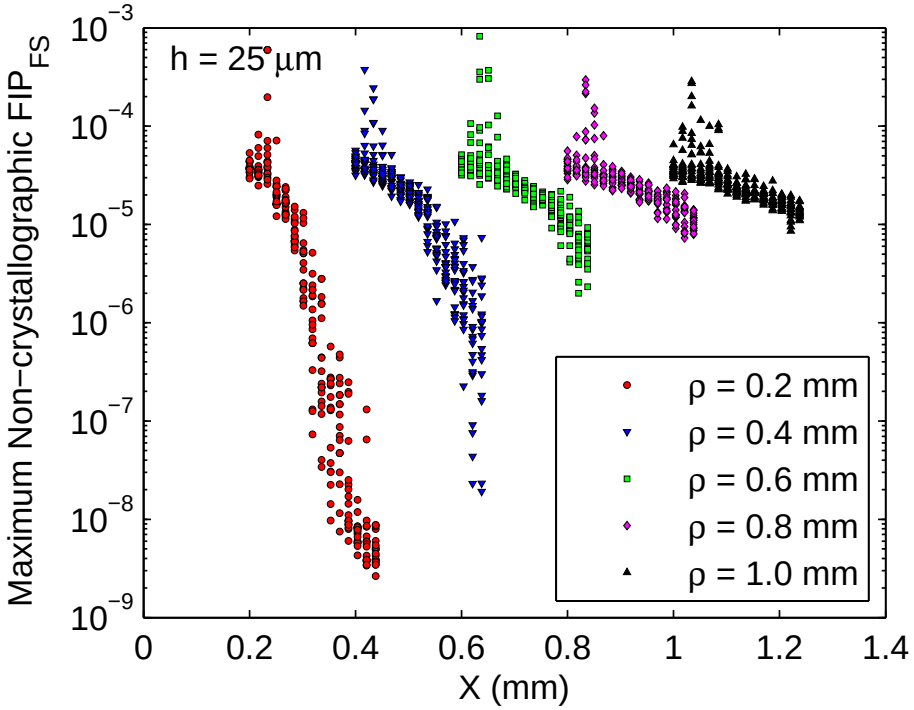

(a) h = 25 μm.

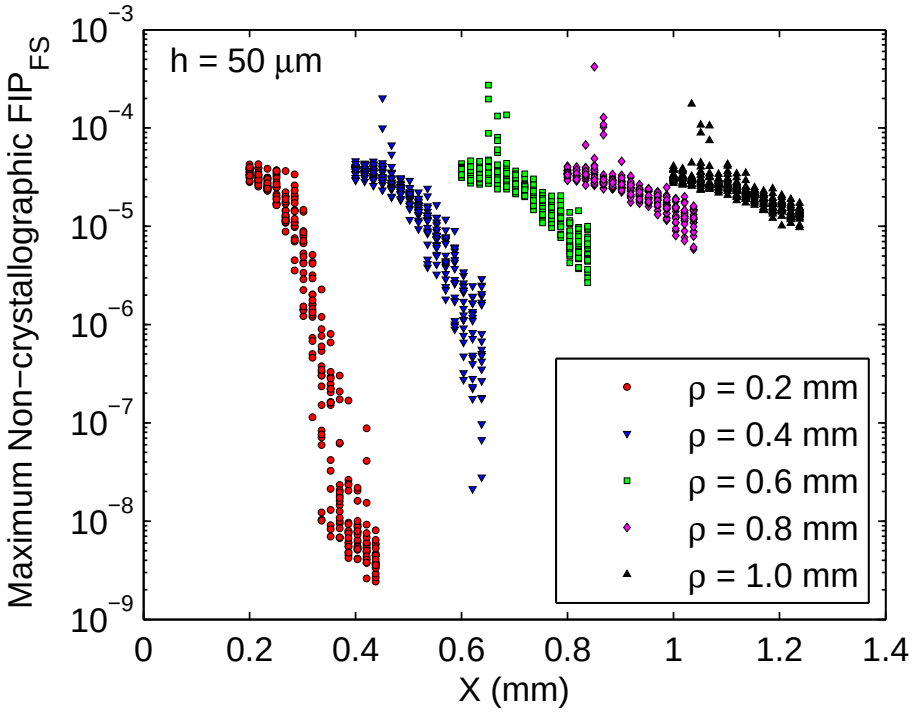

(b) h = 50 μm.

Figure 4.21: Maximum non-crystallographic uncracked FIP as a function of depth for different notch sizes and inclusion depths.

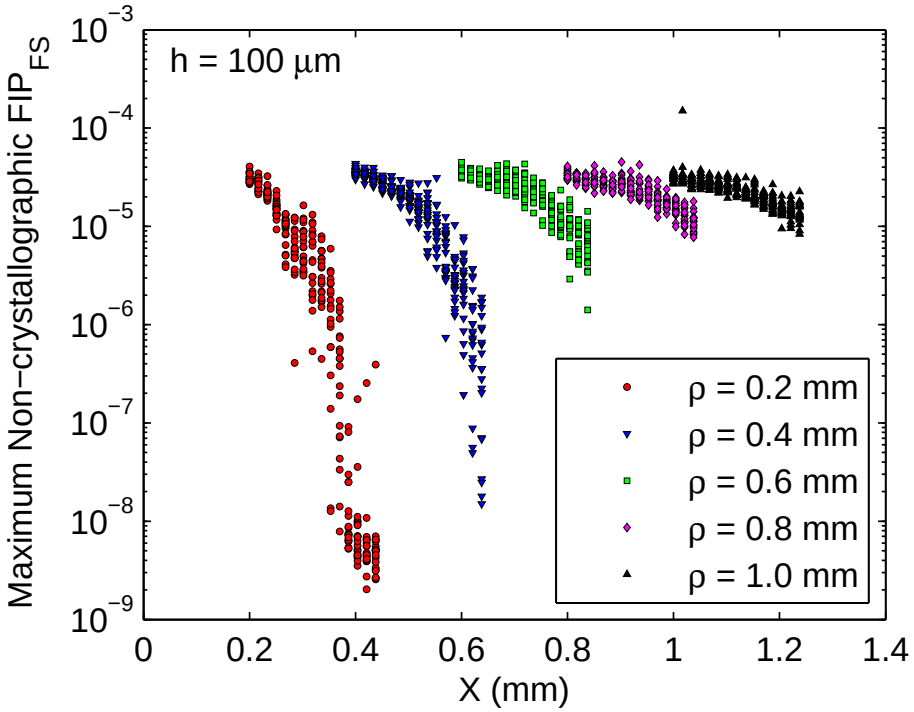

(c) h = 100 μm.

Figure 4.21: (continued) Maximum non-crystallographic uncracked FIP as a function of depth for different notch sizes and inclusion depths.

4.3.3 Estimation method for MSC growth

The technique for estimation of MSC growth developed in Chapter 3 is used here to estimate MSC growth from inclusions located at different depths from the surface of notched components. First, MSC growth was assumed to originate from the inclusion for all cases. To regularize the effect of a somewhat coarse mesh size near the inclusion ($\sim$5μm), the FIPs were nonlocally averaged over the grain scale for the prediction of MSC growth. The MSC growth model in vacuum (ref. Figure 3.31) was used while the simulated crack was not exposed to the surface; when the MSC broke through the surface, the MSC growth model was instantaneously switched to the MSC growth model fit to laboratory air MSC experiments (ref. Figure 3.30) to estimate MSC growth exposed to lab air. The driving force for MSC propagation increases as the subsurface MSC approaches the surface due to the reduction in triaxiality/constraint and increase in concentrated stress in the remaining ligament of material between the

subsurface crack and the surface. While these effects are not specifically modeled in this framework, the MSC growth Equation 3.31 is modified as the subsurface crack approaches the surface to account for the absense of a "next grain boundary" to resist MSC growth by modifying the MSC growth Equation 3.31 (repeated as Equation 4.25, below) as:

- For crack front points near the surface ($\{a_j(x) - \rho\} < 2/3 \times d_{grn}$), grain boundary resistance is negligible, i.e.,

$$\frac{da_N^*}{dN} = A_{FS}^{env}\ FIP^*(N)\ (a_N)^{n_{env}} - \Delta CTD_{th} \tag{4.24}$$

- Otherwise, Equation 3.31 (4.25) is used to account for the effect of grain boundary resistance to MSC propagation via

$$\frac{da_N^*}{dN} = A_{FS}^{env}\ FIP^*(N)\ (a_N)^{n_{env}} \left[1 - R_{GB} \cdot (1 - \overline{d}_{GB})^2\right] - \Delta CTD_{th} \tag{4.25}$$

For MSC propagation, the initial average FIP value for all grains ($\overline{FIP}_o(G_{All})$ in Equation 3.33) is assumed to be spatially dependent on the distance from the notch root. For the current case, an exponential decay function is used to describe the notch FIP gradient and is given by [76]

$$\overline{FIP}_o^{notched}(G_{all}) = FIP_{max} \cdot \exp\left[-\xi(\rho) \cdot (x - \rho)\right] \tag{4.26}$$

where $\xi(\rho)$ controls the rate of FIP decay from the notch root as a function of different radii. On a log-linear plot of FIP versus x-distance, this exponential decay function is represented by a straight line. The application of the FIP exponential decay function for all notch sizes simulated in this study and an inclusion depth of $h = 100\ \mu$m is shown in Figure 4.22. This Figure also shows the log-linear best fit lines that are used for the $\overline{FIP}_o^{notched}(G_{all})$ function in the FIP* expression (Eqn. 3.33).

An additional modification to the numerical implementation of the MSC growth algorithm from Chapter 3 (ref. Figure 3.33) was adopted. In the previous approach of modeling MSC growth from a FIB notch, a constant ΔN was used to increment crack extension for the jth increment by means of $\Delta a_j = da_j/dN \times \Delta N$. For the case of an MSC growing in a notch stress field, a variable ΔN was desired to account for

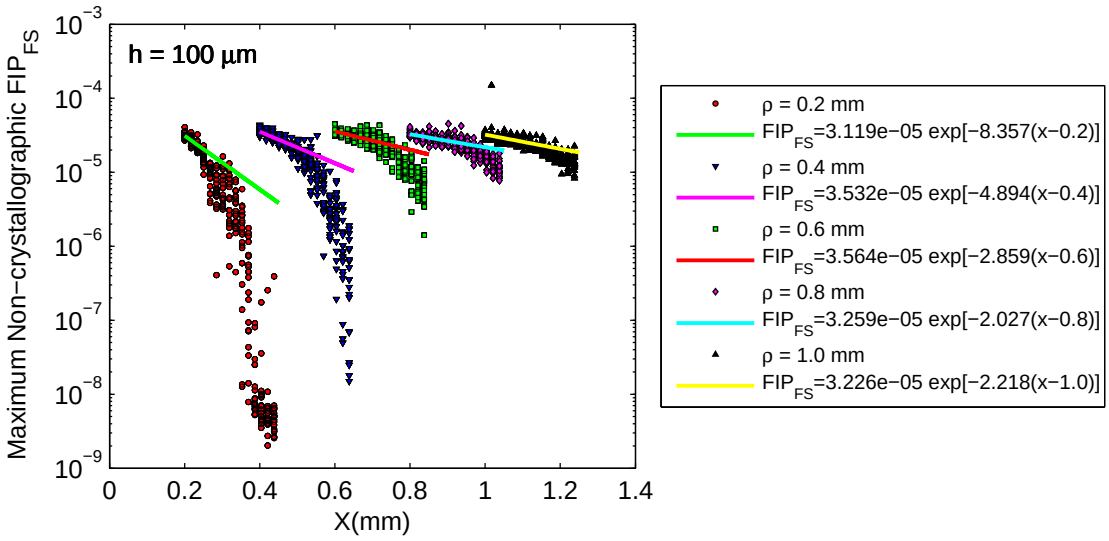

Figure 4.22: Maximum grain-averaged non-crystallographic FIP_{FS} distribution versus x-distance for 5 different notch root sizes for a maximum applied strain value of $\varepsilon_{max} = 0.6\varepsilon_y$.

the differences in MSC growth rate for subsurface versus surface cracks and the notch gradient stress field effect. Therefore, for simulated MSC propagation in notches, the increment in number of cycles for the $j+1$ increment (ΔN_{j+1}) was allowed to change based on the jth increment of crack extension Δa_j. If $\Delta a_j < 0.5$ μm the cycle increment ΔN_{j+1} was doubled and if $\Delta a_j > 5$ μm the cycle increment ΔN_{j+1} was halved. Also, to account for faster growth rate for MSCs exposed to laboratory air versus pseudo-vacuum environment, the cycle increment was reset to $\Delta N_j = 1$ when the subsurface MSC first penetrated the surface. This flexible cycle increment allowed for a more stable/precise MSC growth estimation technique.

4.3.4 MSC growth path results

The estimation of MSC growth was carried out until the simulated crack reached a projected area normal to the y-loading axis of 0.05 mm^2. This area was chosen because it coincided with the approximate projected area that all simulated MSCs reached/penetrated the surface and it ensured that the full effect of "pseudo-vaccum" MSC growth and inclusion depth could be realized for all simulations. Subsequent crack growth behavior beyond this projected area size was similar for all three inclusion depths simulated in this study. Example 3D crack path results (left column) and crack growth through the polycrystalline microstructure projected normal to the y-loading axis (right column) are shown in Figure 4.23 for notch size $\rho = 0.6$ mm and inclusion depths of (a) $h = 25$ μm, (b) $h = 50$ μm, and (c) $h = 100$ μm. In this Figure, the 50-μm inclusion is represented by the white ellipse and circle in the left and right columns, respectively. The different colors in the right hand plot indicate grain ID numbers (ref. colorbar in Figure 4.23 (a)) with lower numbers corresponding to larger grains. Superimposed on these right hand column plots are the crack front isolines at different cycle numbers. The black dotted line in the right hand column Figures indicate the crack front isoline in which the crack first penetrated the surface.

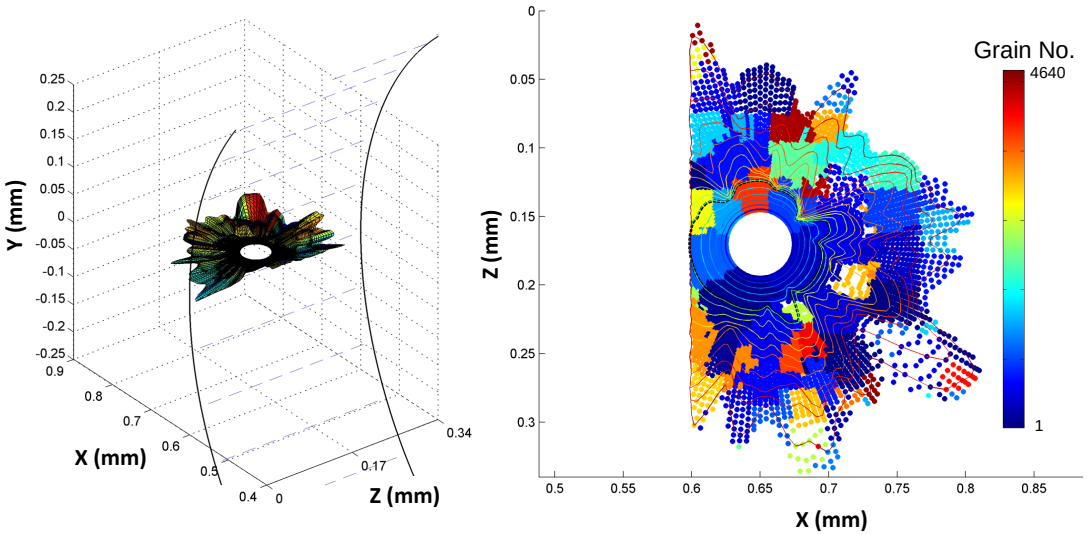

(a) h = 25 μm 3D crack path (left) and growth through polycrystalline microstructure (right).

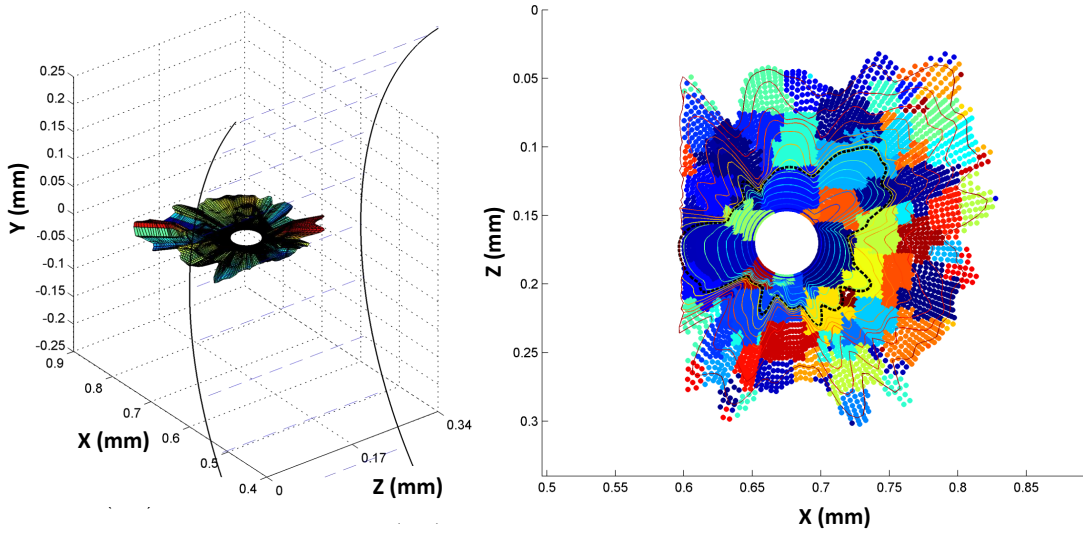

(b) h = 50 μm 3D crack path (left) and growth through polycrystalline microstructure (right).

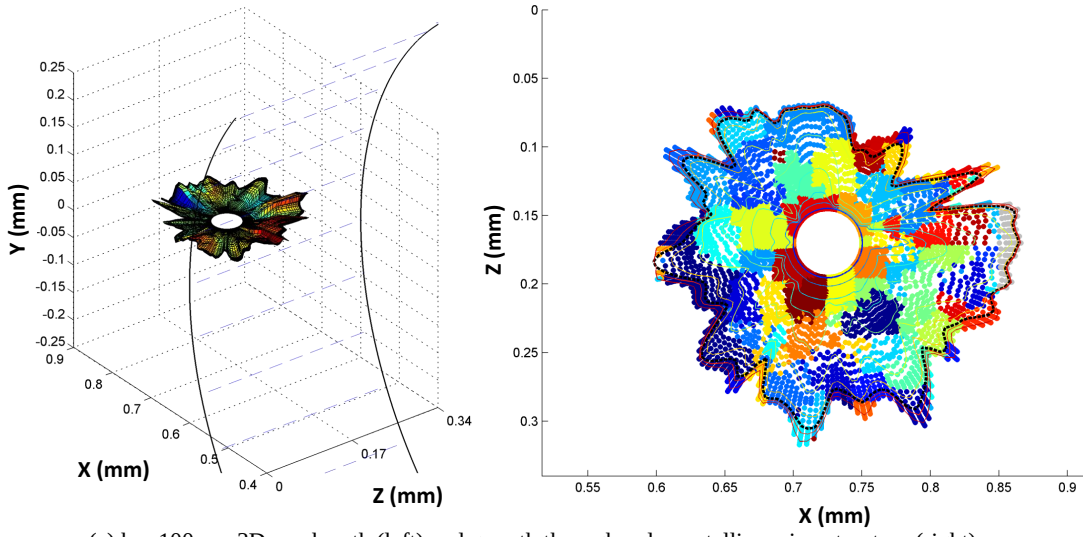

(c) h = 100 μm 3D crack path (left) and growth through polycrystalline microstructure (right).

Figure 4.23: 3D rendering of MSC growth path (left) and projected crack growth through polycrystalline microstructure (right) for $\rho = 0.6$ mm notched specimens.

4.3.5 MSC growth rate (da/dN) versus ΔK results

Figure 4.24 shows computed crack growth rate (da/dN) versus stress intensity factor (ΔK) results for a notch root size of $\rho = 0.6$ mm and inclusion depths of (a, b) $h = 25$ μm, (c, d) $h = 50$ μm, and (e, f) $h = 100$ μm. The crack growth rate versus range of SIF data are only shown for one notch root size to avoid redundancy as the MSC growth results/conclusions for the other four notch root sizes simulated showed similar trends. In Figure 4.24, the left column contains crack growth rate and SIF data based on the square root of the projected area method of computation whereas the right column contains crack growth rate versus SIF data based on the surface crack method of computation. For definitions of surface versus projected area methods, refer to Section 3.7.5. Each plot in Figure 4.24 shows the results for all $N = 20$ instantiations simulated per inclusion depth. Each data point indicates the average da/dN versus ΔK value of the whole crack front at a given numerical increment of crack extension. For comparison, the aforementioned mean MSC growth rate lines in vacuum and laboratory air and the mean LEFM data lines (cf. Section 3.7.2) are also plotted in Figure 4.24.

The abrupt jump in the crack growth rate in the projected area data signifies the initially internal crack breaking through the surface and the subsequent simulated increase in growth rate due to exposure to air. One important thing to note about the SIFs in the left column projected area data is they do not start at the same initial ΔK values for each inclusion depth. This is due to the stress gradient effect; the internal cracks at inclusions located closer to the surface notch experience a higher stress field, and, hence, a higher initial SIF than the internal cracks starting further into the bulk of the material.

As was the case for the MSC growth from FIB notch studies in Chapter 3, the projected area method MSC growth rate data contains less scatter than the surface method data. In addition, it appears that the scatter in MSC growth rate decreases with increasing inclusion depth for the projected area method of MSC growth estimation. For the current study, a crack further into the depth of the notched

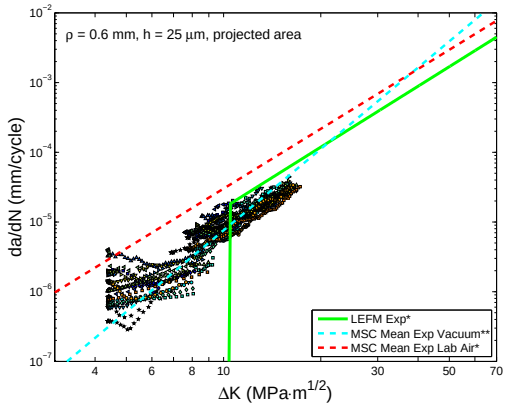

(a) h = 25 μm, projected area method.

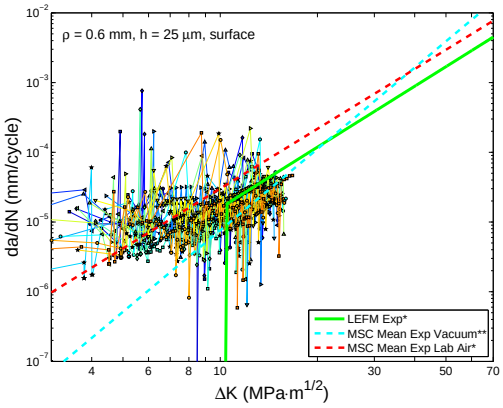

(b) h = 25 μm, surface method.

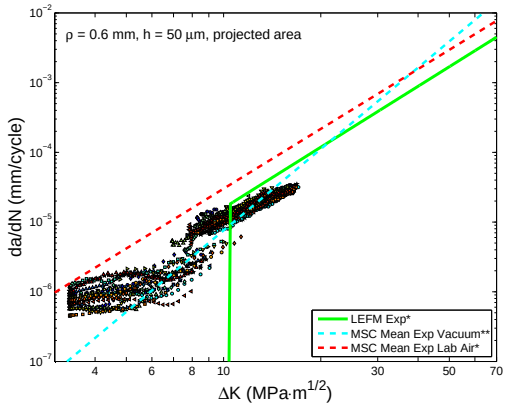

(c) h = 50 μm, projected area method.

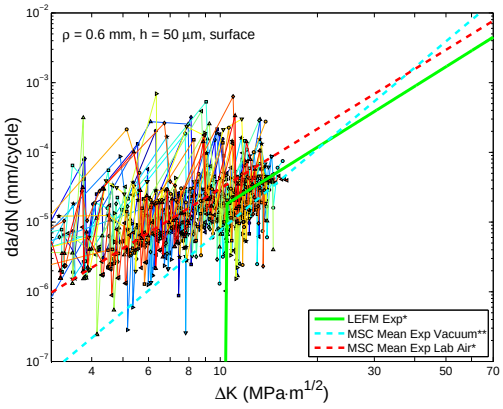

(d) h = 50 μm, surface method.

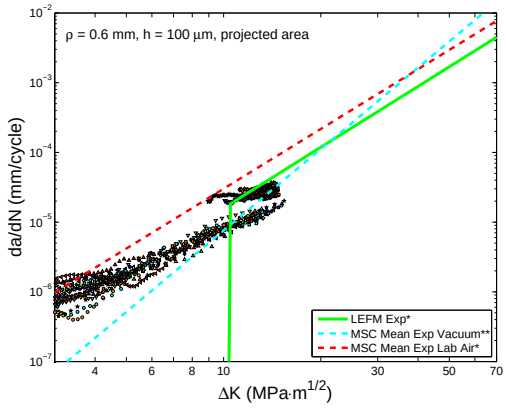

(e) h = 100 μm, projected area method.

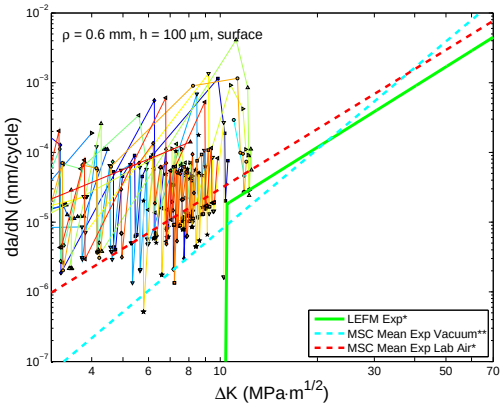

(f) h = 100 μm, surface method.

Figure 4.24: MSC crack growth rate versus stress intensity factor for all $\rho = 0.6$ mm notched specimen instantiations. *MSC mean and LEFM lines were fit to experimental data [137, 138] depicted in Figure 3.26. **MSC mean data line in vacuum was fit to LEFM vacuum data [136] as depicted in Figure 3.28.

specimen needs to be larger than one located at the surface to have the same ΔK value due to the notch stress gradient effect. Therefore, at a given equivalent ΔK, cracks originating further into the bulk of the notched specimen material are larger and statistically sample more grains than cracks starting closer to the notch surface. In the FIB notch studies in Chapter 3, it was found that MSC growth rate scatter decreases among multiple instantiations with crack size due to the crack front sampling more grains. This sampling of more grains effect could explain the reduced scatter in growth rate of cracks emanating from inclusions deeper into the bulk of the material.

The surface MSC growth data in the right column of Figure 4.24 displays more scatter than the MSC growth regime of the projected area method of estimation. The surface MSC growth rate for the inclusion located furthest from the surface, $h = 100$ μm, displays the highest scatter in MSC growth rate and a faster average surface MSC growth rate than the other two inclusion depths, $h = 25$ μm and $h = 50$ μm. There are two reasons for this behavior. First, once the crack penetrates the surface, the surface crack experiences a higher driving force to "catch up" to the internal crack dimension (in the z-direction in Figure 4.23) than the other two cases where inclusions are located closer to the surface; this is due to the internal crack having a larger projected area when the crack first penetrates the surface as compared to the less deep inclusion crack fronts.

The second reason for large spikes in crack growth behavior for the $h = 100$ μm inclusion depth case is due to the waviness of the simulated crack front. For example, in Figure 4.23(c) the crack front initially penetrates the surface at $x = 0.6$ mm and $z = 0.18$ mm and starts to grow outward in the z direction from this surface penetration location. Later, the crack front penetrates the surface in a second location at $x = 0.6$ mm and $z = 0.1$ mm and causes the overall surface length to jump from a length of $2c \sim 0.05$ mm to $2c \sim 0.1$ mm in one increment of crack extension, resulting in a spike in the surface MSC growth rate over that particular increment. Therefore, there is a transient period in which the internal crack initially breaks through the surface and transitions into behaving more like a surface crack. Obviously, this "internal to surface" MSC growth transient period starts earlier in the MSC growth regime as the

inclusion is located closer to the surface.

In general, the projected area and surface da/dN versus ΔK MSC growth results seem to approach the LEFM growth behavior, especially for the inclusion depth of $h = 25$ μm. The transition from internal to surface MSC growth seems to occur in the range of ΔK $\approx$ 8-10 MPa$\sqrt{m}$ for the inclusion depths of $h = 25$ μm and $h = 50$ μm; the transition from internal to surface MSC growth was not reached for the $h = 100$ μm simulated MSC growth depicted in Figure 4.23(c) and Figure 4.24(f). Regardless, once the transient internal to surface MSC growth behavior is reached, the mean MSC growth behavior appears to correlate well with LEFM crack growth rate data.

4.3.6 Probabilistic distribution of fatigue life

The experimental fatigue life data used for comparison to the notched component simulations is from the Master's Thesis work of Ward [138]. In his studies, Ward analyzed notched components made from a supersolvus coarse-grained IN100 microstructure with an average grain size on the order of $\sim$30 μm [138]. These notched components had a gage section of 27 mm in length and two symmetric, 2-mm-circular notches on opposite sides. The gross section width and thickness for these specimens were 9.14 mm by 6.28 mm and the net section width and thickness were 7.14 mm by 6.28 mm. These notched specimens were subjected to load-controlled, constant-amplitude fatigue loading at $T = 650°$, $R_\sigma = 0.05$, and $f = 0.33$ Hz. Two maximum applied stresses were used corresponding to a net section average stress of 800 MPa and 900 MPa, or a gross section average stress of 625 MPa and 703 MPa, respectively.

The estimated fatigue lives for all notch root radii sizes and inclusion depths are shown in Figure 4.25. The fatigue lives for each instantiation are computed as a superposition of incubation life N_{inc} given by Equation 4.17 and the number of cycles to propagate the MSC to a projected area of 0.05 mm^2. Again, this projected area was used because it coincided with the approximate projected area that all simulated MSCs reached/penetrated the surface and it ensured that the full effect of "pseudo-vacuum" MSC growth and inclusion depth could be realized for all simulations. Figure 4.25 displays the notch root radius size minus inclusion depth ($\rho - h$) versus number of

cycles for all instantiations simulated in this study. The fatigue life data was plotted in this manner so that all fatigue life data could be shown on the same plot with minimal overlap of data. In Figure 4.25, the upward pointing arrows, circles, and downward pointing arrows correspond to $h = 25$ μm, $h = 50$ μm, and $h = 100$ μm inclusion depths, respectively. The yellow filled data points indicate mean fatigue life behavior of 20 instantiations simulated for each notch size and inclusion depth combination.

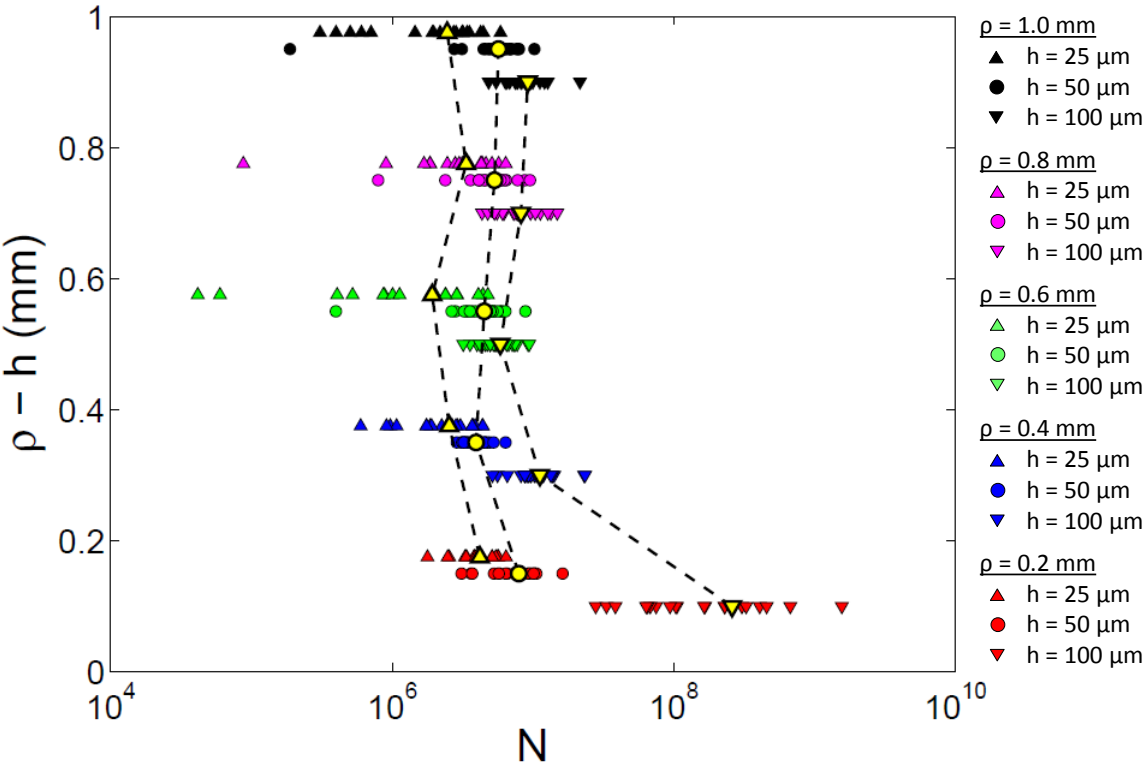

Figure 4.25: Notch size and inclusion depth versus life for 5 different notch radius sizes. The yellow filled data points indicate mean fatigue life behavior.

Several interesting aspects of Figure 4.25 should be further discussed. First, as expected, for a given notch root size, inclusions located closer to the surface are statistically more detrimental and result in a shorter estimated fatigue lifetime than inclusions located further into the bulk. As the notch size increases from $\rho = 0.2$ mm to $\rho = 0.6$ mm, the computed fatigue life generally decreases in accordance with the expected increase in stress concentration within the notch root zone. However, this

trend is not apparent for notch sizes $\rho = 0.6$ mm, 0.8 mm, and 1.0 mm. Based on the 20 instantiations simulated per notch root size, the minimum predicted fatigue life of the 0.6 mm notch with inclusion located at a depth of $h = 25$ μm was shorter than the minimum lives of the 0.8 mm and 1.0 mm notches with inclusion located at a depth of $h = 25$ μm. For the $h = 50$ μm inclusion depth case, the 1.0 mm notch size had the lowest predicted fatigue life followed in order by the 0.6 mm and 0.8 mm notch.

In previous work by Jha et al. [18, 157, 180], a description of a difference between mean and life-limiting fatigue behavior was described based on failure initiation feature (pore, NMI, large grain) and location of failure (surface versus subsurface). In this work, it was found that a limited number of simulated instantiations could be life-limiting even if the failure location (in this case depth of inclusion) was controlled. The only difference among realizations was the random assortment of grains (size, shape, and orientation) surrounding the inclusion within the notch root CPFEM zone. There are certain random assortments of grains that seem to cause fatigue life-limiting outliers that are an order of magnitude shorter than the rest of the population for a given notch size and inclusion depth. These outliers occur at a very low probability of occurrence (1 or 2 out of 20 total instantiations). Since these outliers occurred at such a small probability of occurrence, the simulation of more random instantantiations could be done to fully characterize the features and/or microstructural arrangements that contribute to this life-limiting failure phenomenon. These extreme value tails of the failure distribution are the most important data points for minimum life prediction.

The failure distributions shown in Figure 4.25 are replotted on a Weibull probability plot in Figures 4.26 through 4.28 for inclusion depths of $h = 25$ μm, $h = 50$ μm, and $h = 100$ μm, respectively, to compare the distribution of computed fatigue lives to notched fatigue experiments [138]. The probability plots were plotted using the statistics toolbox in MATLAB [144]. Also plotted in these Figures are the experimental notch fatigue data from Ward [138], as previously described in this section. While the experimental and computational data points are not directly comparable due to differences in notch dimensions and maximum applied stress, qualitative comparisons can be made.

Figure 4.29 shows the Weibull probabilty plot incorporating estimated fatigue life data for all inclusion depths (h = 25 μm, h = 50 μm, and h = 100 μm) together. Note that plotting all of the inclusion data points together on the same probability plot assumes an equal probability of occurrence of each failure location. In reality, the probability of occurence of each failure mode should be unequal. Additionally, for more accurate probabilty of failure analyses, one would also have to consider pores located near the surface as pores are also a frequent location where fatigue cracks can form in Ni-base superalloys [18, 137, 138, 157, 180]. However, pores were not accounted for in this current study.

Figure 4.30 compares the MSC propagation life ($N_{prop,MSC}$) for all notch root radii and inclusion depth simulations to the total life (N_T) data from Figure 4.29. Figure 4.30 shows that the MSC propagation life is only a small portion of the total life in the total lifetime regime of N $\sim 10^5$ to 10^9 fatigue cycles. In this HCF to VHCF regime, total fatigue life is dominated by crack formation rather than crack propagation [5, 181, 182]. The ratio of crack incubation to overall fatigue life estimation is presented for all notch root sizes and inclusion depths together on one plot in Figure 4.31. This Figure indicates that the majority of fatigue life ($(N_{inc}/N_T \times 100\%) > 95\%$) is spent incubating the crack from the debonded inclusion into the matrix for nearly all (>95%) of the instantiations simulated in the current study.

Additionally, for the current study, only MSC propagation originating from the perimeter of the inclusion was considered. For the cases of h = 100 μm, the maximum non-crystallographic FIP at the inclusion depth was on the order of the maximum FIP value from the surface. Therefore, there are potential cases where the crack initiation could occur at the surface regardless of the inclusion at a depth of h = 100 μm and cause the fatigue crack growth life to be shorter than that currently predicted for MSC growth from the inclusion at h = 100 μm. Therefore, proper fatigue life prediction should also consider the potential for surface crack formation when inclusions are above a given distance ($h \approx 100$ μm) from the surface. Regardless of these limitations, qualitative comparison between the distribution of computationally-predicted fatigue lives and experiments indicate that the current framework is promising.

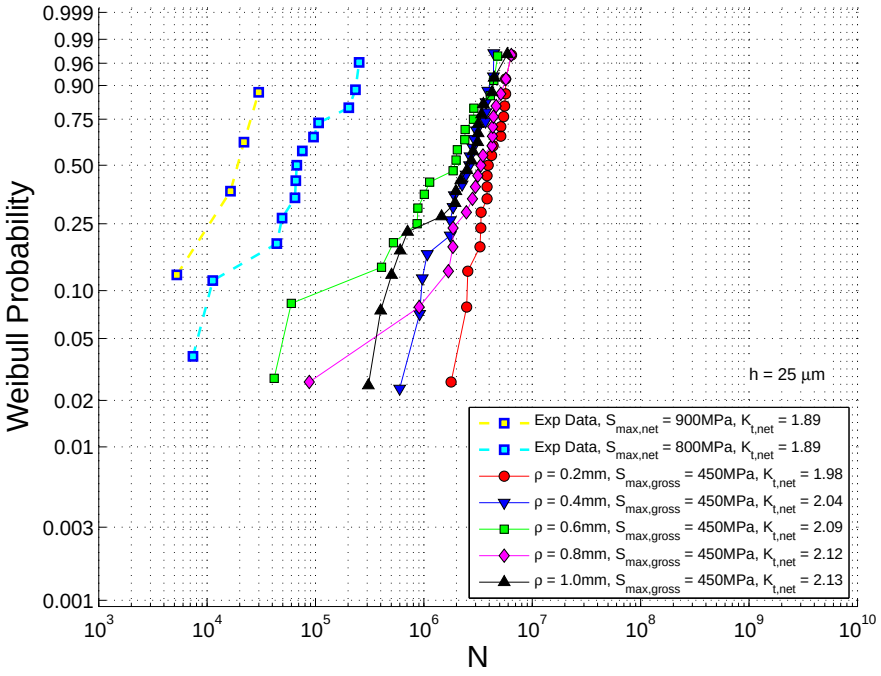

Figure 4.26: Comparison of experimental and computational Weibull distribution of failure lives for 5 different notch radius sizes and an inclusion depth, $h = 25$ μm.

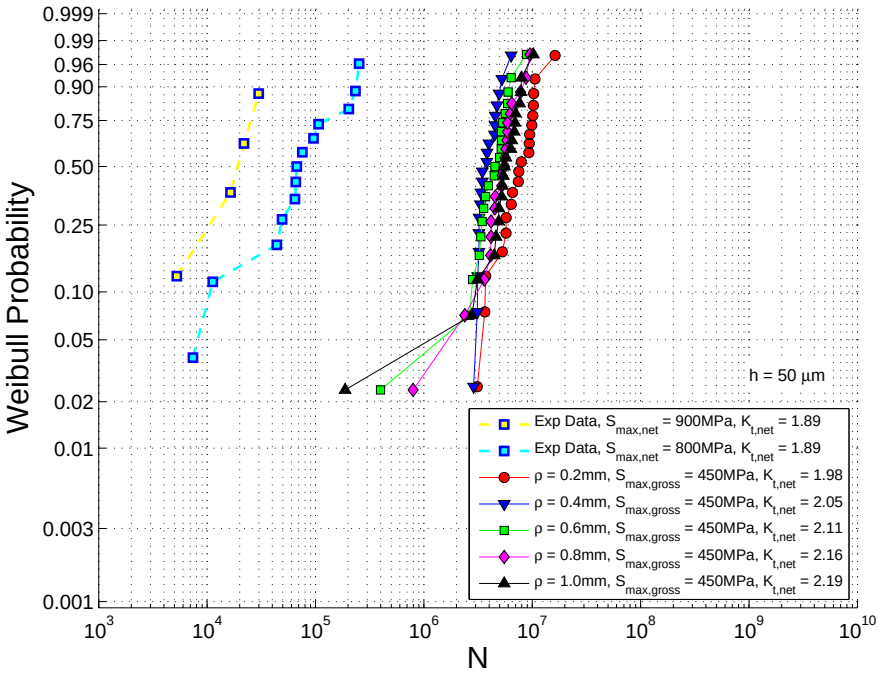

Figure 4.27: Comparison of experimental and computational Weibull distribution of failure lives for 5 different notch radius sizes and an inclusion depth, $h = 50$ μm.

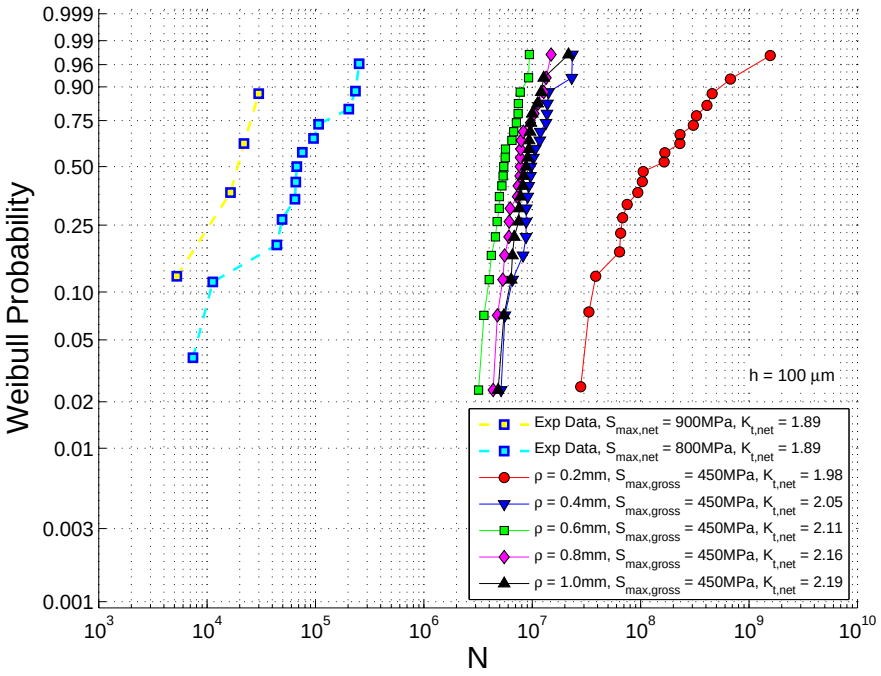

Figure 4.28: Comparison of experimental and computational Weibull distribution of failure lives for 5 different notch radius sizes and an inclusion depth, $h = 100$ μm.

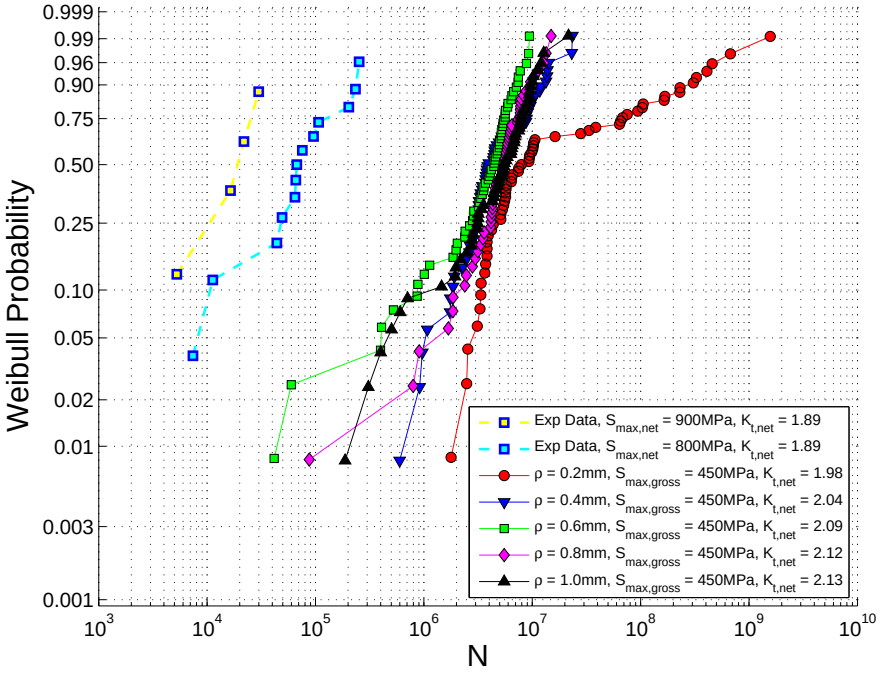

Figure 4.29: Comparison of experimental and computational Weibull distribution of failure lives for 5 different notch radius sizes with all inclusion depths, $h = 25$ μm, 50 μm, 100 μm plotted together.

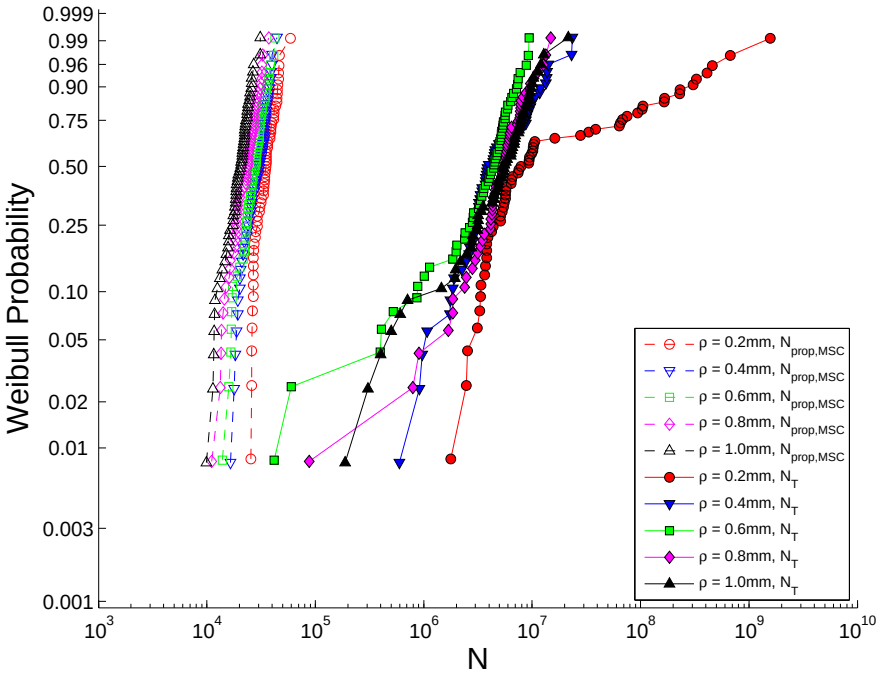

Figure 4.30: Comparison of MSC propagation life (N_{MSC}) and total life (N_T) for 5 different notch radius sizes and all inclusion depths, h = 25 μm, 50 μm, 100 μm plotted together.

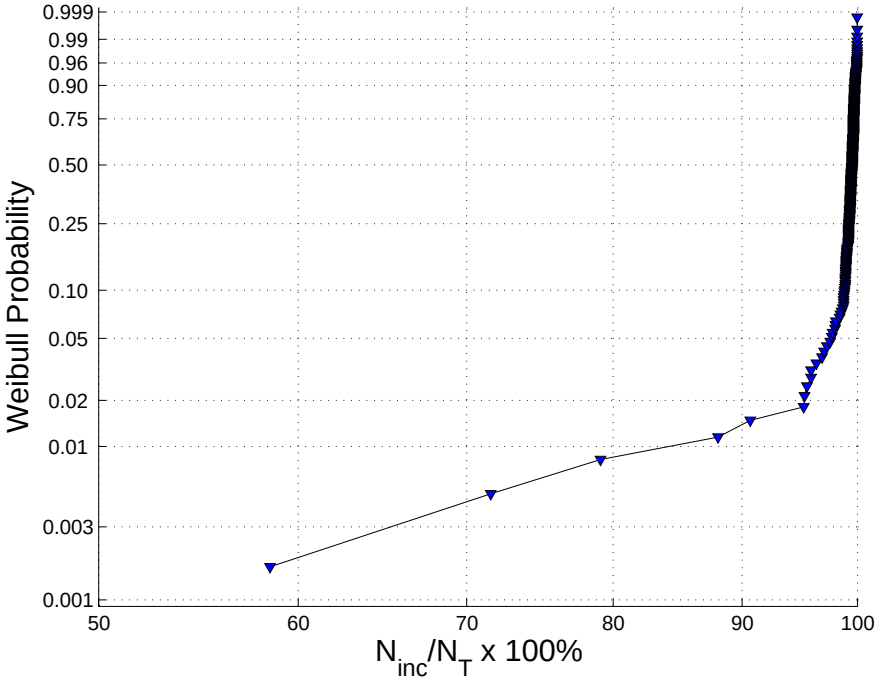

Figure 4.31: Percent contribution of crack incubation to overall fatigue life estimation for all notch root sizes and inclusion depths plotted together.

4.4 Conclusions

In this Chapter, the effect of inclusion depth on fatigue life was investigated for double edge notched components with notch root radii ranging from 0.2 mm to 1.0 mm. The inclusions were initially assumed to be debonded due to the magnitude of the local stresses within in the notch root zone. A *UHypel subroutine in ABAQUS was used to provide a numerically stable means to simulate the inclusion/matrix interfacial debonding material behavior. This *UHypel subroutine material behavior was fully compliant in tension and retained the full stiffness of the matrix material in compression. The predicted MSC growth rate da/dN versus ΔK curves correlated well with previous surface MSC growth experiments in laboratory air [137, 138]. A hierarchical multistage fatigue life estimate technique was used to predict the overall fatigue lives of the notched components as a function of notch size and inclusion depth. It was found that inclusions located closer to the surface were statistically more detrimental than inclusions further into the bulk of the material. The expected trend of decreasing life with larger notch root size was not completely reproduced in this work. This was most likely due to the random nature of microstructure and the ability to determine the life-limiting microstructural aggregate fatigue life with only 20 instantiations. It was argued that more simulations should be performed to see if the predicted trend is sustainable under larger simulation population sizes. However, preliminary results indicate that these simulations could be used as a tool to determine the relative effect of surface versus bulk fatigue crack formation and early growth on overall probability of failure; the predicted computational and experimental fatigue lives showed similar distributions on a Weibull probability plot.

CHAPTER 5
MODELING RESIDUAL STRESS EFFECTS DUE TO SHOT-PEENING

5.1 Introduction

5.1.1 Motivation for use and study of residual stresses

The beneficial effects of compressive surface residual stresses have been well documented in the literature [203–206]. To understand the usefulness of surface residual stresses as applied to Ni-base superalloys, we must discuss the shift from surface to subsurface fatigue crack initiation for the transition from LCF to HCF regimes. Pictured in Figure 5.1 are LCF to HCF transition fatigue stress-life data for notched DA 718 Ni-base superalloy specimens [177] and fine-grained IN100 Ni-base superalloy smooth specimens [157] without initial surface residual stresses. These two figures were recreated from their respective sources to display the origin/mechanism of failure for each data point. The stress amplitude value for each data point in Figure 5.1(a) was not recorded in [177]. However, qualitative experimental trends can be deduced from this data without knowing the exact stress amplitude values for the notched specimen experiments. In each Figure, the open symbols indicate surface crack formation whereas the color-filled symbols indicate subsurface fatigue crack initiation. Three distinct fatigue crack initiation regimes are observed from these data:

- **Surface-dominated crack initiation** ($N < 10^4$ cycles): Higher stress amplitudes induce crack formation predominantly at the surface.
- **Transition regime** ($10^4 < N < 5 \times 10^5$ cycles): Intermediate/transition fatigue stress amplitudes induce both surface and subsurface crack formation sites, which leads to a significant amount of scatter in the stress-life data.
- **Subsurface-dominated crack initiation** ($N > 5 \times 10^5$ cycles): Lower stress amplitudes induce crack formation mostly at large subsurface grains or internal nonmetallic inclusions.

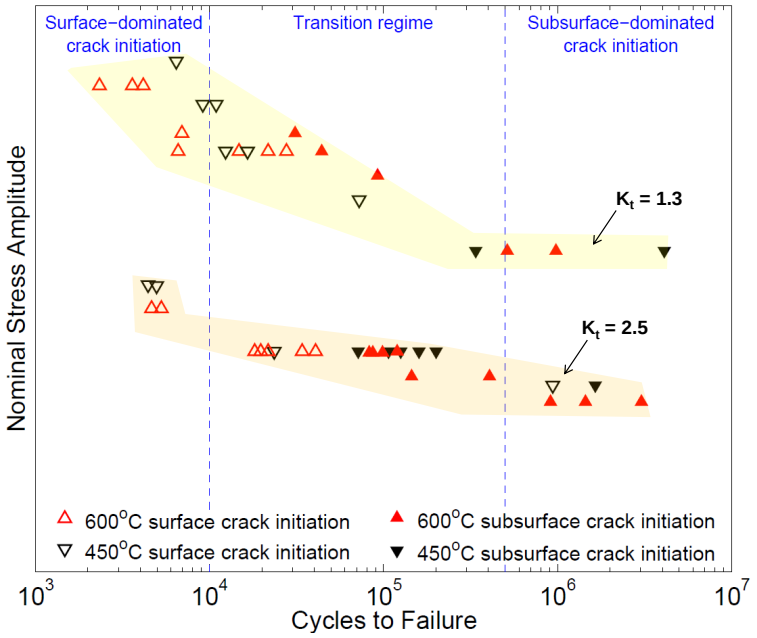

(a) Notched Specimen DA718 Ni-base superalloy. Recreated from data in [177]. (1Hz, average grain size 5-10μm).

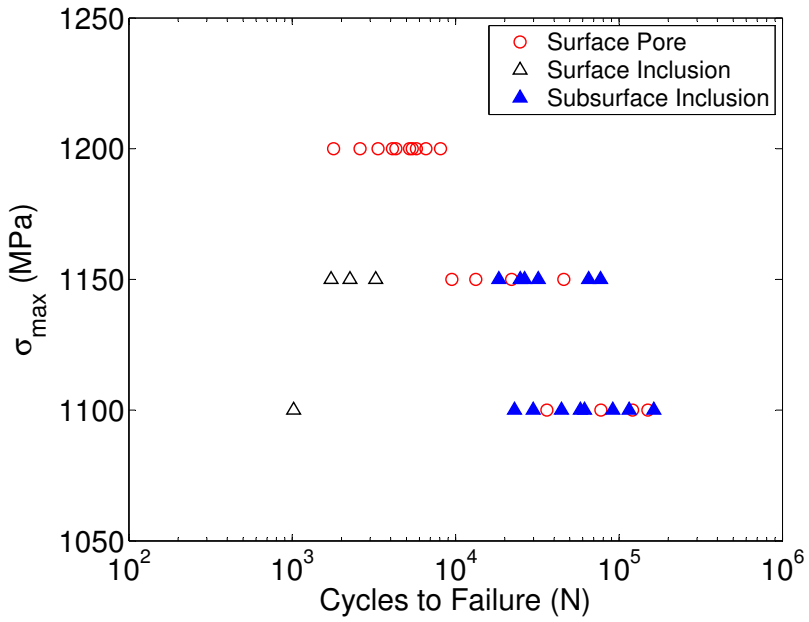

(b) Smooth specimen IN100 Ni-base superalloy. Recreated from data in [157]. (650°C, R=0.05, 0.33Hz, average grain size 4μm).

Figure 5.1: LCF to HCF transition regime data showing the transition from surface- to subsurface-dominated fatigue crack formation.

Thus, there is a transition from surface- to subsurface-dominated failure mechanisms with decreasing stress amplitude (from LCF to HCF). Other authors have reported similar results for the transition from surface- to subsurface-dominated fatigue crack initiation in a variety of materials including: Ni-base superalloys [23, 24, 159], titanium alloys [207, 208], and high strength steels [209, 210]. Since surface compressive residual stresses are introduced in a component to help retard fatigue crack initiation [211] and early growth at near-surface inclusions, and to shift the fatigue crack initiation sites from surface to subsurface locations [203, 204], Figure 5.1 suggests that compressive residual stresses should be useful in the transition and HCF regimes. However, as shown in Figure 5.2, residual stresses are only beneficial in the transition fatigue regime ($N = 10^4 - 5 \times 10^5$ cycles). For example, Barrie et al. [212] investigated the effectiveness of shot peening on suppression of fatigue crack formation at NMIs in Ni-base superalloy Udimet 720. They found that shot peening can improve fatigue performance in the transition regime for strain ranges up to 0.8% for tests at 427°C and 650°C and strain ratios of -1 and 0. Higher strains can reduce the effectiveness of the compressive residual stresses, so that surface initiation could still occur.

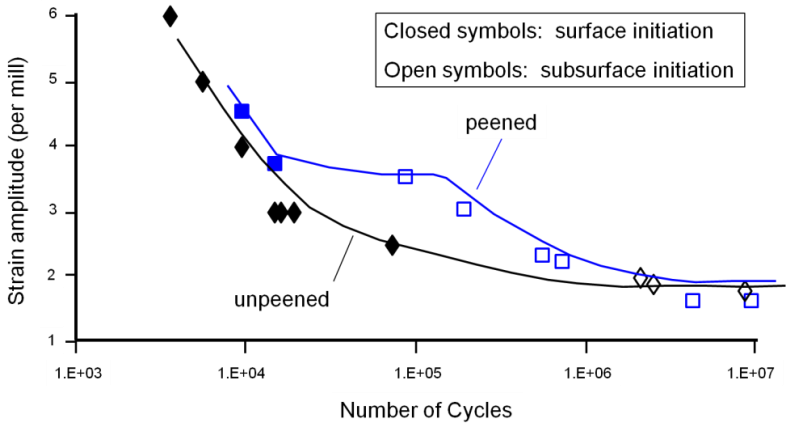

Figure 5.2: Effect of shot peening on strain life diagram for a Ni-base superalloy smooth specimen [213].

The reason that shot-peening is less effective at higher cyclic stress/strain amplitudes is due to residual stress relaxation with cyclic loading. As shown in Figure 5.3 for a coarse grain IN100 microstructure (average grain size = 25μm) subjected to

fatigue loading, if the strain amplitude is high enough, plastic straining of an entire cross section can occur and reverse the residual stress profile so that tensile residual stresses exist at the surface and compressive residual stresses develop in the bulk. This reversal of residual stress phenomenon has also been demonstrated in OFHC copper [214] under a given amount of tensile plastic strain (0.3%) and steel [215] for fatigue loading (R=0, N=800 cycles, σ_{max} = 408MPa, $\sigma_y^{0.2\%}$ = 408 MPa). If residual stresses become tensile near the surface, near-surface inclusions would become even more detrimental to the fatigue life of the component as compared to the absence of shot peening. The effects of residual stress relaxation due to fatigue loading should therefore be considered.

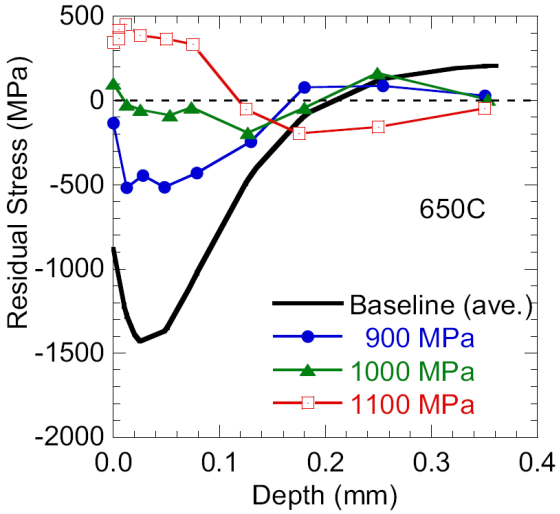

Figure 5.3: Surface residual stress relaxation (following specimen failure in fatigue) in a coarse grained IN100 due to a uniform applied stress [211].

Surface residual stresses can be applied via multiple techniques (shot/gravity peening, low plasticity burnishing, laser shock peening, etc.). The residual stress profile depends on the method of surface treatment (Ref. [216] for residual stress profile examples). Shot peening is the most commonly used technique in industry to induce residual stresses at the surface, and is the focus of this residual stress study.

In addition to the compressive residual stress state induced at the surface, other factors can influence the effectiveness of shot-peened residual stresses on fatigue life. For example, a high intensity of shot peening can induce extensive material damage

and non-metallic inclusion cracking that can override the benefit of the shot peening process [212]. In addition, residual stress relaxation can occur through fatigue loading and by means of thermal recovery [14–16]. Thus, accurate fatigue life modeling of the effects of surface residual stresses due to shot peening should take into account plasticity-induced change in microstructure and load/temperature-induced residual stress relaxation.

While the influence of residual stress on fatigue life has been reported extensively in the literature, the ability to computationally predict the improvement in fatigue resistance and scatter due to induced compressive residual stresses are lacking in the literature. A significant effort in modeling inclusion and residual stress effects in shot-peened martensitic gear steels was done by Prasannavenkatesan et al. [125,175,217,218]. They considered 3D FEM models at discrete depths subjected to the required amount of compressive load/unload strain to induce the required residual stress profile at each particular depth. The simulated inclusion sizes ($< 10\mu$m) were small compared to the overall 3D FEM model dimensions, so the gradient in applied stress and residual stress over the inclusion was considered to be negligible in their analysis. Alternatively, inclusion sizes in powder metallurgy polycrystalline Ni-base superalloy IN100 are on the order of 10-100 μm [18, 157, 180]. For inclusions of these sizes the gradient in residual stress field due to shot peening (ref. RS profile in [14]) can have a significant effect on stress/strain response and should be considered when analyzing inclusion and residual stress effects in Ni-base superalloys. Therefore, a simulation approach that accounts for the entire distribution of residual stress, and not just at discrete surface depths, is warranted. Hence, this work aims to develop a framework to assess (1) the effect of microstructure on the entire residual stress profile due to shot peening and (2) the effect of cyclic loading on residual stress relaxation in polycrystalline Ni-base superalloy components. This section begins with an overview of previous methods to impose residual stresses within components. Next, the method to simulate application of residual stresses to components is discussed and a simple plasticity model is presented for calibrating this model. Finally, the method in which crystal plasticity is incorporated is presented along with results for variability of initial residual

stress and retained residual stress due to a single load/unload.

5.1.2 Previous Methods for Simulated Application of Residual Stresses

Techniques to simulate the shot peening process can be divided into two methods: (1) Simulation of the impact response between the shot bead and the shot peened surface by quasi-static or explicit dynamic analyses to predict the resulting residual stress as a function of shot peening parameters (shot size, speed, coverage, etc.) [219–224] or (2) Simulation of the overall induced mechanical response due to shot peening through a deformation event [125, 225, 226]. Some relevant works regarding these two methods are discussed below.

5.1.2.1 Simulation of single and multiple impact events

Shot peening involves the high-velocity impact of shot beads on a surface of a part. Naturally, some of the first means to model this high-velocity impact were focused on single impact events. The residual stresses due to a single shot on a target substrate has been studied by multiple researchers. Chen and Hutchinson [220, 221] and Boyce et al. [219] studied the effect of the impact between a hard body and an elastic-perfectly plastic substrate on the residual stress profile using 2D axi-symmetric FEM analysis. They performed both quasi-static and explicit dynamic analyses for two different shot velocities (200 and 300 m/s) for a steel ball impacting a Ti-6Al-4V alloy. The dynamic simulations incorporated effects of strain-rate sensitivity, inertia, and elastic wave propagation, and resulted in a better prediction of residual stresses for the high-velocity impact as compared to the quasi-static analyses. This work [219–221] was performed to simulate the effect of foreign object damage (FOD) on the HCF response of a Ti-6Al-4V alloy, which is commonly used in low-temperature gas turbine engine blades. Their work was primarily focused on the effect of residual stresses due to the spherical impact on the critical crack length (threshold ΔK) and the location where fatigue cracks form during subsequent HCF loading.

Frija et al. [222] characterized the dynamic shot been behavior based on the equivalence between the dynamic impact of the shot with the surface and a static

indentation of a shot peen bead. The difference between the kinetic energy before and after impact was assumed to correspond to the amount of energy absorbed by the shot-peened material via plastic deformation, minus a small fraction due to losses (vibrations, heating, etc.). A three-dimensional quasi-static FEM analysis of a single shot bead was performed in [222], where the shot bead was assumed to be a perfectly rigid sphere traveling at a constant velocity and the shot-peened material was considered to be strain rate insensitive and elastic-plastic with isotropic hardening and damage. The residual stresses found along the centerline of the shot bead impact direction using this calibrated model correlated relatively well with XRD residual stress measurements for a Ni-base superalloy Waspaloy.

Zion and Johnson [227] used a two-dimensional axisymmetric FEM model to study the dynamic collision between a hard and soft shot bead and a high-stength steel target material. Using analysis of variance (ANOVA) method, they systematically studied the effects of four different shot peen input parameters (shot diameter, shot velocity, target thickness, and friction coefficient) on five key output parameters (surface and maximum RS, depth of maximum RS, transition depth from compressive to tensile RS, and plastic work done at the target surface). They found that the most highly significant input factor in the FEM model was the value of friction coefficient assumed between the shot bead and the target material.

Dynamic FEM analyses are not just limited to shot peen events. Brockman et al. [228] predicted and characterized residual stresses in a Ti-6Al-4V alloy and 2024-T351 aluminum alloy exposed to laser shock peening using a Johnson-Cook model with Von-Mises J2 flow theory and isotropic hardening. The laser pulse was modeled using a two-step explicit analysis, the first accounting for plastic deformation and the second step returning the system to near-equilibrium conditions. This framework was applied to a 9-shot rosette LSP pattern and found a significant amount of spatial variability in the resulting residual stress profile.

5.1.2.2 Techniques to induce overall mechanical response due to shot peening

The second method of simulating the shot peen process focuses on how the overall residual stress profile can be imposed using a quasi-static finite element framework, which is of interest to the current work. In this approach, the individual shot peen (or laser shock peen) events that were modeled in the previous method are not modeled. Instead, the resulting material deformation and hardening states due to shot peening are (1) induced explicitly within an implicit or explicit FEM model and (2) used as initial conditions for subsequent relaxation/fatigue analysis simulations.

One way to induce residual stresses explictly within an FEM model is to deform the FEM model in displacement-controlled constrained compression. The purpose of this method is to mimic the collective mechanical means in which biaxial residual stresses are imposed within a component during the shot peening process and to trace the evolution of the material state throughout the deformation process. For example, Prasannavenkatesan et al. [125, 218] used a simple displacement-controlled method in conjunction with isotropic plasticity [125] and polycrystal plasticity [218] to induce residual stresses [125] and reproduce experimental trends in residual stress relaxation [218] due to HCF cyclic bending for a martensitic gear steel. For these analyses, individual 3D FEM models were used at discrete depths and subjected to the required amount of compressive load/unload strain to induce the required residual stress profile at each particular depth. This displacement-controlled method presented by [125, 218] is best used for simulated application of residual stresses to the surface of a smooth specimen with well-defined boundary and loading conditions.

An alternative means to initialize residual streses within an FEM model is to use the residual stress and material hardening states for target initial conditions. For example, Buchanan et al. [14, 229] used a coupled creep-plasticity model to investigate residual stress relaxation in polycrystalline Ni-base superalloy IN100 at an elevated temperature. The initial residual stress state and material hardening state (effective plastic strain, backstress) were input into their material model as initial conditions based on experimental XRD and cold work measurements at different

depths [229]. After these initial conditions were applied to the finite element model, a self-equilibration step was used (to solve the stress/strain boundary value problem) prior to performing relaxation simulation studies. A similar method to initialize the hardening state of a material due to shot peening was done by Benedetti et al. [230,231]. In their approach, they assumed that the microhardness of the specimens as a function of the depth were directly related to the work hardening of the material. For the FEM model several thin surface layers were constructed. Each surface layer was assigned an initial local yield strength and hardening variables based on the experimental microhardness measurement at that depth. Additionally, the initial residual stress profile was induced by introducing an experimentally-fit thermal eigenstrain distribution within the FEM model. The method of introducing eigenstrains within an FEM model to produce residual stresses is covered in more detail in the next section.

5.1.2.3 Eigenstrain method of imposing residual stresses

In the eigenstrain method, the amount of induced thermal eigenstrain and resulting residual stress as a function of depth can be controlled by specifying spatial distributions of a thermal expansion coefficient. The main challenge of this method is to determine the amount of eigenstrain that is required to produce a given residual stress profile. General frameworks for the solution to the so-called "inverse eigenstrain problem" have been developed and presented by many authors [226, 232–236]. Universally, these approaches assume that the eigenstrain distribution can be reconstructed as a superposition of a truncated series of basis functions as:

$$\varepsilon^*(x) = \sum_{i=1}^{N} c_i \xi_i(x) \tag{5.1}$$

In this equation, N is the number of basis functions, $\xi_i(x)$, and c_i are the coefficent multipliers for each basis function. The benefit of this model is that the researcher is at liberty to choose the total number of basis functions and the form of each basis function; as a result, there are multiple sets of basis functions that can describe a given eigenstrain distribution. For example, one could use a series of smooth set of basis

functions [232–234], multiple polynomials [226], or even a superposition of multiple kernel density functions including triangular functions [235] or normal distribution functions [236] as the overall eigenstrain distribution estimator. Regardless of the functional form, the most important factor that should be considered is how to solve for the basis function coefficients and whether the given eigenstrain distribution is able to reconstruct the desired residual stress profile. For example, Korsunsky [226] used axisymmetric plate theory to analytically find stresses and deformations arising due to peening and found the necessary eigenstrain as a function of plate depth using polynomial functions as basis functions.

Methods that incorporate both the dynamic process of applying residual stresses and the subsequent effect that these residual stresses have on material behavior require separate analyses due to different time scales (dynamic shot/laser peen process versus quasi-static LCF/HCF/creep loading). An attempt to combine these two analyses was done by Achintha et al. [237–239] for the application of residual stresses due to laser shock peening in a Ti-6Al-4V alloy using an eigenstrain approach. In their work, explicit dynamic FEM analysis was done to determine the residual plastic strain in the material due to a single/multiple laser pulse(s) and later due to an array of laser pulses. For this dynamic analysis they assumed a simple elastic-perfectly plastic material model. The plastic strain as a function of depth calculated from this dynamic analysis was used as an input eigenstrain in a separate implicit FEM model to determine the resulting residual stress distribution in the material. They applied this framework to different thickness specimens and found that although eigenstrain distributions were similar for different specimen thicknesses, the resulting residual stresses were quite different among different specimen thicknesses.

5.2 Methodology for Imposing Residual Stresses Using Eigenstrain Approach

In this section, the methodology used to impose residual stresses within an eigenstrain framework is introduced and its extension to the crystal plasticity finite element method is covered. The eigenstrain approach is used here because of its great versatility. The

eigenstrain is introduced within the microstructure by means of a distribution of pseudo-thermal expansion coefficients. These thermal expansion coefficients can be optimized to fit any targeted/measured residual stress profile. Additionally, this technique can be used for more complex material response (e.g., crystal plasticity) and more complex geometries (e.g., notches), which is the focus of current and future work. The application of a quasi-thermal expansion eigenstrain method is covered below.

5.2.1 Material Model

5.2.1.1 Experiments used to calibrate model

During the shot peening process, equibiaxial compressive residual stresses are introduced near the surface due to constrained plastic deformation. Due to the requirement for equilibrium, tensile stresses form within the subsurface of the material. To simulate the material stress state after the shot peening process, a simple computation model is used and calibrated to experimental residual stress XRD data as reported by Buchanan et al. [14]. In their work, Buchanan et al. [14] performed residual stress relaxation studies of a supersolvus PM Ni-base superalloy IN100 with an average grain size of 25 μm that was shot peened to an Almen intensity of 6A. The resulting residual stress profile is overlaid on the shot peened microstructure in Fig. 5.4. As seen in Fig. 5.4(a), intense plastic deformation (up to ∼30% cold work) is induced near the surface of the specimen. The TEM image in Figure 5.4(b) shows a very dense dislocation network within the γ matrix and within the coherent secondary γ' precipitate channels visible in this Figure. Also, some dislocations are visible within a the γ' precipitates.

Shot-peened residual stress profiles depend strongly on specimen thickness. Regardless of the thickness, one characteristic that all residual stress profiles posess is that residual stress self-equilibrium must be satisfied. That is, the tensile portion of the residual stress curve within the bulk of the material must offset the compressive portion of the residual stress curve at the specimen surface. The main difference between different analytical expressions for residual stress profiles for specimens of different thicknesses is in the definition of the tensile portion of the residual stress

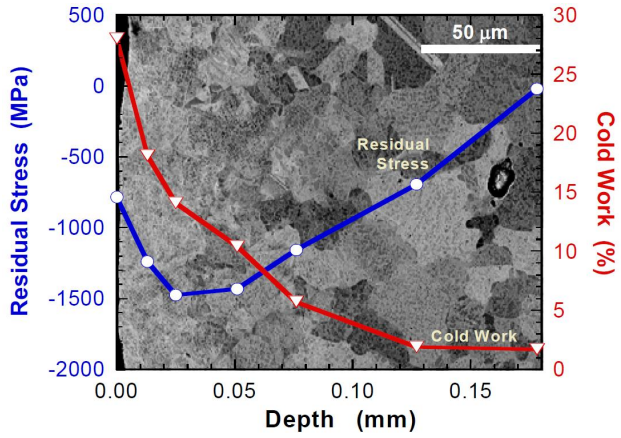

(a) Residual stress and cold work profiles overlaid on SEM image of microstructure [229].

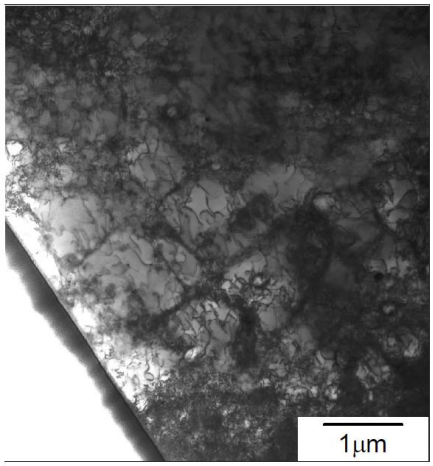

(b) Near surface TEM foil image of microstructure [229].

Figure 5.4: Effect of shot peening on a supersolvus IN100 microstructure shot peened to 6A Almen intensity [229].

curve. For thinner specimens, residual stress curves can approach a steady state tensile value within the bulk of the material. For example, in Buchanan et al. [14], they studied shot-peened specimens with a thickness of 2mm. The residual stress profile given in [14] contains the X-ray diffraction measured values at given depths from the surface. These measured values were fit to a curve of the form [229]

$$\sigma_{RS}(x) = [(\sigma_s - \sigma_{int}) + C_1 \cdot x] \cdot \exp(-C_2 \cdot x) + \sigma_{int} \tag{5.2}$$

where the least square values of $\sigma_s = -879.0$, $\sigma_{int} = 205.7$, $C_1 = -67,028$, and $C_2 = 20.89$ were determined by Buchanan et al. [229] to fit the experimental residual stress data as a function of depth (x) from the surface. It should be noted that Equation 5.2 assumes that the residual stress approaches a steady state internal value of σ_{int} with increasing depth (x) and is applicable for depth values from the surface ($x = 0$) to half depth ($x = 1$mm), where the condition of half-symmetry is assumed.

For larger thickness specimens, to satisfy compressive/tensile stress equilibrium, the tensile portion of the residual stress must decay with increasing depth. An example of a residual stress profile due to shot peening through the entire thickness of a thicker Udimet 720 plate is shown in Figure 5.5. As shown in this Figure, the tensile portion

of the residual stress profile appears to have an exponential or inversely-proportial decay from the maximum tensile stress at a depth of $\sim 0.5 - 1.5\,\text{mm}$ from the surface to a residual stress of zero at a depth of $\sim 2.5 - 3.0\,\text{mm}$ from the surface. Since it is unclear what the functional form of this tensile residual stress decay is as a function of depth, a first-order approximation that the decay is linear can be assumed and used to develop the full residual stress profile. Thus, we construct a residual stress profile for thicker coarse-grain IN100 Ni-base superalloy specimens based on three criteria: (1) the residual stress profile from depths of $x = 0$ mm to $x = 0.35$ mm is represented by the experimental RS profile in Buchanan et al. [14, 229] fit to Equation 5.2, (2) the tensile portion of the curve offsets the compressive portion of the curve at the surface, and (3) the tensile portion of the residual stress profile decays linearly with increasing depth (x) from its maximum tensile stress value at a depth of $x = 0.35$ mm. The controlling factor for the linear decay of the residual stress with depth is the change in residual stress as a function of x-distance, dS/dx. To determine this optimal linear decay value, the areas under the residual stress curve are estimated numerically using the midpoint method with a step size, $dx = 0.001\,\text{mm}$. To exactly offset the tensile and compressive portions of the residual stress profile, a value of $dS/dx = 142.72$ is determined. The estimation of the residual stress profile is shown in Figure 5.6 for a bar step size of $dx = 0.01\,\text{mm}$ so that the bars are distinguishable. Note that this residual stress profile is applicable for thicker specimens.

Another functional form for the residual stress profile of thicker specimens was proposed by Tufft [241, 242] and takes the form:

$$\sigma_{RS}(x) = A \cdot \exp[-x/\lambda] \cdot \sin(B \cdot x + C) \tag{5.3}$$

where A, B, C, and λ are constants fit to experiments. Application of this expression is shown in Figure 5.7 for Rene' 88DT that was shot peened to a 6A intensity with the conditions displayed in the Figure caption. the analytical expression in Equation 5.3 represents the experimental residual stress data well.

As evident from the foregoing discussion, the residual stress profile can change with specimen thickness. Since the work of Buchanan et al. [229] contains information

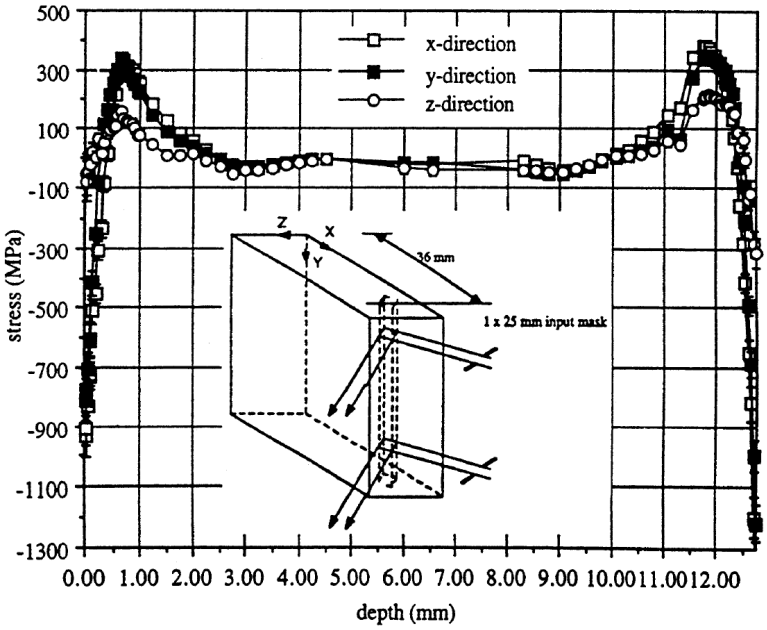

Figure 5.5: Residual stress profile as a function of depth for shot peened Udimet 720 plate [240].

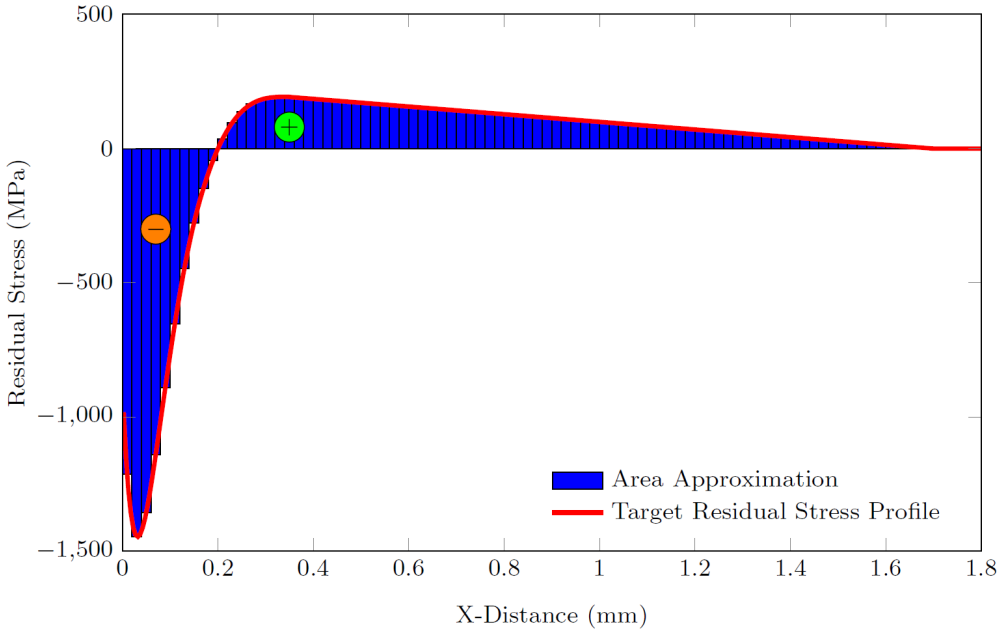

Figure 5.6: Estimation of linear decay of the tensile portion of the residual stress profile as a function of depth. This profile is applicable for "thicker" specimens.

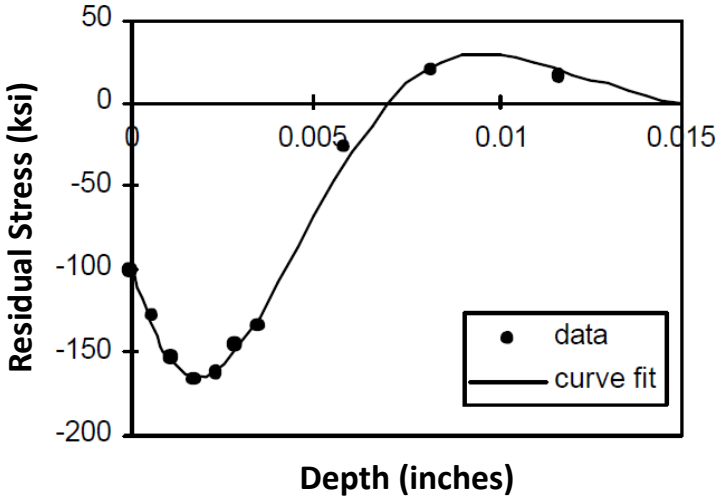

Figure 5.7: Residual stress profile and corresponding curve fit for a shot-peened Rene' 88DT specimen [241, 242]. Peening conditions: CCW31 shot, 6A intensity, 45° incidence angle, 800% coverage.

on both the initial residual stress curve and relaxation of residual stresses with fatigue loading and is applied to thinner (2mm) specimens, we will use the analytical expression in Equation 5.2 for our initial residual stress curve. Additionally, our study will be limited to specimens with a thickness of 2 mm, to ensure that the computational model is consistent with experiments.

5.2.1.2 Isotropic J2 Plasticity Model

A rate-independent J2 plasticity model with combined isotropic/kinematic hardening was used to calibrate the quasi-thermal residual stress application approach. This fitted model was later used as an input for a CPFEM model to assess the effect of microstructure on initial residual stress variability and residual stress relaxation. The J2 plasticity model employed is an existing ABAQUS [45] material model that employs the Von Mises yield surface

$$F = f(\underset{\sim}{\sigma} - \underset{\sim}{\alpha}) - \sigma_{ys} = 0 \tag{5.4}$$

where $F = 0$ during plastic flow, $\underset{\sim}{\sigma}$ and $\underset{\sim}{\alpha}$ are the stress and back stress tensors, respectively, and σ_{ys} is the Von Mises equivalent yield strength. The function f is

given by

$$f(\underset{\sim}{\sigma} - \underset{\sim}{\alpha}) = \sqrt{\frac{3}{2}(\underset{\sim}{S} - \underset{\sim}{\alpha}) : (\underset{\sim}{S} - \underset{\sim}{\alpha})} \tag{5.5}$$

where $\underset{\sim}{S}$ is the deviatoric portion of the stress tensor. An associated flow rule is assumed and takes the form

$$\underset{\sim}{\dot{\varepsilon}}^p = \dot{\overline{\varepsilon}}^p \frac{\partial F}{\partial \underset{\sim}{\sigma}} \tag{5.6}$$

Here, $\underset{\sim}{\dot{\varepsilon}}^p$ is the rate of plastic flow tensor and $\dot{\overline{\varepsilon}}^p = \sqrt{\frac{2}{3}\underset{\sim}{\dot{\varepsilon}}^p : \underset{\sim}{\dot{\varepsilon}}^p}$ is the equivalent plastic strain rate. Cyclic hardening of the yield stress is accounted for by the evolution of isotropic hardening [33, 195], i.e.,

$$\sigma_{ys} = \sigma_o + \kappa_s \left[1 - \exp\left(-b\overline{\varepsilon}^p\right)\right] \tag{5.7}$$

where σ_o is the yield stress at zero plastic strain, κ_s is the maximum change in the size of the yield surface, and b defines the rate at which cyclic hardening occurs. The evolution of the back stress tensor is characterized by [45, 125]

$$\dot{\underset{\sim}{\alpha}}_k = \frac{c_k}{\sigma_{ys}}(\underset{\sim}{\sigma} - \underset{\sim}{\alpha})\dot{\overline{\varepsilon}}^p - r_k \underset{\sim}{\alpha}_k \dot{\overline{\varepsilon}}^p \tag{5.8}$$

In Equation 5.8, the first term represents purely kinematic hardening (linear Ziegler hardening law) and the second is a recall term depicting dynamic recovery. For this study, we employ $k = 2$ backstress terms ($c_1 = 280900$, $c_2 = 10178$, $r_1 = 1163.8$, $r_2 = 55.65$) to facilitate better stress-strain fitting at lower ($k = 1$) and higher ($k = 2$) strains. This computational model was matched to experimental stress-strain data of a coarse-grained IN100 Ni-base superalloy microstructure (Ref. Figure 4 in [30]). The resulting stress-strain plot comparing the computational and experimental data is illustrated in Figure 5.8. The optimized isotropic/kinematic hardening parameters for this J2 plasticity model are listed in the upper left hand corner inset of the Figure. As shown is this Figure, this simple J2 plasticity model mimics the cyclic stress-strain behavior well for a very complex loading history. Thus, this J2 plasticity model is deemed sufficient for the calibration of the thermal expansion eigenstrain method to impose residual stresses in smooth specimen components. These results are covered later in the text.

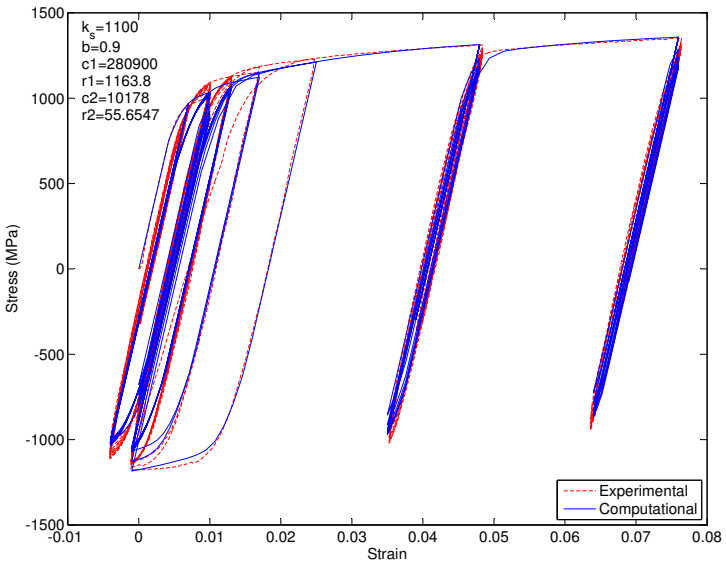

Figure 5.8: Comparison of J2 plasticity model in ABAQUS to experimental data at 650°C. Experimental data are from Ref. [30].

5.2.1.3 Polycrystal plasticity framework with quasi-thermal expansion eigenstrain

This section describes how the concept of thermal expansion eigenstrain finite element method (covered in the next section) was extended in the context of polycrystal plasticity. The benefit of crystal plasticity relative to the J2 plasticity model is that it can characterize fatigue scatter due to microstructure variability; a number of different statistically-representative microstructure instantiations can be simulated to address the probabilistic strain-life distribution. The goal of this study was to develop a framework to induce a full residual stress profile within a crystal plasticity finite element framework to account for this microstructure variability. Such a framework can be used to assess the effectiveness of shot peening in suppressing near surface crack initiation from inclusions located near to the surface of smooth specimens, which is the subject of Chapter 6.

To incorporate thermal expansion eigenstrain within the crystal plasticity finite element method under ostensibly isothermal loading conditions, a "quasi"-thermal expansion portion must be included within the deformation gradient. As shown in Figure 5.9, the total deformation gradient is assumed to be multiplicatively decomposed

via

$$\mathbf{F} = \mathbf{F}^e \cdot \mathbf{F}^p \cdot \mathbf{F}^\theta \tag{5.9}$$

where $\mathbf{F}^e$ denotes elastic distortion and rigid body rotation of the crystal lattice, $\mathbf{F}^p$ accounts for plastic deformation through dislocation glide along crystallographic planes, and $\mathbf{F}^\theta$ constitutes thermal expansion. It is noted that temperature change is introduced *only* to produce an eigenstrain field to induce initial residual stresses from associated elastic-plastic deformation. No other properties need be temperature dependent. Isotropic, linearized thermal expansion is assumed, so the thermal expansion portion of the deformation gradient, $\mathbf{F}^\theta$, is proposed as

$$\mathbf{F}^\theta = \sqrt{1 + 2\alpha\Delta\theta}\ \mathbf{I} \tag{5.10}$$

where α is the isotropic thermal expansion coefficient, $\Delta\theta$ is the change in temperature, and $\mathbf{I}$ is the 2^{nd} rank identity tensor. The form of Eqn. 5.10 was chosen so that the linearized form of the Green finite-strain tensor due to thermal expansion, $\mathbf{E}^\theta$, is [243]

$$\mathbf{E}^\theta = \frac{1}{2}\left([\mathbf{F}^\theta]^T \cdot \mathbf{F}^\theta - \mathbf{I}\right) = \alpha\Delta\theta\ \mathbf{I} \tag{5.11}$$

The rest of the microstructure-sensitive crystal plasticity equations for modeling deformation behavior of IN100 at 650°C follow those outlined by Przybyla and McDowell [46], which was briefly reviewed earlier in Chapter 2.

5.2.2 Finite Element Model Imposition of Eigenstrain Field

To simulate the material stress state after the shot peening process, a simple computation model is used and calibrated to the experimental residual stress XRD data reported by Buchanan et al. [14, 211, 229, 244, 245] on a supersolvus PM Ni-base superalloy IN100 with an average grain size of 25 μm that was shot peened to a Almen intensity of 6A. A quasi-thermal method of application of residual stresses is chosen in this work because it is easy to apply and calibrate and it is easily extended to more complex models for material response (e.g., crystal plasticity) and more complex geometries (e.g., notches).

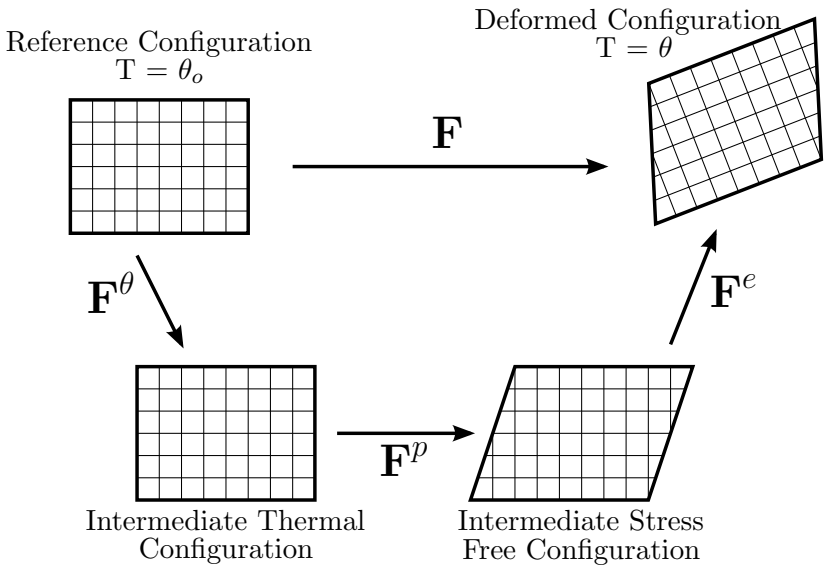

Figure 5.9: Multiplicative decomposition of the deformation gradient, including quasi-thermal expansion.

5.2.2.1 Application to J2 plasticity model

The general methodology for quasi-thermal application of residual stresses to a smooth specimen is shown in Figures 5.10 and 5.11 and can be summarized as follows:

1. **Initial Configuration:** Figure 5.10 shows the finite element model used to simulate residual stress application to a smooth specimen. The experimental smooth specimen [229] had a nominal gage section length, width, and thickness of y =20 mm, z =10 mm and x =2 mm, respectively (ref. Figure 5.10 for x, y, and z directions). Similar to the finite element model employed by Buchanan et al. [14, 229], a small portion in the center of this gage section was used for the finite element model. Half symmetry within the depth ($x-$dimension) of the material was employed so that the overall dimensions of the finite element model for J2 plasticity simulations were $xdim$ = 1 mm, $ydim$ = 34 μm, and $zdim$ = 34 μm. This finite element model was divided into many 2.5 μm-thick finite elements as shown in the rightmost image in Figure 5.10. It should be noted that since the compressive region of residual stress field is very thin ($x-$depth $\sim$ 200μm) and there is a high gradient of residual stress with depth, a very fine finite element thickness of 5 μm is required near the surface to provide

convergence of the FEM response. Buchanan et al. [229] reported a similar FEM mesh size requirement for convergence. In this work, a finer mesh of 2.5 μm was used to provide more coefficient of thermal expansion (CTE) data points (black dots in Figure 5.11) to improve functional form fitting; this fitting is covered later. Each finite element was assigned a given quasi-thermal expansion coefficient α_j and J2 plasticity material properties. The initial distribution of α_j values were assigned so that the resulting residual stress values were within $\pm$250 MPa from the target residual stress profile at a given depth to avoid any numerical instabilities in the numerical optimization scheme described below.

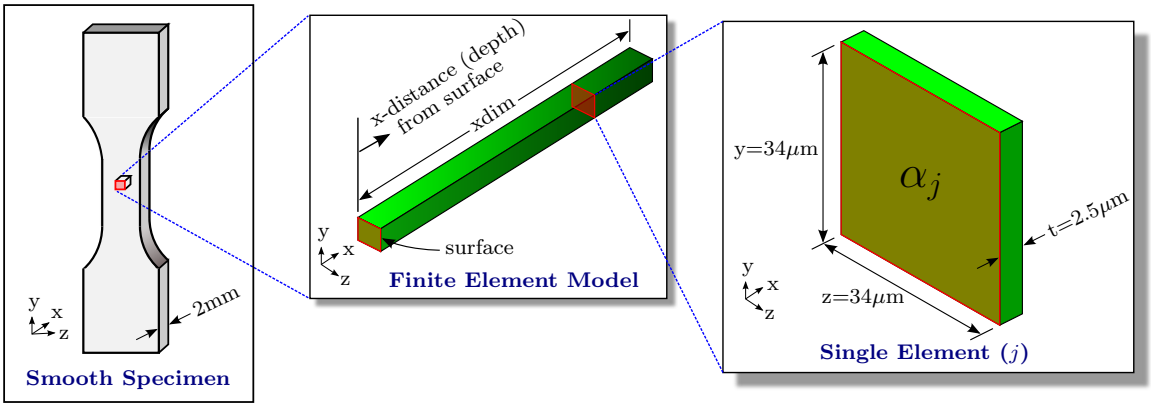

Figure 5.10: Finite element model used to apply residual stress to a smooth specimen.

2. **Eigenstrain Application:** With all surfaces constrained from normal displacement, an eigenstrain ($\varepsilon^*_{therm,j} = \alpha_j \Delta T$) is introduced within the model as shown in the upper left hand corner of Figure 5.11. It should be noted that an arbitrary value of ΔT =1 was applied uniformly throughout the whole specimen, without loss of generality, since temperature is not a physical field variable during the imposition of residual stress.

3. **Release Surface Constraint:** The surface constraint at $x = 0$ is removed to simulate the spring back of the material after shot bead impact (cf. lower left hand portion of Figure 5.11). This step is required to relax the stress component normal to the surface so that σ_{xx} $\sim$0, which is representative of the near-surface stress state at the end of the shot peening process [125]. This relaxation step is

analogous to the "unload" step in the displacement-controlled method of residual stress application presented by Prasannavenkatesan et al. [125].

4. **Optimization of Thermal Expansion Coefficients:** A secant root finding method [246] is used in conjunction with the FEM model to optimize the spatial distribution of thermal expansion parameters to fit the experimental residual stress profile.

5. **Fit Thermal Expansion Coefficients to Functional Form:** Gaussian probability density functions and polynomials are used to fit the optimized thermal expansion coefficient as a function of depth from the surface. More details on this functional form and how it is used within the crystal plasticity framework are covered in the following.

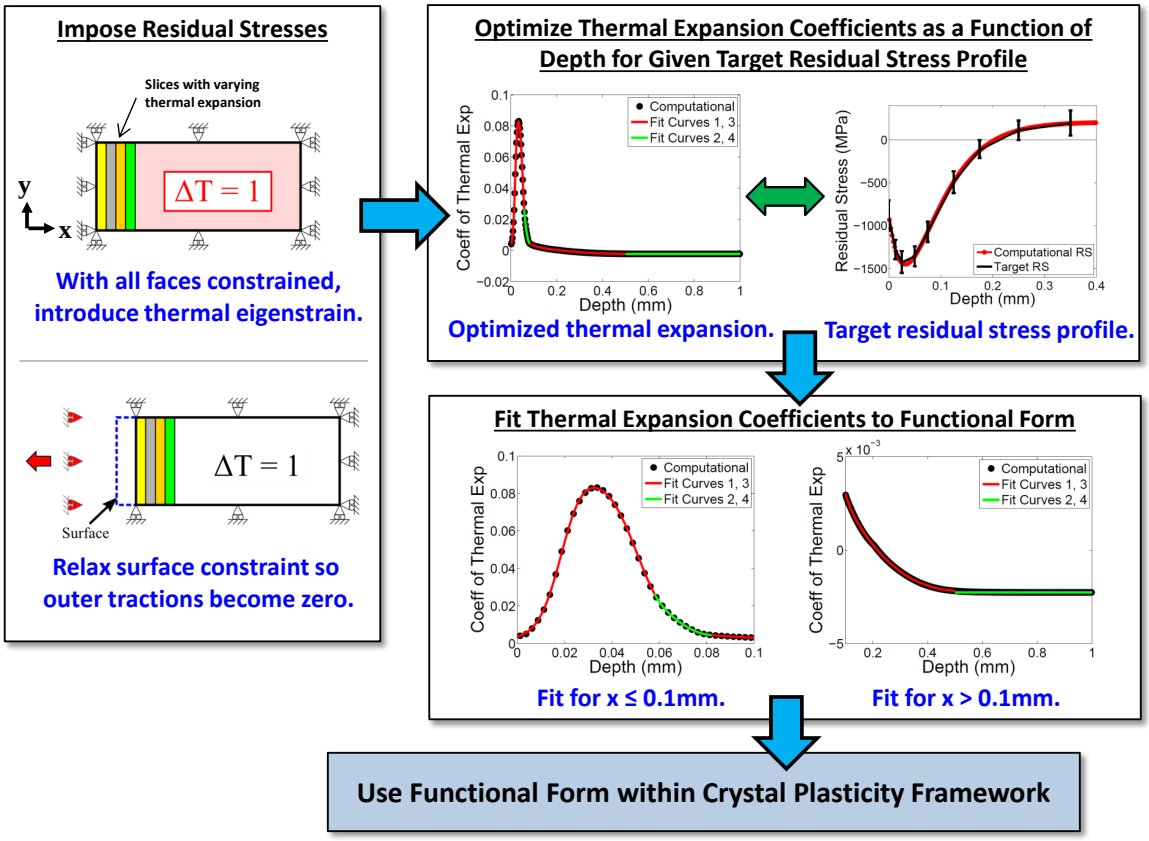

Figure 5.11: Methodology for quasi-thermal application of residual stresses to a smooth specimen.

Some additional discussion is required to justify why an FEM model is used for the optimization of thermal expansion coefficients. In previous work by Prasannavenkatesan et al. [125], they presented an analytical approach to calculate the amount of plastic strain required to retain a given amount of residual stress at a given depth for a J2 plasticity material behavior. They considered separate 3D FEM models at discrete depths and subjected the FEM models to constrained compressive loading/unloading to apply the residual stresses. They then investigated the effect that residual stresses have on inclusions in a martensitic gear steel. For their case, the simulated inclusion sizes considered for analysis were less than or equal to 10 μm in diameter. So, the gradient in applied stress and residual stress were small compared to the overall 3D FEM model dimensions. In fact, there was less than a 100 MPa change in residual stress over a 10 μm depth difference for the residual stress profile used in their work (ref. Figure 1b in [125]). Thus, the gradient in applied stress and residual stress over the inclusion(s) studied were considered negligible in their analysis; therefore, they could use separate models at each depth and subject them to subsequent uniform displacement for residual relaxation studies.

On the other hand, the inclusion sizes in PM Ni-base superalloy IN100 that initiate fatigue failure are on the order of 10-100 μm (ref. [18, 157, 180]). As an example, an inclusion that is 50 μm in diameter could see a greater than 500 MPa change in residual stress (ref. RS profile in [14]) over the diameter of the inclusion. This gradient in the residual stress profile is too large to consider separate 3D FEM models at different depths when modelling combined inclusion/residual stress effects. Hence, in this work, the approach needs to account for the entire distribution of residual stress, and not just at discrete surface depths. Thus, the need to model the full strip (ref. square prism in middle of Figure 5.10) of material in this work.

Since this work models the entire distribution of residual stresses within a single FEM model, the boundary conditions (BCs) and boundary value problem (BVP) are slightly different than the previous approach outlined by Prasannavenkatesan et al. [125]. Prasannavenkatesan et al. considered separate 3D FEM models at discrete depths, and were at liberty to choose relatively simple boundary conditions. As

shown in the left hand side of Figure 5.12, for the simulation of a single subsurface element, they assumed that all faces but the one oriented parallel to the surface (top face in this Figure) were constrained from normal displacement. From this initial configuration they loaded/unloaded the top surface in constrained compression to the desired residual stress value at the given discrete depth.

On the other hand, the eigenstrain approach has a different set of BCs and BVP to solve. Consider (as a simple example) the two element FEM problem on the right hand side of Fig. 5.12 with the top element having a larger coefficient of thermal expansion (CTE) than the bottom element and the outside faces are constrained from normal displacement. When a change in temperature is applied, the top element will "expand" more than the bottom element causing the boundary between the elements to move downward. This FEM BVP must satisfy both strain compatibility and stress equilibrium in the vertical direction. It is relatively easy to use an analytical approach to find the stresses/strains for this essentially 1D problem. However, if we extrapolate this thinking to many more elements with a wide distribution of thermal expansion coefficients, it becomes harder to conceive a closed-form solution that is readily able to be solved. In addition, the next step in the eigenstrain application approach involves removing the surface constraint so that the stress component normal to the surface becomes zero, analogous to the unload step in the displacement-controlled method [125]. This further complicates the problem. Thus, we deem that this eigenstrain application of residual stress initial BVP requires an FEM model to solve.

5.2.2.2 Fitting thermal expansion coefficient to functional form

The right hand side of Figure 5.11 shows the required thermal expansion coefficient as a function of x-distance (depth) from the surface that is used to replicate the target residual stress profile shown in the upper right hand portion of Figure 5.11. The black dots in Figure 5.11 show the optimized thermal expansion coefficient found using the secant root finding method and the red and green solid lines show the functional form fitting of these computationally-optimized thermal expansion coefficients. The top middle plot in Figure 5.11 shows the entire distribution of thermal expansion

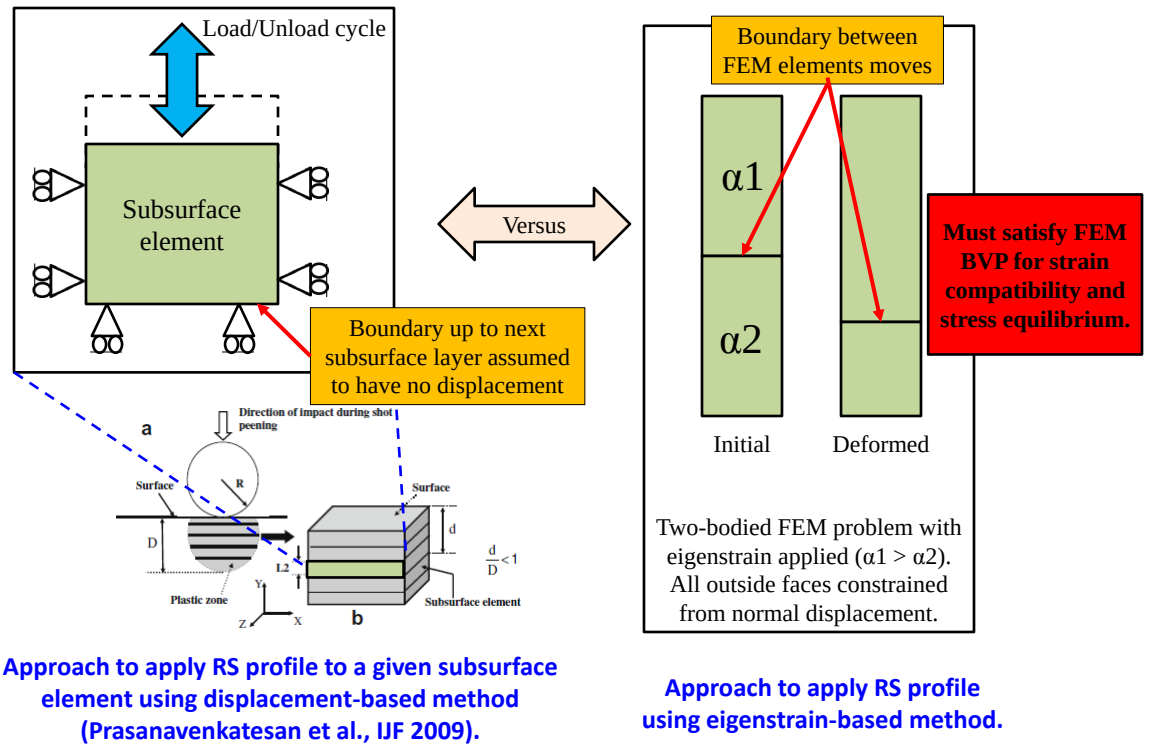

Figure 5.12: Comparison of BCs and BVP for displacement-based method [125] and eigenstrain-based method of residual stress application.

coefficient as a function of x-distance from the surface. The bottom right two plots in Figure 5.11 show zoomed-in versions of the fitting of the required thermal expansion coefficient to the piecewise functional forms described below. A piecewise smooth functional form was required so that the thermal expansion coefficients can be defined independent of mesh size and so that this functional form could be used as an input for the crystal plasticity model described later. The thermal expansion function, $\alpha(x)$, was split into 4 sections described by:

1. **$x < 0.058$ mm :** This section of the curve was fit using a superposition of two Gaussian probability density functions (PDFs). A similar description of using two Gaussian PDFs was demonstrated in [236] to describe the eigenstrains induced by shot-peening a GW103 magnesium alloy. The functional form used to fit the thermal expansion coefficients at $x < 0.1$ mm is

$$\alpha(x) = A \cdot \exp\left[-\frac{(x-\mu_B)^2}{2\sigma_C^2}\right] + D \cdot \exp\left[-\frac{(x-\mu_E)^2}{2\sigma_F^2}\right] + G \cdot x + H \qquad (5.12)$$

2. **0.058 mm $\leq$ x $<$ 0.082 mm :** This section was fit using a 5th order polynomial:

$$\alpha(x) = a_{21} \cdot x^5 + a_{22} \cdot x^4 + a_{23} \cdot x^3 + a_{24} \cdot x^2 + a_{25} \cdot x + a_{26} \tag{5.13}$$

3. **0.082 mm $\leq$ x $<$ 0.5 mm :** This section was fit using a 10th order polynomial with coefficients ranging from highest to lowest ranked terms polynomial coefficients as $a_{31}, a_{32}, \cdots, a_{39}, a_{310}$.

4. **x $\geq$ 0.5 mm :** The last section uses a constant thermal expansion coefficient, a_{41}.

It should be stated that the selection of the x-value bounds on these different curves were selected with the constraint that each section pieced together would represent the overall optimized thermal expansion distribution. Each piecewise function minimized the Euclidean norm (sum of squares error) within its x-value bounds. The constants of the two Gaussian PDFs curve were found using a Gauss-Newton numerical approach [246] and the constants of the polynomial functions were found using the built-in MATLAB "polyfit" function [144]. The constants used for each curve section are listed in Table 5.1 and the resulting fitting, again, is shown on the right hand side of Figure 5.11.

5.2.2.3 Application to polycrystal plasticity model

Using a similar finite element model as previously described for the J2 plasticity model, a combined crystal plasticity and J2 plasticity model was constructed as illustrated in Figure 5.13. The polycrystalline grain structure within the crystal plasticity region is constructed using a random sequential adsorption algorithm similar to that described in [46, 247, 248]. This spherical packing algorithm offers more control over grain sizing as compared to a traditional random seed Voronoi tessellation, which results in a normal distribution. The values of μ = -0.1 and σ = 0.4 were chosen for the target lognormal grain size (mean grain size = 34 μm) distribution function, $f(x; \mu, \sigma) = \frac{1}{x\sigma\sqrt{2\pi}} \exp\left[-\frac{(\ln(x)-\mu)^2}{2\sigma^2}\right]$, based on previous publications of fine grain IN100

Table 5.1: Constants used to fit functional form for thermal expansion coefficients as a function of specimen depth.

Curve 1		**Curve 2**		**Curve 3**		**Curve 4**	
var.	value	var.	value	var.	value	var.	value
A	0.00050647	a_{21}	-4021918.4465	a_{31}	-5450.013	a_{41}	-0.002265
μ_B	0.02410683	a_{22}	147844.2966	a_{32}	14866.4041		
σ_C	000764205	a_{23}	-26103.8897	a_{33}	-17602.9268		
D	0.00226598	a_{24}	15813.7753	a_{34}	11860.8999		
μ_E	0.03770631	a_{25}	-580.0639	a_{35}	-5007.4952		
σ_F	0.01300566	a_{26}	8.5753	a_{36}	1373.2346		
G	0.05573199			a_{37}	-24.7787		
H	0.0025			a_{38}	27.4454		
				a_{39}	-1.79011		
				a_{310}	0.054903		

grain size distributions [28,46,194,248]. An example of the target grain size distribution and the actual grain size distribution created using the spherical packing algorithm is shown in Figure 5.13(a). These grain size distributions are normalized by the mean grain volume, $<V_{grn}>= 4/3\pi(0.034 \text{ mm})^3 = 1.65 \times 10^{-3}$e-3 mm^3.

Figure 5.13(b) shows an isometric view of an example polycrystalline grain structure used for the FEM application of residual stresses. In this Figure, each grain is represented by a different color to visualize the grain structure. The FEM model is a square prism of material with a cross section that is 0.17 mm by 0.17 mm, which corresponds to having approximately five grains through the y- and z-thicknesses of the cross section. Crystal plasticity is employed for elements that are within 0.35 mm of the surface and J2 plasticity is employed for elements that are at a distance greater than 0.35 mm from the surface to the total x-dimension, which is 1 mm in this case.

Figure 5.13(c) shows a scaled side view of the example polycrystalline grain structure show in Figure 5.13(b) overlaid on top of the target residual stress profile to compare the assigned FEM material behavior and mesh refinement to the target residual stress profile as a function of depth from the surface. As shown in Figure 5.13(c) the refinement in mesh was selected to correspond to key areas in the residual stress profile. Since a mesh size of 5 μm provided convergence for the FEM response, this mesh size was used for elements that were within the compressive residual stress

zone, $x \leq 0.2$ mm from the surface. Since the experimental residual stress was given up to a depth of $x = 0.35$ mm, the crystal plasticity zone was extended up to this depth also. Beyond this depth of $x = 0.35$ mm, the residual stress field is relatively flat; thus, J2 plasticity was used for the zone of $x > 0.35$ mm and the mesh size slowly coarsened out to the depth of $x = 1$ mm.

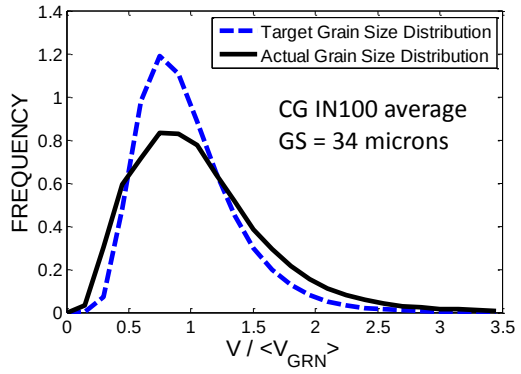

(a) Target versus actual grain size distribution using random sequential adsorption algorithm.

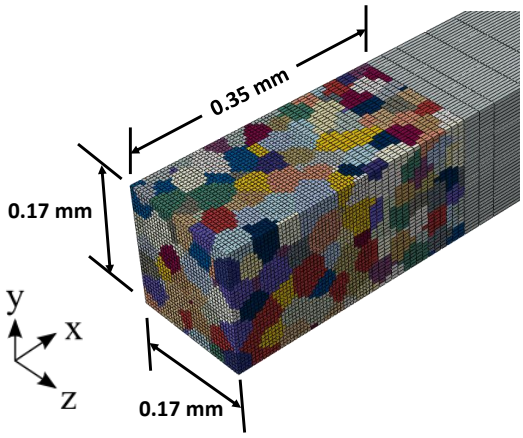

(b) Isometric view of example polycrystalline grain structure used for FEM application of residual stress.

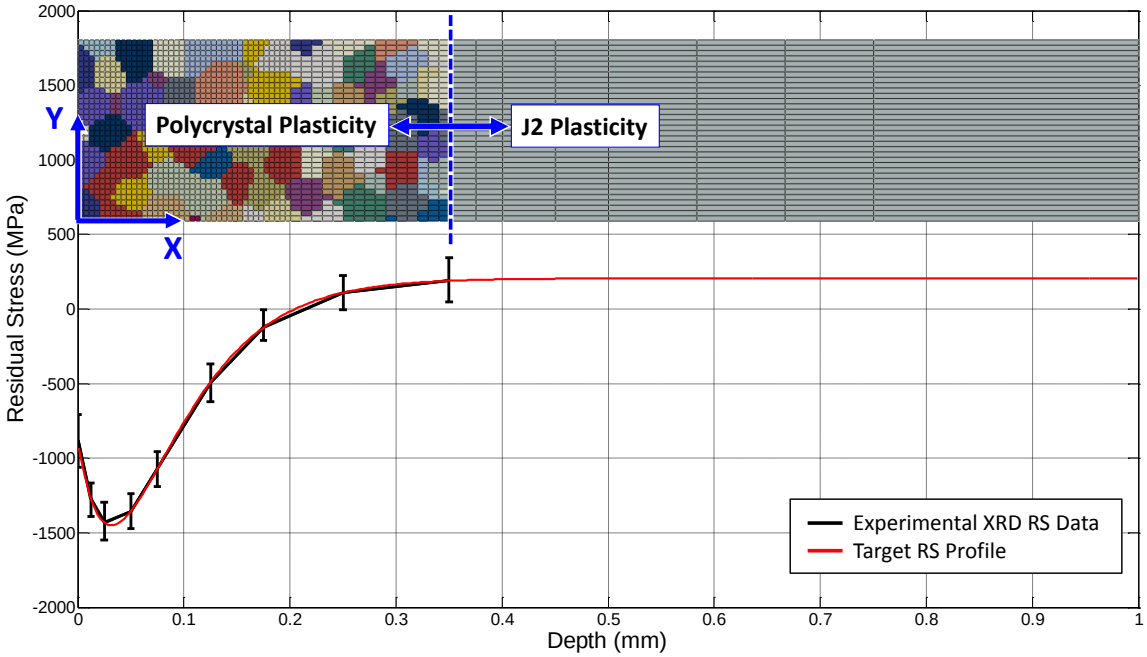

(c) Scaled side view of example polycrystalline grain structure in (b) overlaid on target RS profile to show assigned material behavior and mesh refinement as a function of depth from the surface.

Figure 5.13: Example combined polycrystal plasticity and J2 plasticity finite element model used for eigenstrain-based application of residual stresses. Crystal plasticity is used for depths of $x \leq 0.35$ mm and J2 plasticity for $x > 0.35$ mm. The experimental XRD residual stress profile is from Buchanan et al. [229] and the target residual stress profile is given by Equation 5.2.

5.3 Results and Discussion

5.3.1 Contour Plots of Stress in Specimens

Figures 5.14(b) through 5.14(e) show example stress contour plot results for the polycrystalline grain structure depicted in Figure 5.14(a). The left hand column of this Figure shows contours of the σ_{yy} component of stress and Von Mises stress at the end of eigenstrain application with all finite element surfaces constrained (ref. upper left of Figure 5.11) and the right hand column shows these same contour plots after the surface constraint is released so the outer tractions become zero (ref. lower left of Figure 5.11). For comparison purposes, the contour plot scales of the σ_{yy} component plots (Figures 5.14(b) and (c)) are identical as well as the contour plot scales for the Von Mises plots (Figures 5.14(d) and (e)). These Figures display the ability of the FEM model to induce compressive residual stresses using constrained thermal expansion.

The first thing that is immediately noticed from this contour plot is the high value of σ_{yy} stress (or more precisely, the hydrostatic stress) induced near the surface as the eigenstrain is applied and the faces are constrained (Figure 5.14(b)). This high amount of hydrostatic stress is typical for a component that is loaded in constrained compression. It is also well known that when a component is loaded in constrained compression, larger strain (or equivalently stress) is required for yielding as opposed to an unconstrained compression condition. In fact, constrained compression can increase the apparent yield strength by a factor of 2 as compared to unconstrained compression. In these constrained compression cases, a better indicator of plastic response is to use a deviatoric (or equivalent) stress measurement. Hence, both the σ_{yy} and Von Mises stress measures are shown in these plots. Although during the constrained compression step the maximum compressive stress is $\sigma_{yy} = -3868$MPa, the Von Mises equivalent stress is at a more reasonable maximum value of 1875MPa.

The release of the surface constraint on the $x = 0$ face (ref. the bottom left portion of Figure 5.11) allows the finite element model to expand in the negative x direction. Subsequently, the stress component in the x-direction (σ_{xx}) tends toward zero and the

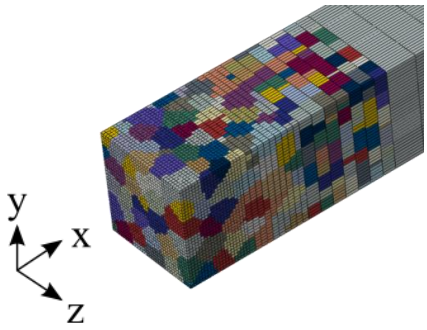

(a) Initial polycrystalline grain structure (0.17 mm x 0.17 mm square cross-section).

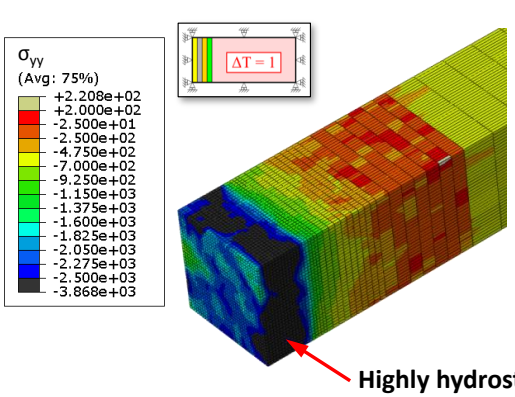

(b) Contour of σ_{yy} at end of eigenstrain application with all faces constrained.

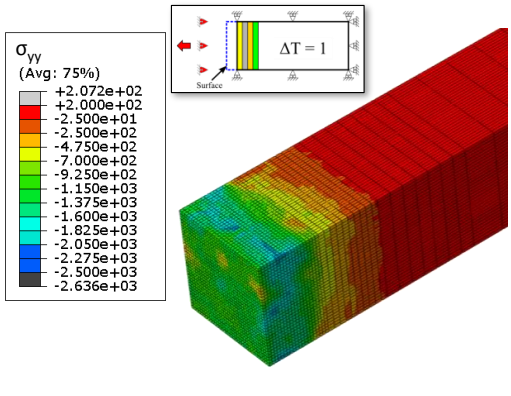

(c) Contour of σ_{yy} after surface constraint has been released.

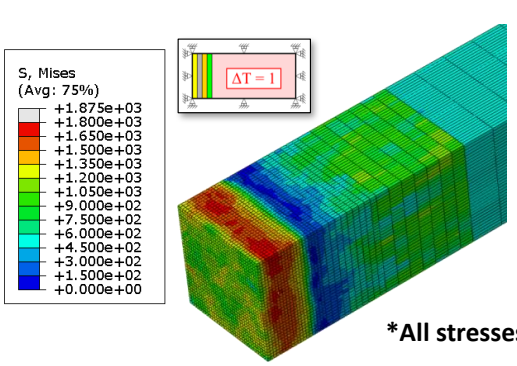

(d) Contour of VM stress at end of eigenstrain application with all faces constrained.

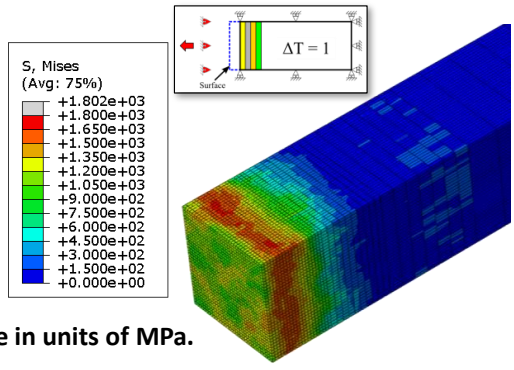

(e) Contour of VM stress after surface constraint has been released.

Figure 5.14: Example stress contour plot results for conditions before and after surface constraint released. All stresses are in units of MPa.

σ_{yy} and σ_{zz} components settle into the desired biaxial residual stress values. It should also be noted that after relaxation of the normal surface traction on $x = 0$ face, all slices normal to the surface also have net zero σ_{xx} traction into the depth.

5.3.2 Scatter in Residual Stress Response Among Multiple Realizations

In this section, the results from $N = 5$ instantiations are presented to determine the amount of scatter exhibited among multiple digitally-created microstructures. Due to the different orientations of the grains, the residual stress value of an element at a given depth will differ depending on the orientation of the grain in which the element is located and its interactions between its neighbors. Therefore, certain combinations of microstructures will cause the overall residual stress profile to deviate above or below a given ideal/target mean stress value. Plotted in Figure 5.15 are results from $N = 5$ random microstructure instantiations. In these Figures, each red dot indicates the residual stress value within a single element. Clearly, there is significant scatter in the elemental residual stress values, especially in the near surface area where compressive residual stresses are highest. Since the finite element model employs a structured, voxelated mesh, the residual stress component values at each finite depth ($x-$distance) are averaged and depicted with a green triangle. Additionally, the target residual stress profile from Buchanan et al. [229] is depicted by the thick black error bar lines. It is clear from these plots that the eigenstrain method of computationally inducing residual stresses within the crystal plasticity framework results in residual stress profiles that are able to match experimental mean values.

Figure 5.16 compares the experimental data from 6 baseline XRD measurements [229] to the statistical spread from $N = 5$ instantiations using the polycrystal plasticity model. The typical definition of the standard deviation from a small population are invoked for these $\pm 3\sigma$ values. As shown in this Figure, there is a strong correlation between the statistical spread of the mean value found from experiments and the mean value predicted by the crystal plasticity simulations for the near surface ($x < 0.1$mm) residual stress values. Based on only $N = 5$ instantiations, the computational model slightly underpredicts the scatter for locations further into the depth of the smooth

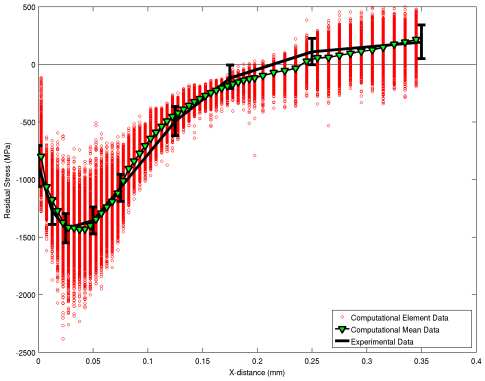

(a) Instantiation 1

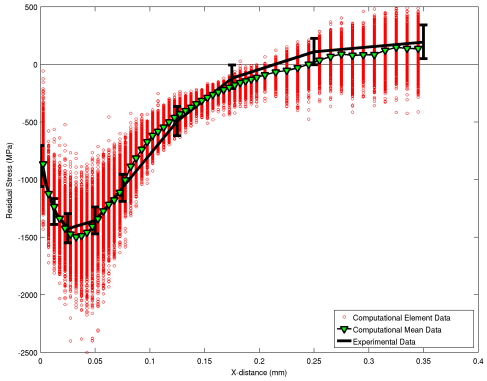

(b) Instantiation 2

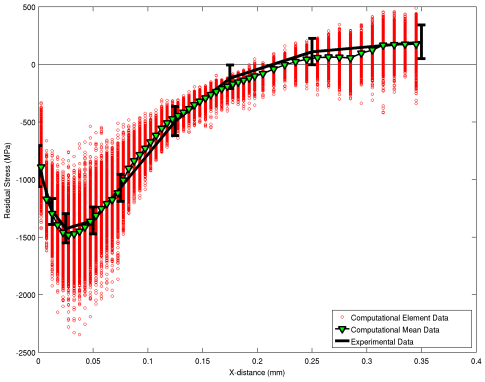

(c) Instantiation 3

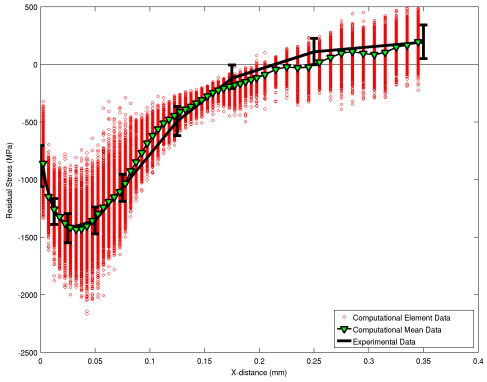

(d) Instantiation 4

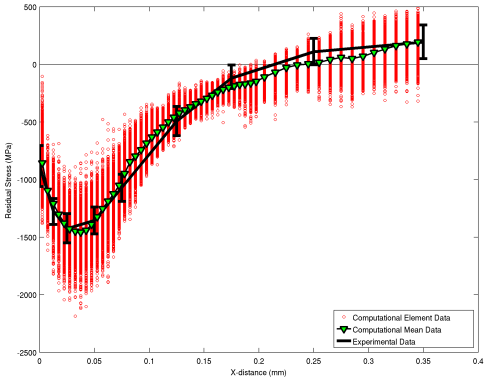

(e) Instantiation 5

Figure 5.15: Computational versus experimental residual stress profile as a function of depth from the surface. Experimental residual stress data is from Buchanan et al. [229].

specimen. However, the current and future studies focus on the role of residual stresses in suppressing crack formation/propagation near the surface. Therefore, we conclude that the method used here adequately supports these current and future residual stress studies. The utility of this model will further be explored with respect to residual stress relaxation in the following section.

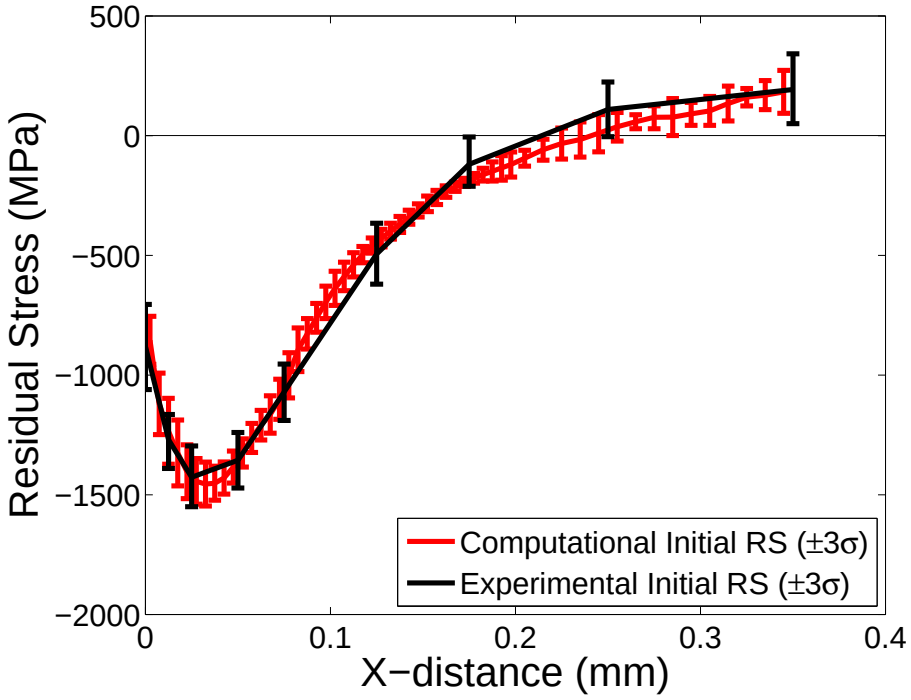

Figure 5.16: Computational versus experimental scatter in residual stress profile as a function of depth from the surface. Experimental residual stress data are from Buchanan et al. [229].

5.3.3 Residual Stress Relaxation with Single Load/Unload

5.3.3.1 Method to impose single load/unload for relaxation studies

In this section, we present the method in which we impose a single, uniaxial load/unload sequence to the model to investigate residual stress relaxation. This analysis subsequent to residual stress imposition uses the **Restart* option in ABAQUS [45], which allows for an analysis to be restarted or continued from a previous step/increment of an analysis that was already performed. To run this restart analysis, the **Restart, write* command must be invoked in the FEM model input file at the end of the residual

stress application step. This input file command tells ABAQUS to write the current state of the model (elemental stresses/strains, nodal displacements, internal state variables (ISVs), etc.) to ABAQUS restart files [45]. This current state of the model is then imported as initial conditions for subsequent analysis by using the **Restart, read* command in the subsequent analysis input file. In addition to carryover of the residual stress/strain state of the FEM model, a provision is made within the user-defined material (UMAT) subroutine to carryover the distribution of quasi-thermal expansion eigenstrain induced in the first step of residual stress application.

The boundary and loading conditions used during the single, uniaxial load/unload sequence to study residual stress relaxation are shown in Figure 5.17. Figure 5.17(b) shows 2D projections of the 3D FEM model (Figure 5.17(a)) as viewed from the surface (left) and side (right). The loading step starts from the condition where the x=0 surface constraint has been released and the stresses in the model have been allowed to relax normal to the surface (ref. bottom left hand side of Figure 5.11). Periodic boundary conditions are applied to the lateral surfaces (at $z = 0$ and $z =$ 0.17 mm) using a multi-point **Equation* constraint in ABAQUS [45]. The bottom surface at $y = 0$ and the surface at full FEM depth ($x = 1$ mm) are constrained from normal displacement during the load/unload sequence. Rigid body rotation and translation are prevented by constraining z-direction displacement for 4 nodes located at coordinates (x, y, z) = {(0, 0, 0), (0, 0.17 mm, 0), (1 mm, 0, 0), (1 mm, 0.17 mm, 0)}; these 4 node locations are denoted in Figure 5.17(b) by the green-filled black circles. With these boundary conditions applied, the top surface ($y = 0.17$ mm) of the model is subjected to a given net normal traction, $\sigma_{yy,net} = \sigma_a$, and then unloaded to $\sigma_{yy,net} = 0$ MPa. During this loading process the top surface is subjected to a multi-point constraint (MPC) to make all of the nodes on the top surface displace the same throughout the deformation process. This MPC ensures a "displacement-controlled" load/unload sequence.

A simple FEM model is used here to illustrate why the displacement-controlled MPC is required for the load/unload sequence. For this FEM model, J2 plasticity material properties are used throughout. Residual stresses are imposed in the FEM

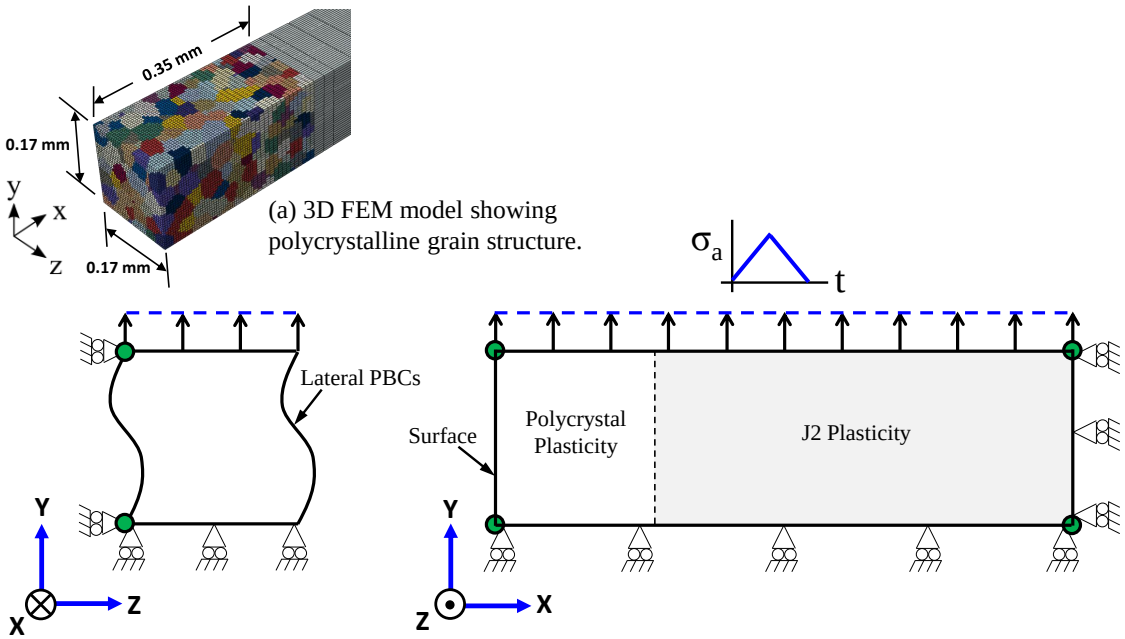

(b) 2D projection of FEM model as viewed from the surface (left) and side (right).

Figure 5.17: Schematic of boundary and loading conditions used for single load/unload residual stress relaxation studies.

model as illustrated on the left hand side of Figure 5.11. For the load/unload sequence, the boundary conditions in Figure 5.17 are simulated with ("displacement-controlled") and without ("stress-controlled") the multi-point constraint applied to the top surface nodes. A maximum net stress in the y-direction of $\sigma_{yy,net} = 1000$ MPa is used for both cases. The resulting residual stress relaxation of the σ_{yy} component as a function of depth is shown for the displacement-controlled and stress-controlled load/unload sequences in Figures 5.18(a) and 5.18(b), respectively. In these Figures, the black lines indicate the initial residual stress (σ_{yy}) profile, the red markers denote the stress (σ_{yy}) at maximum applied displacement/stress, and the blue dotted lines represent the residual stress profile after unloading to zero net stress in the y-direction. Figure 5.18(c) shows the displacement of the top nodes of the FEM model as a function of depth for the displacement-controlled (dotted lines) versus the stress-controlled (solid lines) load/unload sequences.

It is apparent from Figure 5.18(b) that using a stress-controlled loading sequence forces the entire depth of the FEM model to the maximum stress level ($\sigma_{yy} = 1000$ MPa)

imposed in the y-direction. To reach this stress level, the initial highly-compressive portion of the FEM model near the surface must displace more than the portion further into the depth resulting in a large spike in the near-surface y-displacement field for stress-controlled loading. Upon unloading to zero net stress in the y-direction, the residual stress in the y-direction is flatlined. This phenomenon occurs regardless of maximum applied stress level. Therefore, the stress-controlled load/unload sequence is inadequate for modeling residual stress relaxation.

On the other hand, the MPC constraint displacement-controlled method is more representative of the load/unload sequence as it maintains the shape of the residual stress profile upon loading (for $\sigma_{yy,net} = 1000$ MPa) and causes the residual stress to relax in the y-direction upon unloading. Therefore, we employ this MPC displacement-controlled method for residual stress relaxation studies. Obviously, the magnitude of residual stress relaxation will vary depending on the maximum load/displacement applied. Consequently, we study the effect of maximum load/displacement on residual stress relaxation next.

In the next section, we determine the required level of loading stress to apply to the computational model to mimic the experimental load/unload strains for relaxation studies. For the experimental study of coarse-grained IN100 residual stress relaxation [14], a single stress-controlled load/unload cycle with $\sigma_{max} = 900$MPa was performed. Upon unload, a retained macroscopic plastic strain value was reported as $\varepsilon_p \sim 0.0025$. Since the current microstructure and hardening behavior of the computational crystal plasticity model differs from these experiments, we use a slightly different maximum load value to test the relaxation of residual stresses due to a single load/unload cycle. A maximum load sensitivity study was done to determine this value. In separate simulations, starting from the initial residual stress application (bottom left hand portion of Figure 5.11) of the microstructure shown in Figure 5.17, the finite element model was subjected to various peak stresses ($\sigma_{yy,net} = 850$MPa to 1150MPa in 50MPa increments) and then unloaded to zero net stress, $\sigma_{yy,net} = 0$. The resulting overall stress strain behavior and RS relaxation behavior were recorded for each load/unload condition. The following section discusses these results.

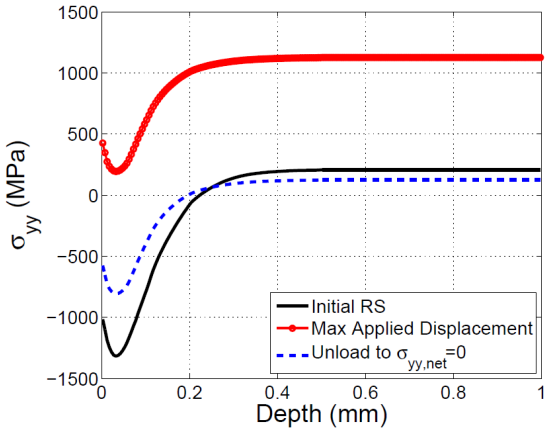

(a) Residual stress (σ_{yy}) relaxation versus depth for displacement-controlled load/unload sequence.

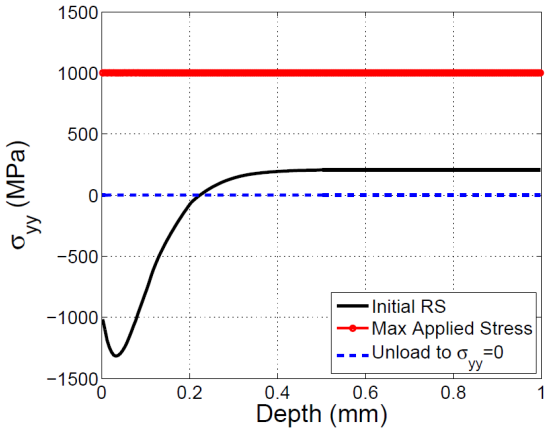

(b) Residual stress (σ_{yy}) relaxation versus depth for stress-controlled load/unload sequence.

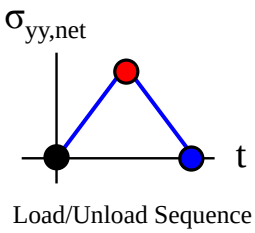

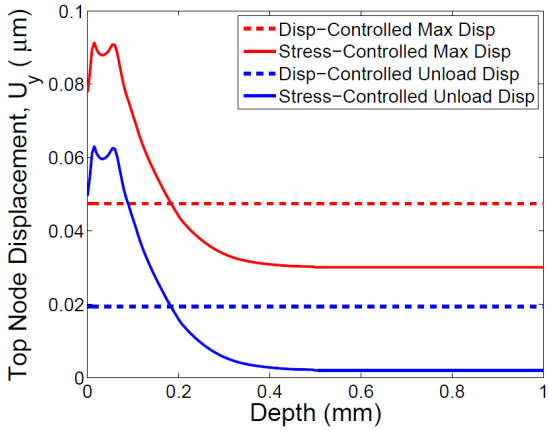

(c) Displacement of top nodes of FEM model as a function of depth for displacement-controlled versus stress-controlled load/unload sequences.

Figure 5.18: Effect of displacement-controlled versus stress-controlled load/unload sequence for residual stress relaxation studies. Maximum net stress in y-direction for both cases is $\sigma_{yy,net} = 1000$ MPa.

5.3.3.2 Residual stress relaxation results

In this section, we compare the simulated relaxation of residual stresses to experimental residual stress relaxation studies on a coarse-grain IN100 at 650°C with average grain size of 25 μm [229]. In Buchanan [229], he presented the residual stress relaxation of two specimens in the axial (y-loading axis) direction and transverse (z) direction due to a single stress-controlled load/unload sequence with σ_{max} = 900 MPa. The XRD measurements of experimental residual stress relaxation are shown in Figure 5.19. The spread in XRD data depicted by the red (axial) and blue (transverse) error bars in this Figure are used for comparison to the simulated residual stress relaxation results presented here.

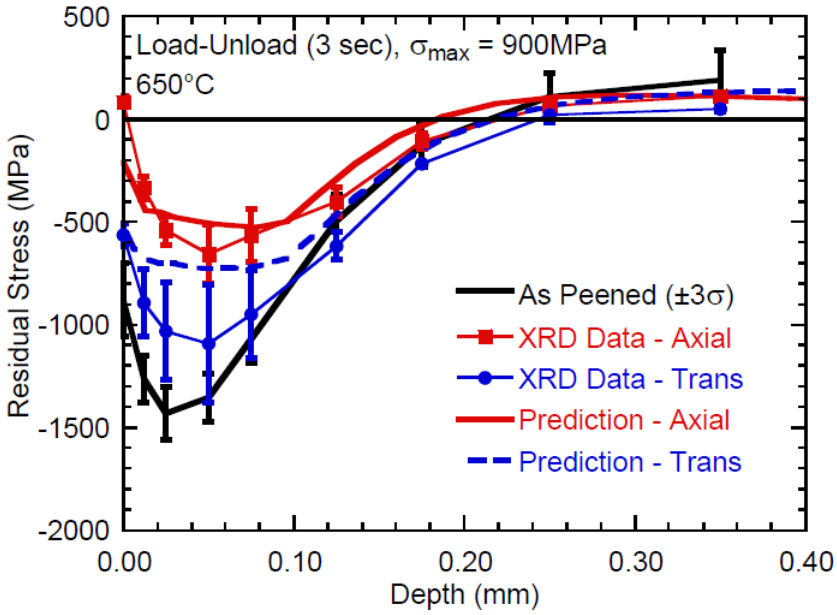

Figure 5.19: Experimental residual stress relaxation in a shot peened CG IN100 dogbone specimen due to a single load/unload sequence at σ_{max} = 900 MPa at 650°C [229].

The average stress-strain behavior of the simulated load/unload sequence for the 1 mm-long specimen as a function of maximum applied stress is shown in Figure 5.20. A peak stress in the range of $\sigma_a = \sigma_{yy,net}$ ~950-1000 MPa was adequate to produce an overall plastic strain in the computational model on the order of that measured in experiments (ε_p ~0.003-0.004).

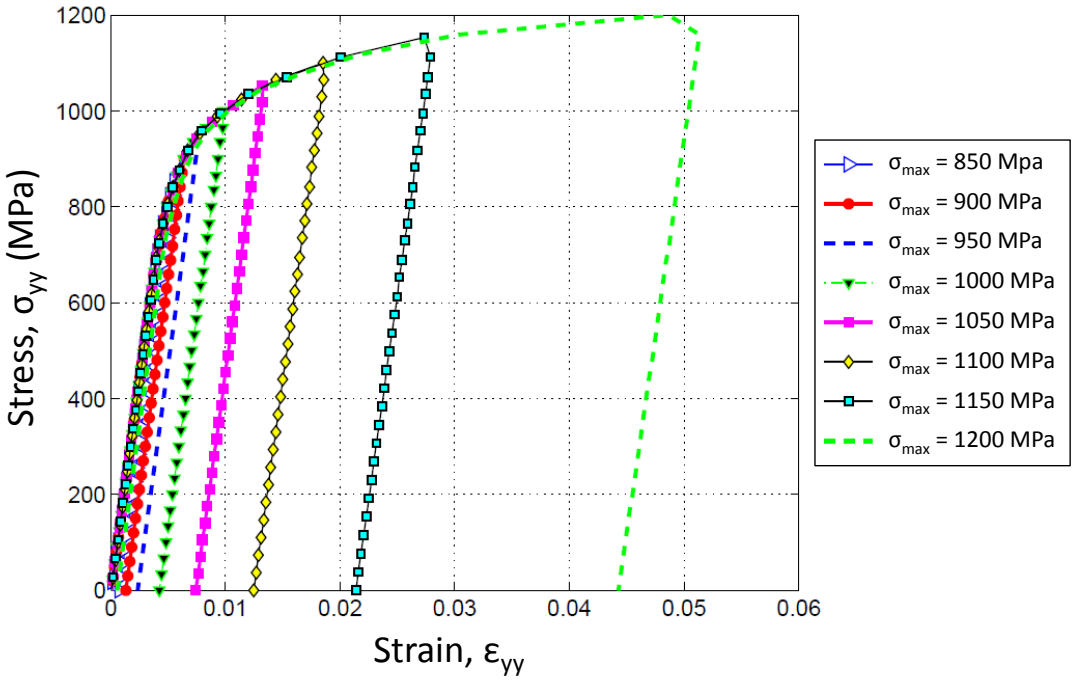

Figure 5.20: Simulated stress-strain (σ_{yy}-ε_{yy}) behavior for different applied maximum stress σ_{yy}.

Pictured in Figure 5.21 is the retained σ_{yy} and σ_{zz} residual stress values as a function of depth and maximum applied stress following the single simulated load/unload sequence. The colors and line types corresponding to each maximum applied stress value are plotted so that they are consistent with those in Figure 5.20. The top portion of this Figure shows the relaxation of the axial (σ_{yy}) stress and the bottom portion shows relaxation of the transverse (σ_{zz}) stress due to the single load/unload sequence. As in previous Figures, the initial residual stress is denoted by the thick black error bars. Also, the gray shaded regions in Figure 5.21 (a) and (b) correspond, respectively, to the axial and transverse target residual stress relaxation profiles depicted in Figure 5.19 that were measured by XRD after unloading [229].

The overall trend of the relaxation curves is as expected: there is an increase in residual stress relaxation as the maximum applied stress is increased. When the maximum stress reaches a value of approximately $\sigma_{max} = 1150$ MPa, the effect of residual stresses are totally negated in the axial direction. As the peak stress increases to a value of $\sigma_{max} = 1200$ MPa, the axial residual stresses become tensile at the surface and go into compression further into the depth ($x > 0.4$ mm, which is not

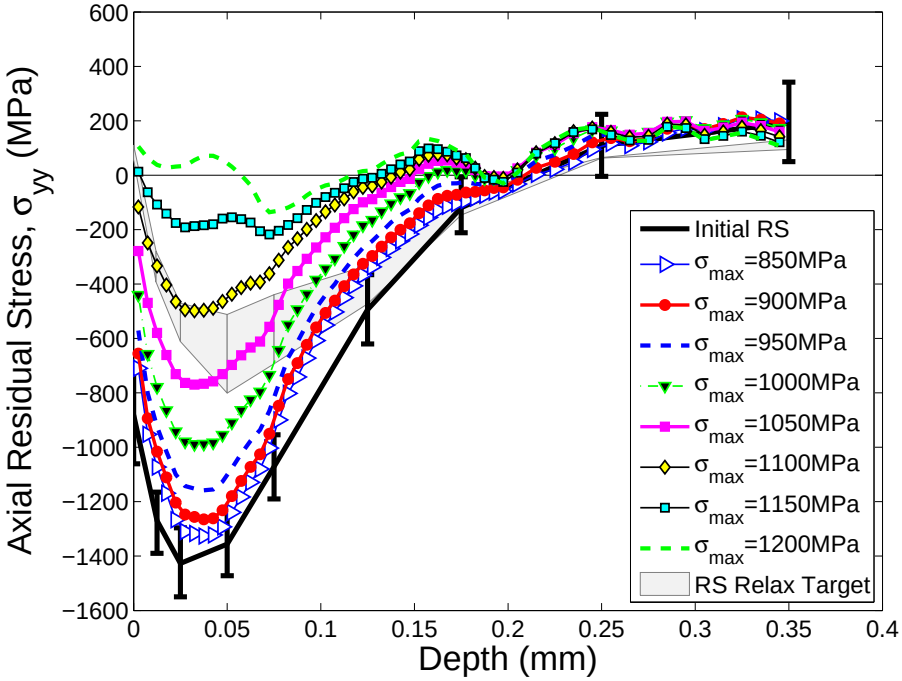

(a) Axial direction (σ_{yy}).

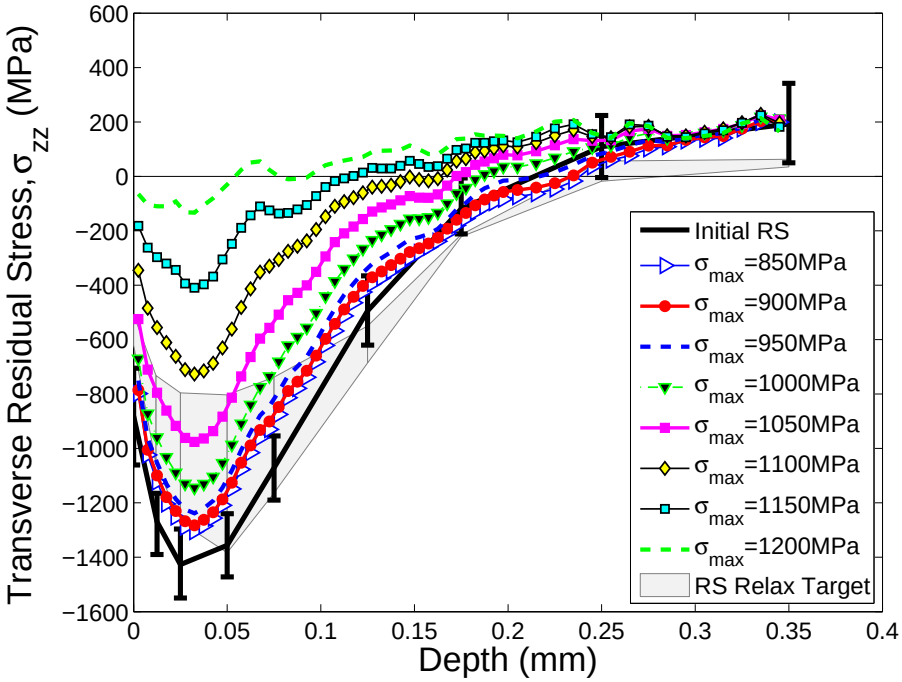

(b) Transverse direction (σ_{zz}).

Figure 5.21: Simulated residual stress relaxation due to a single load/unload sequence as a function of maximum applied stress. The experimental residual stress target relaxation data measured after one cycle are from Buchanan et al. [229].

depicted in these plots) of the model. Although this depth ($x = 0.4$ mm) at which the computational model transitions from tensile to compressive stress is slightly different than the experimental one ($x = 0.2$ mm [211]), the fact that the computational model predicts this reversal of residual stresses is promising.

Comparing the gray-shaded target residual stress relaxation zone to the computational relaxation curves, there is slight difference in curve shape at depths in the range of $x = 0.05$mm to $x = 0.2$mm. The computational model predicts more relaxation (relatively-speaking) in this region as compared to the experimentally-measured relaxation in this region. The reason for this difference is currently unknown, but potential reasons for this discrepancy are discussed in the "Limitations" section below.

The predicted residual stress relaxation at the surface of the specimen in the range of $x < 0.05$ mm seems to follow the experimental trend, despite the error in the range of $x = 0.05$ mm to $x = 0.2$ mm. In the surface region, the peak stress required to get in the range of the experimental residual stress relaxation is around $\sigma_{max} = 1000$-1050 MPa for the axial direction and $\sigma_{max} = 1100$ MPa in the transverse direction. Since there were a range of values of peak stress that resulted in residual relaxation comparable to experiments, three different peak stress values of $\sigma_{max} =$ 1000 MPa, 1050 MPa, and 1100 MPa were used for assessing relaxation behavior scatter.

The same $N = 5$ instantiations that were used for the residual stress profiles in Figure 5.15 were reused here to assess residual stress relaxation scatter. In separate FEM simulations, these finite element models were loaded up to a maximum stress value of $\sigma_{max} = 1000$ MPa, 1050 MPa, or 1100 MPa and then unloaded to zero stress along the $y-$direction. The average residual stress profiles were obtained in the axial and transverse directions. From these values, the statistical spread of the axial and transverse retained residual stresses are plotted in Figure 5.22. In this Figure, the left and right columns contain the retained axial and transverse residual stresses, respectively, for maximum applied stress values of 1000 MPa (top row), 1050 MPa (middle row), and 1100 MPa (bottom row). These simulated values are compared to the statistical spread from 2 separate residual stress relaxation experimental samples

that were depicted in Figure 5.19 [229]. Compared to the experimental residual stress profiles [229], the scatter in residual stress of the computational profiles seems to be within a factor of 2 of the experimental profiles. However, this conclusion is quite preliminary as there were only a limited number ($N = 2$) of data points from the experiments. Further advancement of the residual stress relaxation model would be possible with more experimental and computational replicas.

In the current relaxation study, we only considered relaxation during the first loading cycle. It is well known that relaxation with fatigue cycling occurs in two stages [218]: the majority of residual stress relaxation ocucurs during the first cycle followed by gradual relaxation with continued fatigue cycling. This two stage relaxation process has been reported for multiple materials in several experimental [249–251] and computational [218, 252, 253] studies on residual stress relaxation. In the work of Prasannavenkatesan et al. [125], they considered the effects of shot peening-induced surface residual stresses, pores, and hard and soft primary inclusions in martensitic gear steel on nonlocal FIPs and fatigue crack formation near the inclusions. They concluded that residual stress relaxation could only be modeled using polycrystal plasticity [218].

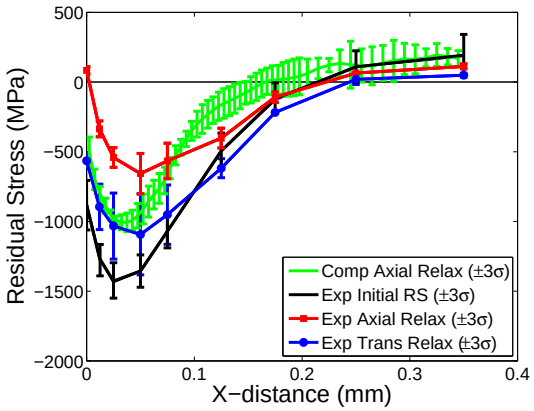

(a) Axial (σ_{yy}) relaxation, $\sigma_{max} = 1000$ MPa.

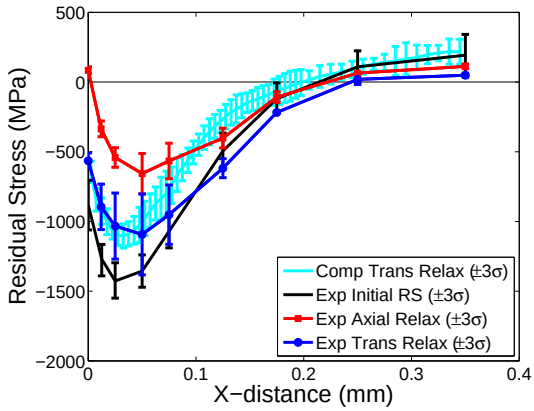

(b) Transverse (σ_{zz}) relaxation, $\sigma_{max} = 1000$ MPa.

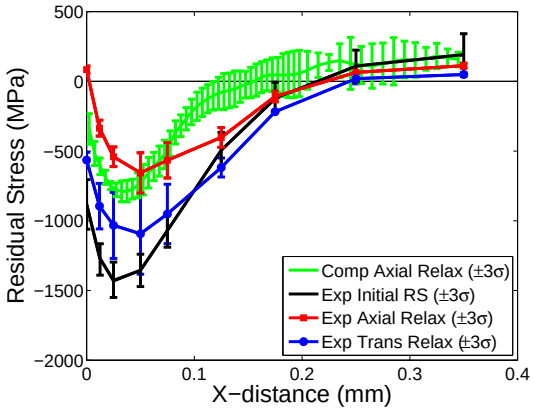

(c) Axial (σ_{yy}) relaxation, $\sigma_{max} = 1050$ MPa.

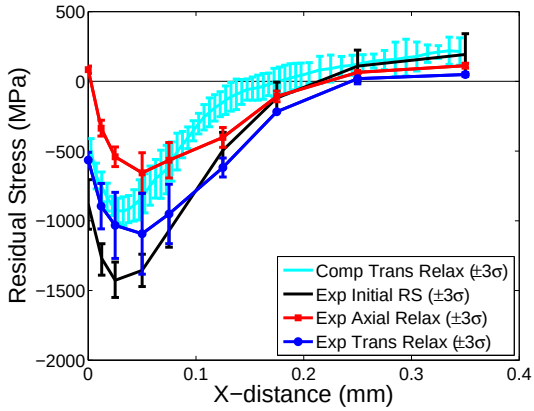

(d) Transverse (σ_{zz}) relaxation, $\sigma_{max} = 1050$ MPa.

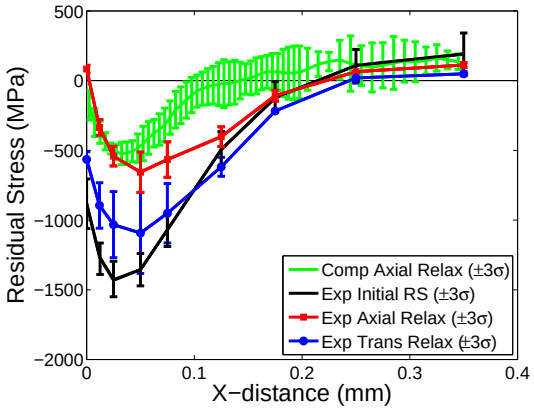

(e) Axial (σ_{yy}) relaxation, $\sigma_{max} = 1100$ MPa.

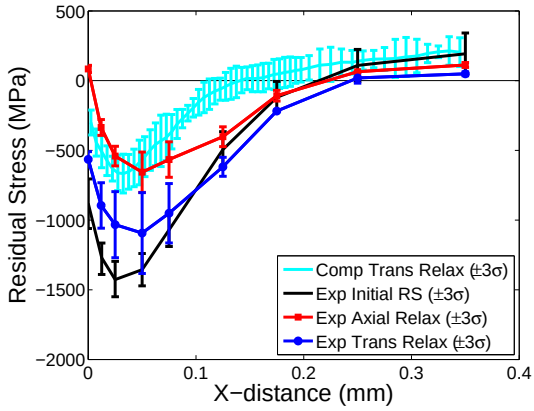

(f) Transverse (σ_{zz}) relaxation, $\sigma_{max} = 1100$ MPa.

Figure 5.22: Simulated versus experimental scatter in residual stress relaxation due to a single load/unload sequence for 3 different maximum applied stresses ($\sigma_{max} = 1000$ MPa, $\sigma_{max} = 1050$ MPa, and $\sigma_{max} = 1100$ MPa) and N = 5 instantiations. The experimental residual stress scatter data are from Buchanan et al. [229].

5.3.4 Limitations of the CPFEM relaxation model

There are many limitations in this model that can cause some errors in the relaxation predictions. First, the computational model contains a domain decomposition of the material into crystal plasticity and J2 plasticity models. Although these two models were calibrated to the same set of experimental data, the difference in anisotropic crystal plasticity and isotropic J2 plasticity can cause differences in material stress/strain behavior over the range of several grains. For example, Figure 5.16 shows that the mean residual stress behavior averaged over a bin size of $x = 5$ μ, $y = 0.17$ μm, and $z = 0.17$ μm can vary up to $\sim$200-250 MPa. This scatter further increases when averaging over individual elements (Figure 5.15) or the scale of individual grains. On the other hand, a J2 plasticity FEM smears the effect of anisotropy and predicts a single residual stress profile as a function of depth with no scatter. Additionally, it should be noted that these material models were fit to a coarse grain IN100 with a slightly larger grain size (34 μm) than the IN100 microstructure used for the residual stress experiments (25 μm).

Another potential source of error could be due to the fact that this model is a quasi-static representation of a dynamic shot peening process. Shot peening involves high speed collision of many shot beads against a surface. The current model does not take into account such dynamic effects as elastic wave propagation, high strain-rate effects, or inertia effects. Previous studies by Chen and Hutchinson [220, 221] and Boyce et al. [219] on single impact events indicated that explicit dynamic analyses incorporating strain-rate sensitivity and elastic wave propagation provided better residual stress prediction for high-velocity (300 m/s in their case) impact as opposed to using a quasi-static analysis. Additionally, the intense amount of cold working and very dense dislocation network produced at the surface (ref. Figure 5.4(b)) can invoke plasticity-induced refinement of the microstructure in the surface layer, as evidenced by the SEM image of the as-peened CG IN100 microstructure in Figure 5.4 from ref. [229]. This refinement in the microstructure was not accounted for in this work. However, the overall purpose of the current model was to simulate the overall induced

mechanical response due to shot peening, rather than individual impact events or grain refinement.

Regardless of these limitations, the current framework does a relatively good job at reproducing the initial residual stress profile scatter and relaxation scatter. While the total profile of the residual stress relaxation curves are not exactly inline with experiments, the computationally-predicted relaxation trends near the surface correlate well with experiments. Therefore, the current quasi-static eigenstrain application of residual stresses is deemed reasonable for assessing the effect of residual stresses and microstructure on fatigue variability.

5.4 Summary

In this work, a framework for imposing shot-peened residual stresses using computational crystal plasticity is presented. The residual stresses are induced by a distribution of quasi-thermal expansion eigenstrains. This distribution was first fitted to an experimentally-measured residual stress curve using an isotropic J2 plasticity material behavior and then applied within a crystal plasticity finite element constitutive model. Good correlation between computational and experimental values were obtained for (1) the initial residual stress profile, (2) the scatter in the initial residual stress profile among multiple instantiations, and (3) near surface residual stress relaxation trends for a single load/unload cycle. This method of coupling the effect of microstructure and residual stresses can be used to investigate the effect of certain microstructural features (such as the largest grain, inclusions, pores, etc.) on microstructure-sensitive fatigue estimation. Thus, this framework has great potential to help advance the field of ICME in the field of predictive probabilistic lifing of components containing shot-peened residual stresses that are subjected to fatigue loading. In the next Chapter, we use it to model the effect of residual stresses on near surface inclusions.

CHAPTER 6
SIMULATING EFFECTIVENESS OF RESIDUAL STRESSES ON FATIGUE OF NEAR-SURFACE NONMETALLIC INCLUSIONS

6.1 Introduction

As indicated in the previous Chapter, surface compressive residual stresses are often induced in components to suppress near-surface fatigue crack initiation and shift the fatigue crack initiation further into the bulk of the material. Since internal fatigue cracks often require more fatigue cycles to failure than cracks emanating from the surface, components containing shot-peened surface compressive residual stresses should be able to withstand more fatigue cycles than their unpeened counterparts. In this Chapter, we build on the MSC growth model established in Chapter 3, the modeling of debonded inclusions in Chapter 4, and the eigenstrain-based application of residual stresses in Chapter 5 to focus on simulating the effect of shot-peened residual stresses on a single inclusion located at different depths from the specimen surface. The overall purpose of this Chapter is to simulate the effectiveness of residual stresses at different strain amplitudes (LCF to VHCF regimes) to be able to reproduce the experimental trends previously discussed in Chapter 5 in Figure 5.2 which is replotted here in Figure 6.1 for convenience. This Figure displays that residual stresses are only beneficial in the transition fatigue regime around $N = 10^4 - 5 \times 10^5$ cycles. At lower strain amplitudes, internal fatigue crack initiation occurs for peened and unpeened conditions, so surface compressive residual stresses have little effect on fatigue performance. At higher strain amplitudes, residual stress relaxation can occur with cyclic loading so that surface initiation can still occur.

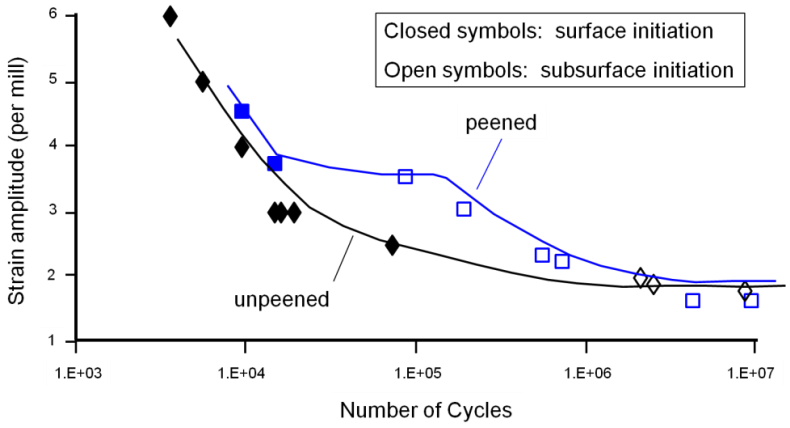

Figure 6.1: Effect of shot peening on strain life diagram for a Ni-base superalloy smooth specimen [213].

6.2 Methodology

In Chapter 5, a methodology for imposing compressive residual stresses within a crystal plasticity finite element framework was established for a simulated smooth specimen. Figure 5.10 showed the approximation of the smooth specimen as a rectangular prism and Figure 5.13 showed an example of a combined polycrystal plasticity and J2 plasticity finite element model used for eigenstrain-based application of residual stresses. In this Chapter, the combined J2 plasticity/CPFEM eigenstrain-based method of residual stress imposition is applied to a smooth specimen finite element model containing a single debonded inclusion. In Chapter 4, the decohesion of the inclusion/matrix interface was simulated using a *UHypel subroutine material behavior in ABAQUS. Direct application of this *UHypel approach to a debonded inclusion in the presence of residual stress caused erroneous predicted residual stresses and convergence issues, which are discussed in the next section. This motivated the use of an alternative means to model the debonded material using a "cast iron plasticity" model in ABAQUS [45].

6.2.1 Issues with *UHypel material behavior in presence of compressive residual stresses

As a first attempt to apply residual stresses to a debonded inclusion within a polycrystalline matrix, the *UHypel material behavior in Figure 6.2 with $A = 1000$ was used to model the debond material between the inclusion and polycrystalline matrix. Frequently in modeling an inclusion within a matrix material, due to the fact that the inclusion is much stiffer than the matrix, it is often assumed that the inclusion is linear elastic and isotropic. The use of a completely linear elastic/isotropic inclusion produced high residual stress values in the region near the inclusion when the eigenstrain-based method of residual stress application was used (ref. Figure 6.3). Figure 6.3(a) shows the full FEM model with dimensions $x = 5$ mm, $y = 0.15$ mm, and $z = 0.15$ mm used to assess the effect of an elastic inclusion and the *UHypel subroutine material behavior depicted in Figure 6.2. The different colors near the surface ($x = 0$) indicate grains where the CPFEM constitutive model was used. Crystal plasticity was used in elements that were $x \leq 0.11$ mm from the surface, minus the volume occupied by the 50-μm inclusion and 1-μm thick debonded region blanketing the upper hemisphere of the inclusion. Figure 6.3(b) is a zoomed-in section view of the FEM model near the surface to show the inclusion (red) centered about the y and z dimensions of the FEM model and located at a depth of $h = 10$ μm from the surface. Figure 6.3(b) displays the domain decomposition of the finite element model showing the debonded material (yellow), the grain structure surrounding the inclusion, and the J2 plasticity region (gray). Figure 6.3(c) shows the side view of the sectioned FEM model displaying the Von Mises equivalent stresses after residual stress application. As evidenced in Figure 6.3(c) there is an intense increase in residual stresses due to the existence of the assumed linear elastic inclusion. These higher residual stress values were due to the inclusion being stiffer than the matrix, which for the same amount of applied eigenstrain, the inclusion will produce higher residual stress values.

In reality, the inclusion would not be able to sustain these very high compressive stresses without yielding. Therefore, the inclusion was assumed to be composed of an elastic-perfectly plastic material with a yield strength of 1345 MPa [197]. A simple J2

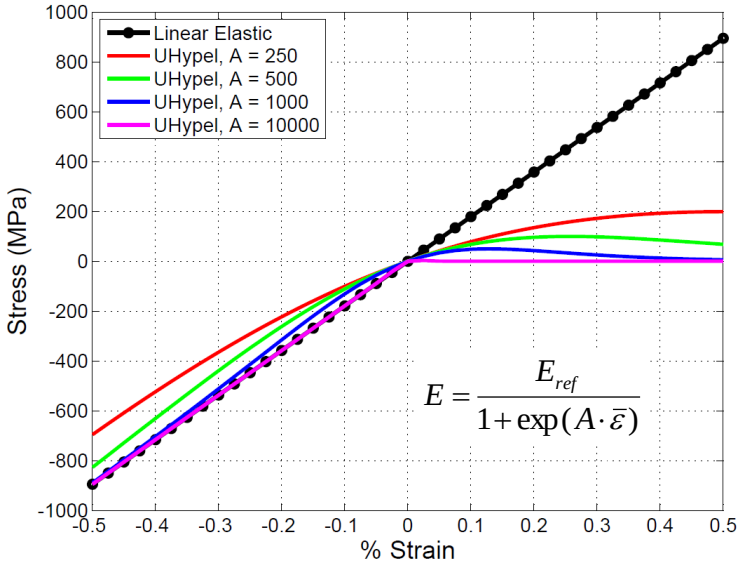

Figure 6.2: Example tension/compression asymmetric behavior of the stress strain diagram comparing different values of the amplification factor, A, within the **UHypel* subroutine in ABAQUS.

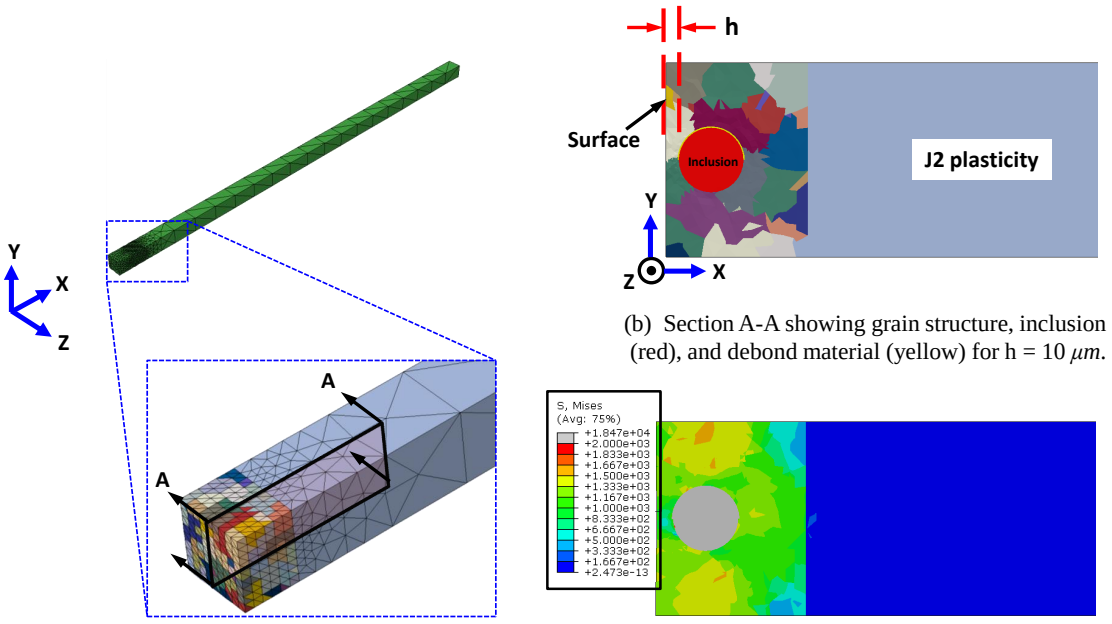

(a) Finite element model mesh for inclusion depth, h = 10 μm.

(b) Section A-A showing grain structure, inclusion (red), and debond material (yellow) for h = 10 μm.

(c) Von Mises stresses after quasi-thermal expansion residual stress application for h = 10 μm.

Figure 6.3: Example grain structure and Von Mises stress distribution for direct application of eigenstrain method for a linear elastic inclusion at depth, $h = 10$ μm.

plasticity model was constructed to test this method out for a fully-bonded inclusion. The resulting residual stress contour plot and binned values of the residual stress as a function of depth from the surface are shown in Figure 6.4. This Figure displays the importance of incorporating inclusion yield stress for the eigenstrain application of residual stress.

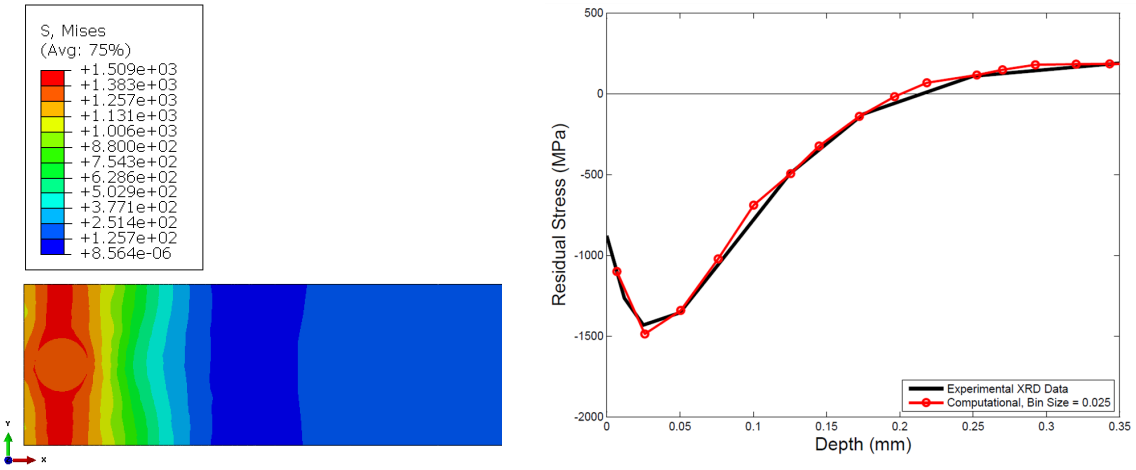

Figure 6.4: Residual stress contour plot and binned residual stress values as a function of depth for the assumption that the inclusion has isotropic elastic-perfectly plastic material properties. The inclusion is located at $h = 10$ μm for a finite element width, $W = 150$ μm, and height, $H = 150$ μm.

6.2.2 UHypel technique incorporating "elastic/plastic" response

Since the inclusion and the matrix require elastic/plastic responses for quasi-thermal eigenstrain application of residual stresses in a finite element framework, an effort was made to incorporate an "elastic/plastic" response for the UHypel subroutine material response of the debonded material. The stress strain response was split into two piecewise smooth curves as

$$\sigma = A \cdot \left[\frac{1}{1 + \exp\left(-B \cdot (\overline{\varepsilon} - C)\right)} - 1 \right] \cdot E_{ref} \tag{6.1}$$

$$\sigma = \frac{D}{F\sqrt{2\pi}} \cdot \exp\left[-\frac{(100 \cdot \overline{\varepsilon} - G)^2}{2F^2} \right] \cdot \overline{\varepsilon} \tag{6.2}$$

where values of A = 0.0075, B = 700, C = -0.0035, D = 1.4965e5, F = 0.3, and G = -0.5 were used in Equations 6.1 and 6.2 to model the left hand side (red) and right hand side (green) of the **UHypel* curves shown in Figure 6.5. The value of E_{ref} = 179 GPa corresponds to the macroscopic elastic modulus of the polycrystalline matrix material. Figure 6.5(a) shows the simulated stress strain behavior for the polycrystalline matrix if it were linear elastic, the assumed elastic-perfectly plastic response of the inclusion, and the proposed two-piece UHypel curve to simulate the debond region. The simulated debond material behavior is elastic-perfectly plastic in compression and fully compliant in tension as signified by the two-piece UHypel "S-curve" in Figure 6.5(a). The form of the two Equations 6.1 and 6.2 for the **UHypel* subroutine are (1) a sigmoidal shape (red curve) for the stress versus strain material behavior and (2) a normal distribution (green curve) for the modulus versus strain plot so that the modulus decays smoothly to zero (fully debonded) as the strain increases above zero. Ideally, it would have been easier to only use one curve, but since ABAQUS requires the modulus to be defined within the **UHypel* subroutine and a sigmoidal curve is specified for the stress versus strain plot (red curve), the modulus is defined in the **UHypel* subroutine by dividing the stress by strain. This becomes problematic as the strain approaches zero (ref. Figure 6.5(b)) because the modulus approaches infinity and the simulation crashes with a divide by zero error. Therefore, the second normal distribution of the modulus versus strain (green curve) was added

with the requirements that (1) there was a smooth transition (C0 and C1 continuity) between the two curves and (2) that the stress smoothly decays to zero as the strain transitions from compressive to tensile strain to simulate the debonded condition.

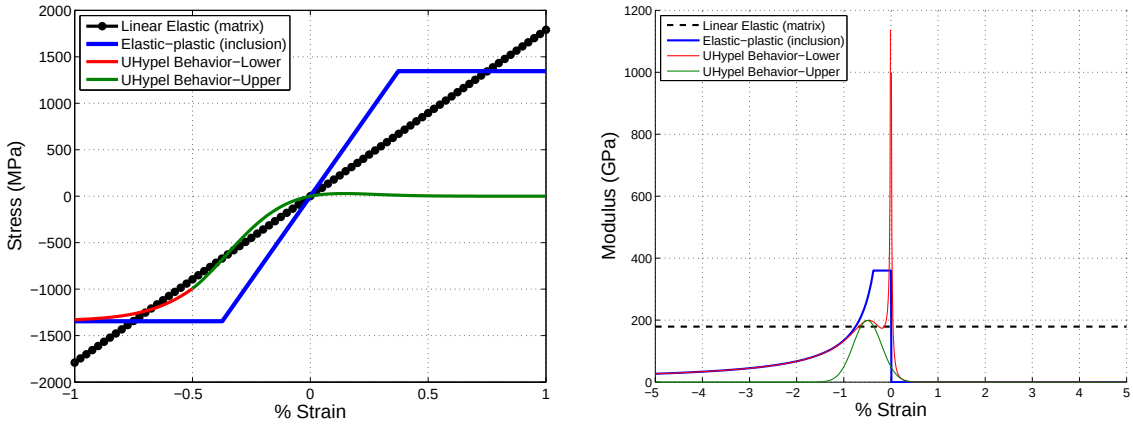

(a) Stress versus strain behavior.

(b) Modulus versus strain behavior.

Figure 6.5: Example tension/compression asymmetric behavior of the (a) stress versus strain and (b) modulus versus strain diagram for the behavior of the debonded region that is implemented in ABAQUS using the **UHypel* subroutine. The green and red portions of the **UHypel* curves can be deduced from Equations 6.1 and 6.2, respectively.

A severe issue was encountered when this 2-curve "elastic/plastic" UHypel subroutine was implemented in ABAQUS. To maintain the elastic-perfectly plastic material behavior in compression, the modulus must continually decrease with increase in compressive strain as shown in Figure 6.5(b). With increasing compressive strain, the finite elements essentially go into an artificial state of buckling, resulting in negative eigenvalues and numerical instability; the simulations eventually crash. Therefore, this 2-curve "elastic/plastic" UHypel subroutine was discarded in favor of the assymetric elastic/plastic "cast iron plasticity" model covered in the next section.

6.2.3 Elastic/plastic material model used for debond region

In the previous sections, we justified the use of an elastic/plastic material response for the simulated non-metallic inclusion and the debond region between the inclusion and the polycrystalline matrix; we also disproved the ability of the UHypel subroutine

to model this behavior successfully for the quasi-thermal eigenstrain application of residual stresses in an FEM scheme. In this section, we discuss the use of a "cast iron plasticity" constitutive model in ABAQUS to mimic the required debond material response in tension (fully compliant) and compression (stiffness retained). While the cast iron plasticity model is intended for constitutive modeling of gray cast iron under monotonic conditions [45], the ability to define different yield strengths, plastic flow, and hardening in tension and compression in a built-in ABAQUS material model [45] were desired characteristics for modeling the debond material. The yield function in tension is a function of the maximum principal stress and the yield function in compression is a Von Mises equivalent stress based function [45].

Figure 6.6 shows results for uniaxial (a) monotonic and (b) cyclic stress strain response of the cast iron plasticity material model. In compression, the elastic/plastic stress strain response was defined by the tabular (stress versus plastic strain response) method in ABAQUS [45]. In tension, the material was assumed to be elastic-perfectly plastic with a yield strength of 300 MPa. The reason for a nonzero yield point in tension is discussed further in the results section. To display the history dependence of the model, one uniaxial strain-controlled load sequence between ε_{max} = 5% and ε_{min} = -5% was simulated in order of compression-tension-compression and another load sequence was simulated in order of tension-compression-tension. The resulting stress strain response for these two sequences are shown in Figure 6.6(b). This Figure shows a slight history difference in tension-compression-tension loading versus compression-tension-compression loading, due to different hardening behaviors in tension and compression. However, with continued cycling, the cast iron plasticity material will harden to a point where both curves will coincide, producing an essentially elastic/perfectly plastic stabilized hysteresis loop with the maximum allowable tensile stress being 300 MPa.

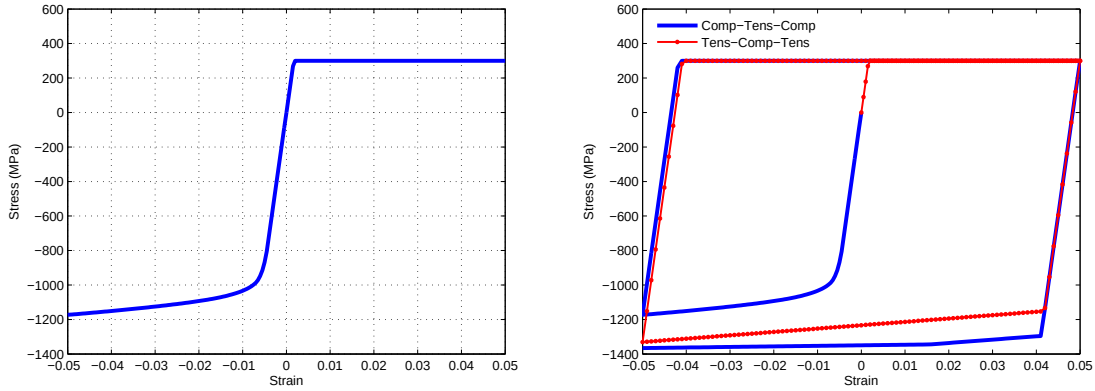

(a) Monotonic stress strain response

(b) Cyclic stress strain response

Figure 6.6: Stress strain response used to model debonded region.

6.2.4 FEM model used to simulate residual stress effects on inclusions at various depths

To analyze the effect of residual stresses on inclusions of various depths, a single inclusion at various depths from the surface was considered. *Only* 5 different finite element meshes were used, one for each depth: h = 10, 25, 50, 100, and 200 μm. For each depth, two initial conditions were considered (with and without initial compressive residual stresses due to shot peening) for fatigue loading at maximum strain values ranging from $\varepsilon_{max} = 0.4\varepsilon_y$ to $1.8\varepsilon_y$ in increments of $0.2\varepsilon_y$, where ε_y = 0.042% is the proportional limit of the material. The purpose of using these selected input variables for inclusions of different depths with and without residual stresses is to assess the predictive capabilities of the FEM model to estimate effectiveness of residual stresses in extending fatigue life over a wide range of fatigue regimes (LCF to VHCF). Strain-controlled loading was used for all cases with $R_\varepsilon = 0.05$. Ten fatigue loading cycles were simulated for the cases where initial residual stresses were present because ten cycles offered a more stabilized cyclic FIP and residual stress response over just using three cycles. The boundary conditions used for the cyclic fatigue loading were identical to those previously used for the residual stress relaxation study in Chapter 5 (ref. Figure 5.17).

The five structured C3D8 finite element meshes used for the simulation of residual

stress effects on inclusions of various depths from the surface are illustrated in Figure 6.7. Each 3D finite element model had dimensions $x = 1.0$ mm, $y = 0.136$ mm, and $z = 0.136$ mm. The x and z dimensions correspond to approximately 4 grains through the thickness of the specimen. The previously described crystal plasticity model (ref. Ch. 5) with quasi-thermal eigenstrain expansion is employed for elements that are within $x = 0.35$ mm from the surface, minus the elements assigned to the inclusion and the debond material (ref. Figure 6.7(b)). The aforementioned J2 plasticity model in Ch. 5 was assigned to elements that are at an x-depth greater than 0.35 mm from the surface. The finite elements are 5 μm $\times$ 5 μm $\times$ 5 μm in size at the surface and inclusion regions and slowly coarsen out with increasing x-depth as shown in Figure 6.7(a).

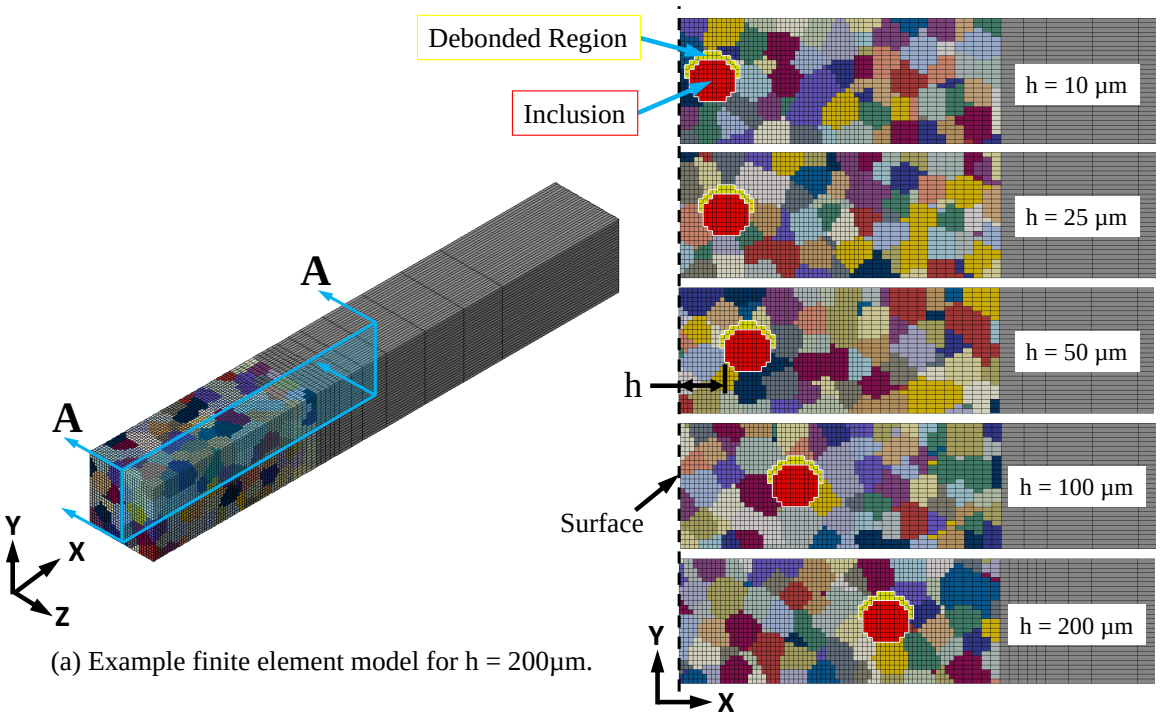

(a) Example finite element model for h = 200µm.

(b) Section A-A showing FEM meshes for inclusions at various depths.

Figure 6.7: Schematic showing example finite element meshes for the simulation of residual stress effects on inclusions of various depths from the surface.

6.3 Results and Discussion

6.3.1 Effect of maximum allowable stress of debond material

An FEM model was created to determine the effect of maximum allowable stress of the debond material on the residual stress field. For this model, the 50-μm inclusion was located at a depth of $h = 25$ μm corresponding to the location of peak compressive residual stress. This FEM model was similar to Figure 6.7 and had overall dimensions of 1 mm $\times$ 0.15 mm $\times$ 0.15 mm. A half-section (Section A-A in Figure 6.7) view of the simulated polycrystalline microstructure, inclusion, and debond material are shown in Figure 6.8(a). Figures 6.8(b)-(d) show contours of the Von Mises equivalent residual stress after the surface constraint has been released (ref. Fig. 5.11) for maximum allowable stresses in the debond region of $\sigma_{T,allow} = 100$ MPa, 200 MPa, and 300 MPa, respectively. The contours of VM stress are all similar in these Figures minus the region circled in Figure 6.8(b), which is enlarged in the inset of this Figure. This lower Von Mises portion in this Figure signifies fallacious debonding of the inclusion from the matrix. This false debonding of the inclusion from the matrix disappears in Figures 6.8(c) and (d) for a higher maximum allowable tensile stress for the debond region material behavior. In fact, a slight increase in the maximum allowable tensile stress from $\sigma_{T,allow} = 100$ MPa to $\sigma_{T,allow} = 200$ MPa increased the VM stress in this false debond region from $\sim$150 MPa to $\sim$850 MPa.

The reason for the false debonding in Figure 6.8(b) is due to the way in which quasi-thermal residual stresses are applied to the smooth specimen. In the "release surface constraint" step (ref. bottom left portion of Figure 5.11) of the imposition of residual stresses, the surface constraint is released so that the *net* stress component normal to the surface is negligle ($\sigma_{xx} \sim 0$). However, stresses within a polycrystalline ensemble are heterogeneous at the grain scale. Although the net stress in the x direction is close to zero, the local stress within the grain next to the debond region could be tensile, causing the artificial debonding of the inclusion from the matrix. Therefore, to avoid the potential for artificial debonding, a maximum allowable tensile stress within the debond material region was set to $\sigma_{T,allow} = 300$ MPa for all subsequent simulations.

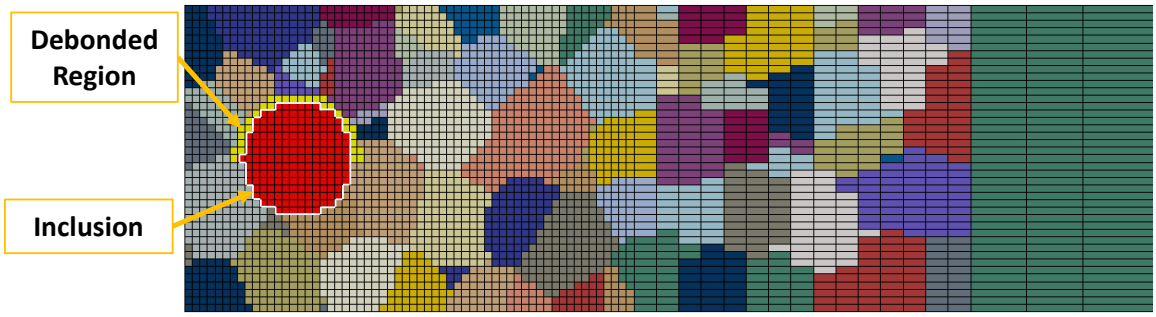

(a) Polycrystalline grain structure for inclusion depth h = 25 µm and inclusion diameter φ = 50 µm.

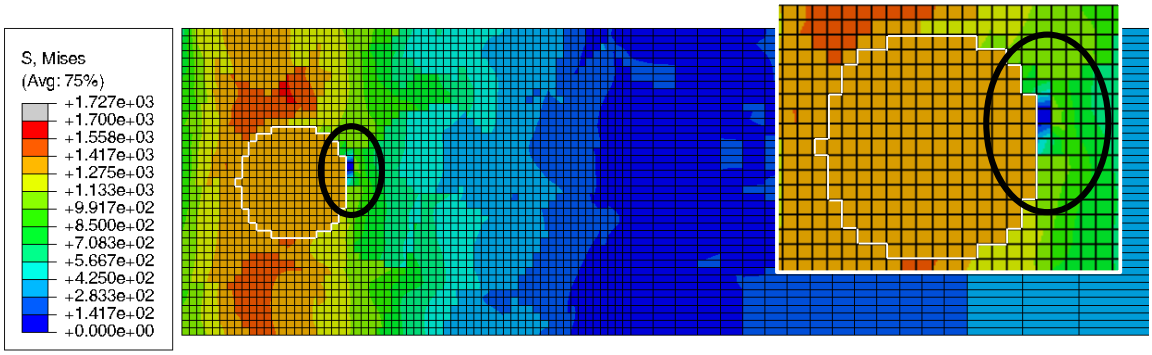

(b) Von Mises residual stress for maximum tensile stress allowable of debonded region, $\sigma_{T,allow}$ = 100 MPa. Inset displays larger view near inclusion.

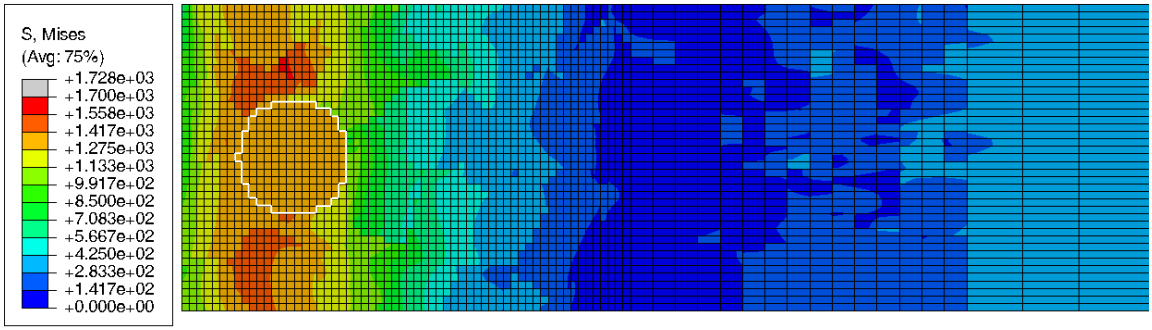

(c) Von Mises residual stress for maximum tensile stress allowable of debonded region, $\sigma_{T,allow}$ = 200 MPa.

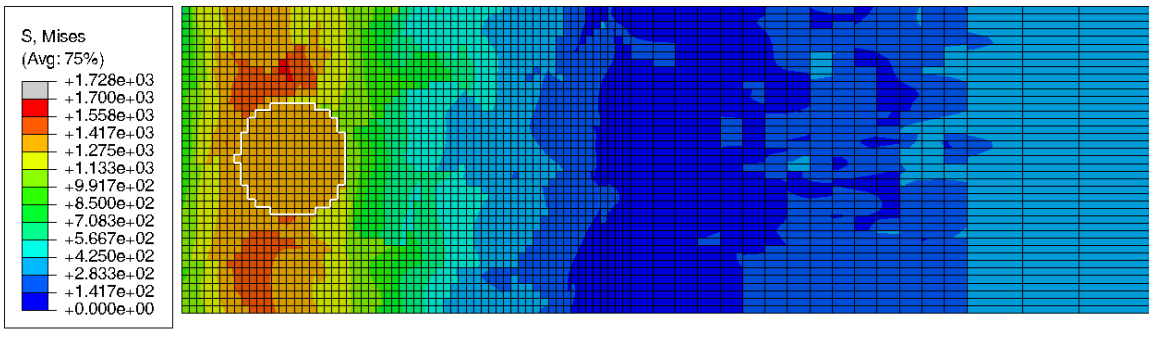

(d) Von Mises residual stress for maximum tensile stress allowable of debonded region, $\sigma_{T,allow}$ = 300 MPa.

Figure 6.8: Residual stress results for debonded region having different maximum allowable stresses. All values of stress are in MPa.

6.3.2 Relaxation of residual stresses with cycling

Figure 6.9 shows the relaxation of residual stresses with cycling for the finite element model in Figure 6.7 containing an inclusion at a depth of $h = 10$ μm for depth measurements of $x = 0$ (surface), 10 μm, 25 μm, and 50 μm. The y-component of residual stress, σ_{yy}, is normalized by the intial y-component of residual stress, $\sigma_{yy,RS}$, at each given depth. The colorbar on the right of each plot indicate the maximum strain amplitude applied for each curve color. For this Figure, maximum strain values between $0.4\varepsilon_y$ and $1.8\varepsilon_y$ ($\varepsilon_y = 0.42\%$ is the proportional limit of the material) in increments of $0.2\varepsilon_y$ are plotted. For constant strain amplitude loading, the majority of relaxation occurs in the first cycle (up to ∼15-30% for the highest strain amplitude). Cyclic relaxation in the subsequent cycles also occurs, but only to a small extent. As expected, the relaxation of residual stresses increases with maximum applied strain amplitude. Similar results have been reported for multiple materials in several experimental [249–251] and computational [218, 252, 253] studies on residual stress relaxation.

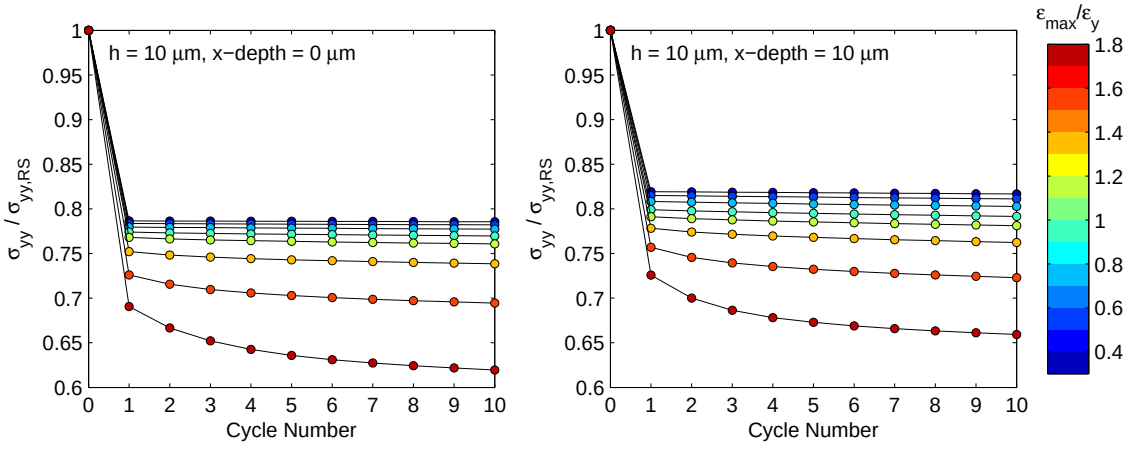

(a) x-depth = 0 μm (surface).

(b) x-depth = 10 μm.

(c) x-depth = 25 μm.

(d) x-depth = 50 μm.

Figure 6.9: Relaxation of residual stresses with cycling for inclusion located at depth of $h = 10$ μm as a function of maximum applied strain amplitude.

6.3.3 Evolution of FIP distribution with cycling

The evolution of grain-averaged maximum noncrystallographic FIP_{FS} with cycle number is shown in Figure 6.10 for the highest maximum applied strain case, ε_{max} = 1.8ε_y (ε_y = 0.42%), and an inclusion depth h = 10 μm. This strain amplitude was chosen because it resulted in the highest amount of cyclic relaxation and FIP evolution. In this Figure, the change in FIP for the jth grain (grn, j) over the kth cycle (cyc, k) is normalized by the FIP value of the jth grain computed over the 10th simulated fatigue cycle $(cyc, 10)$ and is given by

$$\text{normalized } \Delta FIP^{grn,j}_{cyc,k} = \frac{FIP^{grn,j}_{cyc,k} - FIP^{grn,j}_{cyc,k-1}}{FIP^{grn,j}_{cyc,10}} \tag{6.3}$$

This equation was evaluated for each grain (j = 1 to 315) and each cycle (k = 2 to 10, indicated by the colorbar). The results in Figure 6.10 show that the normalized change in FIP decreases with cycle number and approaches a steady state change in normalized FIP with change in cycle.

A clearer illustration of this steady state change in normalized FIP with change in cycle is shown in Figure 6.11. In this Figure, the normalized change in FIP with change in cycle is averaged over all grains, i.e.

$$\text{mean}\left(\text{normalized } \Delta FIP_{cyc,k}\right)\big|_{N\_grns} = \sum_{j=1}^{N\_grns} \frac{1}{N\_grns}\left[\frac{FIP^{grn,j}_{cyc,k} - FIP^{grn,j}_{cyc,k-1}}{FIP^{grn,j}_{cyc,10}}\right] \tag{6.4}$$

Figure 6.11 shows a significant amount of transient change in FIP behavior in the first few cycles due to initial residual stress relaxation and subsequent relaxation with continued cycling. This transient behavior of change in FIP with each cycle begins to approach a steady state behavior around cycle number 8-10. Since we are interested in calculating the driving force for fatigue crack incubation and early propagation over a stabilized loading cycle, the FIP used for estimation of MSC growth in the presence of residual stresses is computed over the 10th loading cycle.

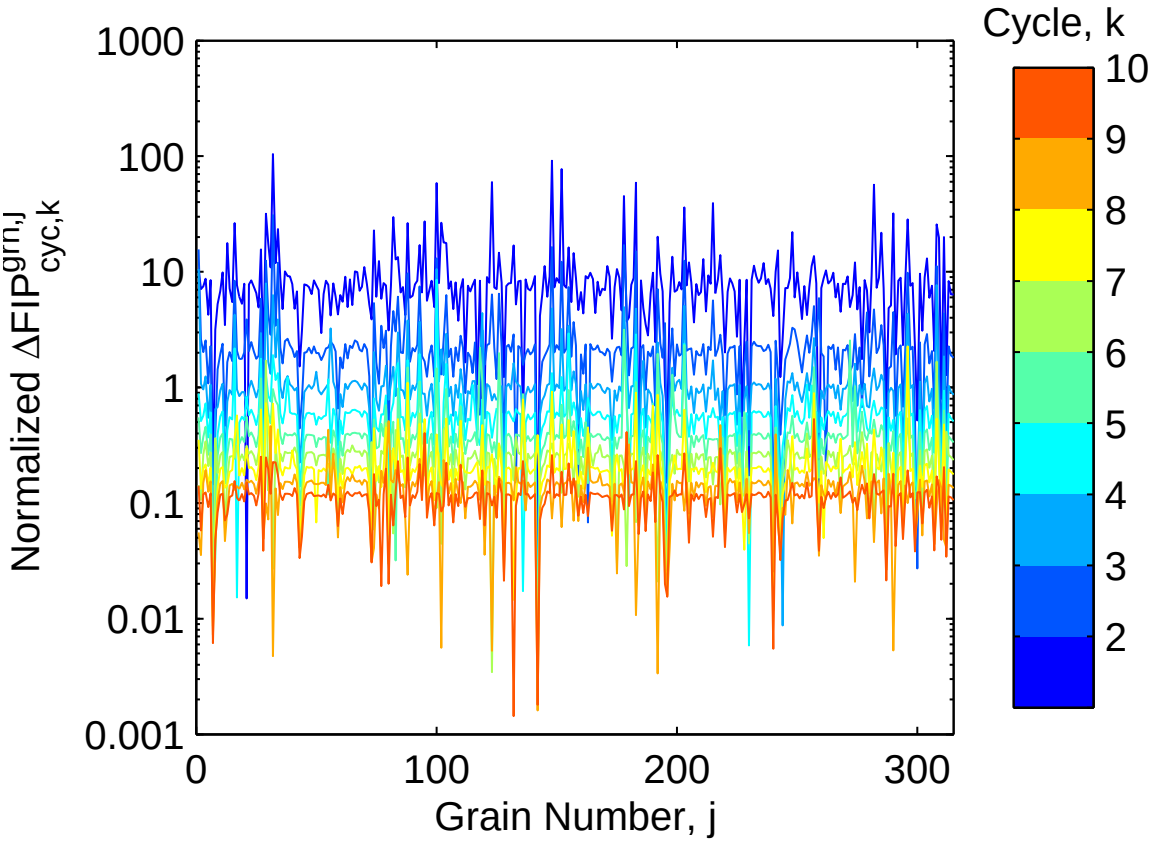

Figure 6.10: Evolution of FIP distribution within grains for all grains in $h = 10$ μm instantiation under $\varepsilon_{max} = 1.8\varepsilon_y$ strain-controlled loading.

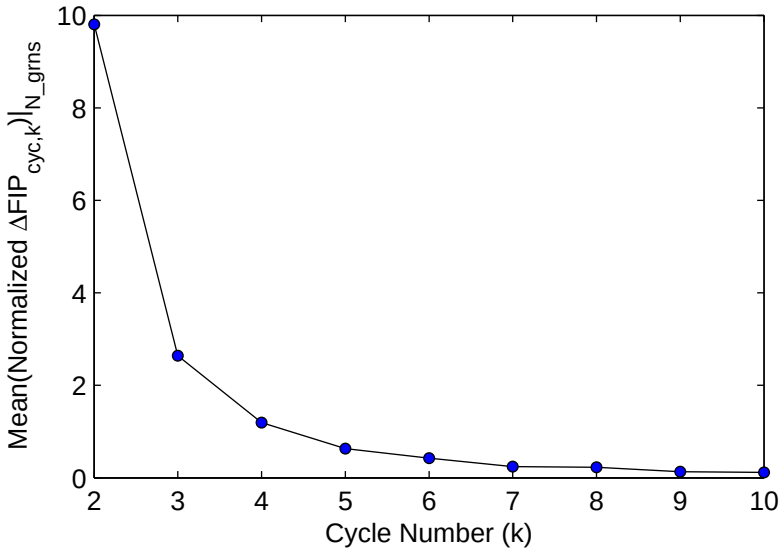

Figure 6.11: Mean evolution of normalized FIP within all grains for $h = 10$ μm instantiation under $\varepsilon_{max} = 1.8\varepsilon_y$ strain-controlled loading.

6.3.4 FIP and maximum stress distribution as a function of applied strain amplitude

Figure 6.12 shows the effect of applied strain amplitude on the maximum grain-averaged non-crystallographic FIP for different inclusion depths for the case of initial residual stresses applied (left column) and no initial residual stresses applied (right column) prior to cyclic loading. The maximum non-crystallographic FIP_{FS} values plotted in Figure 6.12 were binned every $x = 17$ μm for ease of displaying differences among different maximum applied strain loading cases. The colorbar indicates the normalized maximum strain applied $\varepsilon_{max}/\varepsilon_y$, where $\varepsilon_y = 0.042\%$ is the proportional limit of CG IN100. The FIP values for the left column (initial residual stress) are shown for $\varepsilon_{max} = 0.4\varepsilon_y$ to $\varepsilon_{max} = 1.8\varepsilon_y$ in increments of $0.1\varepsilon_y$, whereas the FIP values for the right column (no initial residual stress) are shown for $\varepsilon_{max} = 0.6\varepsilon_y$ to $\varepsilon_{max} = 1.8\varepsilon_y$ in increments of $0.2\varepsilon_y$. The dashed vertical lines in each plot signify the minimum and the maximum x-depth of the inclusion for each simulated FEM model.

The distribution of initial residual stresses has a significant effect on the FIP profiles in the left column of Figure 6.12. For the same amplitude, in the near surface region ($x < 0.1$ mm), the FIP is elevated relative to the FIP values further into the bulk of the material ($x > 0.1$ mm), due to the cyclic relaxation of the residual stresses near the surface. In the depth regime of 0.1 mm$< x < 0.25$ mm, the FIP values are the lowest, but are higher than the FIP values for the same FEM model without residual stresses. Further into the depth at $x > 0.25$, the FIP values for the FEM model with residual stresses are also elevated relative to the FEM model without residual stresses due to the existence of initial tensile residual stresses in this region prior to cyclic loading.

As the applied strain amplitude is increased to values above the proportional limit of the material, $\varepsilon_{max} > \varepsilon_y$, the FIP values tend to converge for the two cases of initial and no initial residual stresses for elements deeper than $x = 0.1$ mm from the surface. This is due to cyclic plastic strain ratcheting and the relaxation of the residual stresses further into the depth of the material towards zero residual stress.

The high values of FIP near the surface at $x < 0.1$ mm, even for lower applied

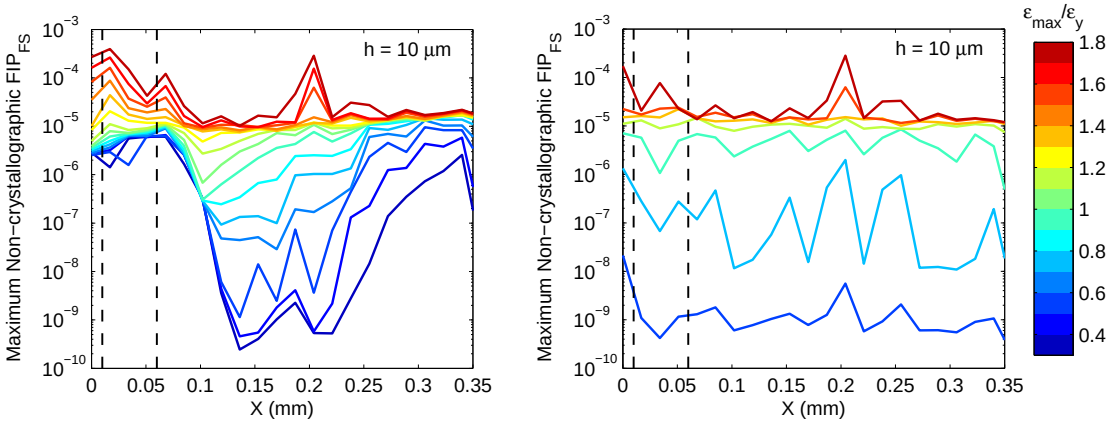

(a) h = 10 μm with RS.

(b) h = 10 μm without RS.

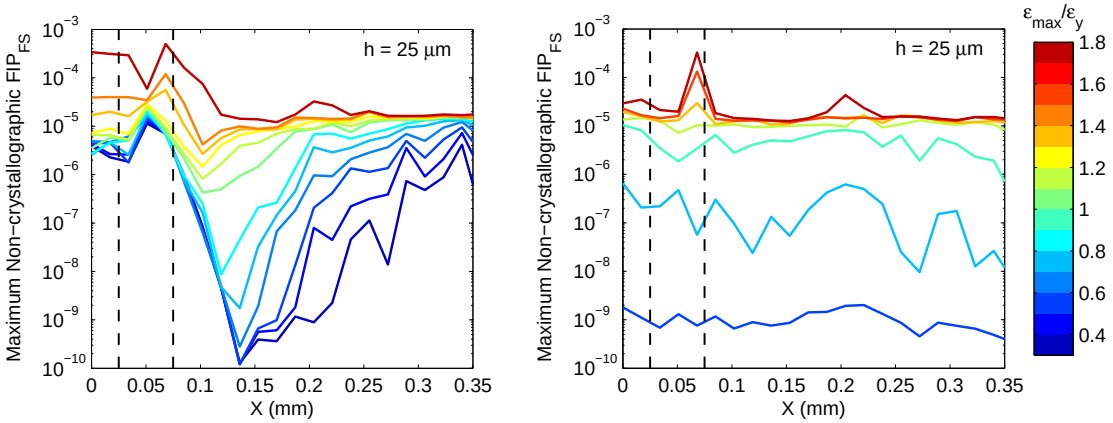

(c) h = 25 μm with RS.

(d) h = 25 μm without RS.

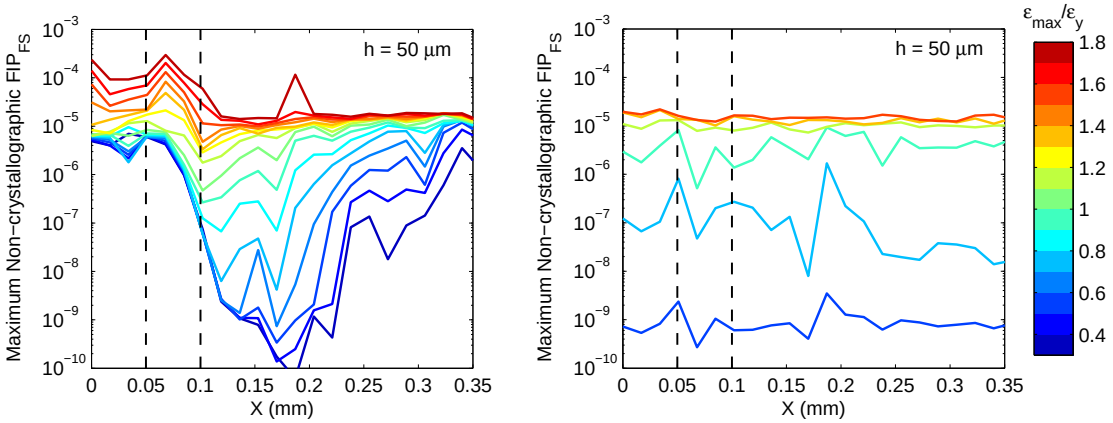

(e) h = 50 μm with RS.

(f) h = 50 μm without RS.

Figure 6.12: Grain-averaged non-crystallographic FIP for different inclusion depths as a function of maximum stress applied for case of residual stress applied (left) and no residual stresses applied (right) prior to cyclic loading. The colorbar indicates normalized maximum strain applied $\varepsilon_{max}/\varepsilon_y$, where $\varepsilon_y = 0.042\%$ is the proportional limit of CG IN100. Dashed vertical lines indicate min/max x-depth of inclusion.

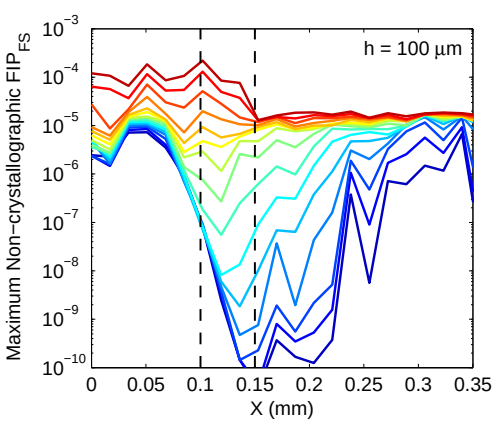

(g) h = 100 μm with RS.

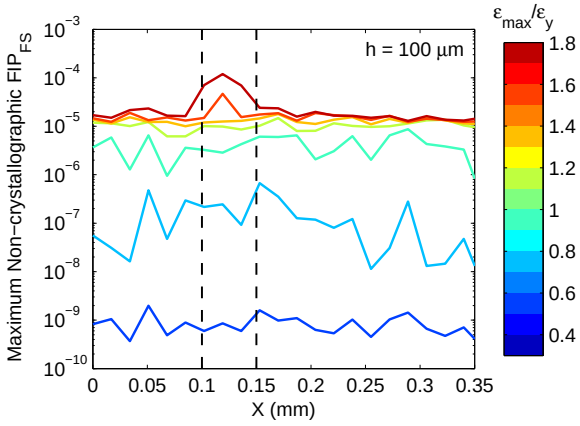

(h) h = 100 μm without RS.

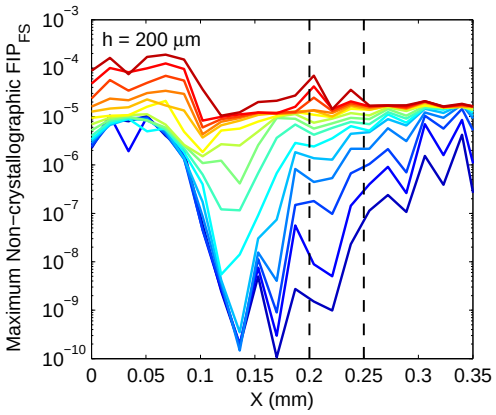

(i) h = 200 μm with RS.

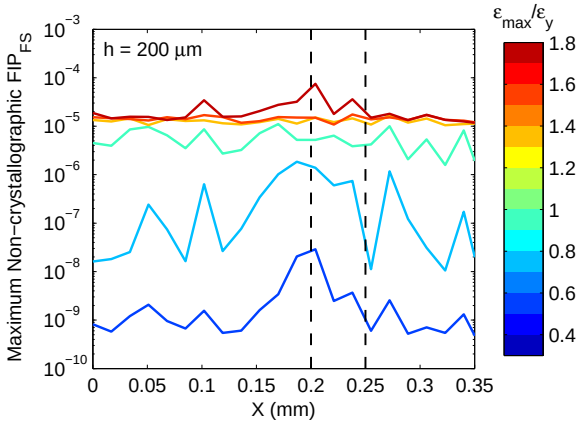

(j) h = 200 μm without RS.

Figure 6.12: (continued) Grain-averaged non-crystallographic FIP for different inclusion depths as a function of maximum stress applied for case of residual stress applied (left) and no residual stresses applied (right) prior to cyclic loading. The colorbar indicates normalized maximum strain applied $\varepsilon_{max}/\varepsilon_y$, where $\varepsilon_y = 0.042\%$ is the proportional limit of CG IN100. Dashed vertical lines indicate min/max x-depth of inclusion.

maximum cyclic strain, may suggest that fatigue crack formation is more preferable in this area at lower strain amplitudes. However, the residual stresses in these lower strain amplitudes are still quite compressive (ref. Figure 6.13). In Figure 6.13 the maximum normal stress in the y loading direction during the 10th fatigue loading cycle is shown as a function of x depth, inclusion depth, and maximum applied strain amplitude (indicated by colorbar). Consistent with Figure 6.12, the maximum normal stresses are binned every $x = 17$ μm and the dashed vertical lines signify the minimum and maximum x-depth of the inclusion in each simulated FEM model. Thus, as demonstrated for Figures 6.12 and 6.13, eventhough the FIP near the surface at $x < 0.1$ mm is higher for applied strain values below the proportional limit of the material, the maximum normal stress remains compressive. This compressive stress decreases the likelihood of inclusion/matrix debonding and should be accounted for in hierarchical fatigue life modeling. The use of a debond law in Figure 4.10 within the hierarchical fatigue life model is covered in the next section.

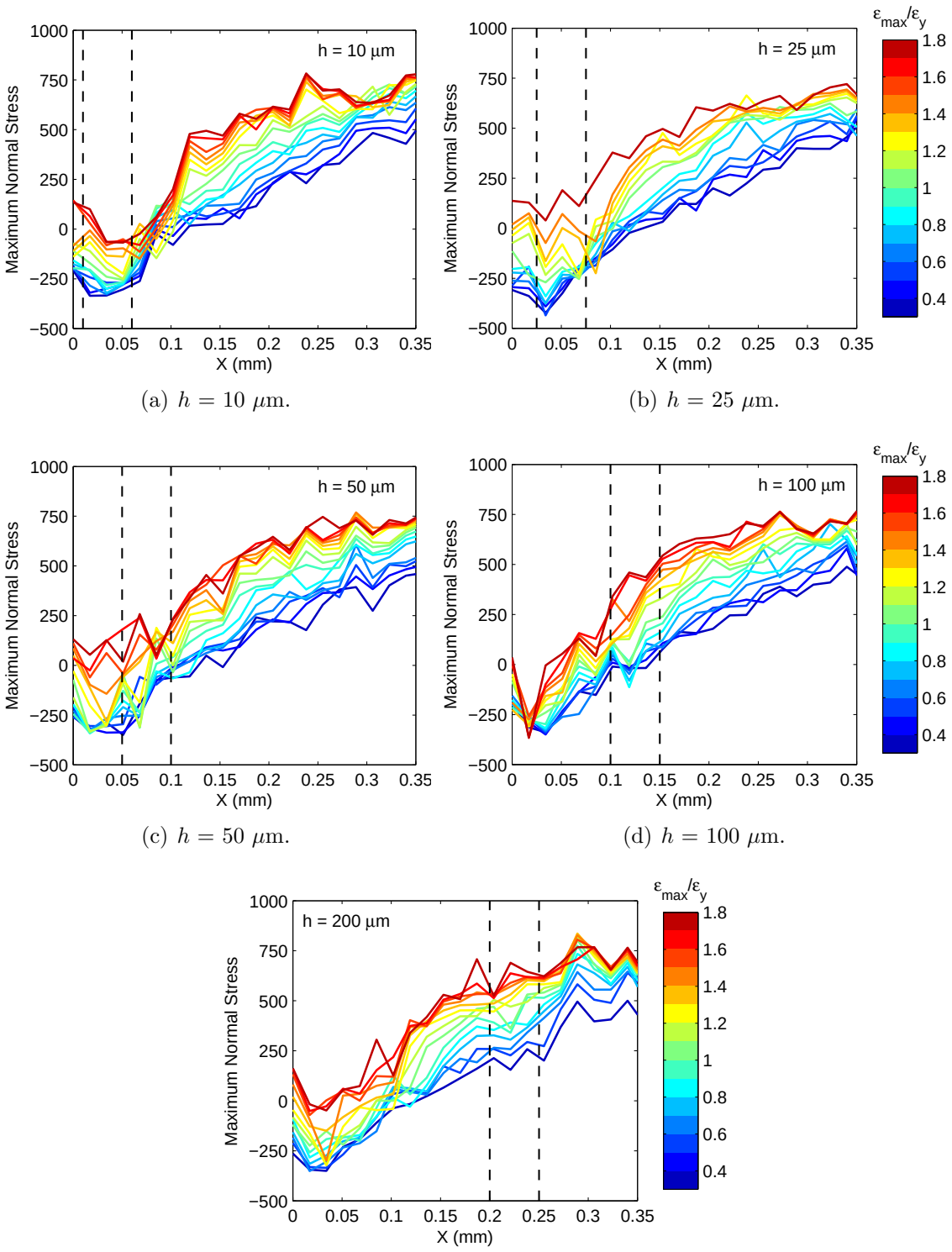

(a) $h = 10$ μm.

(b) $h = 25$ μm.

(c) $h = 50$ μm.

(d) $h = 100$ μm.

(e) $h = 200$ μm.

Figure 6.13: Maximum normal stress (σ_{yy}) as a function of x depth, inclusion depth, and maximum applied strain amplitude. Dashed vertical lines indicate min/max x-depth of inclusion.

6.3.5 Hierarchical fatigue life estimation of MSC growth in presence of residual stresses

The hierarchical fatigue life approach [4, 29, 54, 55] introduced in Section 4.2.2 incorporating inclusion/matrix interfacial separation is used here for fatigue life estimation. The total fatigue life is assumed to be demarcated into stages of inclusion/matrix debonding, fatigue crack formation, early MSC/PSC growth and long crack growth by

$$N_T = N_{DB} + N_{inc} + N_{MSC/PSC} + N_{LEFM} \tag{6.5}$$

where N_{DB} is the number of cycles required to partially debond the inclusion from the matrix, and is assumed to follow the debond law illustrated in Figure 4.10. The maximum nonlocal stress component in the y loading axis averaged over a cylindrical domain around the inclusion (ref. Figure 4.11) is used to determine the number of cycles to debond the inclusion from the matrix.

Following debonding, crack incubation is considered in grains adjacent to the debonded region. A simplified form of the Tanaka and Mura [131] crack incubation model was extended to microplasticity by Shenoy et al. [194] to estimate the incubation life for IN100 for a crack on the order of grain size. In this study, the number of cycles to incubate a crack from the debonded inclusion region ($a = a_{DB}$) into the polycrystalline matrix ($a = a_{DB} + a_{grn}$) is estimated via [194]

$$N_{inc} = \frac{\alpha_g}{d_{grn}} \left(\frac{(\Delta\gamma^p_{grn})_{max}}{2} \right)^{-2} \tag{6.6}$$

A value of $\alpha_g = 1.68{\times}10^{-5}$ μm-cycle was used for the estimation of crack incubation in the presence of residual stresses and d_{grn} is the grain size of the grain where crack incubation occurs. This α_g value is different from the previous α_g value because of cyclic relaxation; the FIP assessed over the tenth cycle is lower relative to the third cycle FIP, so an adjustment has to be made to offset this lower FIP value. For crack incubation, the grain-averaged maximum range of plastic shear strain, $(\Delta\gamma^p_{grn})_{max}$, is computed over the tenth simulated fatigue cycle. Of the grains adjacent to the debonded region, the grain with the lowest computed value of N_{inc} in Equation 6.6 is assumed to incubate the crack.

The technique for estimation of MSC growth developed in Chapter 3 is used here to estimate MSC growth from inclusions with and without initial residual stresses applied. For the case of no initial applied residual stresses, the simulated MSC growth from the inclusion followed the method previously described for the growth of MSCs from inclusions within notched components in Section 4.3.3. The one difference was that the average FIP value for the whole smooth specimen for each strain amplitude was used for the value of $\overline{FIP}_o(G_{All})$ in Equation 3.35. MSC growth was assumed to originate from the inclusion for all cases. The MSC growth model in vacuum (ref. Figure 3.31) was used while the simulated crack was not exposed to the surface; when the MSC broke through the surface, the MSC growth model was instantaneously switched to the MSC growth model fit to laboratory air MSC experiments (ref. Figure 3.30) to estimate MSC growth exposed to lab air.

A modification of the MSC propagation technique was needed to account for residual stress effects on MSC propagation. Figure 6.14 shows a schematic of MSC growth from an inclusion in the presence of residual stresses. The MSC estimation process begins with calculating the average residual stress along each radial line used for MSC propagation estimation. The average residual stress along one radial line is computed from

$$\overline{\sigma}_{yy}^{RS} = \sum_{j=1}^{N_r} \left[\frac{1}{R_\theta} \sigma_{yy}^{j}(\boldsymbol{x}) \; dr_N^j(\boldsymbol{x}) \right] \tag{6.7}$$

where N_r is the number of crack front integration points on the radial line emanating outward from the center of the inclusion, R_θ is the length of the radial line measured from the outer radius of the inclusion to the outward-most (current) crack front integration point, $\sigma_{yy}^{j}(\boldsymbol{x})$ is the residual stress at the jth crack front integration point, and $dr_N^j(\boldsymbol{x})$ is the distance between crack front integration points $a_N^j(\boldsymbol{x})$ and $a_N^{j-1}(\boldsymbol{x})$.

An approximate residual compressive strain is calculated from Equation 6.7 by dividing by the elastic modulus E and is given by

$$\overline{\varepsilon}_{yy}^{RS} \approx \frac{\overline{\sigma}_{yy}^{RS}}{E} = \sum_{j=1}^{N_r} \left[\frac{1}{R_\theta E} \sigma_{yy}^{j}(\boldsymbol{x}) \; dr_N^j(\boldsymbol{x}) \right] \tag{6.8}$$

This computed approximate residual compressive strain is used to modify the first

term of the crack force driving parameter FIP^* Equation 3.33 via

$$FIP^*(\overline{a}_N) = B_{MSC}\left|\Delta\varepsilon_a + \overline{\varepsilon}_{yy}^{RS}\right|^n (\overline{a}_N)^m \text{sgn}\left(\Delta\varepsilon_a + \overline{\varepsilon}_{yy}^{RS}\right) + C_{MSC}\,\overline{a}_N\left[\Phi\left(\overline{X}\middle|\,\mu,\sigma\right) - 0.5\right] \tag{6.9}$$

The incorporation of the residual compressive strain in Equation 6.9 is similar to the principal of superposition for estimated LEFM crack propagation in the presence of residual stress [198], only it is applied to a finer microstructure scale around the simulated MSC. If the value of Equation 6.9 is less than zero, no crack growth for the current crack front radial line is assumed ($da/dN(\boldsymbol{x}^j) = 0$). Otherwise, crack growth rate is calculated in accordance with Equation 3.31. The results from this hierarchical fatigue life estimation approach are presented in the following section.

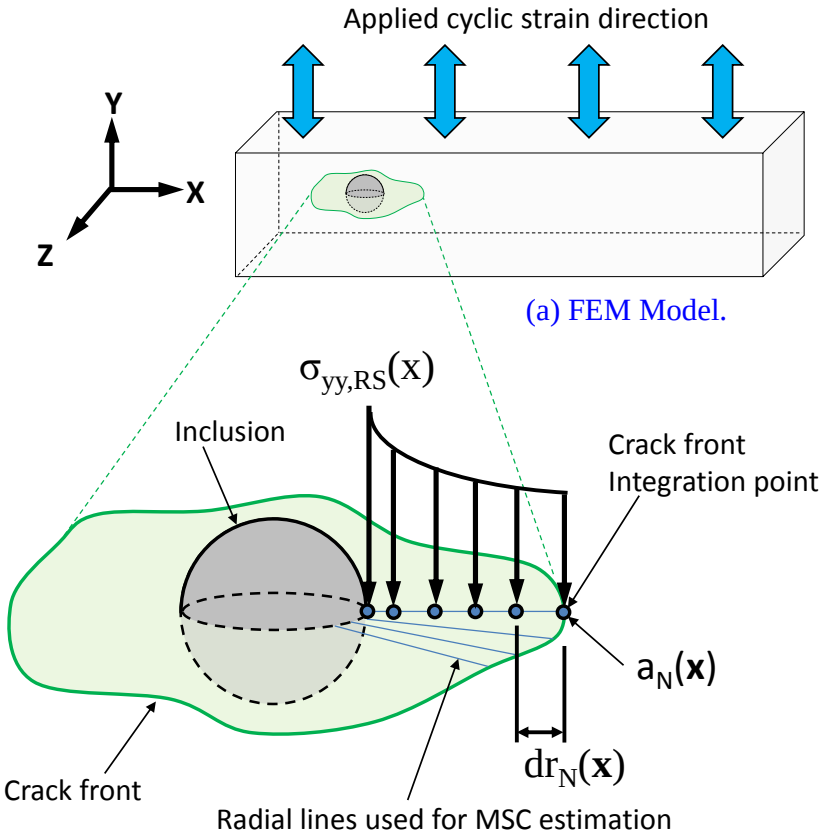

Figure 6.14: Schematic of MSC growth from an inclusion in the presence of residual stresses.

6.3.6 Effect of inclusion depth and residual stresses on fatigue life

The results of the hierarchical fatigue life estimation technique for the five inclusion depths simulated (h = 10 μm, 25 μm, 50 μm, 100 μm, and 200 μm) with and without initially imposed residual stresses are shown in Figure 6.15. For ease of explanation purposes and to reduce wordiness, the case in which residual stresses were initially applied will be referred to as "with initial residual stress" or "wRS" and the case where residual stresses were not initially applied will be referred to as "no initial residual stress" or "nRS" in the following. The estimated number of cycles for (a) debond life, (b) crack incubation life, (c) MSC propagation life, and (d) total life are depicted in this Figure. The data points that had an estimated total fatigue life beyond N_T = 10^{12} were placed at $N_T \sim 8 \times 10^{12}$ in Figure 6.15(d). As evidenced by Figure 6.15, the debond life, crack incubation life, and MSC propagation life of the nRS FEM models follow the same general strain-life trend.

The two main effects of the residual stresses for inclusions located near the surface at h = 10 μm, 25 μm, and 50 μm are (1) to suppress debonding of the inclusion from the matrix and (2) to extend the MSC propagation life due to residual compressive stresses/strains near the surface. These two effects extended the life of the inclusions located at depths of h = 10 μm and 25 μm to the fatigue limit in most cases and extended the life of the inclusion located at a depth of h = 50 μm to a lesser extent. For the inclusions located further into the depth of the material at h = 100 μm and h = 200 μm, the residual stresses were smaller around the inclusion and had less effect on prolonging the fatigue life.

Figure 6.16 shows a comparison of (a) the experimental strain life data from Konig [213] comparing fatigue behavior of a limited number of unpeened and shot-peened Ni-base superalloy components and (b) the minimum life predicted from the wRS and nRS computatational models subjected to fatigue loading. Most of the data points for the minimum life predicted for the nRS computational model is from the h = 50 μm inclusion depth data; the data points for the wRS computational model are from the model with h = 200 μm.

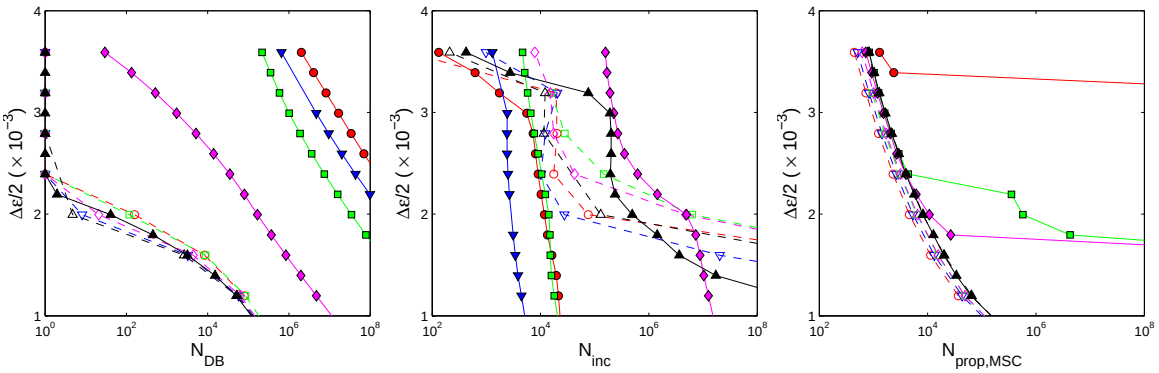

(a) Debond life, N_{DB}. (b) Crack incubation life, N_{inc}. (c) MSC propagation life, $N_{prop,MSC}$.

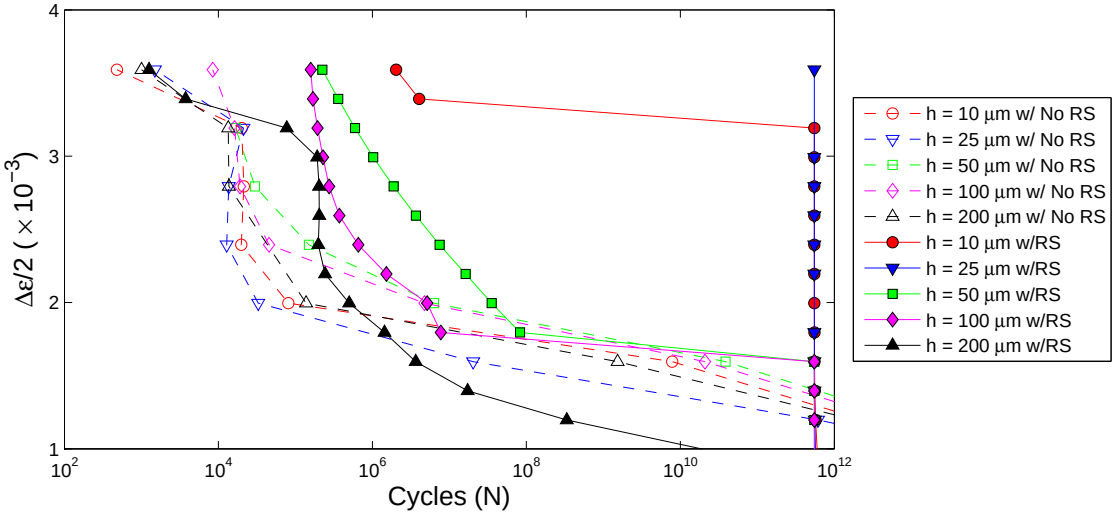

(d) Total life, N_T.

Figure 6.15: Comparison of hierarchical lives of finite element models with and without imposed residual stresses.

Some interesting key characteristics of the experimental fatigue life data are reproduced by the computational model in Figure 6.16(b). First, with decreasing applied maximum strain amplitude, the separation of the minimum fatigue lives of the wRS condition and nRS condition occurs in between $N = 10^4$ and $N = 2{\times}10^4$ cycles, which appears to be consistent with the experiments [213] in Figure 6.16(a). Also similar to the experimental data, the estimated wRS strain-life data has a "knee" in the data at around $N = 2{\times}10^5$ cycles. Beyond this "knee" in the data, the wRS data rejoins the nRS data just past $N = 10^6$ cycles in accordance with the experimental data [213].

While these preliminary computational results seem to mimic experimental data quite well, some unanswered questions still remain and should be investigated in future work. First, it should be stressed that *only one* FEM model was simulated with and without initial residual stresses per inclusion depth in this study. Multiple random instantiations should be simulated to analyze the effect of microstructural variability on scatter in fatigue life and the effectiveness of residual stresses in extending the fatigue life in the transition from LCF to HCF life data.

Second, the assumed debond law was constructed based on severely limited experimental data (3 data points) for a different Ni-base superalloy (a fine-grained Rene' 95 Ni-base superalloy versus a CG IN100 used in this study) at room temperature (versus 650°C in this study). A more robust fatigue life estimation could be constructed with a better understanding of inclusion/matrix interfacial debonding behavior for surface (and bulk) inclusions at elevated temperatures. Once these studies are available, they could be plugged into the highly modular hierarchical multistage fatigue life estimation model used to predict overall fatigue life.

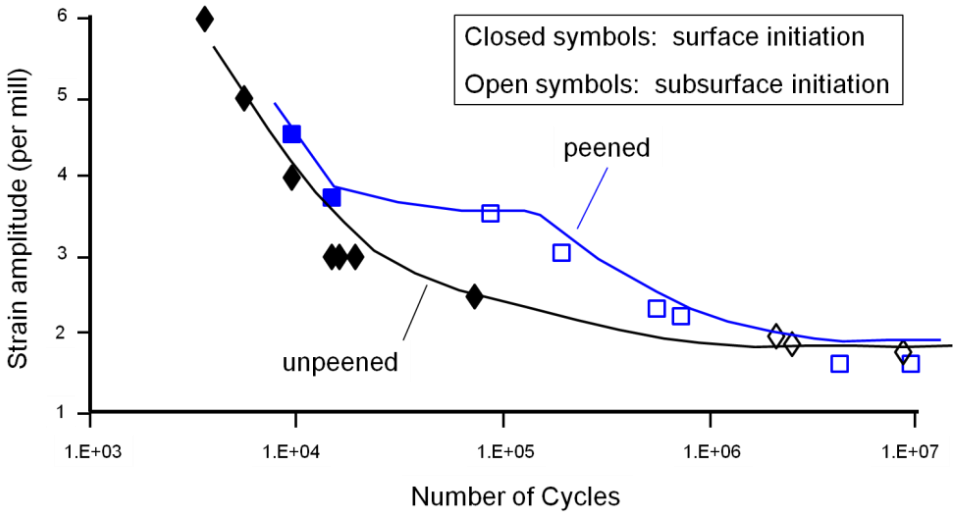

(a) Experimental data [213].

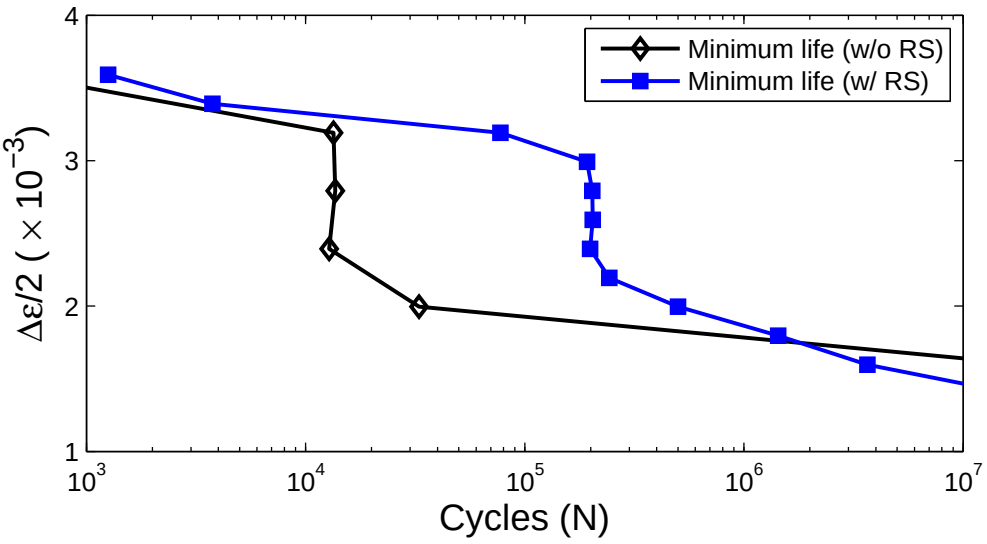

(b) Crack incubation life, N_{inc}.

Figure 6.16: Comparison of experimental data and minimum life predicted from computational model with and without imposed residual stresses.

6.4 Conclusions

The effectiveness of applied surface compressive residual stresses was investigated for simulated smooth specimens containing a single subsurface 50-μm inclusion at different depths from the surface including $h = 10$ μm, $h = 25$ μm, $h = 50$ μm, $h = 100$ μm, and $h = 200$ μm. The ability of the inclusion to debond from the matrix was simulated using an elastic/plastic compression/tension assymetric material behavior given by the "cast iron plasticity" model in ABAQUS [45]. This material behavior allowed for separate yield strengths and hardening behaviors in tension and compression. The cyclic relaxation of residual stresses were characterized over the first ten simulated cycles; it was found that the stabilization of the change in FIP behavior with cycling occurred at around the 8th-10th cycle for the case where initial residual stresses were applied. The MSC growth model from Chapter 3 and 4 was extended in this Chapter to account for the effect of residual stresses on MSC growth. This modified MSC growth model was used in conjunction with an inclusion/matrix interfacial debond law and a crack incubation law of the Tanaka-Mura [131] type to estimate the overall fatigue life of the simulated specimens with inclusions at different depths with and without initial residual stresses applied. The resulting estimated minimum life predictions correlated well with experimental trends.

CHAPTER 7
CONCLUSIONS AND RECOMMENDATIONS

7.1 Summary

In this Dissertation, the effect of shot-peened induced residual stresses and inclusions on microstructure-sensitive fatigue in polycrystalline Ni-base superalloy IN100 components was simulated using the crystal plasticity finite element method. A microstructurally small crack growth equation was developed that took into account (1) the tilt and twist character of the grain boundary, (2) the distance that the MSC was from the next grain boundary, and (3) an estimation of the evolution of driving force FIP with crack extension from initially uncracked simulations. This MSC growth model was fit to experiments (in both laboratory air and vacuum) for the case of 1D crack growth and then computationally applied to 3D crack growth from a FIB notch in a smooth specimen (Ch. 3), from a debonded inclusion located at different depths from notched components containing different notch root radii (Ch. 4), and from inclusions located at different depths from the surface in smooth specimens containing simulated shot-peened induced residuals stresses (Ch. 6).

For the FIB notch studies in Chapter 3, the MSC growth model successfully portrayed the scatter in experimental MSC da/dN versus ΔK behavior of surface cracks. Using the square root of the projected area characterization method, the MSC model predicted the reduction in oscillation behavior of the MSC growth rate and the convergence toward LEFM response with crack extension; this reduced oscillation behavior was due to the crack front statistically sampling more grains with crack extension.

The calibrated MSC growth model from Chapter 3 was then used to study the effect of inclusion depth on fatigue life of notched components. It was found that inclusions located closer to the surface were statistically more detrimental than inclusions further into the bulk of the material. At the strain level tested, the predicted fatigue life behavior showed life-limiting phenomenon for only 1 to 2 out of 20 simulated

instantiations. It was argued that more simulations should be performed to better characterize this life-limiting feature. However, the demonstration of the simulations as a tool to determine the relative effect of surface versus bulk fatigue crack formation and early growth seems promising. Indeed, once the simulated MSC penetrated the surface, the surface MSC growth rate versus range of stress intensity factor results tracked well with MSC experiments (cf. Figure 4.24(b)).

In Chapter 5, a method for inducing shot-peened residual stresses within a computational crystal plasticity framework was presented. In this process, a distribution of quasi-thermal expansion eigenstrains was imposed on the finite element model resulting in a distribution of residual stresses. The eigenstrain distribution was first fitted to an experimentally-measured residual stress curve using an isotropic J2 plasticity material behavior and then applied within a CPFEM model. Good correlation between computational and experimental values were obtained for (1) the initial residual stress profile, (2) the scatter in the initial residual stress profile among multiple instantiations, and (3) near surface residual stress relaxation trends for a single load/unload cycle.

The developed eigenstrain-based residual stress application technique was then used to investigate the effectiveness of residual stresses on near-surface suppression of fatigue crack intiation from non-metallic inclusions. The effect of compression was notable for determining "debond life" for the inclusions located within the region of highest compressive residual stresses. Once the inclusion was debonded from the matrix, the debonded region was simulated using an elastic/plastic compression/tension assymetric material behavior given by the "cast iron plasticity" model in ABAQUS [45]. This material behavior allowed for separate yield strengths and hardening behaviors in tension and compression. The MSC growth model from Chapter 3 and 4 was then extended in this Chapter to account for the effect of residual stresses on MSC growth. This modified MSC growth model was used in conjunction with an inclusion/matrix interfacial debond law and a crack incubation law of the Mura-Tanaka type to estimate the overall fatigue life of the simulated smooth specimens containing inclusions at different depths with and without initial residual stresses applied. The resulting estimated minimum life predictions correlated well with experimental trends, indicating

the effectiveness of residual stresses within the transition fatigue regime between LCF and HCF.

7.2 Novel Contributions

This work resulted in a number of key deliverables that can be used to help advance tools relevant to ICME. The unique contributions from this Dissertation include the following:

- A physically-based MSC growth model incorporating crack tip/grain boundary effects was presented that incorporated key features such as (1) the current crack length, (2) the distance of the crack from the next grain boundary, and (3) the tilt and twist angle of the crack path across the grain boundary. Additionally, this work contributed a method to map evolution of driving force FIP with crack extension based on initially uncracked simulations. This framework allows for the projection of MSC growth based on the stabilized FIP response from a single uncracked CPFEM simulation, which significantly reduces the time required for fatigue life predictions relative to more detailed mesoscale modeling approaches incorporating MSC growth/damage evolution within the CPFEM model (for example, Castelluccio and McDowell [53, 147, 254]). Therefore, the MSC growth and hierarchical modeling frameworks presented here are suitable for larger scale parametric studies and FEM models containing a modest number of finite elements for investigation of microstructural effects on fatigue variability.

- The MSC growth framework predicted a reduction in MSC growth rate oscillatory behavior and convergence to the LEFM solution (based on a da/dN vs. ΔK plot) with crack extension for the square root of the projected crack area method of crack measurement. The predicted transition from MSC to LEFM growth (on a da/dN vs. ΔK plot) was at a crack length of $2a \sim 250$ μm, which was on the order of the MSC to LEFM transition crack length seen in experiments ($a \sim 100$ μm) for a fine-grain IN100 microstructure [12].

- A methodology to incorporate the effect of inclusion depth and differences

in environment (laboratory air exposed surface cracks versus pseudo-vacuum cracks growing from subsurface inclusions) on MSC growth was devised and demonstrated for the problem of subsurface NMIs located near the surface of notched components.

- A method to impose residual stresses within a crystal plasticity framework to demonstrate the beneficial effect that residual stresses have on microstructure-sensitive fatigue. These residual stresses were induced using a distribution of quasi-thermal expansion eigenstrains, that were fit using J2 plasticity. Initial results indicated that the framework developed in this work was able to simulate the effect that residual stresses have on the transition from surface to sub-surface dominated fatigue. This type of framework can be used to assess the combined effects of microstructural variability and shot-peened residual stresses on fatigue variability of shot-peened Ni-base superalloy components.

7.3 Recommendations for Future Work

In this work, a computational framework was demonstrated for simulating the effects of inclusions and residual stresses on microstucture-sensitive fatigue of Ni-base superalloy smooth and notched components. While this Dissertation has advanced computational tools significantly on a number of fronts, there are still many unresolved opportunities for future research directly related to this Dissertation work. Some specific recommendations for future work in each Dissertation (Chapter) focus area include:

MSC Growth Model:

- **Validation of grain level MSC propagation using state-of-the-art in-situ HEDM measurements of evolving 3D MSCs.** Experimental monitoring of three-dimensional evolution of subsurface MSCs at the grain scale is possible with high energy diffraction microscopy (HEDM) and x-ray diffraction contrast tomography (DCT), also known as microCT (μCT) [142, 143, 255]. HEDM non-destructively maps the microstructure (grain size and morphology,

crystal orientation, etc.), while DCT monitors the evolution of cracks or voids. Multiple researchers have monitored in situ microstructure evolution and 3D crack growth using this method for a wide variety of materials (ref. extensive review by Stock [256]). The data obtained from these experimental studies including (1) initial non-destructive mapping of microstructure (grain size and morphology, crystal orientation, inclusion and pore spatial distribution, etc.), (2) grain-level stresses/strains, and (3) microstructure and MSC growth evolution with cyclic loading form a complete basis for validation of CPFEM-based MSC growth modeling. Specifically, the validation of 3D crack front isolines (ref. computational results in Figure 3.39) as a function of number of cycles could be used as a specific metric for comparison to experiments (ref. experimental results in Figure 6 of Herbig et al. [142]).

- **Facet analysis of high temperature MSC propagation and effects of GB of different character.** The assumption of a multislip mechanism in assessing the plane at which the MSC propagates (ref. Equation 3.39) appears to reproduce the RMS roughness of the fracture surface measured in experiments [7]. Recent experimental investigations employing orientation imaging microscopy (OIM) and quantitative tilt fractography measurements in an SEM [93, 94] have been able to characterize the orientation of individual fracture facets relative to the loading axis and crystallographic slip planes. In recent studies of a coarse grain Ni-base superalloy fatigued at 650°C, the facet where failure originated had a majority of the normal vector component in the loading axis direction and was in between two crystallographic slip planes [93], indicating the activation of slip on multiple slip planes. As more data becomes available on the failure facets resulting from elevated fatigue tests of Ni-base superalloy specimens, it would be interesting to compare the orientation of the failure facets relative to the loading axis in experiments and those computationally predicted from the MSC growth model employed in this work.

Inclusion in Notched Specimens Studies:

- **Larger number of simulation instantiations to more fully characterize life-limiting behavior.** In the notched component studies, a limited number of notch sizes ($\rho = 0.2$ mm, 0.4 mm, 0.6 mm, 0.8 mm, and 1.0 mm) and inclusion depths ($h = 25$ μm, 50 μm, and 100 μm) were simulated to investigate the effect of these input parameters on fatigue life. For the population size studied and each permutation of input parameter, only ∼1-2 of the 20 instantiations simulated comprised life-limiting fatigue lives. To be able to fully characterize this minimum life probability distribution, many more computational instantiations should be simulated to warrant a high confidence in the life-limiting distribution [135]. Therefore, the full characterization of the life-limiting failure distribution was not possible for the simulations performed in this inclusion/notch study. However, the prediction of inclusion depth on fatigue life appeared to be well represented with this framework.

- **More comprehensive simulations at different strain amplitudes to characterize breadth of statistical spread.** The current study on inclusion/notch effects only simulated five different notch sizes and three different inclusion sizes for one strain amplitude. It is well known that the spread in fatigue life increases with decreasing applied stress/strain amplitude. The ability of the current framework to predict this trend should be investigated in a more comprehensive parametric study of notched components similar to that previously performed by Musinski and McDowell [76].

- **Extension of current framework to consider near surface pores in Ni-base superalloy components.** In the absence of non-metallic inclusions located near the surface, fatigue crack initiation tends to occur at near-surface pores [7, 18, 157, 180]. In the current work, pores were not considered and fatigue cracks were assumed to originate from the simulated inclusion regardless of inclusion depth. For the inclusion depth of $h = 100$ μm, the maximum driving force FIP for fatigue crack formation and early growth was on the order of

the maximum FIP at the surface. The addition of a pore at the surface would further elevate the driving force FIP so that surface fatigue crack formation/early growth would be more favorable from the surface pore than the inclusion located further into the bulk of the material. As such, it is recommended that the driving force for fatigue crack formation and early growth for surface pores should also be cosidered for the case where the most detrimental inclusion is located at a depth of approximately 100 μm or greater; this depth was also the depth at which subsurface to bulk transition was considered in LCF experiments of a fine-grained Ni-base superalloy N18 [179].

- **Probabilistic considerations for fatigue of component-sized specimens.** In the current study, only a single 50-μm inclusion was considered at three distinct depths from the surface notch. This size inclusion was considered because it tended to be the statistically largest inclusion found to cause failure in notched component experiments [138]. In reality, for proper probabilistic life prediction, the full distribution of inclusion sizes and interaction effects of clusters of inclusions should be considered. Also, the statistically weakest inclusion/defect size within a volume increases with increasing material volume size [13, 165]. In the current work, the distribution of failures for each inclusion depth were grouped together in one probability distribution function (ref. Figure 4.29). However, the total probability of failure distribution function should consider the probability of occurrence of each inclusion depth. Regardless, the type of information obtained from these simulations, such as the probability of failure distribution as a function of inclusion depth, could be used in conjunction with macroscopic probabilistic crack growth models (e.g., DARWIN [257]) to determine the overall probability of failure for more complex geometries and full turbine engine components.

Eigenstrain-Based Application of Shot-Peened Residual Stresses:

- **Effect of grain refinement in the surface layer of shot-peened specimens.** The process of shot-peening produces an intense increase in dislocation

density and plasticity-induced grain refinement near the surface. In the current study, the eigenstrain-based application of shot-peened residual stresses assumed that there was no refinement in the grain structure for the simulations performed. Rather, the amount of quasi-thermal expansion needed to induce a given residual stress profile for a constant (non-refined) grain structure was assumed to be applicable. It would be interesting to investigate the effect of the refined near-surface refined microstructure on residual stress relaxation. Can it be simulated by using a gradient in the microstructure, i.e., using a finer grain size at the surface? This type of research question should be addressed in future work.

- **Incorporation of residual stresses in notched components.** A natural extension of this Dissertation work would be to investigate the combined aspects of all topics investigated: effects of inclusion, residual stresses, and notch gradient on fatigue life of notched components.

Effectiveness of Residual Stresses on Near-Surface Suppression of FCI from NMIs:

- **Improvement of modeled inclusion/matrix interfacial debond law at elevated temperatures.** The current study assumed a somewhat rudimentary assumption for the process of the inclusion debonding from the matrix based on limited in-situ fatigue studies at room temperature from Xie et al. [20]. For the applied constant strain amplitude and inclusion depths considered for the notched component study, the debond law predicted that the inclusion would debond from the matrix within the first 1-20 cycles, which was a very small portion of the total predicted life of the component. On the other hand, when residual stresses were imposed on the smooth specimens simulated in Chapter 6, the inclusions located near to the surface experienced compressive residual stresses for applied strain amplitudes below the yield (proportional limit) strength of the material. In these cases, the "debond life" of the inclusion/matrix interface was significant, and could partly account for the shift in crack initiation loacation to subsurface. To improve the debond law, it is suggested that careful in-situ

studies (similar to Xie et al., [20]) should be performed at elevated temperatures for a range of (seeded) inclusion sizes, depths, and strain amplitudes. An even higher fidelity experimental procedure could involve using HEDM to determine debond and intial MSC growth behavior from inclusions.

- **Scatter in inclusion with residual stress simulations to determine transition fatigue life window scatter.** In the last part of this Dissertation, the effectiveness of residual stresses in prolonging life in smooth specimens was simulating using CPFEM. A single microstructural configuration/instantiation was considered for each of 5 inclusion depths (h = 10 μm, 25 μm, 50 μm, 100 μm, and 200 μm). The results showed an effective fatigue life window in which residual stresses were effective in prolonging fatigue life based on minimum life for all specimens tested with and without intial compressive residual stresses imposed. To test the sensitivity of this fatigue life window to variability of microstructure, this study should be duplicated for multiple microstructural instantiations to determine the scatter in the surface to subsurface transition fatigue life window for shot-peened induced residual stresses.

REFERENCES

[1] McDowell, D. L., "Basic issues in the mechanics of high cycle metal fatigue," *International Journal of Fracture*, vol. 80, no. 2-3, pp. 103–145, 1996.

[2] Suresh, S., *Fatigue of Materials*. Cambridge University Press, Cambridge, UK, 2nd ed., 1998.

[3] Chan, K. S., "Roles of microstructure in fatigue crack initiation," *International Journal of Fatigue*, vol. 32, no. 9, pp. 1428–1447, 2010.

[4] McDowell, D. and Dunne, F., "Microstructure-sensitive computational modeling of fatigue crack formation," *International Journal of Fatigue*, vol. 32, no. 9, pp. 1521–1542, 2010.

[5] Jha, S., Larsen, J., and Rosenberger, A., "Towards a physics-based description of fatigue variability behavior in probabilistic life-prediction," *Engineering Fracture Mechanics*, vol. 76, pp. 681–694, Mar. 2009.

[6] Gabb, T., Kantzos, P., Telesman, J., Gayda, J., Sudbrack, C., and Palsa, B., "Fatigue resistance of the grain size transition zone in a dual microstructure superalloy disk," *International Journal of Fatigue*, vol. 33, pp. 414–426, Mar. 2011.

[7] Porter III, W., Li, K., Caton, M., Jha, S., Bartha, B., and Larsen, J., "Microstructural conditions contributing to fatigue variability in P/M nickel-base superalloys," in *Superalloys 2008*, (Champion, PA, United states), pp. 541–548, TMS, 2008.

[8] Elliott, A., Tin, S., King, W., Huang, S.-C., Gigliotti, M., and Pollock, T., "Directional solidification of large superalloy castings with radiation and liquid-metal cooling: A comparitive assesssment," *Metallurgical and Materials Transactions A*, vol. 35A, pp. 3221–3231, Oct. 2004.

[9] Gabb, T., Gayda, J., and Miner, R., "Orientation and temperature dependence of some mechanical properties of the single-crystal nickel-base superalloy rene n4: Part II. low cycle fatigue behavior," *Metallurgical Transactions A*, vol. 17A, pp. 497–505, Mar. 1986.

[10] Wusatowska-Sarnek, A. M., Blackburn, M. J., and Aindow, M., "Techniques for microstructural characterization of powder-processed nickel-based superalloys," *Materials Science and Engineering*, vol. A360, pp. 390–395, 2003.

[11] Kupkovits, R. A. and Neu, R. W., "Thermomechanical fatigue of a directionally-solidified ni-base superalloy: Smooth and cylindrically-notched specimens," *International Journal of Fatigue*, vol. 32, pp. 1330–1342, Aug. 2010.

[12] Caton, M. and Jha, S., "Small fatigue crack growth and failure mode transitions in a ni-base superalloy at elevated temperature," *International Journal of Fatigue*, vol. 32, pp. 1461–1472, Sept. 2010.

[13] Reed, R., *The Superalloys; Fundamentals and Applications*. Cambridge University Press, Cambridge, UK, 2006.

[14] Buchanan, D. J., John, R., Brockman, R. A., and Rosenberger, A. H., "A coupled creep plasticity model for residual stress relaxation of a shot peened nickel-base superalloy," in *Superalloys 2008*, (Champion, PA, United States), pp. 965–974, TMS, 2008.

[15] Khadhraoui, M., Cao, W., Castex, L., Gue, and dou, J. Y., "Experimental investigations and modelling of relaxation behaviour of shot peening residual stresses at high temperature for nickel base superalloys," *Materials Science and Technology*, vol. 13, pp. 360–367, Apr. 1997.

[16] Cao, W., Khadhraoui, M., Brenier, B., Gue, dou, J. Y., and Castex, L., "Thermomechanical relaxation of residual stress in shot peened nickel base superalloy," *Materials Science and Technology*, vol. 10, pp. 947–954, Nov. 1994.

[17] Marines, I., Bin, X., and Bathias, C., "An understanding of very high cycle fatigue of metals," *International Journal of Fatigue*, vol. 25, pp. 1101–1107, Sept. 2003.

[18] Jha, S., Caton, M., and Larsen, J., "Mean vs. life-limiting fatigue behavior of a nickel-based superalloy," in *Superalloys 2008*, (Champion, PA, USA), pp. 565–572, TMS, 2008.

[19] Padula, S. A., Shyam, A., Ritchie, R. O., and Milligan, W. W., "High frequency fatigue crack propagation behavior of a nickel-base turbine disk alloy," pp. 725–731, 1999.

[20] Xie, X., Zhang, L., Zhang, M., Dong, J., and Bain, K., "Micro-mechanical behavior study of non-metallic inclusions in P/M disk superalloy rene'95," pp. 451–458, TMS, 2004.

[21] Buchanan, D. J. and John, R., "Relaxation of shot-peened residual stresses under creep loading," *Scripta Materialia*, vol. 59, pp. 286–289, Aug. 2008.

[22] Pratt and Whitney, "IGT {parts & repairs}," 2009.

[23] Hyzak, J. and Bernstein, I., "Effect of defects on the fatigue crack initiation process in two P/M superalloys - 1. fatigue origins.," *Metallurgical transactions. A, Physical metallurgy and materials science*, vol. 13 A, no. 1, pp. 33–43, 1982.

[24] Hyzak, J. and Bernstein, I., "Effect of defects on the fatigue crack initiation process in two P/M superalloys - 2. surface-subsurface transition.," *Metallurgical transactions. A, Physical metallurgy and materials science*, vol. 13 A, no. 1, pp. 45–52, 1982.

[25] de Bussac, A. and Lautridou, J., "A probabilistic model for prediction of LCF surface crack initiation in PM alloys," *Fatigue & Fracture of Engineering Materials & Structures*, vol. 16, no. 8, pp. 861–74, 1993.

[26] Milligan, W., Orth, E., Schirra, J., and Savage, M., "Effects of microstructure on the high temperature constitutive behavior of IN100," *Superalloys 2004, TMS, Warrendale, PA*, pp. 331–339, 2004.

[27] Kozar, R., Suzuki, A., Milligan, W., Schirra, J., Savage, M., and Pollock, T., "Strengthening mechanisms in polycrystalline multimodal nickel-base superalloys," *Metallurgical and Materials Transactions*, vol. 40A, p. 1588, July 2009.

[28] Wusatowska-Sarnek, A. M., Ghosh, G., Olson, G. B., Blackburn, M. J., and Aindow, M., "Characterization of the microstructure and phase equilibria calculations for the powder metallurgy superalloy IN100," *Journal of Materials Research*, vol. 18, pp. 2653–2663, Nov. 2003.

[29] Przybyla, C., Prasannavenkatesan, R., Salajegheh, N., and McDowell, D. L., "Microstructure-sensitive modeling of high cycle fatigue," *International Journal of Fatigue*, vol. 32, pp. 512–525, Mar. 2010.

[30] Shenoy, M., Tjiptowidjojo, Y., and McDowell, D., "Microstructure-sensitive modeling of polycrystalline IN 100," *International Journal of Plasticity*, vol. 24, no. 10, pp. 1694–1730, 2008.

[31] Shenoy, M. M., "Constitutive modeling and life prediction in ni-base superalloys," 2006.

[32] McGinty, R., *Multiscale representation of polycrystalline inelasticity*. PhD thesis, Georgia Institute of Technology, 2001.

[33] Chaboche, J. L., "Constitutive equations for cyclic plasticity and cyclic viscoplasticity," *International Journal of Plasticity*, vol. 5, no. 3, pp. 247–302, 1989.

[34] Bettge, D. and Osterle, W., ""Cube slip" in near-[111] oriented specimens of a single-crystal nickel-base superalloy," *Scripta Materialia*, vol. 40, pp. 389–395, Jan. 1999.

[35] Heilmaier, M., Leetz, U., and Reppich, B., "Order strengthening in the cast nickel-based superalloy IN 100 at room temperature," pp. 375–378, 2001.

[36] Reppich, B., Schepp, P., and Wehner, G., "Some new aspects concerning particle hardening mechanicsms in gamma' precipitating nickel-base alloys. 2. experiments," *Acta Metallurgica*, vol. 30, no. 1, pp. 95–104, 1982.

[37] Qin, Q. and Bassani, J. L., "Non-schmid yield behavior in single crystals," *Journal of the Mechanics and Physics of Solids*, vol. 40, no. 4, pp. 813–833, 1992.

[38] Qin, Q. and Bassani, J. L., "Non-associated plastic flow in single crystals," *Journal of the Mechanics and Physics of Solids*, vol. 40, pp. 835–862, May 1992.

[39] Shenoy, M. M., Gordon, A. P., McDowell, D. L., and Neu, R. W., "Thermomechanical fatigue behavior of a directionally solidified ni-base superalloy," *Journal of Engineering Materials and Technology-Transactions of the Asme*, vol. 127, no. 3, pp. 325–336, 2005.

[40] Paidar, V., Pope, D. P., and Vitek, V., "A theory of the anomalous yield behavior in LL2 ordered alloys," *Acta Metallurgica*, vol. 32, no. 3, pp. 435–448, 1984.

[41] Huther, W. and Reppich, B., "Interaction of dislocations with coherent, stress-free, ordered particles," *Zeitschrift fur Metallkunde*, vol. 69, pp. 628–34, Oct. 1978. Copyright 1979, IEE.

[42] Sinharoy, S., Virro-Nic, P., and Milligan, W. W., "Deformation and strength behavior of two nickel-base turbine disk alloys at 650 degrees c," *Metallurgical and Materials Transactions a-Physical Metallurgy and Materials Science*, vol. 32, no. 8, pp. 2021–2032, 2001.

[43] Mecking, H. and Kocks, U., "Kinetics of flow and strain-hardening," *Acta Metallurgica*, vol. 29, pp. 1865–1875, Nov. 1981.

[44] Feaugas, X. and Haddou, H., "Grain-size effects on tensile behavior of nickel and AISI 316L stainless steel," *Metallurgical and Materials Transactions A*, vol. 34, pp. 2329–2340, Oct. 2003.

[45] ABAQUS, *Standard User's Manual*. Simulia, Providence, RI, 2012.

[46] Przybyla, C. P. and McDowell, D. L., "Microstructure-sensitive extreme value probabilities for high cycle fatigue of ni-base superalloy IN100," *International Journal of Plasticity*, vol. 26, pp. 372–394, Mar. 2010.

[47] Luo, J. and Bowen, P., "Small and long fatigue crack growth behaviour of a PM ni-based superalloy, udimet 720," *International Journal of Fatigue*, vol. 26, pp. 113–124, Feb. 2004.

[48] Tokaji, K. and Ogawa, T., "The growth behavior of microstructurally small fatigue cracks in metals," in *Short fatigue cracks, ESIS* (Miller, K. and De los Rios, E., eds.), vol. 13, pp. 85–99, Mechanical Engineering Publications, London, 1992.

[49] Zhai, T., Wilkinson, A. J., and Martin, J. W., "A crystallographic mechanism for fatigue crack propagation through grain boundaries," *Acta Materialia*, vol. 48, pp. 4917–4927, Dec. 2000.

[50] Qiao, Y. and Argon, A. S., "Cleavage crack-growth-resistance of grain boundaries in polycrystalline fe-2%Si alloy: experiments and modeling," *Mechanics of Materials*, vol. 35, pp. 129–154, Jan. 2003.

[51] Gell, M. and Smith, E., "The propagation of cracks through grain boundaries in polycrystalline 3% silicon-iron," *Acta Metallurgica*, vol. 15, pp. 253–258, Feb. 1967.

[52] Wen, W. and Zhai, T., "Quantification of resistance of grain boundaries to short-fatigue crack growth in three dimensions in high-strength al alloys," *Metallurgical and Materials Transactions A*, vol. 43A, pp. 2743–2752, 2012.

[53] Castelluccio, G. M., *A study on the influence of microstructure on small fatigue cracks*. Ph.D., Georgia Institute of Technology, 2012.

[54] McDowell, D. L., Gall, K., Horstemeyer, M. F., and Fan, J., "Microstructure-based fatigue modeling of cast a356-t6 alloy," *Engineering Fracture Mechanics*, vol. 70, no. 1, pp. 49–80, 2003.

[55] McDowell, D. L., "Simulation-based strategies for microstructure-sensitive fatigue modeling," pp. 4–14, 2007.

[56] Christ, H.-J., Duber, O., Fritzen, C.-P., Knobbe, H., Koster, P., Krupp, U., and Knkler, B., "Propagation behaviour of microstructural short fatigue cracks in the high-cycle fatigue regime," *Computational Materials Science*, vol. 46, pp. 561–565, Sept. 2009.

[57] Wang, Q., Berard, J., Rathery, S., and Bathias, C., "High-cycle fatigue crack initiation and propagation behaviour of high-strength spring steel wires," *Fatigue and Fracture of Engineering Materials and Structures*, vol. 22, pp. 673–677, 1999.

[58] Hobson, P., Brown, M., and de los Rios, E., "Two phases of short crack growth in a medium carbon steel," in *The behavior of short fatigue cracks (EGF 1)* (Miller, K. and de los Rios, E., eds.), Mechanical Engineering Publications, London, 1986.

[59] Hobson, P. D., "The formulation of a crack growth equation for short cracks," *Fatigue & Fracture of Engineering Materials & Structures*, vol. 5, no. 4, p. 323327, 1982.

[60] Miller, K. J., "Three thresholds for fatigue crack propagation," vol. 1296 of *ASTM Special Technical Publication*, (Williamsburg, VA, USA), pp. 267–286, ASTM, 1997.

[61] Miller, K., Mohamed, H., and de los Rios, E., "Fatigue damage accumulation above and below the fatigue limit," in *The behavior of short fatigue cracks (EGF 1)*, pp. 491–511, Mechanical Engineering Publications, London, 1986.

[62] Nisitani, H. and Goto, M., "A small-crack growth law and its application to the evaluation of fatigue life," in *The behavior of short fatigue cracks (EGF 1)*, pp. 461–478, Mechanical Engineering Publications, London, 1986.

[63] Goto, M., Kamil, K., Han, S., Euh, K., Kim, S., and Yokoho, Y., "Effects of grain refinement due to severe plastic deformation on the growth behavior of small cracks in copper," *International Journal of Fatigue*, vol. 50, pp. 63–71, 2013.

[64] Frost, N. and Dugdale, D., "The propagation of fatigue cracks in sheet specimens," *Journal of the Mechanics and Physics of Solids*, vol. 6, pp. 92–110, 1958.

[65] Chan, K. and Lankford, J., "A crack-tip strain model for the growth of small fatigue cracks," *Scripta Metallurgica*, vol. 17, pp. 529–532, 1983.

[66] Tanaka, K., Akiniwa, Y., Nakai, Y., and Wei, R. P., "Modelling of small fatigue crack growth interacting with grain boundary," *Engineering Fracture Mechanics*, vol. 24, no. 6, pp. 803–819, 1986.

[67] Navarro, A. and de los Rios, E., "A model for short fatigue crack propagation with an interpretation of the short-long crack transition," *Fatigue & Fracture of Engineering Materials & Structures*, vol. 10, no. 2, pp. 169–186, 1987.

[68] Bilby, B., Cottrell, A., and Swinden, K., "The spread of plastic yield from a notch," *Proceedings of the Royal Society of London*, vol. A272, pp. 304–314, 1963.

[69] Kunkler, B., Duber, O., Koster, P., Krupp, U., Fritzen, C.-P., and Christ, H.-J., "Modelling of short crack propagation - transition from stage i to stage II," *Engineering Fracture Mechanics*, vol. 75, pp. 715–725, Feb. 2008.

[70] Marx, M., Schaef, W., and Welsch, M., "The microstructure as crack initiation point and barrier against fatigue damaging," *International Journal of Fatigue*, vol. 41, pp. 57–63, Aug. 2012.

[71] Schaef, W. and Marx, M., "A numerical description of short fatigue cracks interacting with grain boundaries," *Acta Materialia*, vol. 60, pp. 2425–2436, 2012.

[72] Simonovski, I., Nilsson, K.-F., and Cizelj, L., "The influence of crystallographic orientation on crack tip displacements of microstructurally small, kinked crack crossing the grain boundary," *Computational Materials Science*, vol. 39, pp. 817–828, 2007.

[73] Simonovski, I. and Cizelj, L., "The influence of grains' crystallographic orientations on advancing short crack," *International Journal of Fatigue*, vol. 29, pp. 2005–2014, 2007.

[74] Simonovski, I. and Cizelj, L., "The influence of the grain structure size on microstructurally short cracks," *Journal of Engineering for Gas Turbines and Power*, vol. 131, pp. 042903–1–8, 2009.

[75] Castelluccio, G. and McDowell, D., "Assessment of small fatigue crack growth driving forces in single crystals with and without slip bands," *International Journal of Fracture*, vol. 176, pp. 49–64, 2012.

[76] Musinski, W. D. and McDowell, D. L., "Microstructure-sensitive probabilistic modeling of HCF crack initiation and early crack growth in ni-base superalloy IN100 notched components," *International Journal of Fatigue*, vol. 37, pp. 41–53, Apr. 2012.

[77] Phillips, P., Unocic, R., and Mills, M., "Low cycle fatigue of a polycrystalline ni-based superalloy: Deformation substructure analysis," *International Journal of Fatigue*, vol. 57, pp. 50–57, 2013.

[78] Li, K., Ashbaugh, N., and Rosenberger, A., "Crystallographic initiation of nickel-base superalloy IN100 at RT and 538C under low cycle fatigue conditions.," pp. 251–258, 2004.

[79] Ma, X. and Shi, H.-J., "On the fatigue small crack behaviors of directionally solidified superalloy DZ4 by in situ SEM observations," *International Journal of Fatigue*, vol. 35, pp. 91–98, Feb. 2012.

[80] Hardt, S., Maier, H., and Christ, H.-J., "High-temperature fatigue damage mechanisms in near-alpha titanium alloy IMI 834," *International Journal of Fatigue*, vol. 21, pp. 779–789, 1999.

[81] Pototzky, P., Maier, H., and Christ, H.-J., "Thermomechanical fatigue behavior of the high-temperature titanium alloy IMi 834," *Metallurgical and Materials Transactions A*, vol. 29A, pp. 2995–3004, 1998.

[82] Leo Prakash, D., Walsh, M., Maclachlan, D., and Korsunsky, A., "Crack growth micro-mechanisms in the IN718 alloy under the combined influence of fatigue, creep and oxidation," *International Journal of Fatigue*, vol. 31, pp. 1966–1977, Nov. 2009.

[83] Andrieu, E., Molins, R., Ghonem, H., and Pineau, A., "Intergranular crack tip oxidation mechanism in a nickel-based superalloy," *Materials Science and Engineering: A*, vol. 154, pp. 21–28, June 1992.

[84] Chen, D., Weiss, B., and Stickler, R., "A model for crack closure," *Engineering Fracture Mechanics*, vol. 53, pp. 493–509, 1996.

[85] Gayda, J. and Miner, R. V., "Fatigue crack initiation and propagation in several nickel-base superalloys at 650C," *International Journal of Fatigue*, vol. 5, no. 3, pp. 135–143, 1983.

[86] Pang, H. and Reed, P., "Microstructure effects on high temperature fatigue crack initiation and short crack growth in turbine disc nickel-base superalloy udimet 720Li," *Materials Science and Engineering: A*, vol. 448, pp. 67–79, Mar. 2007.

[87] Pineau, A. and Antolovich, S. D., "High temperature fatigue of nickel-base superalloys - a review with special emphasis on deformation modes and oxidation," *Engineering Failure Analysis*, vol. 16, pp. 2668–2697, Dec. 2009.

[88] Stocker, C., Zimmermann, M., and Christ, H.-J., "Localized cyclic deformation and corresponding dislocation arrangements of polycrystalline ni-base superalloys and pure nickel in the VHCF regime," *International Journal of Fatigue*, vol. 33, pp. 2–9, Jan. 2011.

[89] Miao, J., Pollock, T. M., and Wayne Jones, J., "Crystallographic fatigue crack initiation in nickel-based superalloy ren 88DT at elevated temperature," *Acta Materialia*, vol. 57, pp. 5964–5974, Dec. 2009.

[90] Shyam, A., Torbet, C., Jha, S., Larsen, J., Caton, M., Szczepanski, C., Pollock, T., and Jones, J., "Development of ultrasonic fatigue for rapid, high temperature fatigue studies in turbine engine materials," in *Superalloys 2004*, (Champion, PA, United states), pp. 259–268, TMS, 2004.

[91] Jha, S. K., Caton, M. J., Rosenberger, A. H., Li, K., and Porter, W. J., "Superimposing mechanisms and their effect on the variability in fatigue lives of a nickel-based superalloy," in *Materials Damage Prognosis*, Materials Damage Prognosis, (New Orleans, LA, United states), pp. 343–350, TMS, 2005.

[92] Boittin, G., Locq, D., Rafray, A., Caron, P., Kanoute, P., Gallerneau, F., and Cailletaud, G., "Influence of gamma' precipitate size and distribution on LCF behavior of a PM disk superalloy," pp. 167–176, TMS, 2012.

[93] Sinha, V., Jha, S., Porter III, W., John, R., Rosenberger, A., Caton, M., and Larsen, J., "Fatigue fracture mechanisms in nickel-base superalloy IN100," in *TMS Annual Meeting*, (San Diego, CA, United states), TMS, 2014.

[94] Sinha, V., Mills, M., and Williams, J., "Crystallography of fracture facets in a near-alpha titanium alloy," *Metallurgical and Materials Transactions A*, vol. 37A, pp. 2015–2026, 2006.

[95] Dahal, J., Maciejewski, K., and Ghonem, H., "Loading frequency and microstructure interactions in intergranular fatigue crack growth in a disk ni-based superalloy," *International Journal of Fatigue*, vol. 57, pp. 93–102, 2013.

[96] Pedron, J. and Pineau, A., "The effect of microstructure and environment on the crack growth behaviour of inconel 718 alloy at 650 C under fatigue, creep and combined loading," *Materials Science and Engineering*, vol. 56, pp. 143–156, Nov. 1982.

[97] Reger, M. and Remy, L., "High temperature, low cycle fatigue of IN-100 superalloy II: influence of frequency and environment at high temperatures," *Materials Science and Engineering: A*, vol. 101, pp. 55–63, May 1988.

[98] Everitt, S., Starink, M., and Reed, P., "Temperature and dwell dependence of fatigue crack propagation in various heat treated turbine disk alloys," pp. 741–750, TMS, 2008.

[99] Carroll, L., Cabet, C., Carroll, M., and Wright, R., "The development of microstructural damage during high temperature creep-fatigue of a nickel alloy," *International Journal of Fatigue*, vol. 47, pp. 15–125, 2013.

[100] Yang, H., Bao, R., Zhang, J., Peng, L., and Fei, B., "Creep-fatigue crack growth behaviour of a nickel-based powder metallurgy superalloy under high temperature," *Engineering Failure Analysis*, vol. 18, pp. 1058–1066, 2011.

[101] Lu, Y., Liaw, P., Wang, G., Benson, M., Thompson, S., Blust, J., Browning, P., Bhattacharya, A., Aurrecoechea, J., and Klarstrom, D., "Fracture modes of HAYNES 230 alloy during fatigue-crack-growth at room and elevated temperatures," *Materials Science and Engineering A*, vol. 397, pp. 122–131, 2005.

[102] Chen, X., Yang, Z., Sokolov, M., Erdman III, D., Mo, K., and Stubbins, J., "Low cycle fatigue and creep-fatigue behavior of ni-based alloy 230 at 850C," *Materials Science and Engineering A*, vol. 563, pp. 152–162, 2013.

[103] Byrne, J., Hall, R., and Grabowski, L., "Elevated temperature fatigue crack growth under dwell conditions in waspaloy," *International Journal of Fatigue*, vol. 19, no. 5, pp. 359–367, 1997.

[104] Knowles, D. and Hunt, D., "The influence of microstructure and environment on the crack growth behavior of powder metallurgy nickel superalloy RR1000," *Metallurgical and Materials Transactions A*, vol. 33, no. 10, pp. 3165–3172, 2002.

[105] Mitchell, R., Lemsky, J., Ramanathan, R., Li, H., Perkins, K., and Connor, L., "Process development and microstructure and mechanical property evaluation of a dual microstructure heat treated advanced nickel disc alloy," in *Superalloys 2008*, TMS, 2008.

[106] Saylor, D., Morawiec, A., and Rohrer, G., "Distribution of grain boundaries in magnesia as a function of five macroscopic parameters," *Acta Materialia*, vol. 51, pp. 3663–3674, 2003.

[107] Engler, O. and Randle, V., *Introduction to Texture Analysis: Macrotexture, Microtexture, and Orientation Mapping*. CRC Press, Taylor & Francis Group, Boca Raton, FL, 2010.

[108] Randle, V., *The measurement of grain boundary geometry*. Institute of Physics Publishing, Bristol, UK, 1993.

[109] Birosca, S., Buffiere, J., Garcia-Pastor, F., Karadge, M., Babout, L., and Preuss, M., "Three-dimensional characterization of fatigue cracks in ti-6246 using x-ray tomography and electron backscatter diffraction," *Acta Materialia*, vol. 57, pp. 5834–5847, Nov. 2009.

[110] Sangid, M. D., Maier, H. J., and Sehitoglu, H., "The role of grain boundaries on fatigue crack initiation - an energy approach," *International Journal of Plasticity*, vol. 27, no. 5, pp. 801–821, 2011.

[111] Sangid, M. D., Maier, H. J., and Sehitoglu, H., "An energy-based microstructure model to account for fatigue scatter in polycrystals," *Journal of the Mechanics and Physics of Solids*, vol. 59, no. 3, pp. 595–609, 2011.

[112] Osterstock, S., Robertson, C., Sauzay, M., Aubin, V., and Degallaix, S., "Stage i surface crack formation in thermal fatigue: A predictive multi-scale approach," *Materials Science and Engineering: A*, vol. 528, pp. 379–390, Nov. 2010.

[113] Duber, O., Kunkler, B., Krupp, U., Christ, H.-J., and Fritzen, C.-P., "Experimental characterization and two-dimensional simulation of short-crack propagation in an austenitic-ferritic duplex steel," *International Journal of Fatigue*, vol. 28, pp. 983–992, Sept. 2006.

[114] Krupp, U., Knobbe, H., Christ, H.-J., Koster, P., and Fritzen, C.-P., "The significance of microstructural barriers during fatigue of a duplex steel in the high- and very-high-cycle-fatigue (HCF/VHCF) regime," *International Journal of Fatigue*, vol. 32, pp. 914–920, June 2010.

[115] Abuzaid, W., Sangid, M. D., Carroll, J. D., Sehitoglu, H., and Lambros, J., "Slip transfer and plastic strain accumulation across grain boundaries in hastelloy x," *Journal of the Mechanics and Physics of Solids*, 2012.

[116] Patriarca, L., Abuzaid, W., Sehitoglu, H., and Maier, H. J., "Slip transmission in bcc FeCr polycrystal," *Materials Science & Engineering A*, vol. 588, pp. 308–317, 2013.

[117] Fatemi, A. and Kurath, P., "Multiaxial fatigue life predictions under the influence of mean-stresses," *Journal of Engineering Materials and Technology - Transactions of the ASME*, vol. 110, pp. 380–388, Oct. 1988.

[118] Socie, D. and Marquis, G., *Multiaxial Fatigue*. SAE International, 1999.

[119] Kallmeyer, A. R., Krgo, A., and Kurath, P., "Evaluation of multiaxial fatigue life prediction methodologies for ti-6Al-4V," *J. Eng. Mater. Technol.-Trans. ASME*, vol. 124, no. 2, pp. 229–237, 2002.

[120] Coffin, L., "A study of the effect of cyclic thermal stresses on a ductile metal," *Transactions ASME*, vol. 76, pp. 931–950, 1954.

[121] Manson, S., "Behavior of materials under conditions of thermal stress," Tech. Rep. 110, Cleveland, OH: Lewis Flight Propulsion Laboratory, 1954.

[122] Findley, W., "Fatigue of metals under combinations of stresses," *American Society of Mechanical Engineers – Transactions*, vol. 79, no. 6, pp. 1337–1347, 1957.

[123] Fatemi, A. and Socie, D., "A critical plane approach to multiaxial fatigue damage including out-of-phase loading," *Fatigue & Fracture of Engineering Materials & Structures*, vol. 11, no. 3, pp. 149–165, 1988.

[124] Salajegheh, N., *Microstructure-Sensitive Weighted Probability Approach for Modeling Surface to Bulk Transition of High Cycle Fatigue Failures Dominated by Primary Inclusions*. Ph.D., Georgia Institute of Technology, 2011.

[125] Prasannavenkatesan, R., Zhang, J., McDowell, D. L., Olson, G. B., and Jou, H.-J., "3D modeling of subsurface fatigue crack nucleation potency of primary inclusions in heat treated and shot peened martensitic gear steels," *International Journal of Fatigue*, vol. 31, pp. 1176–1189, July 2009.

[126] Castelluccio, G. and McDowell, D., "Variability of the fatigue driving force within grains of polycrystals," in *13th International Conference on Fracture*, (Beijing, China), pp. 1–10, June 2013.

[127] Essmann, U., Goesele, U., and Mughrabi, H., "Model of extrusions and intrusions in fatigued metals - 1. point-defect production and the growth of extrusions," *Philosophical Magazine A*, vol. 44, no. 2, pp. 405–426, 1981.

[128] Man, J., Vystavel, T., Weidner, A., Kubena, I., Petrenec, M., Kruml, T., and Polak, J., "Study of cyclic strain localization and fatigue crack initiation using FIB technique," *International Journal of Fatigue*, vol. 39, pp. 44–53, June 2012.

[129] Mughrabi, H., "Cyclic slip irreversibilities and the evolution of fatigue damage," *Metallurgical and Materials Transactions A*, vol. 40, pp. 1257–1279, Apr. 2009.

[130] Morrison, D. and Moosbrugger, J., "Effects of grain size on cyclic plasticity and fatigue crack initiation in nickel," *International Journal of Fatigue*, vol. 19, no. Suppl 1, pp. S51–S59, 1997.

[131] Tanaka, K. and Mura, T., "A dislocation model for fatigue crack initiaion," *Journal of Applied Mechanics*, vol. 48, no. 1, pp. 97–103, 1981.

[132] Mikkola, E., Marquis, G., and Solin, J., "Mesoscale modelling of crack nucleation from defects in steel," *International Journal of Fatigue*, vol. 41, pp. 64–71, Aug. 2012.

[133] Alexandre, F., Deyber, S., and Pineau, A., "Modelling the optimum grain size on the low cycle fatigue life of a ni based superalloy in the presence of two possible crack initiation sites," *Scripta Materialia*, vol. 50, pp. 25–30, Jan. 2004.

[134] Przybyla, C. and McDowell, D., "Microstructure-sensitive extreme-value probabilities of high-cycle fatigue for surface vs. subsurface crack formation in duplex ti-6Al-4V," *Acta Materialia*, vol. 60, no. 1, pp. 293–305, 2012.

[135] Salajegheh, N. and McDowell, D., "Microstructure-sensitive weighted probability approach for modeling surface to bulk transition of high cycle fatigue failures dominated by primary inclusions," *International Journal of Fatigue*, vol. 59, pp. 188–199, 2014.

[136] Rosenberger, A. H., "The effect of partial vacuum on the fatigue crack growth of nickel base superalloys," pp. 233–239, TMS, 2004.

[137] Rosenberger, A., Buchanan, D., Ward, D., and Jha, S., "The variability of fatigue in notched bars of IN100," pp. 143–148, TMS, 2012.

[138] Ward, D., *The effect of dwell loading on the small fatigue crack growth at notches in IN100*. Master's thesis, University of Dayton, 2012.

[139] Wen, W. and Zhai, T., "Three-dimensional effects of microstructures on short fatigue crack growth in an al-li 8090 alloy," *Philosophical Magazine*, vol. 91, no. 27, pp. 3557–3577, 2011.

[140] Zhai, T., Jiang, X., Li, J., Garratt, M., and Bray, G., "The grain boundary geometry for optimum resistance to growth of short fatigue cracks in high strength al-alloys," *International Journal of Fatigue*, vol. 27, pp. 1202–1209, 2005.

[141] Wen, W., *A three-dimensional quantitative understanding of short fatigue crack growth in high strength aluminum alloys*. PhD thesis, University of Kentucky, 2013.

[142] Herbig, M., King, A., Reischig, P., Proudhon, H., Lauridsen, E. M., Marrow, J., Buffiere, J.-Y., and Ludwig, W., "3-d growth of a short fatigue crack within a polycrystalline microstructure studied using combined diffraction and phase-contrast x-ray tomography," *Acta Materialia*, vol. 59, pp. 590–601, Jan. 2011.

[143] King, A., Ludwig, W., Herbig, M., Buffire, J.-Y., Khan, A., Stevens, N., and Marrow, T., "Three-dimensional in situ observations of short fatigue crack growth in magnesium," *Acta Materialia*, vol. 59, pp. 6761–6771, Oct. 2011.

[144] MATLAB, *User's Manual*. The MathWorks, Inc., Natick, MA, 2012.

[145] Bachmann, F., Hielscher, R., and Schaeben, H., "Texture analysis with MTEX - free and open source software toolbox," *Solid State Phenomena*, vol. 160, pp. 63–68, 2010.

[146] Schaef, W., Marx, M., Vehoff, H., Heckl, A., and Randelzhofer, P., "A 3-d view on the mechanisms of short fatigue cracks interacting with grain boundaries," *Acta Materialia*, vol. 59, pp. 1849–1861, 2011.

[147] Castelluccio, G. and McDowell, D., "A mesoscale approach for growth of 3D microstructurally small fatigue cracks in polycrystals," *International Journal of Damage Mechanics*, pp. 1–28, 2013.

[148] E647-11, *Standard Test Method for Measurement of Fatigue Crack Growth Rates*. ASTM International, 2011.

[149] Caton, M., Rosenberger, A., Gockel, B., Jha, S., and Szczepanski, C., "Developing the capability to monitor small fatigue crack growth under elevated temperature, ultra-high vacuum conditions," Tech. Rep. AFRL-RX-WP-TP-2011-4236, 2011.

[150] Raju, I. and Newman, J., "Stress-intensity factors for a wide range of semi-elliptical surface cracks in finite-thickness plates," *Engineering Fracture Mechanics*, vol. 11, no. 4, pp. 817–829, 1979.

[151] Jha, S. K., John, R., and Larsen, J. M., "Incorporating small fatigue crack growth in probabilistic life prediction: Effect of stress ratio in ti-6Al-2Sn-4Zr-6Mo," *International Journal of Fatigue*, vol. 51, pp. 83–95, 2013.

[152] Murakami, Y. and Endo, M., "Quantitative evaluation of fatigue strength of metals containing various small defects or cracks," *Engineering Fracture Mechanics*, vol. 17, no. 1, pp. 1–15, 1983.

[153] Murakami, Y., Kodama, S., and Konuma, S., "Quantitative evaluation of effects of non-metallic inclusions on fatigue strength of high strength steels. i: Basic fatigue mechanism and evaluation of correlation between the fatigue fracture stress and the size and location of non-metallic inclusions," *International Journal of Fatigue*, vol. 11, pp. 291–298, Sept. 1989.

[154] Murakami, Y. and Usuki, H., "Quantitative evaluation of effects of non-metallic inclusions on fatigue strength of high strength steels. II: fatigue limit evaluation based on statistics for extreme values of inclusion size," *International Journal of Fatigue*, vol. 11, pp. 299–307, Sept. 1989.

[155] Huron, E. and Roth, P., "The influence of inclusions on low cycle fatigue life in a P/M nickel-base disk superalloy," in *Superalloys 1996*, pp. 359–368, 1996.

[156] Jablonski, D., "The effect of ceramic inclusions on the low cycle fatigue life of low carbon astroloy subjected to hot isostatic pressing," *Materials Science and Engineering*, vol. 48, pp. 189–198, May 1981.

[157] Jha, S. K., Caton, M., and Larsen, J., "The mean vs life-limiting fatigue response of a ni-base superalloy, part 1: mechanisms," Tech. Rep. AFRL-RX-WP-TP-2009-4210, Sept. 2008.

[158] Caton, M., Jha, S., Rosenberger, A., and Larsen, J., "Divergence of mechanisms and the effect on the fatigue life variability of rene' 88 DT," in *Superalloys 2004*, (Champion, PA, United states), pp. 305–312, TMS, 2004.

[159] Findley, K. and Saxena, A., "Low cycle fatigue in rene 88DT at 650 C: crack nucleation mechanisms and modeling," *Metallurgical and Materials Transactions A*, vol. 37, pp. 1469–1475, May 2006.

[160] Ravi Chandran, K., Chang, P., and Cashman, G., "Competing failure modes and complex s-n curves in fatigue of structural materials," *International Journal of Fatigue*, vol. 32, pp. 482–491, Mar. 2010.

[161] Cashman, G., "A mathematical model for competing failure modes in strain cycle fatigue," *Journal of Engineering Materials and Technology*, vol. 129, pp. 293–303, 2007.

[162] Cashman, G., "A review of competing modes fatigue behavior," *International Journal of Fatigue*, vol. 32, pp. 492–496, 2010.

[163] Sakai, T., Lian, B., Takeda, M., Shiozawa, K., Oguma, N., Ochi, Y., Nakajima, M., and Nakamura, T., "Statistical duplex s-n characteristics of high carbon chromium bearing steel in rotating bending in very high cycle regime," *International Journal of Fatigue*, vol. 32, pp. 497–504, Mar. 2010.

[164] Wusatowska-Sarnek, A., Bhowal, P., Gynther, D., and Montero, R., "Effect of non-metallic inclusions on notched low cycle fatigue in P/M IN100 nickel-base superalloy," in *5th International Conference on Processing and Manufacturing of Advanced Materials*, vol. 539-543, (Vancouver, Canada), pp. 2960–2965, 2007.

[165] Pineau, A., "Superalloy discs durability and damage tolerance in relation to inclusions," *Proceedings of a Conference on High Temperature Materials for Power Engineering 1990*, pp. 913–934, 1990.

[166] Weibull, W., "A statistical distribution function of wide applicability," *J. Appl. Mech.-Trans. ASME*, vol. 18, no. 3, pp. 293–297, 1951.

[167] Gumbel, E., *Statistics of Extremes*. Columbia University Press, New York, NY, 1958.

[168] Todinov, M., "Probability distribution of fatigue life controlled by defects," *Computers and Structures*, vol. 79, pp. 313–318, 2001.

[169] Todinov, M., "Equations and a fast algorithm for determining the probability of failure initiated by flaws," *International Journal of Solids and Structures*, vol. 43, pp. 5182–5195, 2006.

[170] Wormsen, A., Sjodin, B., Harkegard, G., and Fjeldstad, A., "Non-local stress approach for fatigue assessment based on weakest-link theory and statistics of extremes," *Fatigue & Fracture of Engineering Materials & Structures*, vol. 30, no. 12, pp. 1214–1227, 2007.

[171] Besel, M., Bruckner-Foit, A., Motoyashiki, Y., and Schafer, O., "Lifetime distribution of notched components containing void defects," *Archive of Applied Mechanics*, vol. 76, pp. 645–653, Dec. 2006.

[172] Doudard, C., Calloch, S., Cugy, P., Galtier, A., and Hild, F., "A probabilistic two-scale model for high-cycle fatigue life predictions.," *Fatigue & Fracture of Engineering Materials & Structures*, vol. 28, pp. 279–288, Mar. 2005.

[173] Przybyla, C. P. and McDowell, D. L., "Simulated microstructure-sensitive extreme value probabilities for high cycle fatigue of duplex ti-6Al-4V," vol. 27 of *International Journal of Plasticity*, pp. 1871–1895, 2011.

[174] Smith, B., Shih, D., and McDowell, D., "Fatigue hot spot simulation for two widmanstatten titanium microstructures," *International Journal of Fatigue*, 2013.

[175] Prasannavenkatesan, R., Przybyla, C. P., Salajegheh, N., and McDowell, D., "Simulated extreme value fatigue sensitivity to inclusions and pores in martensitic gear steels," *Engineering Fracture Mechanics*, vol. 78, pp. 1140–1155, Apr. 2011.

[176] Weibull, W., "Statistical theory of strength of materials," *Ingeniors Vetenskaps Akademien – Handlingar*, no. 151, p. 45, 1939.

[177] Deyber, S., Alexandre, F., Vaissaud, J., and Pineau, A., "Probabilistic life of DA718 for aircraft engine disks," in *Superalloys 718,625,706 and Derivatives*, (Warrendale, PA, USA), pp. 97–110, TMS, 2005.

[178] Tomkins, B., "Fatigue crack propagation-an analysis," *Philosophical Magazine*, vol. 18, no. 155, pp. 1041–66, 1968.

[179] de Bussac, A., "Prediction of the competition between surface and internal fatigue crack initiation in PM alloys," *Fatigue and Fracture of Engineering Materials and Structures*, vol. 17, no. 11, pp. 1319–1325, 1994.

[180] Jha, S., Caton, M., and Larsen, J., "The mean vs life-limiting fatigue response of a ni-base superalloy, part 2: life prediction methodology," Tech. Rep. AFRL-RX-WP-TP-2009-4212, Sept. 2008.

[181] Jha, S., Caton, M., and Larsen, J., "A new paradigm of fatigue variability behavior and implications for life prediction," *Materials Science and Engineering: A*, vol. 468-470, pp. 23–32, Nov. 2007.

[182] Larsen, J., Jha, S., Szczepanski, C., Caton, M., John, R., Rosenberger, A., Buchanan, D., Golden, P., and Jira, J., "Reducing uncertainty in fatigue life limits of turbine engine alloys," *International Journal of Fatigue*, 2014.

[183] Jha, S. K., Larsen, J. M., Rosenberger, A. H., and Hartman, G. A., "Dual fatigue failure modes in ti-6Al-2Sn-4Zr-6Mo and consequences on probabilistic life prediction," *Scripta Materialia*, vol. 48, pp. 1637–1642, June 2003.

[184] Musinski, W. and McDowell, D., "Microstructure-sensitive probabilistic fatigue of ni-base superalloy IN100: modeling the effect of inclusions on strain-life curve in the HCF and VHCF regimes," in *VHCF-5* (Berger, C. and Christ, H.-J., eds.), (Berlin, Germany), pp. 231–236, June 2011.

[185] Cowles, B., Warren, J., and Haake, F., "Evaluation of the cyclic behavior of aircraft turbine disk alloys, part II," Tech. Rep. NASA CR-165123, 1980.

[186] Bathias, C. and Paris, P. C., "Gigacycle fatigue of metallic aircraft components," *International Journal of Fatigue*, vol. 32, pp. 894–897, June 2010.

[187] Cashman, G., "A perspective on competing modes fatigue behavior," (Pittsburgh, PA), 2008.

[188] Shenoy, M. M., Kumar, R. S., and McDowell, D. L., "Modeling effects of nonmetallic inclusions on LCF in DS nickel-base superalloys," *International Journal of Fatigue*, vol. 27, no. 2, pp. 113–127, 2005.

[189] Owolabi, G., Prasannavenkatesan, R., and McDowell, D., "Probabilistic framework for a microstructure-sensitive fatigue notch factor," *International Journal of Fatigue*, vol. 32, pp. 1378–1388, Aug. 2010.

[190] Owolabi, G. and Whitworth, H., "Modeling and simulation of microstructurally small crack formation and growth in notched ni-base superalloy component," *Journal of Materials Science & Technology*, pp. 1–10, 2013.

[191] Murakami, Y., "Material defects as the basis of fatigue design," *International Journal of Fatigue*, 2012.

[192] Fan, J. H., McDowell, D. L., Horstemeyer, M. F., and Gall, K., "Cyclic plasticity at pores and inclusions in cast al-si alloys," *Engineering Fracture Mechanics*, vol. 70, no. 10, pp. 1281–1302, 2003.

[193] Zeid, I., *Mastering CAD/CAM*. McGraw-Hill, New York, NY, first ed., 2004.

[194] Shenoy, M., Zhang, J., and McDowell, D. L., "Estimating fatigue sensitivity to polycrystalline ni-base superalloy microstructures using a computational approach," *Fatigue & Fracture of Engineering Materials & Structures*, vol. 30, no. 10, pp. 889–904, 2007.

[195] Khan, A. and Huang, S., *Continuum Theory of Plasticity*. John Wiley & Sons, Inc., New York, NY, 1995.

[196] Soga, N. and Anderson, O. L., "High-temperature elastic properties of polycrystalline MgO and Al2O3," *Journal of the American Ceramic Society*, vol. 49, pp. 355–359, July 1966.

[197] Shackelford, J. F., Alexander, W., and Park, J. S., *CRC Materials Science and Engineering Handbook*. CRC Press, Boca Raton, FL, second ed., 1994.

[198] Anderson, T., *Fracture Mechanics - Fundamentals and Applications*. Taylor & Francis Group, Boca Raton, FL, third ed., 2005.

[199] Golden, P. and Grandt Jr., A., "Fracture mechanics based fretting fatigue life predictions in ti-6Al-4V," *Engineering Fracture Mechanics*, vol. 71, pp. 2229–2243, 2004.

[200] Shen, G. and Glinka, G., "Determination of weight functions from reference stress intensity factors," *Theoretical and Applied Fracture Mechanics*, vol. 15, pp. 237–245, 1991.

[201] Newman Jr., J. and Raju, I., "Stress-intensity factor equations for cracks in three-dimensional finite bodies subjected to tension and bending loads," Tech. Rep. NASA TM-85793, Apr. 1984.

[202] Golden, P., *High cycle fatigue of fretting induced cracks*. Ph.D., Purdue University, 2001.

[203] Shiozawa, K. and Lu, L., "Very high-cycle fatigue behaviour of shot-peened high-carbon-chromium bearing steel," *Fatigue & Fracture of Engineering Materials and Structures*, vol. 25, pp. 813–822, Sept. 2002.

[204] Larsson, M., Melander, A., Blom, R., and Preston, S., "Effects of shot peening on bending fatigue strength of spring steel SS 2090," *Materials Science and Technology*, vol. 7, pp. 998–1004, Nov. 1991.

[205] Montross, C. S., Wei, T., Ye, L., Clark, G., and Mai, Y.-W., "Laser shock processing and its effects on microstructure and properties of metal alloys: a review," *International Journal of Fatigue*, vol. 24, pp. 1021–1036, Oct. 2002.

[206] Peyre, P., Fabbro, R., Merrien, P., and Lieurade, H. P., "Laser shock processing of aluminium alloys. application to high cycle fatigue behaviour," *Materials Science and Engineering A*, vol. 210, pp. 102–113, June 1996.

[207] Ravi Chandran, K. and Jha, S., "Duality of the s-n fatigue curve caused by competing failure modes in a titanium alloy and the role of poisson defect statistics," *Acta Materialia*, vol. 53, pp. 1867–1881, Apr. 2005.

[208] Tokaji, K., Ohya, K., and Kariya, H., "Subsurface fatigue crack initiation in beta titanium alloys," *Fatigue and Fracture of Engineering Materials and Structures*, vol. 23, no. 9, pp. 759–766, 2000.

[209] Shiozawa, K., Hasegawa, T., Kashiwagi, Y., and Lu, L., "Very high cycle fatigue properties of bearing steel under axial loading condition," *International Journal of Fatigue*, vol. 31, pp. 880–888, May 2009.

[210] Wang, Q., Berard, J., Dubarre, A., Baudry, G., Rathery, S., and Bathias, C., "Gigacycle fatigue of ferrous alloys," *Fatigue and Fracture of Engineering Materials and Structures*, vol. 22, no. 8, pp. 667–672, 1999.

[211] John, R., Buchanan, D. J., Caton, M. J., and Jha, S. K., "Stability of shot peen residual stresses in IN100 subjected to creep and fatigue loading," *Procedia Engineering*, vol. 2, pp. 1887–1893, Apr. 2010.

[212] Barrie, R., Gabb, T., Telesman, J., Kantzos, P., Prescenzi, A., Biles, T., and Bonacuse, P., "Effectiveness of shot peening in suppressing fatigue cracking at non-metallic inclusions in udimet 720," *Materials Science and Engineering: A*, vol. 474, pp. 71–81, Feb. 2008.

[213] Konig, G., "Life enhancement of aero engine components by shot peening: opportunities and risks," in *ICSP-8 Sept. 16-20*, (Garmisch-Partenkirchen, Germany), 2002.

[214] Kirk, D., "Effects of plastic straining on residual stresses induced by shot-peening," in *ICSP-3*, pp. 213–220, 1987.

[215] McClinton, M. and Cohen, J., "Changes in residual stress during the tension fatigue of normalized and peened SAE 1040 steel," *Materials Science and Engineering*, vol. 56, pp. 259–263, Dec. 1982.

[216] Prevey, P., "The effect of cold work on the thermal stability of residual compression in surface enhanced IN718," in *Heat Treating: Proceedings of the 20th Conference*, vol. 1, (St. Louis, MO, United states), pp. 426–434, ASM International, 2000.

[217] Prasannavenkatesan, R., *Microstructure-sensitive fatigue modeling of heat treated and shot peened martensitic gear steels*. PhD thesis, Georgia Institute of Technology, 2009.

[218] Prasannavenkatesan, R. and McDowell, D., "Polycrystal plasticity modeling of cyclic residual stress relaxation in shot peened martensitic gear steel," *Journal of Engineering Materials and Technology*, vol. 132, pp. 031011–1–8, 2010.

[219] Boyce, B. L., Chen, X., Hutchinson, J. W., and Ritchie, R. O., "The residual stress state due to a spherical hard-body impact," *Mechanics of Materials*, vol. 33, pp. 441–454, Aug. 2001.

[220] Chen, X. and Hutchinson, J. W., "Foreign object damage and fatigue crack threshold: Cracking outside shallow indents," *International Journal of Fracture*, vol. 107, pp. 31–51, Jan. 2001.

[221] Chen, X. and Hutchinson, J. W., "Particle impact on metal substrates with application to foreign object damage to aircraft engines," *Journal of the Mechanics and Physics of Solids*, vol. 50, pp. 2669–2690, Dec. 2002.

[222] Frija, M., Hassine, T., Fathallah, R., Bouraoui, C., and Dogui, A., "Finite element modelling of shot peening process: Prediction of the compressive residual stresses, the plastic deformations and the surface integrity," *Materials Science and Engineering: A*, vol. 426, pp. 173–180, June 2006.

[223] Schulze, V., Klemenz, M., and Zimmermann, M., "State of the art in shot peening simulation," in *ICSP-10*, (Tokyo, Japan), 2008.

[224] Zimmermann, M., Schulze, V., Baron, H., and Lohe, D., "A novel 3D finite element simulation model for the prediction of the residual stress state after shot peenine," in *ICSP-10*, (Tokyo, Japan), 2008.

[225] Satraki, M., Evans, A., King, A., Bruno, G., and Withers, P., "Eigenstrain generated by shot peening in udimet 720Li inferred by means of finite element and analytical models," in *ICSP-9*, pp. 442–447, 2005.

[226] Korsunsky, A., "On the modelling of residual stresses due to surface peening using eigenstrain distributions," *The Journal of Strain Analysis for Engineering Design*, vol. 40, no. 8, pp. 817–824, 2005.

[227] Zion, H. and Johnson, W., "Parametric two-dimensional finite element investigation: Shot peening of high-strength steel," *AIAA Journal*, vol. 44, no. 9, pp. 1973–1982, 2006.

[228] Brockman, R. A., Braisted, W. R., Olson, S. E., Tenaglia, R. D., Clauer, A. H., Langer, K., and Shepard, M. J., "Prediction and characterization of residual stresses from laser shock peening," *International Journal of Fatigue*, 2011.

[229] Buchanan, D., *A coupled creep-plasticity model for residual stress relaxation of a shot-peened nickel-base superalloy.* Ph.D., University of Dayton, 2007.

[230] Benedetti, M., Fontanari, V., and Monelli, B., "Numerical simulation of residual stress relaxation in shot peened high-strength aluminum alloys under reverse bending fatigue," *Journal of Engineering Materials and Technology*, vol. 132, pp. 011012–1–9, 2010.

[231] Benedetti, M., Fontanari, V., Santus, C., and Bandini, M., "Notch fatigue behaviour of shot peened high-strength aluminium alloys: Experiments and predictions using a critical distance method," *International Journal of Fatigue*, vol. 32, pp. 1600–1611, Oct. 2010.

[232] Cao, Y., Hu, N., Lu, J., Fukunaga, H., and Yao, Z., "An inverse approach for constructing the residual stress field induced by welding," *The Journal of Strain Analysis for Engineering Design*, vol. 37, no. 4, pp. 345–359, 2002.

[233] Qian, X., Yao, Z., Cao, Y., and Lu, J., "An inverse approach for constructing residual stress using BEM," *Engineering Analysis with Boundary Elements*, vol. 28, pp. 205–211, 2004.

[234] Qian, X., Yao, Z., Cao, Y., and Lu, J., "An inverse approach to construct residual stresses existing in axisymmetric structures using BEM," *Engineering Analysis with Boundary Elements*, vol. 29, pp. 986–999, 2005.

[235] Jun, T.-S. and Korsunsky, A. M., "Evaluation of residual stresses and strains using the eigenstrain reconstruction method," *International Journal of Solids and Structures*, vol. 47, pp. 1678–1686, June 2010.

[236] Song, X., Liu, W., Belnoue, J., Dong, J., Wu, G., Ding, W., Kimber, S., Buslaps, T., Lunt, A., and Korsunsky, A., "An eigenstrain-based finite element model and the evolution of shot peening residual stresses during fatigue of GW103 magnesium alloy," *International Journal of Fatigue*, 2012.

[237] Achintha, M. and Nowell, D., "Eigenstrain modelling of residual stresses generated by arrays of LSP shots," *Procedia Engineering*, vol. 10, pp. 1327–1332, 2011.

[238] Achintha, M. and Nowell, D., "Eigenstrain modelling of residual stresses generated by laser shock peening," *Journal of Materials Processing Technology*, vol. 211, pp. 1091–1101, 2011.

[239] Achintha, M., Nowell, D., Fufari, D., Sackett, E., and Bache, M., "Fatigue behaviour of geometric features subjected to laser shock peening: Experiments and modelling," *International Journal of Fatigue*, pp. 1–9, 2013.

[240] Webster, G. and Ezeilo, A., "Residual stress distributions and their influence on fatigue lifetimes," *International Journal of Fatigue*, vol. 23, pp. S375–S383, 2001.

[241] Tufft, M., "Shot peen impact on life, part 3: Development of a fracture mechanics / threshold behavior predictive model," in *ICSP-7*, (Warsaw, Poland), pp. 264–273, 1999.

[242] Tufft, M., "Modeling of fatigue behavior due to shot peening conditions," in *ICSP-8*, (Munich, Germany), pp. 530–539, 2002.

[243] Malvern, L. E., *Introduction to the Mechanics of a Continuous Medium*. Prentice-Hall, Inc., Englewood Cliffs, NJ, 1969.

[244] Buchanan, D. J., John, R., and Brockman, R. A., "Relaxation of shot-peened residual stresses under creep loading," *Journal of Engineering Materials and Technology*, vol. 131, pp. 031008–10, July 2009.

[245] Buchanan, D., John, R., Brockman, R., and Rosenberger, A., "A coupled creep plasticity model for residual stress relaxation of a shot-peened nickel-based superalloy," *JOM Journal of the Minerals, Metals and Materials Society*, vol. 62, pp. 75–79, Jan. 2010.

[246] Chapra, S. and Canale, R., *Numerical Methods for Engineers*. McGraw-Hill, New York, NY, 2002.

[247] Groeber, M., Ghosh, S., Uchic, M. D., and Dimiduk, D. M., "A framework for automated analysis and simulation of 3D polycrystalline microstructures. part 2: Synthetic structure generation," *Acta Materialia*, vol. 56, pp. 1274–1287, Apr. 2008.

[248] Groeber, M., Ghosh, S., Uchic, M. D., and Dimiduk, D. M., "A framework for automated analysis and simulation of 3D polycrystalline microstructures.: Part 1: Statistical characterization," *Acta Materialia*, vol. 56, pp. 1257–1273, Apr. 2008.

[249] Dalaei, K. and Karlsson, B., "Influence of shot peening on fatigue durability of normalized steel subjected to variable amplitude loading," *International Journal of Fatigue*, vol. 38, pp. 75–83, May 2012.

[250] Holzapfel, H., Schulze, V., Vohringer, O., and Macherauch, E., "Residual stress relaxation in an AISI 4140 steel due to quasistatic and cyclic loading at higher temperatures," *Materials Science and Engineering*, vol. A248, pp. 9–18, 1998.

[251] Wick, A., Schulze, V., and Vohringer, O., "Effects of warm peening on fatigue life and relaxation behaviour of residual stresses in AISI 4140 steel," *Materials Science and Engineering*, vol. A293, pp. 191–197, 2000.

[252] Zhuang, W. Z. and Halford, G. R., "Investigation of residual stress relaxation under cyclic load," *International Journal of Fatigue*, vol. 23, no. Supplement 1, pp. 31–37, 2001.

[253] Zaroog, O. S., Ali, A., Sahari, B., and Zahari, R., "Modeling of residual stress relaxation of fatigue in 2024-t351 aluminium alloy," *International Journal of Fatigue*, vol. 33, pp. 279–285, Feb. 2011.

[254] Castelluccio, G. and McDowell, D., "Mesoscale modeling of microstructurally small fatigue cracks in metallic polycrystals," *Materials Science & Engineering A*, vol. 598, pp. 34–55, 2014.

[255] Proudhon, H., Moffat, A., Sinclair, I., and Buffiere, J.-Y., "Three-dimensional characterisation and modelling of small fatigue corner cracks in high strength al-alloys," *Comptes Rendus Physique*, vol. 13, pp. 316–327, 2012.

[256] Stock, S. R., "Recent advances in x-ray microtomography applied to materials," *International Materials Reviews*, vol. 53, pp. 129–181, May 2008.

[257] DARWIN, *User's Guide*. 2008.